Scale-up of nanoparticle fabrication via laser ablation synthesis in solution

Brian Freeland, M.Sc. B.Eng (Hons)

Thesis Submitted for the Award of Doctor of Philosophy (PhD)

School of Mechanical & Manufacturing Engineering

Dublin City University

Supervisor: Prof. Dermot Brabazon
Co-supervisor: Assoc. Prof. Greg Foley

March 2020

Declaration

I hereby certify that this material, which I now submit for assessment on the programme of study leading to the award of PhD in Mechanical and Manufacturing Engineering is entirely my own work, that I have exercised reasonable care to ensure that the work is original, and does not to the best of my knowledge breach any law of copyright, and has not been taken from the work of others save and to the extent that such work has been cited and acknowledged within the text of my work.

Signed: _____ (Candidate) ID No.: 51730207, Date: _____

Dedication

Dedicated to the memory of my father, Joseph Freeland who encouraged his children to

follow their dreams.

Acknowledgements

Publications

This work has been disseminated through the following publications;

Book Chapters

Chapter 2

1. Pulsed Laser Ablation in Liquid (PLAL) for nano-particle generation, B. Freeland, E. McCarthy, G. Foley & D. Brabazon, In: IoP Laser processing (Accepted May 2020).

2. Advanced Characterisation Techniques for Nanostructures, Brian Freeland, Inam Ul Ahad, Greg Foley & Dermot Brabazon (2017), In: 'Micro and Nanomanufacturing' UK: Elsevier.

Peer reviewed papers

Chapter 3

1. High-efficiency generation of nanomaterials via laser ablation synthesis in solution with in-situ diagnostics for closed-loop control, B. Freeland, R. McCann, G. Foley, D. Brabazon, Proc. SPIE 11269, Synthesis and Photonics of Nanoscale Materials XVII, 112690M. (Published 2nd March).

2. Flow-regime and laser wavelength optimization of Silicon Nanoparticle fabrication via laser ablation synthesis in solution (LASiS), B. Freeland, R. McCann, P. O'Neill, K. Bagga, G. Foley, D. Brabazon, 22nd Sir Bernard Crossland event, Ulster University, 17th - 18th April 2019.

Chapter 4

1. Real-time monitoring and control for high-efficiency autonomous laser fabrication of Silicon nanoparticle colloids, B. Freeland, R. McCann, P. O'Neill, S. Sreenilayam, M. Tiefenthaler, M. Dabros, M. Juillerat, G. Foley and D. Brabazon, International Journal of Precision Engineering and Manufacturing-Green Technology, (Under peer review May 2020).

Chapter 6

1. Stable nano-silver colloid production via Laser Ablation Synthesis in Solution (LASiS) under laminar recirculatory flow, B. Freeland, R. McCann, G. Foley, D. Brabazon, Advances in Materials & Processing Technologies, (Published 15th March 2020).

Other papers

1. Control of specific growth rate in fed-batch bioprocesses: novel controller design for improved noise management, Y. Brignoli, B. Freeland & M. Dabros, MDPI Processes (Accepted June 2020).

2. A High-Density Yeast Propagation System for Brewery Yeast, D. Donnelly, L. Blanchard, M. Dabros, S. O'Hara, D. Brabazon, G. Foley and B. Freeland, Journal of American Society of Brewing Chemists (Under peer review May 2020).

Conferences oral presentations

1. High-efficiency generation of nanomaterials via laser ablation synthesis in solution with in-situ diagnostics for closed-loop control, R.McCann, B. Freeland, G.Foley, D.Brabazon, Paper Number 11269-22, Synthesis and Photonics of Nanoscale Materials XVII, Paper Number 11269-22, SPIE LASE, 1 - 6 February 2020, San Francisco, California United States.

2. 22nd Sir Bernard Crossland Symposium, B Freeland, R McCann, P.O'Neill1, K.Bagga, G.Foley and D.Brabazon (2019), Flow-regime and laser wavelength optimization of Silicon Nanoparticle fabrication via laser ablation synthesis in solution (LASiS) 22nd Sir Bernard Crossland Symposium Belfast, University of Ulster, , 17-APR-19 - 18-APR-19.

3. Advances in Materials and Processing Technologies (AMPT), B.Freeland,R.McCann, T.Stornetta, P.O'Neill, G.Foley, D.Brabazon (2018) Scalable laser based synthesis of nanoparticles via integrative process control. [Oral Presentation], Advances in Materials and Processing Technologies (AMPT), Dublin City University, 03-SEP-18 - 07-SEP-18.

4. Applied Microbial bioprocessing research, B.Freeland (2018) Science Faculty Research conversations. [Oral Presentation], Applied Microbial bioprocessing research, DCU.

5. Bioprocessing India 2017, B Freeland, R McCann, K Bagga, P O Neill, G Foley, D Brabazon (2017) Targeted laser-based synthesis of nanoparticles for biotechnology. [Invited Oral Presentation], Bioprocessing India 2017, Guwahati, India, 09-DEC-17 - 11-MAR-18.

6. ESAFORM 2017, B Freeland, R McCann, K Bagga, P O'Neill, G Foley, D Brabazon (2017) Nanoparticle fabrication via pulsed laser ablation in liquids: Steps towards scale up. [Invited Oral Presentation], ESAFORM 2017, Dublin, 26-APR-17 - 26-MAY-17.

7. ACTTiVAte, Horizon 2020, B.Freeland, D.Brabazon (2016) APT Elevator pitch. [], ACTTiVAte, Horizon 2020, Madrid.

8. On-line Dynamic Light Scattering Measurement for Real time Control of Nanoparticle. B Freeland, R McCann, K Bagga, P O'Neill, G Foley, D Brabazon (November 2017). Online Article.

9. Advantages of the 180° Frequency Power Spectrum (FPS) Method in DLS. B Freeland, R McCann, K Bagga, P O'Neill, G Foley, D Brabazon (2017). Online Article.

Conferences poster presentations
1. Laser direct writing and colloidal ink jetting for conductive track fabrication on organic substrates, R. McCann, C. Hughes, B. Freeland, D. Brabazon (2018) NANOTEXNOLOGY 2018. [Conference Organising Committee Chairperson], Laser direct writing and colloidal ink jetting for conductive track fabrication on organic substrates, Thessaloniki, Greece, 30-JUN-18 - 07-JUL-18.

2. COLA 2017, B.Freeland, R.McCann, K.Bagga, P.Pulito, A.Nogue, G.Foley and D.Brabazon (2017) Optimisation of Multi-wavelength continuous nanoparticle fabrication via Pulsed Laser Ablation in Liquids. [Conference Organising Committee Chairperson], COLA 2017, Marseille, 03-SEP-17 - 08-SEP-17.

3. Materials Science & Technology 2016, K. Bagga, R. McCann, R. Groarke, B. Freeland, M. Vázquez, D. Brabazon, (2016) Laser assisted synthesis of ligand free nanostructures for sensing applications. [], Materials Science & Technology 2016, Salt Lake City, UT, USA, 23-OCT-16 - 27-OCT-16.

4. IOP Spring Meeting, R.McCann, C.Hughes, B.Freeland, K.Bagga, R.Groarke, A.Stalcup, M.Vázquez, D.Brabazon (2016) Confined atmospheric pulsed laser

deposition: A new route to nanostructured ultrathin films. [Poster Presentation], IOP Spring Meeting, (Belfast , 20-FEB-16 - 21-FEB-16.

5. 4th Conference on Advanced Nanoparticle Generation and Excitation by Lasers in Liquids, B.Freeland, K.Bagga, R.McCann, E.McCarthy, G.Foley, R.O'Kennedy, D.Brabazon (2016) Laser assisted synthesis of nanostructures with controlled viscosity for printing and biological sensing applications. [Poster Presentation], 4th Conference on Advanced Nanoparticle Generation and Excitation by Lasers in Liquids, Essen, Germany , 09-MAY-16 - 12-MAY-16.

Table of Contents

Table of Figures

xv

xvii

List of Tables

List of abbreviations

2FI – Two factor interaction

AES - Auger electron spectroscopy

ANN - Artificial Neural Network

ANOVA - Analysis of Variance

ATR - Attenuated total reflection

AU – Absorbance units

CIP - Clean in place

CNT - Carbon nanotube

COP - Cyclic olefin polymer

CPPs - Critical process parameters

CSV - Comma separated variable

DI - Deionized

DLS - Dynamic light scattering

DOE - Design of experiments

DoF – Degrees of freedom

F - Fluence

FDA - Food and drug association

FESEM - Field emission scanning electron microscopy

FFD - Full factorial design

FR - Liquid flowrate

FRET - Fluorescence resonance energy transfer

FTIR - Fourier-transform infrared spectroscopy

LASiS - Laser Ablation Synthesis in Solution

LOD – Limit of detection

LP - Laser command power

MPC - Model predictive control

MRE – Mean relative error

Nd:YAG - Neodymium-doped yttrium aluminium   garnet

NIR – Near infrared

Nps - Nanoparticles

OD – Outer diameter

P - Pressure

PAT - Process analytical technology

PLAL - Laser ablation in liquids

PPTT - Plasmonic photo-thermal therapy

Q - Liquid mass flowrate

QbD - Quality by Design

RR - Repetition rate

SEM - Scanning electron microscopy

SPR - Surface plasmon response

SS - Beam scan speed

STP - Signal transduction probe

TEM - Transmission electron microscopy

THMS - Triple helix molecular switch

USP - Ultra-sonic Spray Pyrolysis

UV-vis - Ultraviolet–visible spectroscopy

XPS - X-ray photoelectron spectroscopy

List of symbols

Symbol	Description	Units
A	Area	[m^2]
α	Absorption coefficient	[cm^{-1}]
θ	Angle	[degrees]
% wt	Percentage weight	[-]
D_1	Inlet pipe diameter	[m]
D_2	Internal flow cell diameter at target	[m]
D_{hyd}	Wetted or hydro diameter	[m]
D_i	Thermal diffusivity	[cm^2 s^{-1}]
D_t	Target diameter	[m]
D_{th}	Thermal diffusion distance	[nm]
e	Euler's constant	[-]
E_0	Pulse energy output from laser optics	[μJ]
E_m	Fluorescence emission wavelength	[nm]
F_0	Fluence output from laser optics	[J/cm^2]
F_t	Applied fluence on the target in air	[J/cm^2]
F_{th}	Target fluence threshold	[J/cm^2]
F_{th}^{app}	Apparent fluence threshold	[J/cm^2]
k	Laser energy penetration depth	[nm]
M_a	Ablated mass per pulse	[ng]
η	Ablation efficiency coefficient	[g/J]
p_{amb}	Ambient pressure of liquid	[kPa]
P_{ave}	Average laser output power	[W]
p_v	Cavitation bubble pressure	[kPa]
ρ	Density of liquid/solid	kg/m^3
R_{max}	Maximum bubble radius	[μm]
s	Laser beam cross sectional area on target	[μm^2]
S_0	Laser beam cross sectional area in air	[μm^2]
σ	Sample/population standard deviation	[-]
Σ	Process standard deviation	[-]

T	Depth of material removed per pulse	[nm]
t_c	Time interval between max. radius extension to collapse	[s]
τ_p	Pulse duration	[ps]
$\overline{x}$	Process mean	[-]

Abstract

Scale-up of nanoparticle fabrication via laser ablation synthesis in solution
Brian Freeland

Throughout the previous decade, extensive advancements have been made in the field of nanomaterial synthesis via laser ablation synthesis in solution (LASiS). In this technique, a solid target is ablated using high-intensity pulsed laser irradiation while immersed in a liquid. This "green" technique allows ligand-free nanoparticles (Nps) to be fabricated without the need for environmentally harmful solvents, paving the way for the production of chemically pure surface coatings. LASiS allows for an in-situ, single-step and post-production surface functionalization, enabling its use in areas such as chemical separation, biosensing, cellular labelling, display technology. Despite these advances, the challenge of reliable production scale-up from batch to continuous production has yet to be realized. A current approach to LASiS scale-up has been to increase average laser power, while minimizing pulse width, resulting in an increased nanoparticle production rate. However, this route on its own has struggled to bridge the commercialization gap with chemical techniques due to the high capital costs of high-power laser systems. In this work, LASiS scale-up has been implemented under continuous flow conditions using low-powered micro-machining laser systems. A 3D printed Nps flow-cell reactor was developed, along with the application of real-time monitoring and control tools to enable autonomous nanoparticle production and characterization. The quality of nano-colloids produced was determined in real-time via at-line process analyzers, including dynamic light scattering (DLS) and UV-vis spectroscopy. At-line measurements were validated versus off-line characterization tools, including Transmission Electron Microscopy (TEM). Process optimization of the developed system yielded the highest Np production efficiencies to date in reported in literature for gold, silicon and zinc oxide nanoparticles. This work concludes that high-efficiency, low-cost laser systems can produce Nps that are comparable with wet chemical synthesis, while maintaining the environmental and functional advantages of the LASiS technique.

Chapter 1: Introduction

1.1 Motivation and context

Owing to their unique chemical and biological functionality, high surface area, superior electrical and mechanical properties compared to their bulk counterparts, nanomaterials are finding increased use in a variety of fields and technologies in recent times including separation science [1], display technology [2], drug delivery [3]–[15], bio-sensing [10], [12] and anti-microbial surfaces [16]–[24]. Significant to this work, silicon (SiNps) nanomaterials have been finding applications in electronics and biomedical fields such as for energy storage [25], printable electronics [26], [27], functional materials for lab-on-a-chip systems [28] and drug delivery [29]. Recently, our group has reported the use of these laser synthesized nanomaterials for use in biomimetic surfaces [30] and biological sensing applications [31].

To-date, wet chemical techniques have been successful in the creation of commercial quantities of nanomaterials. However, these techniques frequently require the use of environmentally harmful solvents and reagents and produce nanoparticles with precursors or stabilizers on their surface which must be removed prior to further functionalization. A new approach for the "green" synthesis of nanomaterials via "Pulsed Laser Ablation in Liquid" (PLAL), more recently known as "Laser Ablation Synthesis in Solution" (LASiS) is developed in this work. LASiS offers unique control over the morphology of the produced nanomaterials by altering process parameters such as laser fluence, wavelength or ablation medium. In contrast to wet-chemical techniques, the Nps are produced with bare, ligand-free surface chemistry, and without the need for environmentally harmful chemicals as stabilizers. Currently, the LASiS technique cannot compete with chemical synthesis at commercial scale, this work looks to investigate routes towards optimizing the LASiS process to aid commercial viability of the technique in the years to come.

1.2   LASiS mechanism overview

During LASiS a solid metal or composite target is immersed in a solvent and subjected to high-intensity laser irradiation [32]. The solvent is selected according to the Nps surface functionalization properties required. The laser irradiation of the target material surface results in the formation of a plasma confined within the liquid environment [27] as illustrated in Figure 1.1 (*step a*). The energy absorbed by the target surface is released as a shockwave into the liquid, producing a vapor (*step b*). This vapor and molten material form a gas cavitation bubble (*step c*). Within 200 µs [39] the cavitation bubble collapses, producing a second shockwave that expels the Nps into the liquid (*step d*), instantaneously condensing them into solid form as Nps [40], [41]. Generally electrostatic stability of solid metal ions in an aqueous solution is achieved due to partial or full oxidization, occurring as the Np is formed [33].
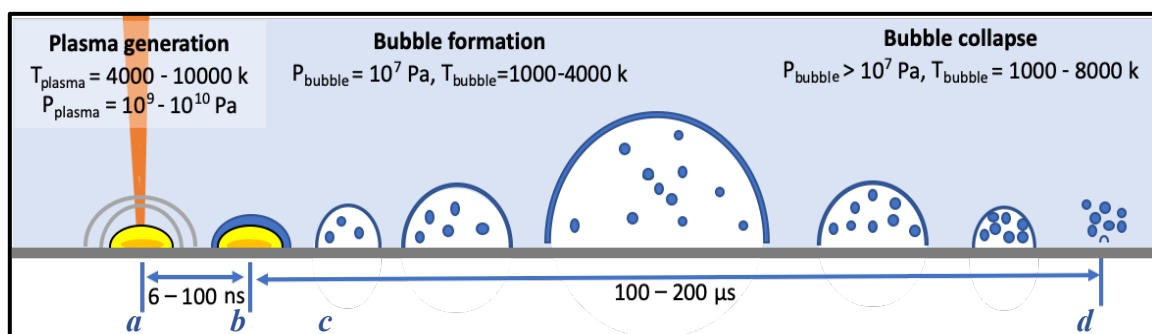
Figure 1.1: Stages of Nps formation during LASiS, image based on optical imaging results published by J.Lam et al.(2014), [34].

LASiS allows for an adaptable process including a wide variety of target materials and solvents allowing for the formation of compound nanoparticles by ablating the target in several solvents, such as; alcohols (forming nano-oxides) or hydrocarbon solvents such as toluene (forming nano-carbides). A further advantage to LASiS is that the nanoparticle surface can be formed without ligands or surfactants, opening the pathway towards single-step post-process functionalization.

1.3   Linking the project to the research field

The majority of LASiS research to-date has been examined in the "static" or "batch" regimes i.e. ablation performed in a container without forced solvent flow. This technique, though successful for fast-optimization of the generated nanomaterial, lacks process scalability due in-part to the nanoparticles saturating the colloid, occluding the laser and reducing ablation efficiency. The additional problems of local thermal effects, and plume occlusion described by [33], [35], [36] & [37] lead to an inefficient production process. Recently, there has been a paradigm shift towards "continuous flow" LASiS; whereby the target is immersed in a continuous solvent flow [38] during ablation, as proposed by Ceinde et al. (2012) [38] and Ceinde et al. (2018). This has the benefit of avoiding colloid saturation, while also reducing plume occlusion effects, maintaining ablation efficiency allowing for the process to be scaled towards bulk production. The state-of-the-art LASiS process has been developed by Ditterch et al.*(2019)*, producing gold nanoparticles at an efficiency of 42.5 mg/Wh for a 10 s ablation [39]. To-date there is not a widespread implementation of advanced, on-line process analyzers such as Dynamic Light Scattering (DLS) and UV-vis spectroscopy into the continuous Np ablation process to enact process change and determine process variability.

1.4   Overview of work and structure of the thesis

The work carried out for this thesis focused on successfully developing a scalable high efficiency LASiS process. In this work we present the scale-up of LASiS for the production of nanoparticles utilizing low power industrial Neodymium-doped Yttrium Aluminium Garnet (Nd:YAG) lasers. The PhD thesis comprises of a brief introductory chapter 1, giving background and context to the project. Chapter 2 discusses the application of nanomaterials in general along with placing the laser-based Np production process within the wider Np production field. Chapter 3 is the starting point for development of a LASiS production process. It examines progressing the background technology of batch Np production towards a continuous flow production process, while examining the effects of laser wavelength on Np productivity. Chapter 4 examines the development of a continuous, autonomous Np production rig, including ablation flow cell design, PAT tool implementation and machine automation. The quality and reliability of Np production from the rig is determined, along

with examining the possible benefits of on-line characterisation. The rig performance was determined in "continuous flow" and "semi-batch" production modes. Chapter 5 presents an investigation of the impacts of laser and process conditions on Np productivity and size. As the chapter progresses it describes a rapid parameter testing method and utilises it to produce a range of nanomaterials. The production efficiency of the rig is compared with the current state of the art. Chapter 6 examines the stability and production of silver Nps, a widely utilized nanomaterial using the rig in semi-batch mode. Chapter 7 describes efforts to merge a design of experiments approach with autonomous Nps fabrication to maximise production efficiency, while reducing experimental time. Chapter 8 summarises the work completed in the thesis and details how this work could be progressed in future. The appendix, along with containing details of the LabVIEW code, indicates the possible progression of future Np applications.

1.5   Research aims and objectives

The focus for this thesis is to examine the batch and continuous Np production methods via LASiS. The aims are as follows:

1. To investigate the LASiS process, understand the process conditions and how they affect the Nps produced.
2. To develop a nanoparticle fabrication rig that produces nanoparticles at efficiencies greater than the current state-of-the-art LASiS processes.

Objectives:
1. Construct a test rig for performing rapid process characterization of the Np production process and implement real-time process analytical technology tools (PAT) in the production process.
2. Examine the application of continuous flow Np production compared with batch production.
3. Examine the LASiS process in terms of laser and process parameters, toward optimizing production efficiency.

Goals:
1. Determine if LASiS can compete in terms of quality and production efficiency with chemical synthesis.

1.6 References

[1] F.-K. Liu, "Analysis and applications of nanoparticles in the separation sciences: A case of gold nanoparticles.," *J. Chromatogr. A*, vol. 1216, no. 52, pp. 9034–47, Dec. 2009.

[2] Y.-H. Yu *et al.*, "Electrical, morphological, and electromagnetic interference shielding properties of silver nanowires and nanoparticles conductive composites," *Mater. Chem. Phys.*, vol. 136, no. 2, pp. 334–340, 2012.

[3] A. Silva, M. Amaral, J. Sousa Lobo, and C. Lopes, "Lipid Nanoparticles for the Delivery of Biopharmaceuticals," *Curr. Pharm. Biotechnol.*, vol. 16, no. 999, pp. 1–1, 2016.

[4] S. Bhattacharjee, "DLS and zeta potential - What they are and what they are not?," *J. Control. Release*, vol. 235, pp. 337–351, 2016.

[5] E. Bagheri *et al.*, "Silica based hybrid materials for drug delivery and bioimaging," *J. Control. Release*, vol. 277, pp. 57–76, 2018.

[6] C. de la Torre and V. Ceña, "The delivery challenge in neurodegenerative disorders: The nanoparticles role in alzheimer's disease therapeutics and diagnostics," *Pharmaceutics*, vol. 10, no. 4, 2018.

[7] M. E. Wechsler, J. E. Vela Ramirez, and N. A. Peppas, " 110th Anniversary : Nanoparticle Mediated Drug Delivery for the Treatment of Alzheimer's Disease: Crossing the Blood–Brain Barrier ," *Ind. Eng. Chem. Res.*, vol. 58, pp. 15079–15087, 2019.

[8] X. Li, H. Xu, Z. S. Chen, and G. Chen, "Biosynthesis of nanoparticles by microorganisms and their applications," *J. Nanomater.*, vol. 2011, 2011.

[9] D. Paolino *et al.*, "Targeting the thyroid gland with thyroid-stimulating hormone (TSH)-nanoliposomes," *Biomaterials*, vol. 35, no. 25, pp. 7101–7109, 2014.

[10] S. H. Lee and B. H. Jun, "Silver nanoparticles: Synthesis and application for nanomedicine," *Int. J. Mol. Sci.*, vol. 20, no. 4, 2019.

[11] P. Singh, S. Pandit, V. R. S. S. Mokkapati, A. Garg, V. Ravikumar, and I. Mijakovic, "Gold nanoparticles in diagnostics and therapeutics for human cancer," *Int. J. Mol. Sci.*, vol. 19, no. 7, 2018.

[12] K. Bagga *et al.*, "Laser-assisted synthesis of Staphylococcus aureus protein-capped silicon quantum dots as bio-functional nanoprobes," *Laser Phys. Lett.*, vol. 10, no. 6, p. 065603, 2013.

[13] R. Zamiri, A. Zakaria, H. A. Ahangar, M. Darroudi, A. K. Zak, and G. P. C. Drummen, "Aqueous starch as a stabilizer in zinc oxide nanoparticle synthesis via laser ablation," *J. Alloys Compd.*, vol. 516, pp. 41–48, 2012.

[14] D. Liu, Z. Wang, and X. Jiang, "Gold nanoparticles for the colorimetric and fluorescent detection of ions and small organic molecules," *Nanoscale*, vol. 3, no. 4, pp. 1421–1433, 2011.

[15] D. Flak, L. Yate, G. Nowaczyk, and S. Jurga, "Hybrid ZnPc@TiO 2 nanostructures for targeted photodynamic therapy, bioimaging and doxorubicin delivery," *Mater. Sci. Eng. C*, vol. 78, pp. 1072–1085, 2017.

[16] A. Panáček *et al.*, "Antifungal activity of silver nanoparticles against Candida spp.," *Biomaterials*, vol. 30, no. 31, pp. 6333–6340, 2009.

[17] B. Calderón-Jiménez, M. E. Johnson, A. R. Montoro Bustos, K. E. Murphy, M. R. Winchester, and J. R. Vega Baudrit, "Silver Nanoparticles: Technological Advances, Societal Impacts, and Metrological Challenges," *Front. Chem.*, vol. 5, no. February, pp. 1–26, 2017.

[18] M. Muniz-Miranda, C. Gellini, E. Giorgetti, and G. Margheri, "Bifunctional Fe3O4/Ag nanoparticles obtained by two-step laser ablation in pure water," *J. Colloid Interface Sci.*, 2016.

[19] J. R. González-Castillo *et al.*, "Synthesis of Ag@Silica Nanoparticles by Assisted Laser Ablation," *Nanoscale Res. Lett.*, vol. 10, no. 1, pp. 1–9, 2015.

[20] C. Rehbock *et al.*, "Current state of laser synthesis of metal and alloy nanoparticles as ligand-free reference materials for nano-toxicological assays," *Beilstein J. Nanotechnol.*, vol. 5, no. 1, pp. 1523–1541, 2014.

[21] K. S. Siddiqi, A. ur Rahman, Tajuddin, and A. Husen, "Properties of Zinc Oxide Nanoparticles and Their Activity Against Microbes," *Nanoscale Res. Lett.*, vol. 13, 2018.

[22] A. Sirelkhatim *et al.*, "Review on zinc oxide nanoparticles: Antibacterial activity and toxicity mechanism," *Nano-Micro Lett.*, vol. 7, no. 3, pp. 219–242, 2015.

[23] C. N. Lok *et al.*, "Silver nanoparticles: Partial oxidation and antibacterial activities," *J. Biol. Inorg. Chem.*, vol. 12, no. 4, pp. 527–534, 2007.

[24] M. Carbone, D. T. Donia, G. Sabbatella, and R. Antiochia, "Silver nanoparticles in polymeric matrices for fresh food packaging," *J. King Saud Univ. - Sci.*, vol. 28, no. 4, pp. 273–279, 2016.

[25]   J.-B. Park, K.-H. Lee, Y.-J. Jeon, S.-H. Lim, and S.-M. Lee, "Si/C composite lithium-ion battery anodes synthesized using silicon nanoparticles from porous silicon," *Electrochim. Acta*, vol. 133, pp. 73–81, 2014.

[26]   B. Yun Jang and C. Hyun Ko, "Effects of Annealing Conditions on Microstructures of Thin Film Using Crystalline Silicon Nanoparticles for Printable Electronics," *J. Nanosci. Nanotechnol.*, vol. 12, pp. 1629–1633, 2012.

[27]   K. Bagga, R. McCann, M. Wang, a. Stalcup, M. Vázquez, and D. Brabazon, "Laser assisted synthesis of carbon nanoparticles with controlled viscosities for printing applications," *J. Colloid Interface Sci.*, vol. 447, pp. 263–268, 2015.

[28]   Y. Li *et al.*, "Microchip-based immunoassays with application of silicon dioxide nanoparticle film," *Anal. Bioanal. Chem.*, vol. 403, no. 8, pp. 2449–2457, Jun. 2012.

[29]   S. M. Haidary, E. P. Córcoles, and N. K. Ali, "Nanoporous silicon as drug delivery systems for cancer therapies," *J. Nanomater.*, vol. 2012, 2012.

[30]   K. Bagga *et al.*, "Nanoparticle functionalized laser patterned substrate: an innovative route towards low cost biomimetic platforms," *RSC Adv.*, vol. 7, no. 13, pp. 8060–8069, 2017.

[31]   K. Bagga *et al.*, "Laser-assisted synthesis of ultrapure nanostructures for biological sensing applications," in *Proceedings of SPIE*, Sep. 2016, p. 99280O, doi: 10.1117/12.2237147.

[32]   S. Barcikowski and G. Compagnini, "Advanced nanoparticle generation and excitation by lasers in liquids.," *Phys. Chem. Chem. Phys.*, vol. 15, no. 9, pp. 3022–6, 2013.

[33]   S. Barcikowski *et al.*, "Handbook of Laser Synthesis of Colloids," 2016.

[34]   J. Lam *et al.*, "γ-Al2O3 nanoparticles synthesised by pulsed laser ablation in liquids: A plasma analysis," *Phys. Chem. Chem. Phys.*, vol. 16, no. 3, pp. 963–973, 2014.

[35]   R. Streubel, S. Barcikowski, and B. Gökce, "Continuous multigram nanoparticle synthesis by high-power, high-repetition-rate ultrafast laser ablation in liquids," *Opt. Lett.*, vol. 41, no. 7, p. 1486, 2016.

[36]   V. Amendola and M. Meneghetti, "Laser ablation synthesis in solution and size manipulation of noble metal nanoparticles.," *Phys. Chem. Chem. Phys.*, vol. 11, no. 20, pp. 3805–3821, 2009.

[37]   V. Amendola and M. Meneghetti, "What controls the composition and the structure of nanomaterials generated by laser ablation in liquid solution?," *Phys. Chem. Chem.*

Phys., vol. 15, pp. 3027–3046, 2013.

[38] D. Cenide, R. Streubel, N. Bärsch, and S. Barcikowski, "Advanced liquid flow reactor design for laser ablation in liquid Motivation : Task : Continuous Fabrication of Nanoparticles State of the art : Stationary ablation Task : Properties : Production Chamber : Laser Bio-conjugation Chamber," vol. 115, no. May, pp. 6–7, 2012.

[39] S. Dittrich, R. Streubel, C. McDonnell, H. P. Huber, S. Barcikowski, and B. Gökce, "Comparison of the productivity and ablation efficiency of different laser classes for laser ablation of gold in water and air," *Appl. Phys. A Mater. Sci. Process.*, vol. 125, no. 6, pp. 1–10, 2019.

Chapter 2:   Literature review

Nanomaterials are objects with one or more dimension in the nanoscale range, typically defined between 1 nm - 100 nm [1], however the term is often used to describe particles up to 500 nm [2]. Nanomaterials that contain a single nanoscale dimension are defined as thin films or sheets. Material with two nanoscale dimensions are nanowires or nanotubes. Material with three nanoscale dimensions are defined as nanoparticles. Nanoparticles (Nps) can range from small clusters of atoms to larger colloidal particles [1] consisting of a single homogenous material or multiple materials, in terms of core-shells [3] and functionalized surfaces [4]. Nanomaterials possess special physical, chemical and biological functionality due to their high surface-area to volume ratio. This functionality allows for unique electrical, mechanical and optical properties make them highly suited to a number of applications such as sensing [1], [5], [6], separations [7], energy storage [8], display technology [9], printable circuits [10], and drug delivery [11]. The global nanotechnology market was valued at $1 billion USD in 2018 and is expected to reach $2.2 billion USD by 2025 [12], with nanoparticles holding a 75% share of the entire nanomaterials market. The European Commission places nanomaterials into different material classifications described as; inorganic non-metallic nanomaterials, metal and metal alloys, carbon based nanomaterials and nano polymers and dendrimers [13]. Within these classifications silicon and zinc oxide are some of the most widely used inorganic non-metallic nanomaterials, with gold and silver examples of widely used metals [14]. A range of the most common nanoparticles produced by LASiS is displayed in Figure 2.1. In this chapter, the key applications of nanoparticles will be reviewed, a general overview of nanoparticle production is presented along with the LASiS process, and issues facing its commercialisation will be discussed.
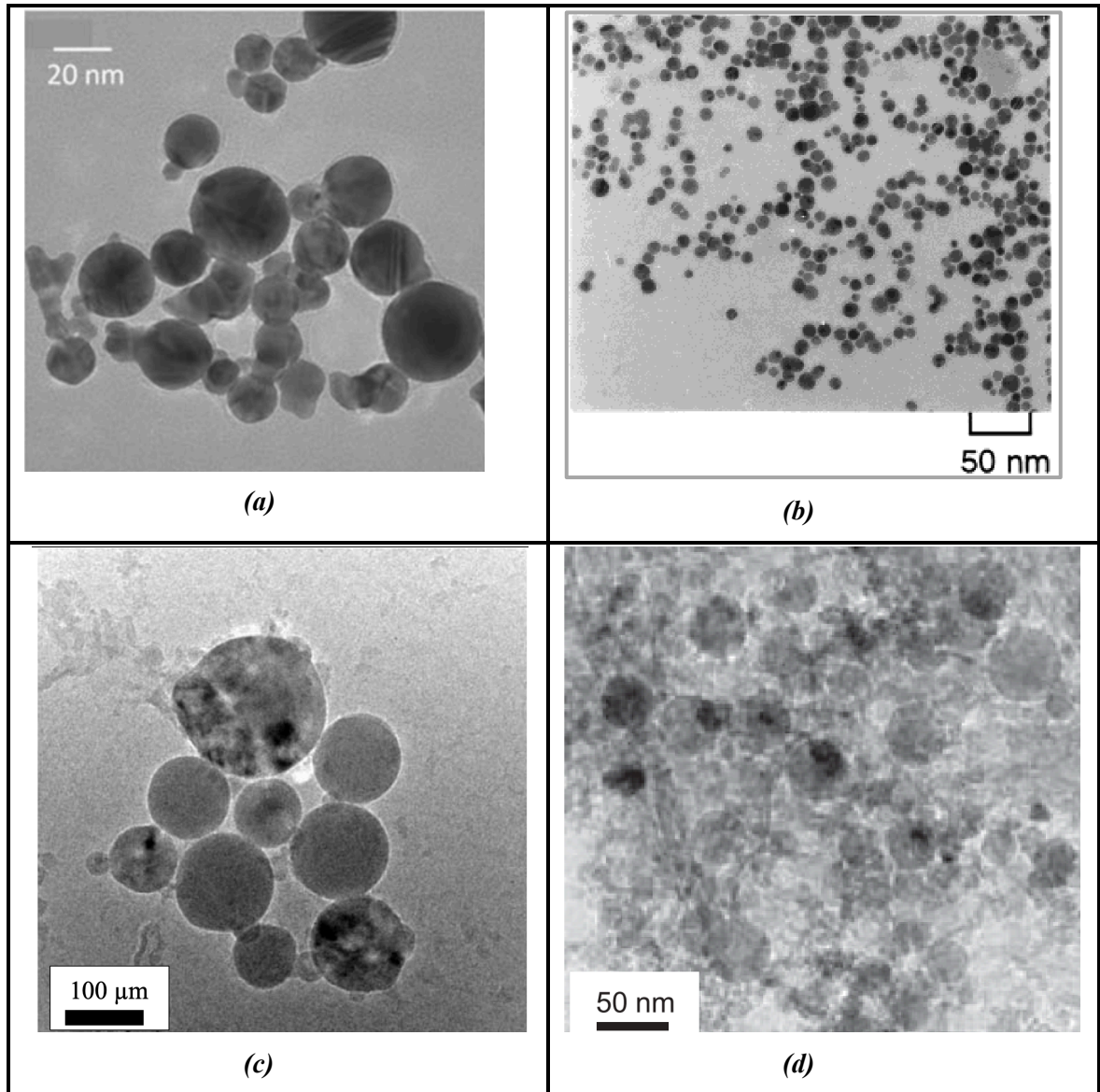
Figure 2.1: TEM of images of (a) AuNps (reproduced from [15]), (b) AgNps (reproduced from [16]), (c) SiNps (reproduced from [17]) and (d) ZnONps ([18]).

2.1 Nano functionality

Nanomaterials' high surface-to-volume ratio has a result of increasing the component material functionality, leading to their applicability to many sensing applications [1], [5], [6]. For example, in a fully 1-D single-walled carbon nanotube (CNT), every atom is on its surface, providing an ideal surface-to-volume ratio [5] and the highest functionality possible. The relationship between the percentage of atoms on, or adjoining the surface to the diameter of a nanoparticle was determined by Navrotsky et al. as seen in Figure 2.2. It can be determined from this relationship that a nanoparticle's functionality increases exponentially

with the inverse of its diameter. The smaller particle diameter increases the fraction of atoms on the Nps surface, providing fewer terminating locations for the bonds, resulting in "dangling" or "unsaturated" bonds on the surface. These "dangling bonds" increase the particles surface energy. This would in turn lead to smaller particles being more reactive. For example a 1nm Nps would possess 1000 times greater surface energy than a 1 μm particle [19].
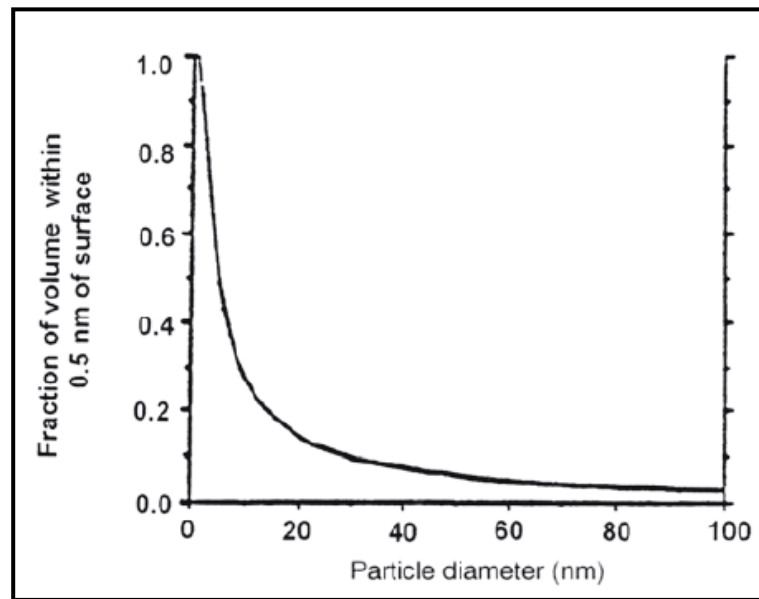
Figure 2.2: Fraction of atoms within 0.5 nm of the surface of a nanoparticle as a function of its diameter [1].

Nanomaterials possess useful electronic properties [20]–[25]. It has been seen that if a nanomaterial's dimensions are greater than the mean-free-path of a carrier within the material, a nanoscale object will have the same electron transport properties as the bulk material. However, if one or more of its dimensions are less than the mean-free-path, the electronic properties become dependent on the nanomaterials dimension(s) [26]. This allows electronic properties to be tuned via nanomaterial design by controlling the nanoscale dimensions [27]–[29] of the carrier material, leading to control of electrical properties such as voltage, current, resistance and other characteristic sensor responses.

Nanomaterial optical properties are also a function of their size and morphology. An example from Dreaden et. al. is presented in Figure 2.3, showing different photon absorption behaviour and hence optical colour (due to collective conduction, electron excitation or

plasmon resonance) of gold nanomaterials due to their varied size and morphology [30]. It has been shown experimentally that the surface plasmon response (SPR) of nanoparticles is a function of their diameter, Haiss et al.,(2007) showed that AuNps SPR changed from 510 nm to 585 nm as their diameter increased from 3 nm to 110 nm [31].
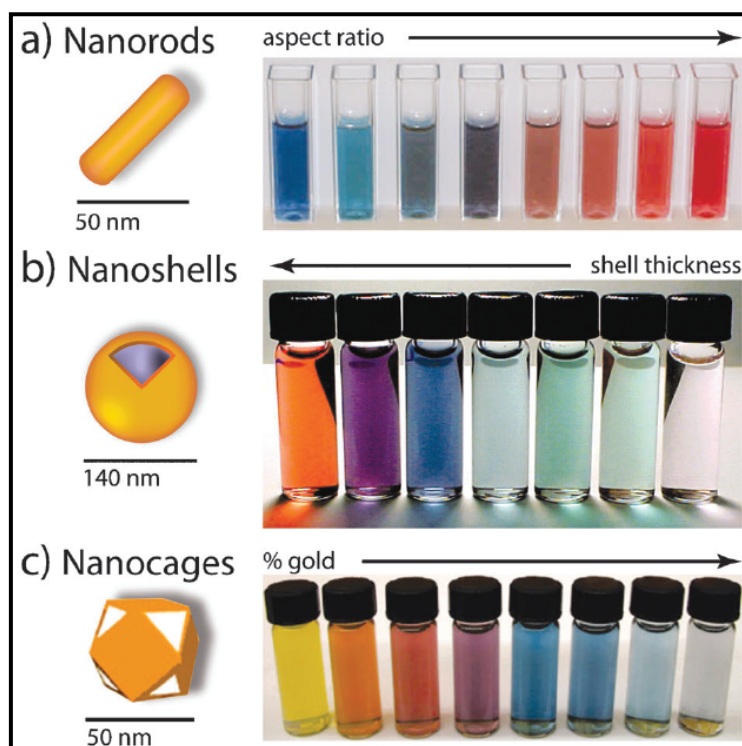
Figure 2.3: Gold nanomaterials with differing shapes and dimensions: (a) Nanorods of varying aspect ratio, (b) Nanoshells of varying shell thickness, and (c) Nanocages of varying % gold [30].

2.2   General nanoparticle applications

2.2.1   Sensing

The high surface areas, and the specific optical and electrical properties of nanoparticles make them ideal for sensing applications. Most nanoparticle-based sensors can be broken down into colorimetric, fluorescence, or electrochemical sensors [32]. As shown in Figure 2.3, the photon absorption behaviour, and thus the visual colour, of nanoparticles is strongly dependant on the size and shape of the particles [30]. These colourful light-scattering properties allow nanoparticles to be used similarly to fluorescent dyes. The light-scattering power of a single nanoparticle label is stronger than a single fluorescent label, and the light signals are not subject to photobleaching and require less complex instrumentation [33].

Typically, colorimetric sensing uses larger nanoparticles (>30 nm) which exhibit strong visible light-scattering properties. Gold nanoparticles are particularly popular, as they have a surface plasmon resonance, where conduction electrons near the surface of the metal are stimulated into oscillation by an external electromagnetic wave, with a maximum absorption at a resonance frequency [34]. For nanoparticles, the wavelength of this resonance is strongly dependant on the size, shape, aggregation, and medium refractive index [35]. Changing these parameters will change the visual colour of the nanoparticles. For example, well-dispersed gold nanoparticles with sizes of 10 - 50 nm will appear red, while aggregation of the particles will change the colour to blue [36]–[38]. This provides a mechanism for colorimetric sensing [39].

A typical aggregation based sensing process was detailed in a work by Chen et al., describing colorimetric detection of melamine in milk using gold nanoparticles [39]. Melamine is an industrial compound used in manufacturing that can be used to adulterate milk to create false high protein values, a problem in the dairy industry. Excessive melamine intake is harmful, especially to infants and adolescents, driving the need for reliable methods of detecting melamine in milk [40]. The gold nanoparticles were chemically synthesised by a trisodium citrate reduction, then chemically modified to asymmetrically graft polyethylene glycol (PEG) as a stabiliser. The presence of melamine in the milk disturbs the electrostatic balance on the surface of the nanoparticles, promoting the formation of aggregates, shown in Figure 2.4. This results in a colour shift, as described above, which can be detected by eye or with spectrophotometry. The authors found this method to be sensitive and reliable.

Methods may also be based on "anti-aggregation", where the target prevents or impedes aggregation of the nanoparticles [32]. An example of an anti-aggregation method is presented by Ramezani et al., in a work where gold nanoparticles were used in colorimetric sensing of tetracycline [41]. Tetracyclines are broad-spectrum antibiotics used in veterinary medicine. Residues of tetracyclines in food products could have undesirable side-effects on human consumers, creating a need for tetracycline sensing. Gold nanoparticles were chemically synthesised by a citrate reduction and combined with a triple helix molecular switch (THMS) made up of a purchased aptamer and signal transduction probe (STP). As

shown in Figure 2.5, the THMS is stable in the absence of tetracycline allowing ambient salt (NaCl) in the medium (serum or milk in this study) to trigger aggregation of the nanoparticles, leading to a colour change to blue [41]. When the targeted tetracycline is present, the aptamer in the THMS binds to the target, and the released STP binds to the nanoparticles inhibiting aggregation leaving the red colour. As with other aggregation-based methods, the colour can be identified visually or with spectrophotometry.
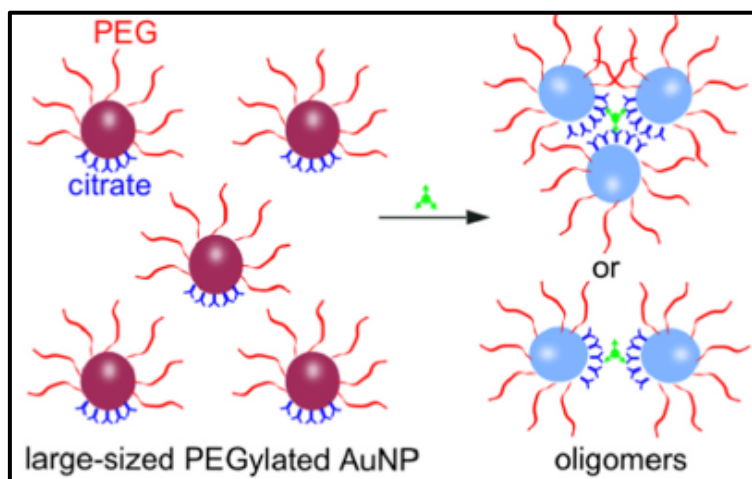
Figure 2.4: Principle of asymmetrically PEG-modified gold nanoparticle aggregation based colorimetric sensor for detection of melamine [39].
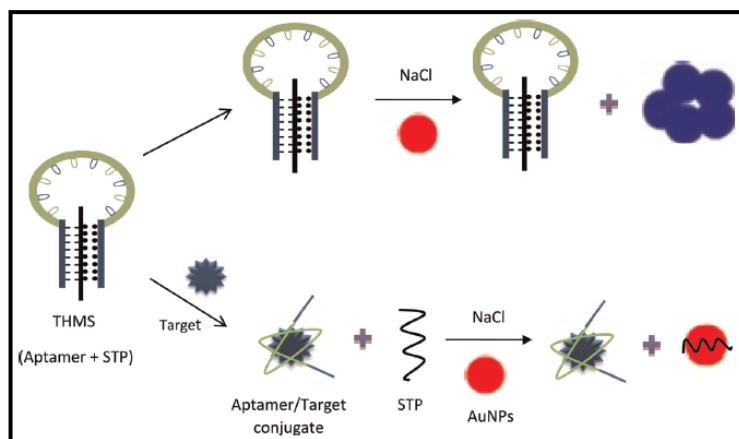
Figure 2.5: Principle of THMS gold nanoparticle anti-aggregation based colorimetric sensing of tetracycline [41].

Fluorescence sensing is based on the use of organic or inorganic fluorophore dyes, which suffer from some limitations. The dyes can have low absorption coefficients and weak signals, limiting sensitivity and response, are prone to photo-bleaching, leading to short

14

lifetimes, and are potentially toxic [33], [42]. Fluorescent nanoparticles, made up of organic fluorophores encapsulated in a particle matrix, are much brighter than single dye molecules, and are more stable and biocompatible than un-encapsulated fluorophores [42]. Nanoparticles can also be used as quenchers in fluorescence resonance energy transfer (FRET) based sensing [43]. FRET is a highly distant dependant, non-radiative process where an excited donor fluorophore transfers energy to an acceptor [32], [43]. The initiation of FRET can act to quench or turn-off fluorescence, as energy that would be otherwise radiatively released through fluorescence is transferred into the acceptor, which can act as a sensing method [32]. For example, *Xu et. al.* describe the use of gold nanoparticles in a FRET based sensing strategy for sensing the neurotransmitter dopamine [43]. In this work, a dopamine binding aptamer and a fluorescent dye (rhodmine B) were used with citrate-synthesised gold nanoparticles. When dopamine is not present, the aptamer attaches to the gold nanoparticles, preventing NaCl induced aggregation, and FRET quenching can take place between the nanoparticles and the fluorophores. When dopamine is present, the aptamer will preferentially attach to the target dopamine, allowing the nanoparticles to cluster, preventing FRET quenching. A schematic of this process can be seen in Figure 2.6 [43]. The authors found the method to be rapid, simple, selective, and sensitive.
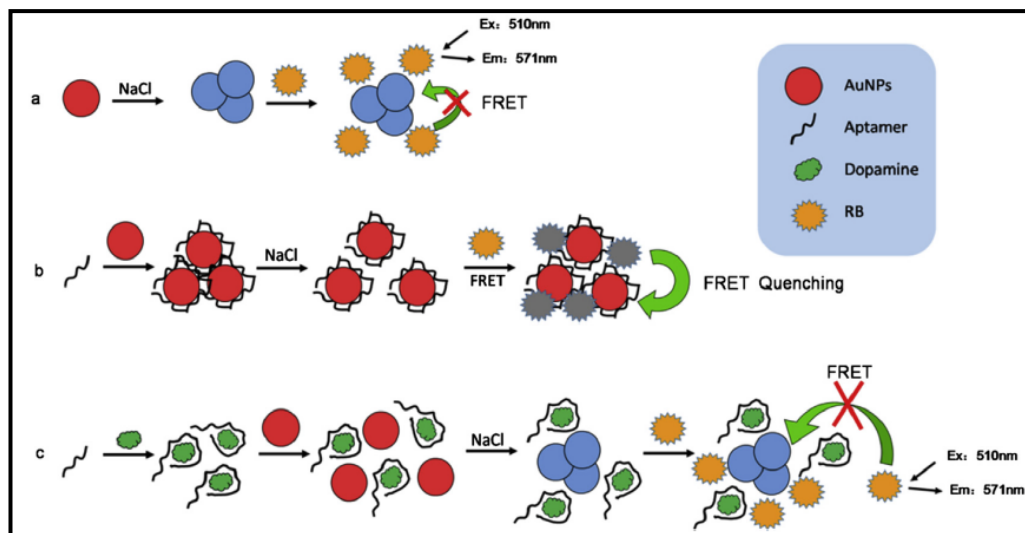
Figure 2.6: Schematic illustrating FRET quenching based dopamine sensing using gold nanoparticles (AuNPs) and rhodamine B (RB) [43].

In electrochemical sensing, nanoparticles are often used to modify sensing electrodes to achieve the desired sensitivity and selectivity [32]. Electrochemical sensors work by the variation of the electric response of a device due to chemical interactions between target

analytes and the surface of the electrode [44], [45]. A general schematic for an operating electrochemical biosensor is presented in Figure 2.7 [46]. The high surface-to-volume ratio of nanoparticles offers a large sensing surface, and they also offer excellent electrical conductivity and biocompatibility [47]. An example of nanoparticle use in electrochemical sensing can be seen in a work by Raj et. al. where immobilised gold nanoparticle arrays were used for voltammetric sensing of dopamine [48]. The authors note that detection of dopamine is inhibited by the presence of interfering compounds in biological samples, and as such ensuring good selectivity in sensing electrodes is a major goal. Treatment or coating of electrodes is one way to the achieve this. The authors applied an amine terminated self-assembled monolayer (cystamine) to a gold electrode, then immobilised chemically synthesised gold nanoparticles on the surface. The nanoparticle coated electrode was shown to be able to distinguish between dopamine and a typical interfering compound (ascorbate), which was not possible with the bare gold electrode and with good sensitivity, selectivity, and anti-fouling properties.
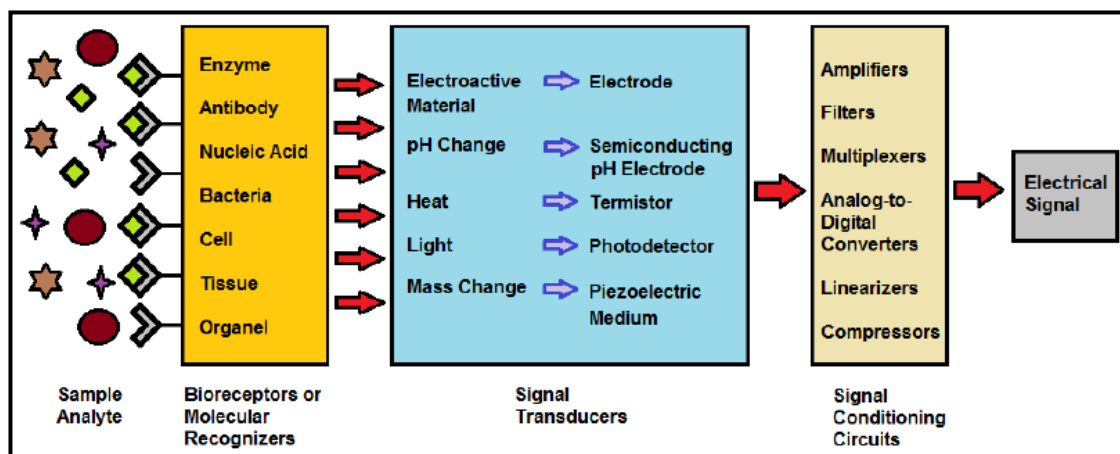
Figure 2.7: Schematic of the main subsystems of an operating biosensor [46].

2.2.2 Conductive Inks

Deposition or printing of conductive inks is an efficient method for the production of conductive coatings and circuits [49]. Printed electronics can be low cost, light weight, optically transparent, and used in flexible electronics [50]. Conductive patterns can be printed to flexible substrates such as paper [51]–[53] or polymer [54], [55]. Flexible electronics are of interest for radio frequency identification (RFID) tags [51], [53], robotics [56], [57], and biomedical applications [58], [59]. Conductive inks containing nanomaterials in solution are commonly used, such as silver nanowires [20], silver nanoparticles [54], [60],

copper nanoparticles [23], and carbon nanotubes [61], with gold Nps applied to the surface as conductors aiding the miniaturisation of circuits [62]. Silver nanoparticle inks are one of the most commonly used, due to their high conductivity, and low oxidisation [21], [22]. Silver nanoparticle inks are typically in aqueous or solvent media, stabilised with surfactants or polymers, and then dried and/or sintered after printing [22]. An example of silver nanoparticles being used in a conductive ink can be seen in a work by Matyas et al. [54]. In this work, silver nanoparticles were produced by a solvothermal precipitation synthesis method using silver nitrate salt, an organic precipitation agent, and a polymer stabilising agent. The ink was prepared by dispersing the nanoparticles in deionised water with ultrasonication, with 0.1 ml of dispersion stabiliser added per 10 ml of dispersion fluid. The final viscosity of the ink ranged from 8 to 12 cPs. The ink was then ink-jet printed at 35 °C onto a PET-based PCB substrate at 45 °C. After printing, the substrate and printed circuit were dried in a vacuum oven at 120 °C for 20 min to sinter the nanoparticles. An SEM image of the printed silver nanoparticle layer can be seen in Figure 2.8 [54]. With this method, a working flexible antenna was successfully created. SiNps are used as thin film semi-conductors in the electronics industry and for their thermal properties is utilised for both thin films [63] and as thermal fluids in the solar industry [64].
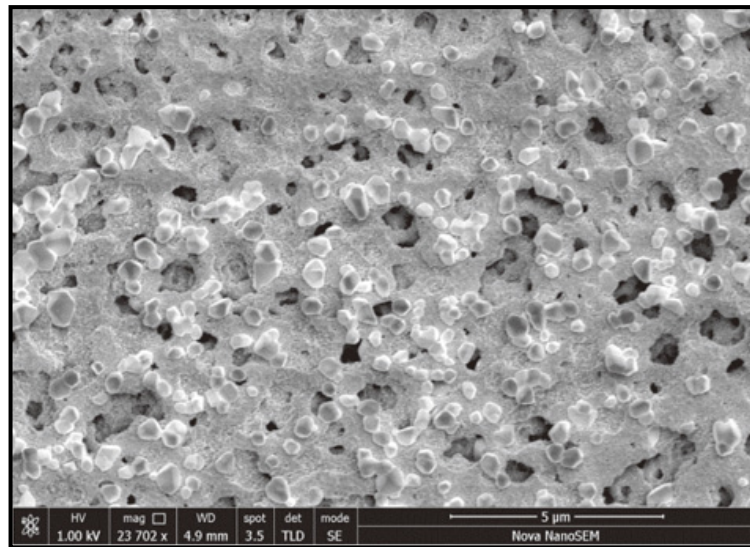
Figure 2.8: SEM image of a printed silver nanoparticle circuit on a PET substrate [54].

2.2.3 Anti-fouling

Fouling is the deposition or accumulation of unwanted material on the surface of a solid. This gathering of material can inhibit the mechanical, chemical, or electrical function of devices, lead to contamination, or, in the case of medical tools or devices, lead to infection. Fouling is a significant problem for applications like sensing electrodes [65] and osmosis membranes [66]. Anti-fouling surfaces, with properties such as super hydrophobicity, self-cleaning, and drag reduction, which resist fouling are therefore highly desirable [67].

Silver and its compounds are well known for their antimicrobial, biocidal effects [68]–[70]. Silver nanoparticles are particularly popular for use in antimicrobial coatings due to the high surface area, allowing for more reactive surface-oriented groups compared with the bulk material [69]. Silver nanoparticles have a number of mechanisms against micro-organisms: particles attaching to the cell surfaces, disrupting the function of the cell wall [71], [72]; permeating the cell and damaging the DNA, proteins, or other cell constituents [72], [73]; and releasing reactive silver ions [72], [74]. Titanium dioxide particles also have good anti-fouling properties and wettability [4]. A work by Nguyen et al. describes the use of silver nanoparticles and titanium dioxide nanoparticles for antifouling effects on a forward osmosis membrane [66]. The build-up of deposits of organic matter on osmosis membranes can reduce their permeability and shorten their lifetime. The authors note that silver nanoparticles' antibacterial effect can be lost if the particles become covered by a biofilm. In this work silver nanoparticles were combined with titanium dioxide, which is known for its propensity to decompose organic matter, to create an improved anti-fouling surface. Silver and titanium oxide nanoparticles were deposited in separate wet chemical processes onto the porous surface of commercial forward osmosis membranes, which were tested for their anti-fouling behaviour. They found the modified membrane had excellent antibacterial effect, almost 11 times less bacterial growth compared to the as-received membrane, and that the flux reduction due to fouling was lessened for the modified membrane due to the delayed onset of fouling.

2.2.4 Anti-bacterial applications

It has been seen that nanoparticles display antibacterial properties, exhibited via several mechanisms including disruption of the cell membrane, through the release of ions [75] and by preventing cell adherence and proliferation [76]. Silver nanoparticles (AgNps) have been applied to various applications such as; wastewater treatment [77], skin care [78], therapeutics [79] and surface coatings of biomedical products [76]. In the medical industry, post-surgery infection remains a significant issue [80]. With *E. coli* and other bacteria becoming resistant to current antibiotics, a different control method needs to be investigated. Nanoparticle surface coatings have shown promise in this area, where they have been applied to the surfaces of medical instrumentation and medical implants [81]. Recently there have been developments in applying coatings on hospital working surfaces such as door handles and operating tables to prevent cell adherence and hence, prevent biofilm formation [82]. The problem shows itself just after surgery and prevention of the initial infection is key to controlling persistent and serious illness. Once a biofilm has established itself, it can be very difficult to remove and can result in severe illness.

AgNps are thought to exhibit antibacterial properties through the release of Ag ions and interactions with the cell membrane of the bacteria cell [83]. Some studies insist that it is the positive charge of silver interacting with the negative charge of the outer cell membrane through electrostatic attraction [84]. However, more recent studies have used negatively charged silver nanoparticles and have shown similar anti-bacterial activity [71]. There have been numerous studies conducted in recent years considering the anti-bacterial properties of silver nanoparticles which conclude that one mechanism is the AgNps interaction with the cell membrane that induces cell death [85]. There have been differences in inhibitory effects observed between gram-negative and gram-positive bacteria. This suggests silver induced anti-bacterial effects involves a reaction with the cell membrane, and the differences in peptidoglycan thickness contributes to differences observed [83]. However, more recent studies have shown AgNps can be used to coat surfaces and exhibit antibacterial effects. These nanoparticles are immobilised, which leads to the conclusion that it is the release of silver ions attributing the anti-bacterial activity, rather than direct nanoparticle-cell membrane interaction [86].

Zinc oxide nanoparticles (ZnONps) have also been seen to possess anti-microbial properties, they have been reported to be toxic to gram-negative and gram-positive bacteria, with similar properties to AgNps [87]–[93]. These properties allow for a wide range of applications in the sanitation of surfaces such as medical devices [90], food packaging [87] and towards treatment of waste water. Specifically, the treatment of "blackwater" contaminated with biologically hazardous effluent is of particular interest for the application of nanomaterials [93]. Also ZnO Nps have seen applications as coating in filters [88] that, in future would be applied towards water treatment.

2.2.5   Nano-medicine

Nanoparticles have been used in therapeutics for illnesses such as Alzheimer's disease [94]– [96], cancer [97]–[99], and atherosclerosis [100]. Nanoparticles may be used in imaging based therapeutic techniques [98], drug delivery [94], or gene delivery [101]. Chemical synthesis is a common method of producing nanoparticles, however the chemicals involved in their production may be hazardous to human health, and as such alternative production methods may be more attractive for therapeutic applications [98].

The biocompatibility, unique optical properties and the surface plasmon resonance of gold nanoparticles make them of interest for imaging-based therapeutic techniques or photo-thermal therapy [98]. Photo-thermal therapy is a cancer therapy where photon energy is converted into heat energy to destroy cancer cells [102]. Synthetic molecules which absorb the incident photons more strongly than the surrounding tissue can be applied to a tumour to localise the heating. In plasmonic photo-thermal therapy (PPTT), gold nanoparticles are introduced to the cancerous cells by intravenous injection, and then exposed to light [102], [103], [104]. The light, typically near infra-red, causes oscillation of the free electrons in the gold nanoparticles due to surface plasmon resonance, and this oscillation energy can be emitted as heat through nonradiative decay. This strong localised heating then destroys the cancer cells [102].

Nanoparticles can also be a drug delivery method [94]–[96], [99]. As carriers or vessels for drugs, nanoparticles have the potential advantages of penetration of biological barriers like

cell membranes or the blood brain barrier, protection of the drug from premature chemical or physical breakdown, and surface modification to help with solubility and delivery or limit toxicity [94], [99], [105], [106]. Improving the specificity/targeting of drugs is also possible [94], [98]. SiNps has gained traction in biological fields in recent times, due in-part to their bio-compatibility [107] and biodegradability [25] features. They are applied in therapeutics where they act as drug delivery agents [11], [62], [107]–[110] either by attaching drugs directly to their porous structure [11] or by functionalising the protein to their solid surface or core shell [107]. Recently SiNps are applied to bio-medical imaging; where they are utilized to increase the contrast and the quality of imaging by tuning the Nps fluorescence [108], [109], [111]–[114].

Chemotherapy drugs, for treatment of cancer, are traditionally delivered orally or intravenously, causing them to affect the entire body [98]. The resulting negative side effects drive an interest in targeted or localised drug delivery methods. Nanoparticles are one method of achieving this. Chemotherapy drugs can be loaded or attached to nanoparticles. Tumour tissue tends to have leaky vasculature, which will cause an accumulation of intravenously applied nanoparticles from the blood stream as a form of "passive" targeting [98]. However the strength of this targeting varies with the type of tumour due to variation in the vasculature [115]. In "active" targeting, ligands of tumour specific biomarkers are conjugated to the nanoparticle carrier. The ligand's interaction with the tumour causes the nanoparticles to be internalised by the tumour cells by endocytosis [115]. Careful selection of the ligand is necessary, but greater targeting can be achieved for a greater range of tumours using active compared to passive targeting. Gold nanoparticles are well-suited to this application due to their biocompatibility, non-toxic nature, and tuneable sizes, geometries, and properties [116], [117]. For example, Chen et al. describe the conjugation of a chemotherapy agent methotrexate to gold nanoparticles to treat tumours [118]. The gold nanoparticles were chemically synthesised with a citrate-reduction. A colloidal solution of the nanoparticles was then mixed with methotrexate and a sodium phosphate buffer. The mixture was centrifuged and rinsed, and then dispersed in the buffer. A diagram of the conjugation can be seen in Figure 2.9 [118]. A coordinate-covalent bond attaches the methotrexate molecule to the gold nanoparticle. The authors observed that the drug accumulates at a faster rate, to a higher amount, when conjugated to the gold nanoparticles compared to the drug alone being administered.

21

Diseases such as Alzheimer's disease (AD) which affect the brain and central nervous system can be difficult to treat, due to the blood brain barrier [94]. Drugs used in AD therapy, typically orally administered, tend to have side effects due to a lack of selectivity for the therapeutic targets [95], [96]. This issue can be mitigated with drug carriers capable of crossing the blood brain barrier, allowing sufficient amounts of the drug to be delivered to the brain and central nervous system at lower overall doses, minimising off-target effects [94]. Nanoparticle drug carriers can successfully deliver drugs through the blood brain barrier [119]. The nanoparticles used are typically dendrimers (dendritically branched molecules), polymer nanoparticles, and lipid nanoparticles [94], [119].
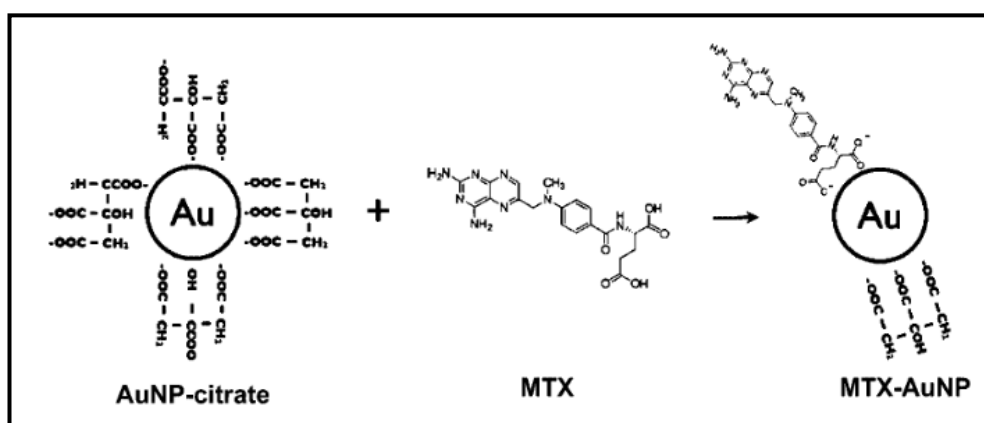
Figure 2.9: Schematic of the conjugation of methotrexate (MTX) to the citrate-reduced gold nanoparticles (AuNps) [118].

2.3   Nanoparticle production methods

2.3.1   Chemical synthesis

Chemical synthesis is one of the most common methods of producing metal nanoparticles [120]. Reduction-based methods in solution are typical for metallic and alloy nanoparticles [121]. Silver nanoparticles are most commonly produced by chemical reduction with organic or inorganic reducing agents, such as sodium citrate, ascorbate, sodium borohydride, elemental hydrogen, polyol process, Tollens reagent, N-dimethylformamide (DMF), and poly (ethylene glycol) block copolymers [122]. The reducing agents reduce Ag^+ leading to the formation of metallic silver, which agglomerates into nanoparticles. Stabilising agents are employed to prevent further agglomeration of the nanoparticles into larger clusters [123]. The particles may also be functionalised with ligands. Similar chemical reduction methods are used for gold nanoparticles, using reducing

agents such as borohydrides, amino boranes, hydrazine, formaldehyde, hydroxylamine, saturated and unsaturated alcohols, citric and oxalic acids, polyols, sugars, hydrogen peroxide, sulphites, carbon monoxide, hydrogen, acetylene, and monoelectronic reducing agents [124]. As with silver, stabilising agents are added to maintain dispersion of the particles. Citrate-based reduction methods are most common for gold. Citrate can act as both a reducing and a stabilising agent for gold nanoparticles. This method is known as the Turkevich method, developed by Turkevich et al. in 1951 [125], and then improved upon by Frens in 1973 [126]. In this method chloroauric acid ($HAuCl_4$) is boiled and trisodium citrate is then added under stirring [124]. Citrate can also be used solely as a stabilising agent, with a separate reducing agent [127]. A considerable disadvantage of chemical synthesis methods are their use of chemicals and solvents (such as hydrazine and sodium borohydride) which are hazardous to humans and the environment [98], [128].
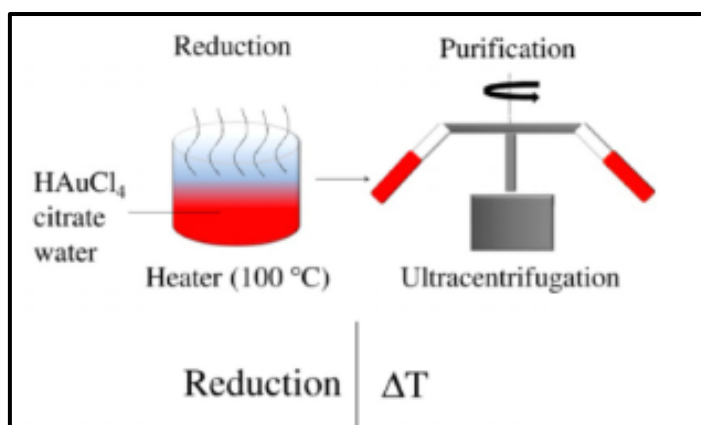
Figure 2.10: Chemical synthesis of Gold NPs [129].

2.3.2 *Biological synthesis*

An interest in "green", ecologically safe, synthesis has driven some movement away from chemical synthesis to other methods such as LASiS, but also in developing green synthesis methods using biological agents in the reducing process [128]. These methods are generally based on reducing metal salt solutions with a biological agent, and have been used with silver, gold, platinum, mercury, selenium, palladium, and others, including alloys and metal oxides [128], [130], [131]. A general diagram for the process, for silver nanoparticles, can be seen in Figure 2.11 [128]. Biological agents may be taken from plants, microbial, algal, and cyanobacterial sources, and typically the agents chosen act as both reducing and stabilising agents [128]. For example, Dwivedi and Gopal report on the production of silver and gold nanoparticles using an extract from Chenopodium album leaves [132], a plant

found in Asia, North America, and Europe. An extract from the plant was used as a reducing agent to produce silver and gold nanoparticles from silver nitrate and auric acid, respectively, in aqueous solution. The reaction was carried out at room temperature for 15 min. This simple, convenient, green method successfully produced 10-30 nm nanoparticles for both silver and gold.
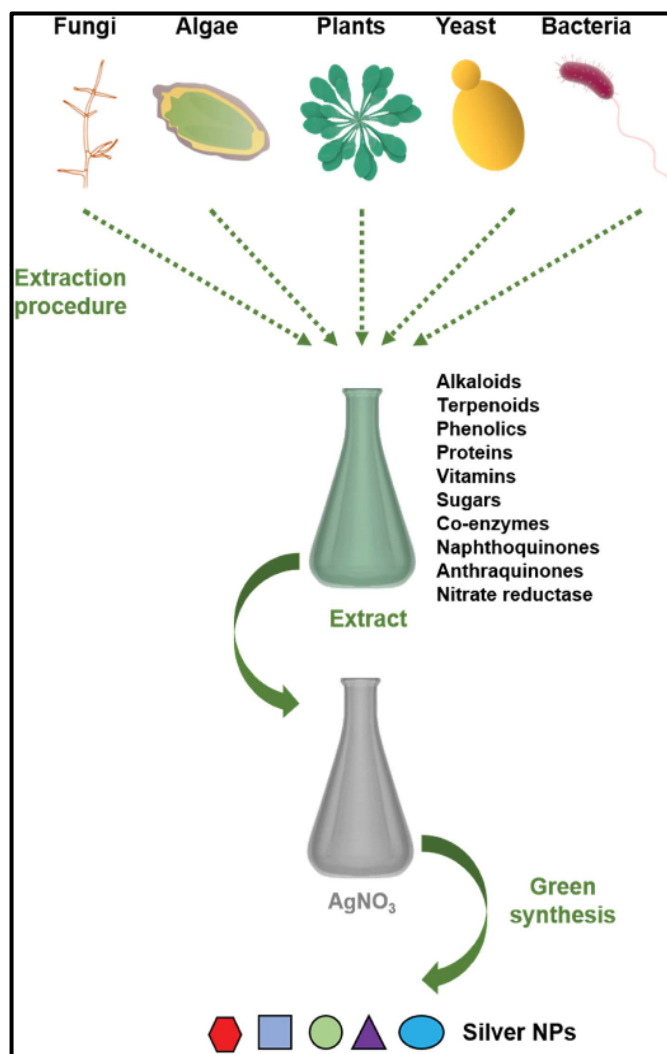
Figure 2.11: Schematic for green synthesis of silver nanoparticles using various biological agents [128].

2.3.3   Physical synthesis

Methods of nanoparticle generation based on physical processes can avoid the use of potentially hazardous or contaminating chemicals and solvents, and can achieve more uniform distribution of nanoparticles compared to chemical processes, however they may require higher capital costs for equipment, and higher energy consumption, for thermal or laser based processes [122].

2.3.3.1   Evaporation-condensation methods

Evaporation-condensation methods describes a technique where a source material is evaporated by heating, for example in a tube furnace, and condensed into nanoparticles. Magnusson et al. report on the production of gold nanoparticles by evaporation with a tube furnace, aerosolization, size selection, and thermal reshaping [133]. A schematic of the process is presented in Figure 2.12 [133]. In this method, the source material is placed in a ceramic boat in a tube furnace, heated to create a high pressure vapour which is then carried by a nitrogen carrier gas flowed through the furnace, creating the aerosolised particles. The particles are size selected in a differential mobility analyser (DMA), which relies on the particles being charged beforehand. The selected particles are then reheated in a second furnace to allow reshaping of the particles, and then size selected again by a second DMA. With this method, the authors were able to produce gold nanoparticles in the 20 nm size range, with near spherical shape and near single crystallinity.
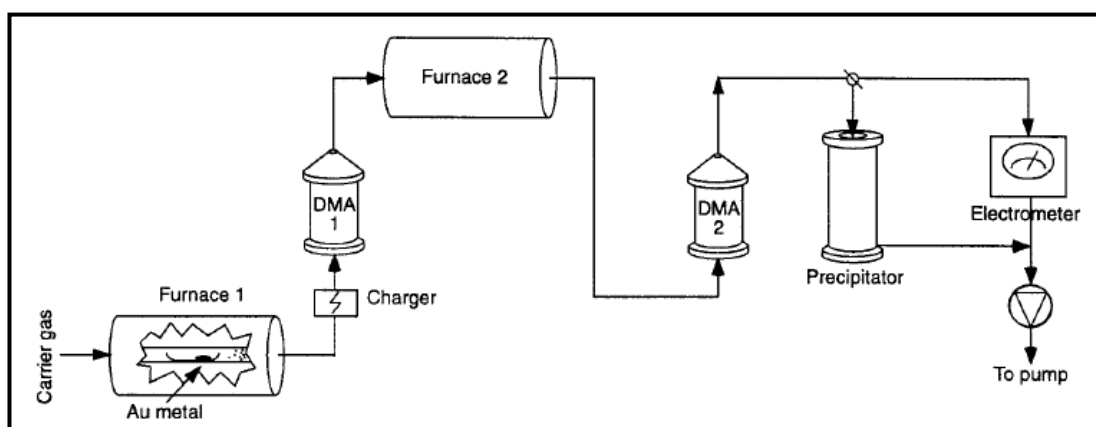
Figure 2.12: Schematic of an evaporation based gold nanoparticle generation method, using tube furnaces and differential mobility analysers (DMA) [133].

25

2.3.3.2 Ultra-sonic Spray Pyrolysis (USP)

Another physical technique reported for Np generation is Ultrasonic Spray Pyrolysis (USP) whereby a liquid solution is atomized into submicron droplets and carried through the heating and reaction zone by gas flow within which the Np formation takes place. In the heating zone, each droplet follows an evaporation and drying cycle, precipitation and then thermal reduction into the desired product with high particle heating and high surface reaction rates [134]. Since the decomposition and precipitation occur at the level of several micrometer sized droplets, USP can provide control of nanoparticle size, morphology, chemical and phase composition by adjustments of the solvent and process parameters [85], [135]. Previous studies revealed that USP is promising for achieving control over the size and shape of silver nanoparticles by adjusting solution molarity and reaction temperature [136]. Increasing molarity yielded an increased spherical shape with higher density of particles produced. Furthermore, it has been reported that the size of AgNps can be adjusted in the range of 20 nm to 300 nm by varying the precursor concentration and ultrasonic frequency [137]. Another study reported that the carrier gas (inert or reductive) has no impact on the morphology, size, chemical purity and crystallinity of the particles [138].

2.3.3.3 Arc discharge

Arc discharge have been implemented for physical nanoparticle generation, Lo et al. describe the use of arc discharge to produce silver nanoparticle suspensions [139]. A diagram of the experimental setup is presented in Figure 2.13 [139]. A silver bar submerged in a dielectric liquid is used as the electrode. An electric arc is generated, heating the metal to 6,000-12,000 °C. The evaporated material quickly cools in the surrounding low temperature dielectric liquid and forms silver nanoparticles dispersed in this cooling medium. The authors report the novel process was, with the correct processing parameters, successful in producing well dispersed nanoparticles in deionised water with average sizes ranging 6 nm - 25 nm, and avoiding aggregation. Lung et al. describe the use of arc discharge to produce gold nanoparticles [140]. Gold wires submerged in deionised water were used as both the positive and negative electrodes. Arc discharge between the wires, as with the process described by Lo et al. [139], evaporates the metal, which cools and condenses in the surrounding deionised water. The authors report the method is cheap, rapid, environmentally

friendly, and successfully produces gold nanoparticles, without the need for any surfactants or stabilisers.
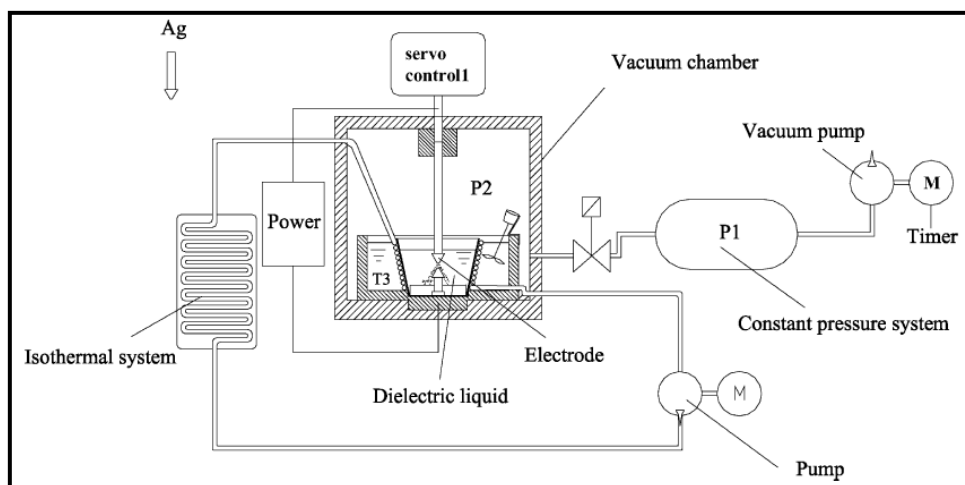
Figure 2.13: Schematic diagram of the arc discharge process for silver nanoparticle generation [139].

2.3.4 Milling

Nanoparticles can also be produced with physical grinding or milling. Grinding methods can be divided into dry or wet grinding [141]–[143]. Production of nanoparticles by dry ball milling presents a simple, low cost, environmentally friendly, high yield method [141], [143]. Arbain et al. report on the production of iron oxide nanoparticles by dry milling [143]. In this work a planetary ball-mill was used under atmospheric conditions with steel grinding media in a 3:1 ratio with the raw material, which was high purity hematite (Fe_2O_3) powder. Nanoparticles were successfully produced with a minimum size of 76.6 nm, without the need for any chemical additives, however there was some aggregation of the particles.

Wet milling allows the production of suspensions, and can produce more stable nanoparticles with the use of stabilising agents, however this reduces the simplicity of the method, and may add cost and reduce the environmental friendliness. Knieke et al. report the production of tin oxide and aluminium oxide nanoparticles by wet grinding [144]. Aluminium oxide powder of average particle size 2 μm or tin oxide powder of average particle size 1.6 μm were used, in deionised water and denatured ethanol, with a zirconia grinding medium. The powders were premixed with the wet chemicals in a stirred vessel,

pumped through a heat exchanger into the mill, and returned to the stirred vessel (see Figure 2.14) [144].

Gold and silver nanoparticles have also been produced by wet grinding. Pimpang et al. report on manual grinding of silver and gold nanoparticles [142]. Silver powder and gold foil were used as raw materials, with deionised water and ethylene glycol and 5 wt% polyvinyl alcohol as medium and stabilisers. The nanoparticles were produced by hand grinding in an agate mortar. The authors successfully produced gold and silver nanoparticles with optical properties indicating particle sizes of 140 nm - 150 nm. Grinding or milling may be used as part of a chemical production process to shape or stabilise the nanoparticles. Balaz et al report on a combined chemical-physical production method for silver nanoparticles, by wet milling using a plant-based reducing agent [145]. Silver nitrate and polyvinylpyrrolidone were used with an extract from *Origanum vulagare* L. plants. The leaves, flowers, and stems of *Origanum vulgare* L., a herb in the mint family, were dried and powdered to fine particles, which were then added by 10g to 100 mL of distilled water.
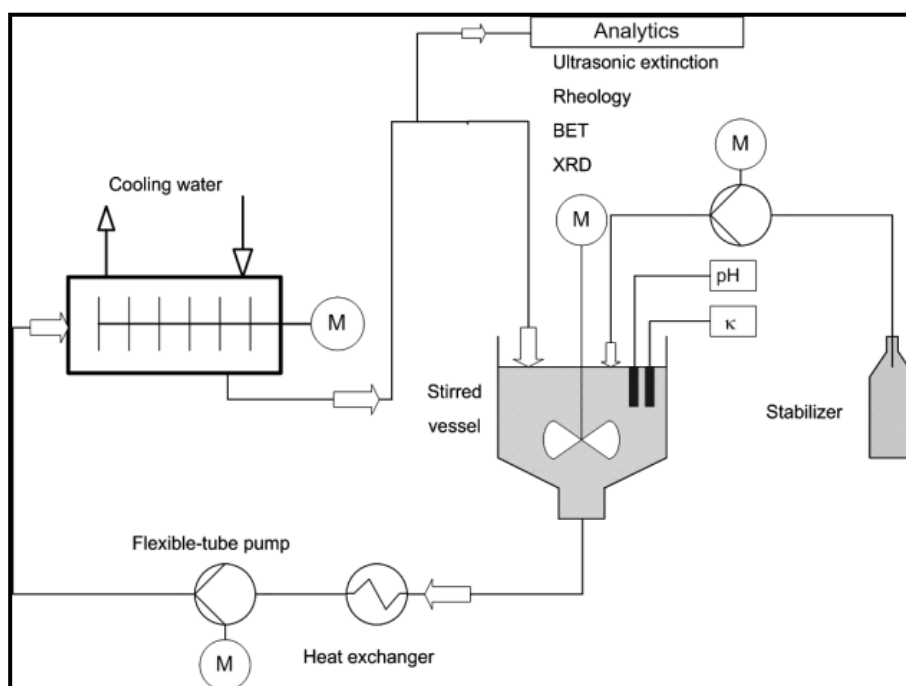
Figure 2.14: Experimental setup for wet milling of ceramic nanoparticles [144].

The mixture was then heated to 60 °C for 10 minutes, cooled down, and filtered to produce the reducing agent. The nanoparticles were produced in solution by chemical reduction with

the reducing agent, then processed in a stirring-media mill with a zirconium dioxide milling medium. The stabilising agent, polyvinylpyrrolidone, was added in this milling process. This method successfully produced stable silver nanoparticle suspensions, with two size groups of average size 7 nm and 38 nm, respectively.

2.3.5 *Laser synthesis of Nanoparticles*

Laser ablation synthesis in solution (LASiS) or pulsed laser ablation in liquids (PLAL) is a physical method of nanoparticle generation where a pulsed laser is focused on a solid target in a liquid medium, to ablate material from the target, creating nanoparticles in solution [146]. The laser light irradiating the solid target is partially absorbed by the target (with the remaining light being scattered or transmitted). The energy is absorbed by the excitation of bound electrons in the target. If the absorbed energy is high enough, the bound electrons will be released, ionising the material. These free electrons can continue to absorb the laser light by inverse Bremsstrahlung, leading to further heating and ionisation [147]. In the case of metals there is an abundance of free electrons within the material. The beam energy is absorbed by the free electrons, followed by thermalization inside the electrons and direct transfer of the energy into the lattice [148]. This interaction promotes greater ablation rates than other materials.

The result of the beam energy transfer is the formation of a high pressure plasma (10^9-10^{10} Pa), which cools and expands out from the target in a plume, initially with high speeds generating a shockwave through the liquid. As the plume expands it forms a gas cavitation bubble in the liquid, which collapses under the surrounding pressure, producing another shockwave which expels material into the liquid, cooling and condensing it into solid form, producing nanomaterials such as nanoparticle colloids. A diagram for this process is shown in Figure 2.15 [149]. The collapse of the bubble may produce a bubble rebound which then collapses, providing the behaviour similar to a damped oscillator [150]–[152].
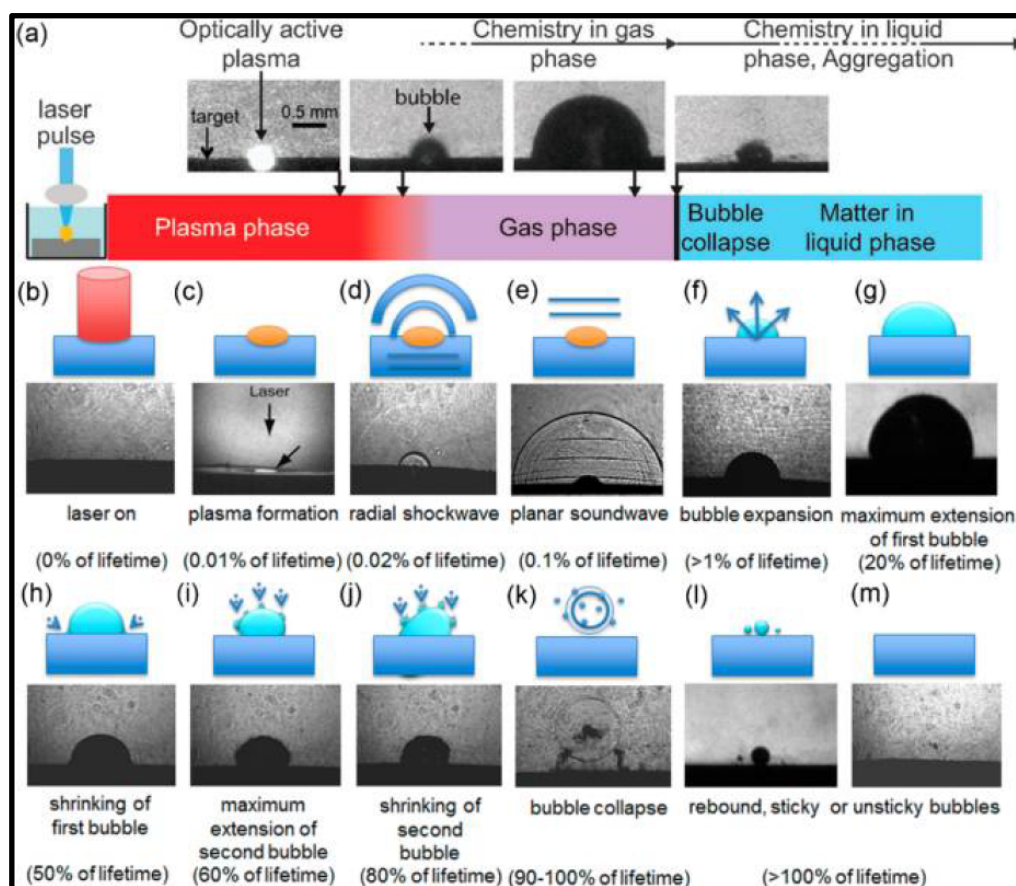
Figure 2.15: Plasma and bubble dynamics, the formation lifecycle of NPs [153].

The morphology of the nanomaterials produced can be controlled by altering the process parameters such as laser fluence, wavelength, and ablation medium. The LASiS process is highly adaptable, capable of producing a variety of nanomaterials (nanoparticles, nanocubes, & nanorods) with a variety of compositions (metals, alloys, oxides, carbides, hydroxides, etc.) [154]. The method generally does not require additional chemical agents, beyond the liquid solvent medium. Therefore LASiS is seen as a "green" route towards Np synthesis, producing Nps free from surfactant and additional ligands, required for chemical synthesis. Applications, particularly in the biopharma industry, require bare, ligand free nanoparticles [107], that would otherwise need to be obtained through an additional cleaning step, post fabrication of the nanoparticles [155].

2.3.5.1 Cavitation bubble dynamics

There has been considerable investigations into the cavitation bubble dynamics and its effect on nanoparticle formation. Ibrahimkutty et al. monitored the formation of nanoparticles in

the cavitation bubble using high-speed, small angle x-ray scattering [156]. Nanoparticles were produced by LASiS of a gold ribbon target in water by an Nd:YAG laser (1064 nm, 6 ns, 10 mJ, 200 Hz) focused to a 100 μm diameter spot size. The gold ribbon was continuously in motion perpendicular to the laser, providing a fresh ablation site for each pulse. De-ionised water flowed continuously along the plane of the target travel, transporting the Nps from the ablation site. The Small angle X-ray scattering (SAXS) 13.6 keV beamline at the Swiss Light Source was used as the x-ray source. The experimental setup is illustrated in Figure 2.16, showing the x-rays transmitted through the cavitation bubble. Some of the transmitted photons will be deflected by interaction with the fabricated nanoparticles, this interaction being monitored by the Pilatus x-ray detector based on hybrid-photon counting technology [156].
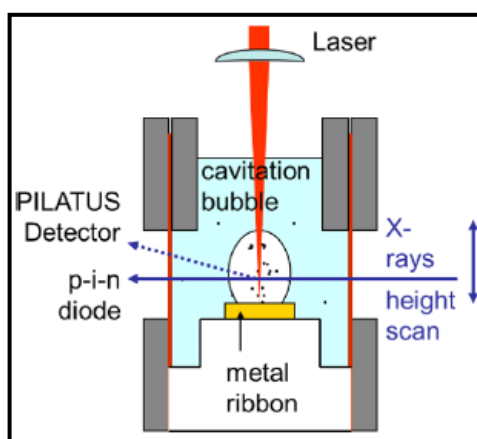
Figure 2.16: Diagram of x-ray scattering monitoring of cavitation bubble in PLAL gold nanoparticle generation [156].

The authors reported detection of two species within the ablation region: small particles of 8 nm - 10 nm, and larger, agglomerated, particles of ~45 nm diameter. Such bi-modal size distributions are commonly reported for LASiS fabricated nanoparticles [157]–[160]. The distribution of particles presented in Figure 2.17 illustrated the size of particles at various heights above the target material. Measurements were taken at the maximum cavitation bubble radius (R_{max}), 110 μs post-pulse, where the x-ray scattering intensity to indicate particle size was integrated, indicating a mass   [156]. It can be seen in Figure 2.17 the presence of primary particles decays towards the top of the bubble, with some primary particles found outside of the bubble perimeter prior to its collapse. The authors note that initial plasma velocities for laser plasma plumes created in vacuum have been found to be

10^8 mm/s, which is sufficient to allow injection of atomic species from the cavitation bubble into the surrounding liquid [161], [162]. Larger particles have already formed, possibly due to collisions between the primary particles in the plume/bubble, or a critical concentration being reached. These particles are not detected close to the target, which the authors attribute to the probability of agglomeration over time and height, and the confinement and cooling of particles nearer the vapour-liquid interface.
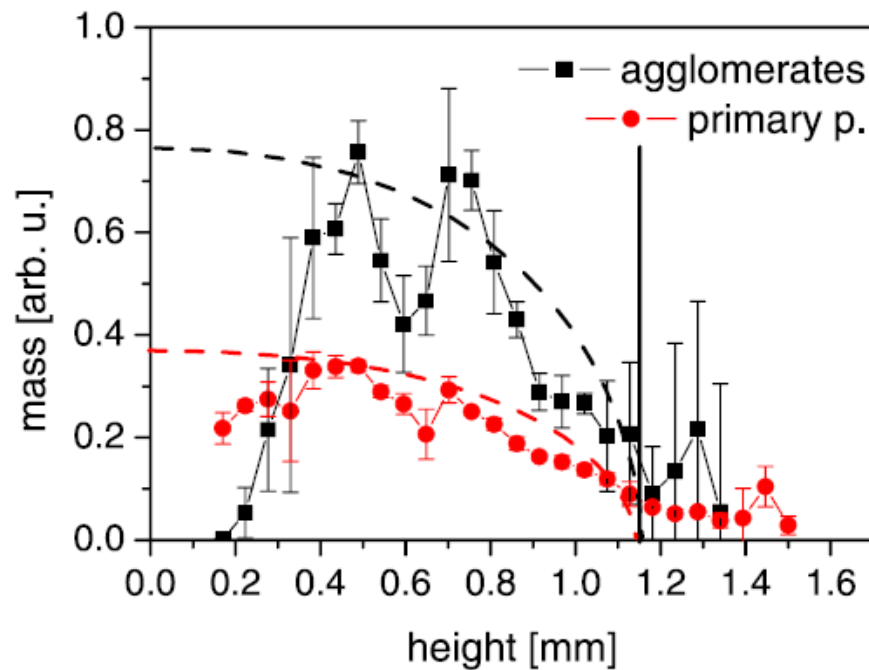
Figure 2.17: Distribution of particles vs. height above the target, identified by x-ray scattering. Small primary particles are denoted with red circles, and larger agglomerated particles with black squares. The vertical line marks the maximum bubble extension, and the dashed lines indicate the relative bubble thickness [156].

Shih et al. investigated the bimodal distribution which commonly occurs in LASiS by experiment and modelling [163]. Atomistic modelling of picosecond laser ablation of silver in water was carried out. Imaging of cavitation bubbles was performed to examine the mechanics behind the formation of the bi-modal size distribution. Their model suggests the formation of a transient hot molten metal layer at the interface with the surrounding liquid which plays a critical role in the nanoparticle formation process. The liquid in contact the hot molten layer becomes supercritical creating a metal-water mixing region which is a precursor to the cavitation bubble. The conditions in this relatively low-density mixing

region are conducive to the formation of small nanoparticles from the evaporating metal (<10 nm). The authors note a secondary formation process, where the molten layer itself may seperate under the pressure exerted by the surrounding supercritical liquid, forming larger nanoparticles (10-20 nm) without evaporation. This suggests a bimodal distribution, even in the absence of agglomeration. The model indicates ejection of this material from the mixing region into the surrounding, cooler, liquid, which was confirmed by the imaging experiments. The authors note good agreement between the model, the imaging results, and the resulting nanoparticles (analysed by centrifuge and transverse electron microscopy), supporting the conclusion that these two formation mechanisms lead to the bimodal particle size distributions commonly observed for LASiS.

De Giacomo et al. investigated the dynamics of LASiS cavitation bubbles during nanoparticle production using three complementary optical techniques: optical emission spectroscopy (OES) to characterise the plasma, fast shadowgraphs for the plasma and cavitation dynamics, and laser scattering for the produced materials in the liquid [147]. A diagram of the set-up can be seen in Figure 2.19 [147]. An Nd:YAG laser (532 nm, 8 ns, 10 Hz) was used for ablation of a solid metal target, in the form of a wire or a solid bulk, in water. By measuring the plasma temperature using OES and the initial volume from the shadowgraph images, the authors could calculate an initial pressure of the cavitation bubble, estimating values of 10^8 Pa for metal bulk targets ablated with laser fluences of 6 J/cm^2. When the bubble reaches its maximum expansion, the temperature of the bubble will be approximately equal to that of the surrounding liquid, and the pressure will be equal to the saturation pressure at that temperature. This pressure will be orders of magnitude lower than the surrounding liquid pressure, causing the bubble to contract. The authors note that this process is important, as nanomaterials produced may be deposited onto the surface of the target instead of being driven out into the solution. The shadowgraph, and laser scattering, images of the process for a titanium target are presented in Figure 2.18 [147].
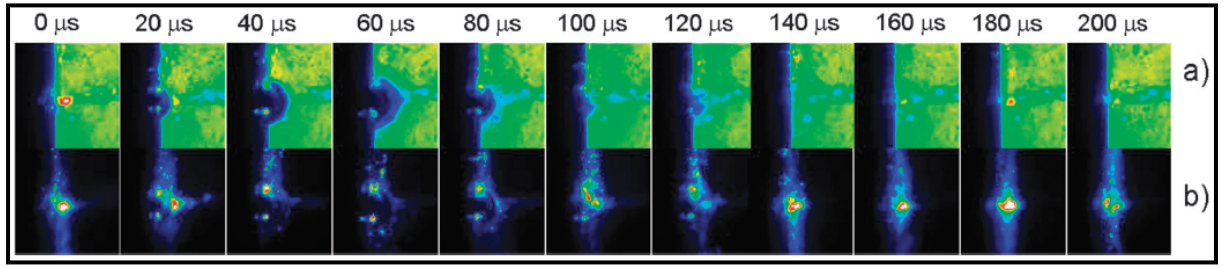
Figure 2.18: Temporally resolved (a) shadowgraph and (b) laser scattering images of a PLAL bubble on a Ti bulk target in water [147].
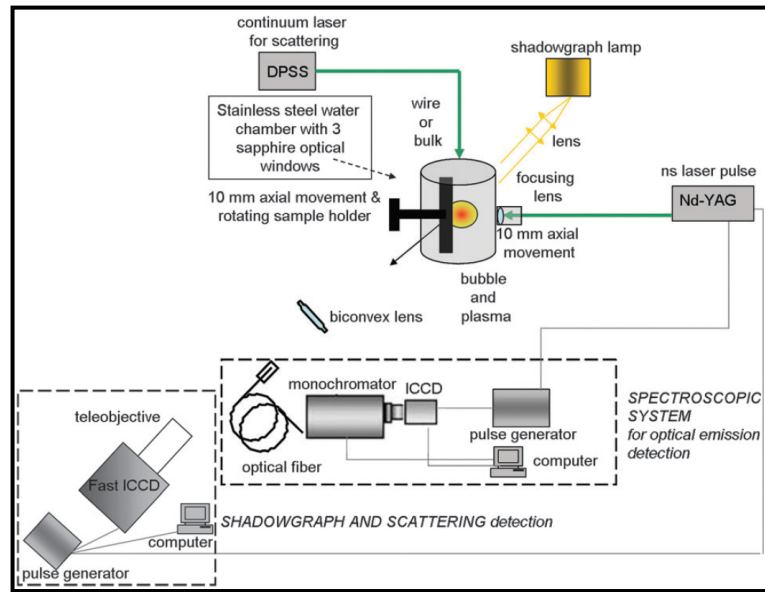
Figure 2.19: Experimental set-up to monitor LASiS nanoparticle generation using optical emission spectroscopy, shadowgraph, and laser scattering [147].

From shadowgraph results in Figure 2.20 it can be seen that the primary bubble reaches maximum expansion around 60 μs, and after collapse there is a secondary rebound bubble. The laser scattering signal indicates the produced particles lie close to the target surface. This is undesirable; as particles may deposit onto the surface of the target. It is more desirable that the produced nanoparticles are ejected into the solution. Post-LASiS scanning electron microscope (SEM) examination of the target showed the presence of deposited nanoparticles on the surface. Using the bubble radii determined from the shadowgraph images, the authors estimate the pressure and temperature in the cavitation bubble at each observation time using the Van der Waals model below [147]:

34

$$P(t) = \left(P_\infty + \frac{2\sigma}{R}\right)\left(\frac{R_\infty{}^3 - h^3}{R^3 - h^3}\right)^\gamma \qquad Eq.\,2.1.,\,[147]$$

$$T(t) = T_\infty \left(\frac{R_\infty{}^3 - h^3}{R^3 - h^3}\right)^{\gamma - 1} \qquad Eq.\,2.2.\,,\,[147]$$

Where P_∞ and T_∞ are the pressure and temperature of the liquid, R is the bubble radius, R_∞ is the radius at which the pressure in the bubble corresponds to the liquid pressure, σ is the surface tension of the liquid, $h = R_\infty/9.174$, and $\gamma = 1.22$. From this, they estimated that the temperature and pressure in the bubble exceeds 1000 K and 10^7 Pa respectively as the bubble collapses. The values they obtain are limited by the time interval of the shadowgraphs compared to the rapid changes of the bubble. These findings agree with models developed by Fabbro et al. (1990) for plasmas in confined environments, where the pressures generated within the plasmas were several orders of magnitude higher than for unconfined plasmas [164].

Theoretical modelling of laser-induced cavitation bubble collapse by Akhatov et al. has shown internal temperature values of 5000 - 10 000 K, and pressures of thousands of MPa [152]. These high pressure and temperature values may be responsible for the deposition of nanoparticles onto the target [147]. Ablation of wire targets was shown to give ejection of the nanoparticles into the solution, unlike the bulk targets, indicating the influence that target shape can have on nanoparticle generation output. For a wire target, the cavitation bubble was found to detach from the surface as it collapses, ejecting the particles. Shadowgraph images for wire targets of increasing thickness and a bulk target can be seen in Figure 2.20 [147]. The authors suggest this may affect the formation of the colloid, meriting further investigation, but also improves the output/scalability. The process parameters were also related to the results, indicating increased repetition rate improves yield. However, if pulses are delivered before the cavitation bubble created by the previous pulse has collapsed, the target will be shielded from the laser energy by the bubble. The authors estimate, based on the durations determined by shadowgraph, that repetition rates higher than 7 kHz will lead to bubble shielding, and that repetition rates higher than 3 kHz will lead to absorption and scattering by produced nanoparticles, limiting the ablation efficiency.
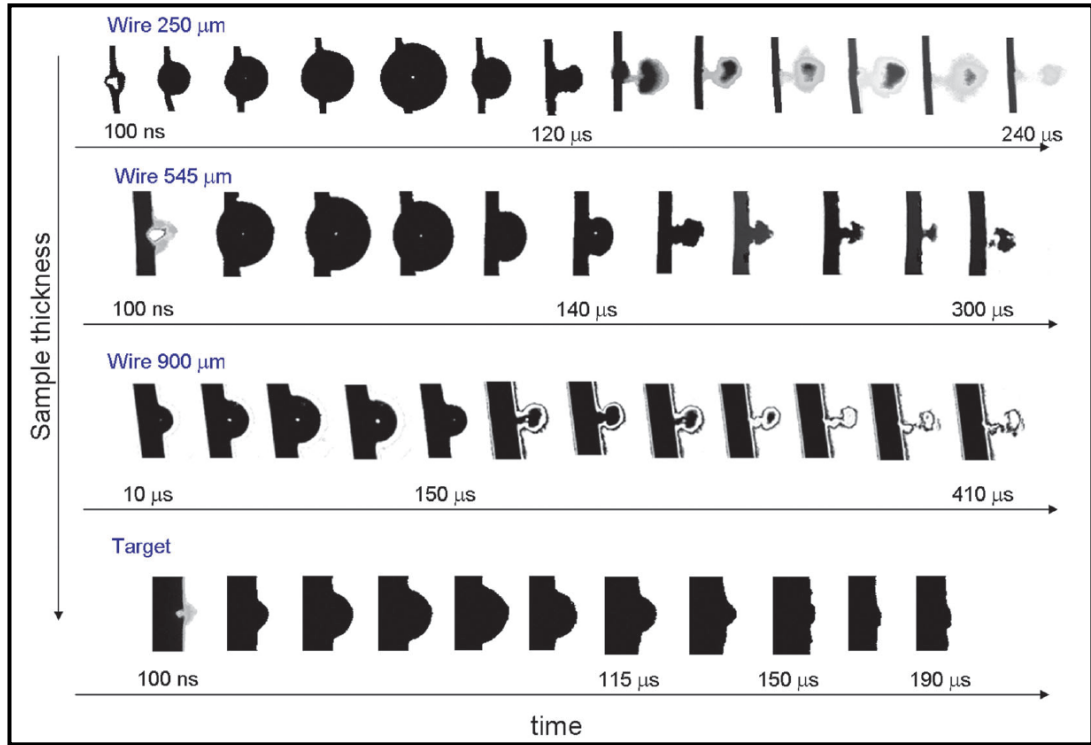
Figure 2.20: Time-resolved shadowgraph images of LASiS cavitation bubbles on different targets [147].

2.3.5.2   Batch Nps production

The majority of LASiS fabrication work presented in the literature is static, or batch, production. During batch production the ablation of a solid target is performed within a container of liquid. To increase the volume of production the nano colloid must be removed and replaced with fresh solvent. The cavitation bubble and ejected nanomaterials may act to shield the ablation target at higher repetition rates [147]. Furthermore, as production continues, the liquid will begin to saturate with nanoparticles, reducing the ablation efficiency and increasing photofragmentation [63]. This static approach has the advantage of simplicity, but limits scalability and output. The low productivity for LASiS has been noted as the bottleneck for the method, inhibiting its uptake in industry [165]. This has driven the development of batch and continuous or semi-continuous methods, where the target is immersed in a flow of solvent [166], [167].

36

2.3.5.3 Semi batch/recirculatory production

Barcikowski et al. reported the developments of a flow-based LASiS method to generate silver nanoparticles [167]. In this method, a magnetic stirrer is utilised to produce flow over the target in a bypass flow cell, shown in Figure 2.21 [167]. While the method is still batch based, the flow of solvent will remove nanoparticles, vapour bubbles, and heated liquid away from the ablation site, reducing occluding effects and transferring temperature evenly within the solvent, reducing evaporation, due to the flow regime this system has been classed as a "semi-batch" production [168].
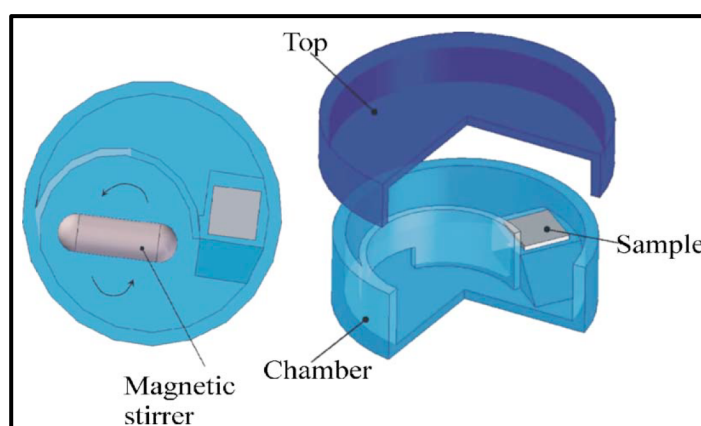
Figure 2.21: Bypass flow cell with magnetic stirrer to create flow over the ablation target during LASiS [167].

A commercial picosecond laser (1064 nm, 10 ps) was focused on a solid silver target in water in the flow cell, scanning the spot linearly. The experiment was carried out with the same processing parameters for static conditions, for comparison. The authors note that the production rate and nanoparticle size distribution for the static process is not reproducible. Microscope images showing the target after PLAL with static and flow conditions are presented in Figure 2.22 [167]. A non-linear and inconsistent appearance can be observed in the ablation lines on the target used under static conditions, and the effective spot size on the surface was found to be larger due to scattering of the laser light. The production rate was increased by 380% for flow conditions compared with static conditions, with the picosecond laser ablation system achieving a maximum productivity of 8.6 µg/s.
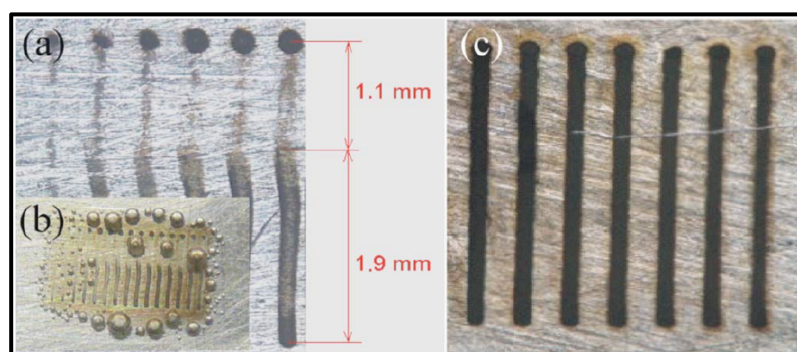
Figure 2.22: Ablated line geometries on silver targets produce by pulse laser ablation (5.5 W (0.1 mJ), 50 kHz, and 20 repetitions per line) in (a) & (b) stationary and (c) flow conditions, with linear scan speed of 0.5 mm/s [167].

2.3.5.4 Continuous production

Messina et al. report the production of silver nanoparticles with a continuously-fed wire target under flow conditions [166]. An Nd:YAG laser (1064 nm, 10 ns) was reduced to a collimated 3 mm using telescope optics and passed through an ablation chamber where a silver wire target (of 125 – 1000 µm diameter) is continuously fed by motor (shown in Figure 2.23 [166]). The water in the chamber is pumped parallel to the direction of the wire feeding, to avoid deformation of the wire under water pressure, at flow rates of 540 ml/min. As discussed by Barcikowski et al. [167], the geometry of the target was found to have an effect on ablation efficiency, with wire targets giving higher ablation efficiency than bulk targets due to the release of the cavitation bubble from the surface, along with the destruction of the target at the ablation site. They found three main factors related to the diameter of the wire influencing the ablation efficiency:

1. the area irradiated by the laser, and thus the operating fluence (F_t);
2. the heat dispersion, which, for cylinders, decreases with decreasing diameter, and also the thermal diffusivity (*Di*) of the material;
3. Bubble dynamics on larger wire diameters - cavitation bubble behaviour will approach that of a bulk target, with the bubble remaining on the surface as it collapses.

In all cases, the wire targets provided higher ablation efficiency compared with using bulk targets. Wire with a diameter of 750 µm was found to give production efficiencies $15x$ greater than a comparable bulk target ablation.

Productivity was seen to increase linearly with repetition rates tested, from 1-100 Hz, as the interval between pulses was longer than the lifetime of the cavitation bubble (~250 μs). The linear increase should continue, until the pulse interval overlaps with the cavitation bubble, with maximum repetition rates of about 2 kHz. The authors estimate for higher repetition rates a theoretical maximal productivity of >25 g/h should be achievable with a 750 μm diameter wire target. Fluence ranges of 0.4 J/cm^2 to 1.5 J/cm^2 was found provide a linear relationship with productivity. The silver nanoparticles produced had diameters ranging 15 nm to 20 nm, with no difference between those produced from wire and bulk targets, indicating that the temperature and pressure in the cavitation bubble were not affected by the geometry [147], [166].
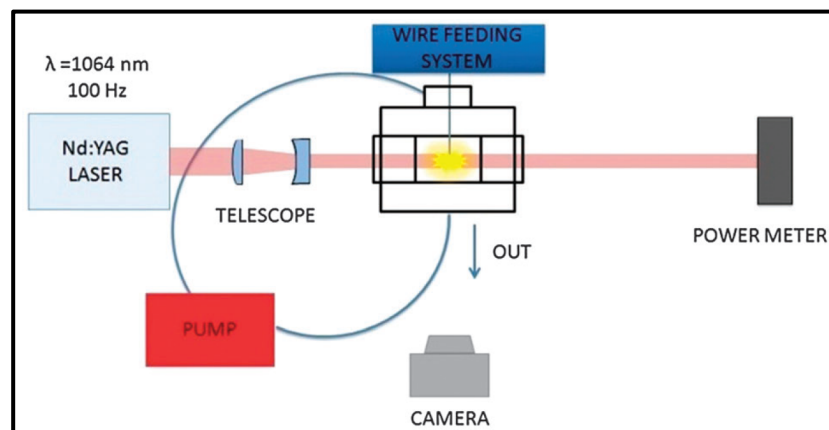
Figure 2.23: Experimental setup for continuous wire target PLAL [166].

2.3.5.5 Spatial by-passing occluding material

Streubel et al. describe a high speed LASiS process for continuous metal nanoparticle generation [165]. A picosecond laser (1030 nm, 3 ps, 10 MHz, 500 W) combined with a polygon scanner was used to scan the laser spot at speeds of up to 500 m/s over metal (platinum, silver, gold, aluminium, copper, and titanium) targets under flow conditions. With high scanning speeds, a subsequent pulse can be spatially removed from its prior ablation site, allowing higher repetition rates to be used without the issue of cavitation bubble shielding. The authors acknowledge the productivity bottleneck facing PLAL, and point out that studies which report ablation rates ≥ 1 g/h often extrapolate from rates measured over seconds or minutes [169], [170].

Schwenke et al. investigated the influence of processing time on nanoparticle generation [171]. In this work they studied ablation rates using picosecond LASiS for times of up to 1 hour. They found evidence that ablated mass did not increase linearly with ablation time, attributed to the absorption or scattering of laser light by the produced nanoparticles, indicating that extrapolating from seconds or minutes of ablation may not be valid, which is significant when using results to estimate pilot scale production processes.
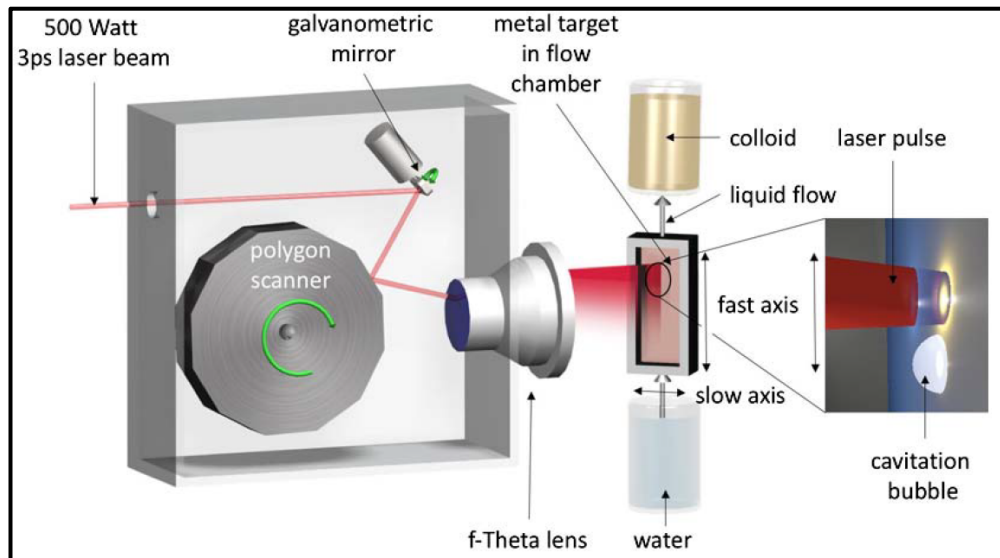
Figure 2.24: Ultrafast polygon scanner PLAL process for continuous metal nanoparticle generation, with a magnified insert showing the spatial bypassing of cavitation bubble shielding [165].

In the work by Streubel et al., bypassing of cavitation bubble and nanoparticle shielding using an advanced beam scanner and flow conditions presents an opportunity to achieve high productivity over long time frames (see Figure 2.24) [165]. An ultrafast laser beam is directed by two scanning systems, a polygon scanner for fast, vertical translation, and a galvanometric mirror for slower, horizontal translation. Water is pumped through the ablation chamber, with the colloid being collected in a different vessel, allowing for semi-continuous production. The authors carried out optimisation experiments with 10 minute durations to optimise the process parameters, then used the optimised parameters (500 W, 10.1 MHz, 484 m/s) for 1 hour of continuous production for six different metal targets (platinum, gold, silver, aluminium, copper, and titanium). The resulting production rates are presented in Figure 2.25 [165]. The highest productivity achieved was 4.1 g/h, for the platinum target.
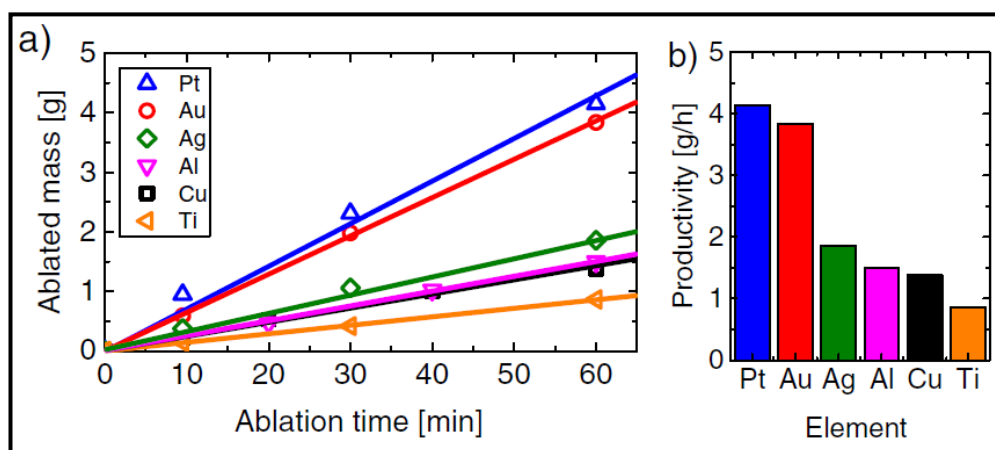
Figure 2.25: Productivities for fast scan PLAL (a) ablated mass as a function of time for six metal targets (b) the productivity in g/h for the different targets [165].

2.3.5.6 Influence of liquid layer

Another factor affecting the yield for LASiS is the thickness of the liquid layer covering the target [172]–[174]. As light travels through a liquid medium some of the light will be absorbed, attenuating the beam, with thicker layers of water leading to a greater portion of the laser energy being absorbed. However, if the liquid layer is too thin it may insufficiently confine the plasma plume, even allowing the plume to expand beyond the surface of the liquid [174]. Jiang et al investigated the yield for LASiS generation of germanium nanoparticles in deionised water using a 532 nm wavelength Nd:YAG laser [173]. They found the optimum water layer thickness for these conditions to be 1.2 mm. It has been reported that medium and higher power laser systems a liquid height of 4 mm is a good starting point to optimise [175]. This dept of liquid mitigates liquid breakdown and plume interaction with the liquid/air boundary.

Kohsakowski et al. reports on a continuous method for nanoparticle generation using wire-targets in a liquid jet [155]. Previous works have shown the increased effectiveness and productivity of wire targets [166], [167]. Kohsakowski et al. present an experimental method for PLAL nanoparticle generation in which a wire target is continuously fed, as in Messina et al. [166], under a liquid jet. This method combines continuous liquid flow, with a thin liquid layer, a wire target geometry, and continuous feeding of the target. The experimental setup is shown in Figure 2.26 [155]. Wires of different materials and diameters could be fed through the jet nozzle, with interchangeable nozzles of 1- 4 mm diameter to allow varying

of the liquid layer thickness. Water flow was controlled by pump to give a flow rate of up to 480 ml/min, and the layer thickness was measured by imaging with a camera system. A nanosecond Nd:YAG laser (1064 nm, 0.1 - 15 kHz, Pulse energy (E_0) = 2 - 8 mJ per pulse) was used for the ablation. A power meter behind the jet was used to ensure good illumination of the wire target, where lower power was related to higher wire laser energy interaction.
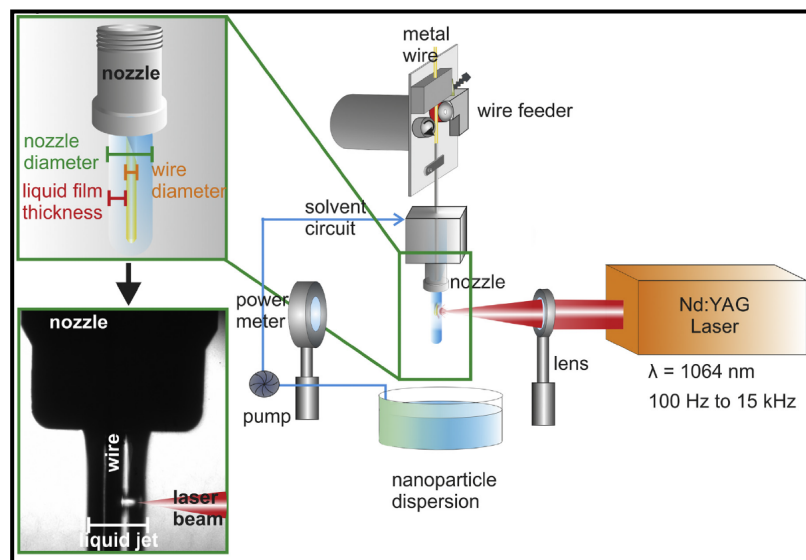
Figure 2.26: Experimental setup for continuous PLAL using a continuously fed wire target and water jet [155].

The authors determined the process was successful as a continuous and stable nanoparticle production process, with consistent particle sizes. High productivities were obtained, over a 1 hour process time: 220, 410, and 550 mg/h for gold, platinum, and silver, respectively. The values are lower than those obtained by Streubel et al. [165], however Kohsakowski et al. applied a ns pulse with an average laser power output of 32.5 W, compared to Streubel et al. using ps pulses with 250 W average laser power. The power specific productivity, in terms of the ablated mass per unit of laser power, was comparable for the two works; ranging 6.77 - 16.92 mg/Wh for Kohsakowski et al. and 7.6 - 16.20 mg/Wh for Streubel et al. [155], [165]. Highest productivities were found with a liquid layer thickness of 500 μm.

2.3.5.7   LASiS commercial outlook

Today 10 % of nanoparticles are produced via top-down processes such as milling, grinding and laser synthesis with the remaining 90% produced via chemical synthesis either through vapour phase or liquid phase synthesis [176]**.** An advantage of LASiS compared with

chemical synthesis is the simplicity of the experimental setup; the only equipment required for LASiS is a laser system, beaker, solvent and target material. It has been reported that a typical bulk gold target (99.99% purity) costs 40 €/g can be transformed into an Au Nano colloid valued at 10,000 €/g [177]. This leads to the question: why has LASiS not taken a larger percentage share of the methods used for Np fabrication, especially given the purity of nano colloids produced and the lower requirement of surfactants and binding agents, leading to the possibility of high-purity and high-reactivity Nps [178]? The problem arises with scale-up from laboratory to commercial production. Jendrzej et. al., (2017) conducted a study examining the scale-up costs of AuNps from 1 mg production towards 1000 mg, considering labour, energy, capital equipment investment and material costs, they stated that 1 g Np production was a feasible commercial requirement, and an appropriate benchmark point [129]. Given the reasonably low production volumes, as discussed by Jendrzej et. al., (2017), from the outset LASiS should be considered as a technique for high purity, high value Nps production rather than a catalyst production method.

Jendrzej et. al., (2017) compared production of AuNps via LASiS and chemical synthesis, stating that both techniques produced Nps of similar size, morphology and chemical structure. They determined LASiS labour costs to be 48% lower than wet chemical synthesis due to the fewer manufacturing steps required. They extrapolated that 1g of AuNps would be produced in 12 hours at a maximum rate of 85 mg/h by LASiS, while the chemical synthesis would take 18 hours at a production rate of 57 mg/h. Material costs for laser ablation consisted of the gold foil ($154/g) compared with gold precursor and salts addition (chloroauric acid $296/g & tri-sodium citrate $0.9/g) required for chemical synthesis. The capital investment of the laser system used as an example in the study was $60k for a 90 mg/h estimated Np producing system (8.9 W, 10 ns), compared with $45k for the total equipment costs associated with chemical synthesis. An additional maintenance of the laser system would be required, with the diode needing replacement after 15k hours of operation. The estimated costs for LASiS production was $521/g with $371/g for chemical synthesis, where the relative capital costs of the laser system were seen to decline with increased production, whereas chemical synthesis labour costs rose. Also, bulk target material was determined to be of lower cost than the required chemical precursors and salts. Therefore, Jendrzej et. al., (2017) proposed a theoretical break-even point when total AuNps production exceeds 65 g, in 773 working hours, see Figure 2.27. Therefore, they state that within a year

of continuous production of AuNps, continuous LASiS should be more cost efficient compared with chemical synthesis.
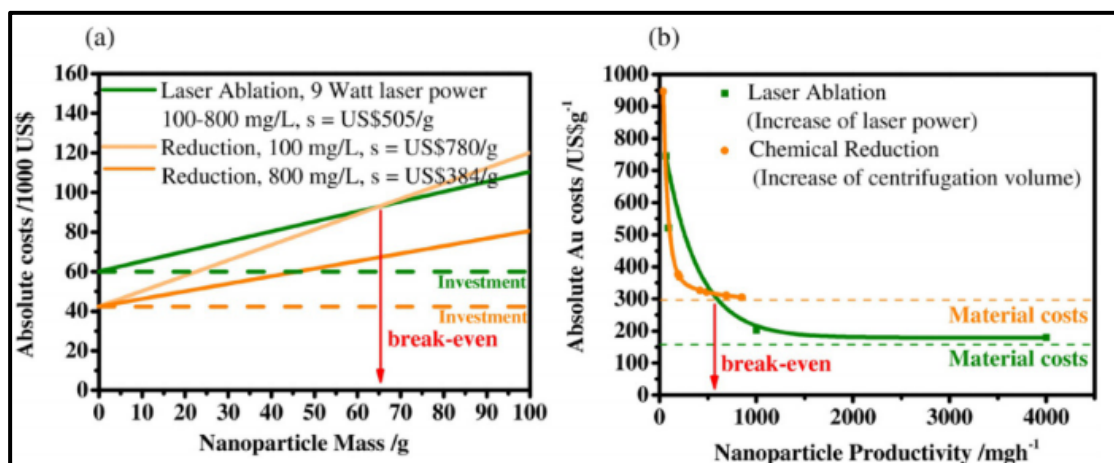
Figure 2.27: Break-even points for LASiS vs chemical Np synthesis routes [177].

2.3.6   *Summary of Nps production methods*

The various nanoparticle production techniques discussed above is summarized in Table 2.1, all techniques discussed can produce nano colloids with spherical nanoparticles to varying degrees of process control and productivity. When considering production performance, capital costs and running costs, LASiS offers the clearest route towards competition with chemical synthesis, especially when considering biotechnology applications.

Table 2.1: Summary of nanoparticle production techniques

Nps fabrication method	Method type	Nps produced	Features	Drawbacks	Refs
Wet chemical synthesis	Reduction based via inorganic reducing agents & salts.	Metallic, alloy, polymer Nps in solution.	High volume production (>1000 L). Lowest cost of production. Developed manufacturing process.	Hazardous waste by-products, Ligands and surfactants on Np surface for stability.	[118], [119], [120]
Biological synthesis	Reducing process via biological agents.	Metallic Nps in solution.	Ecologically safe.	Less size control than physical techniques, low production volumes.	[126], [128], [129]
Ultra-sonic spray pyrolysis (USP)	A liquid solution is atomized into submicron droplets, interacts with gas flow to create Nps.	Metallic, alloy Nps in solution.	Good control over Nps size and shape.	Hazardous waste by-products, Ligands and surfactants on Np surface for stability.	[132], [135]
Arc discharge	A material is submerged in a dielectric liquid. An electric arc evaporates the material which condenses into Nps in the surrounding liquid.	Metallic, alloy Nps in solution.	Sustainable production, no waste by-products, surfactant and stabiliser free.	High running costs, difficulty to control alloy production.	[137], [138]

Milling	Physical technique: grinding and milling of microparticles.	Metallic, alloy and ceramic Nps in dry powder or solution.	Sustainable production, no waste by-products, produces bare, surfactant & ligand free Nps. Produces dry powders or colloids. High volumes.	Stabilising agents and grinding medium may be required.	[139], [140]
Laser synthesis in solution (LASiS)	Physical technique: reducing via laser ablation.	Metallic, alloy, semiconduct or, polymer and ceramic in solution.	Sustainable production, no waste by-products, produces bare, surfactant & ligand free Nps. Ideal production of metal alloys.	High capital costs of equipment. Lower productivity than Chemical synthesis. Technique in development.	[164]

2.4   Selected Nanoparticle monitoring techniques

This section presents some of the most important techniques for the characterisation of nanostructures and nanoparticles. The techniques presented here are grouped into categories of topology, internal structure and material composition. Morphological techniques include field emission scanning electron microscopy (FESEM) and particle size distribution with dynamic light scattering (DLS). Internal structure techniques presented are transmission electron microscope (TEM). To highlight the current capabilities and applications of these techniques, case studies from recent literature are presented.

2.4.1   *Measurement of the topology of nanostructures*

2.4.1.1   *Scanning Electron Microscope (SEM)*
Scanning electron microscopes (SEM) have been used by researchers since 1935 to examine micrometer scale structures and is currently the most widely used non-optical microscopy technique. In the past fifteen years, more focus has been brought on its application towards

nanostructures. This technique allows for a comparably large sample window and for dimensional measurements to be performed. The principle of operation of the SEM involves a focused electron beam which is directed onto the surface of the sample, resulting in electrons being emitted from the surface that are then collected by a positively charged detector grid. These are termed secondary electrons. These secondary electrons are recorded for the scanned surface and provide a surface topology. The factors that affect SEM resolution are the primary electron beam spot size and the volume of material with which the electrons interact. In order to ensure best possible resolutions, a high accelerating voltage should be employed (20-30kV), along with a smaller current and small spot size. Care is needed however in some cases to avoid high electron energies where these can modify or destroy the material structure to be observed. Tungsten and carbon are the traditional filaments used for SEM with LaB_6 emission sources being commonly adopted now due to their offering longer gun lives and not necessitating nitrogen cooling. Another type of emitted electrons "backscattered electrons" are collected by a backscatter collector, they are high energy electrons resulting from the incident electron beam. The response of these electrons is directly proportional to the density of atoms in the material, allowing surface composition, via relative density difference, to be visualised.

SEM case studies

Recently the SEM technique has been applied towards a range of applications such as determining the effects of gelling agents on the morphology of $ZnSnO_3$ nanostructures [179], examining the surface morphology and nano surface features of flat objects [180] and measuring the diameters of silicon, latex and gold spherical nanoparticles with mean diameter of 15nm [181].

It has been observed that SEM performance can be increased by applying the secondary electron detector at low magnifications to image TaS_2 nano tube bundles as seen in figure 2.28. This configuration allowed for larger scan areas and faster processing times. A 10kV beam voltage was used with a magnification of 12.4kx [182].
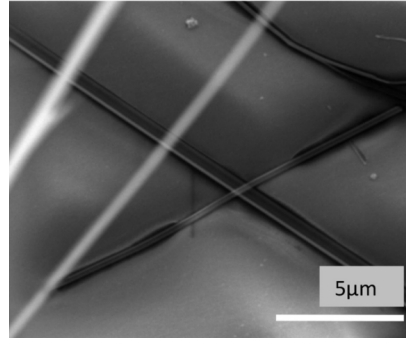
Figure 2.28: SEM image of a silica fragment within a TaS2 nanotube bundle [129].

SEM typically has at best a spatial resolution of 1 nm to 10 nm and therefore it is generally used to characterise structures greater than 10 nm. Over the year's efforts have been made to break this 10nm barrier. Recently Villarrubia et al. (2015) have proposed a technique to improve the resolution of SEM inspection of lithographically patterned SiO_2 used by Intel. The authors fitted the measured intensity vs. position to a physics-based model which included the lithography lines' dimensions as parameters. A 3D model for patterned SiO_2 was developed as shown in figure 2.29. They concluded that with the aid of the model, sub-nanometer resolution could be achieved, an improvement of almost ten-fold.
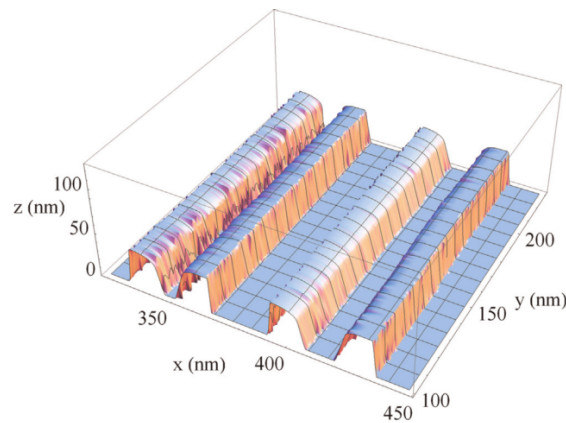
Figure 2.29: SEM generated 3D reconstruction data of lithography produced SiO2channels [130].

2.4.2   *Field Emission Scanning Electron Microscope (FESEM)*

A field emission cathode in the electron gun of a SEM provides narrower probing beams resulting in both improved spatial resolution and less sample charging. Such systems are designated as Field Emission Scanning Electron Microscopes (FESEM). To achieve this increased electron focusing a different gun design is required [183]. In this design, electrons

48

are expelled by applying a high electric field very close to the filament tip. The size and proximity of the electric field to the electron reservoir in the filament controls the degree to which electrons tunnel out of the reservoir. One type of field emission gun commonly used is known as the Schottky in-lens thermal FESEM electron gun. Cold gun alternatives are available for even finer FESEM resolution; however, these suffer rapid degradation and can therefore lead to expensive operation due to relatively frequent placement. The field emission guns have higher stability, can allow higher current and hence provide a smaller spot size. Under good operating conditions a typical FESEM resolution of 1 nm is achievable. Elements that add to improved operation and FESEM resolution include designs with a beam booster to maintain high beam energy, an electromagnetic multi-hole beam aperture changer, a magnetic field lens, and a beam path was designed to prevent electron beam crossover. Nanostructures have been characterised by FESEM in different morphological formations including nanoflowers [184], nanosheets [185], nanoparticles [186], and thin films [187]–[190].

Molybdenum disulphide (MoS_2) nanosheets exhibit interesting conductive/semi conductive, magnetic, photoluminescence, photocatalytic, and field - effect transistor properties. The properties of MoS_2 nanosheets depends upon the method used to generate them and depending upon the structural properties, these nanosheets can be used for applications in optoelectronics, energy harvesting, and spinelectronics (fluxtroincs) etc. The characterisation of MoS_2 nanosheets morphology has been performed by FESEM in various studies [191]–[195].

FESEM case studies

In one study, nanostructured Tin(II) sulphide (SnS) thin film was deposited on FTO glass substrate by electro-deposition (ED) with and with ultrasound assistance electro-deposition (UAED) [196]. Figure 2.3 shows the FESEM micrographs of the ED-SnS and the UAED-SnS produced nanostructures [196]. The effect of using ultrasound waves during electrodeposition on the morphology of the nanostructured SnS films can be clearly seen. The FESEM images showed that without using ultrasound waves, the deposited SnS film had grain-like morphology. Using ultrasound assistance during electrodeposition, the FESEM showed the formation of two distinct nanostructures. The first type was in a formation of 20 nm to 60 nm thin plane nanostructures. The second type was in cubical rods

49

type structures with less than one micron height [196]. Other workers have applied FESEM characterisation for the implementation of cryo-SEM natural state colloidal solution capturing and studied the process of simultaneous deposition by immersion plating of palladium and silver seeds from 1 to 100 nm in size on porous silicon [5, 6].
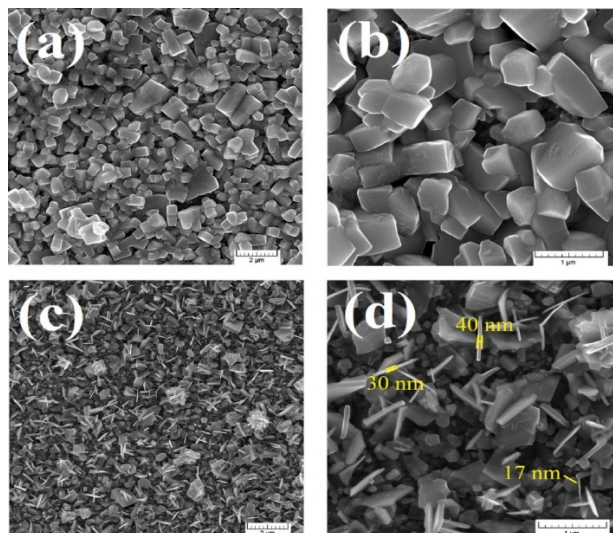
Figure 2.30: FESEM micrographs of the (a), (b) the ED-SnS and (c), (d) the UAED-SnS produced nanostructures [144].

2.4.2.1 Dynamic light scattering (DLS)

Dynamic light scattering (DLS) techniques have been adopted as the primary on-the-bench method for measurement of nanoparticle size distribution in liquid suspensions. DLS is widely used in research and industry, it provides rapid size analysis of nanoparticle colloids. It has attained such market coverage that many nano-colloid researchers rely on it as their sole size characterisation technique. The technique is used for particle analysis in inks, paints, and more recently biological diagnostics and disease treatment systems [10], [197], indeed many fields where nanoparticle size is critical. The technique offers possibilities of in-situ measurement, which can be important for time sensitive process and industrial manufacturing.

Unlike microscopy techniques, the size measured is not just a function of the material core size in air, but the hydrodynamic diameter; including effects from fluid stabilizers, surfactants, and the electrical double layer thickness [198] while also providing an overall size distribution of the bulk colloid. Thus, DLS offers a more representative measurement of NPs size while in the liquid phase. This may provide more useful data if the nanoparticle

applications are in liquid suspension. Generally, the size distribution measured by DLS is larger than for microscopy techniques such as TEM and SEM where nano colloids must be transferred to a substrate and dried. During this process the hydrodynamic properties are lost and drying aggregation may occur. It should be noted that the sample size of drop-cast particles for TEM and SEM is smaller compared with the "bulk" measurement of DLS. However there are factors which affect the technique's precision, due mainly to its base technology, how light interacts with differing size particles [199], leading to measurement masking effects. DLS operates on the principle that the diffusion coefficient (D) of a particle is size dependent where the Stokes-Einstein equation [199] describes the diffusion coefficient as:

$$D = \frac{K_B\,T}{6\,\pi\,\eta\,R_S} \tag{3.1}$$

with K_B being the Boltzmann constant, T the colloid temperature, η the solvent viscosity and R_S the sphere radius. This basically describes that light scatters at different rates with differing particle sizes [200]. During its operation samples are irradiated with a coherent monochromatic polarized laser beam light source, as seen in the figure 2.31. A scattering detector, positioned typically at an angle of 173˚ backscatter [201] to the beam collects the dispersed pattern containing intensity fluctuations of light. This dispersed light intensity pattern is due to constructive and destructive interference on different areas of the detector [202]. The scattering of light is related to the position of particles in the sample and the scattered light from each particle will be in its unique phase while striking the detector surface. This scattering intensity is a function of: particle size, solute-particle concentration, refractive-index difference of solvent and solute particles [203]. Therefore, if measurements are repeated at known time intervals, the intensity change of the scattered patterns over time is accounted for by Brownian motion of particles and the intensity change can be related to the diffusion coefficient and particle size.
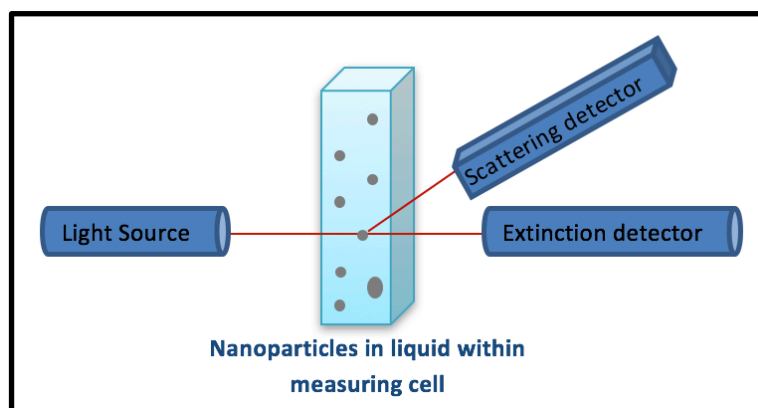
Figure 2.31: Schematic showing DLS operation, including coherent monochromatic polarized light source, extinction detector and scattering detector placed at a defined incident angle.

DLS case studies

Tomaszewska et al. (2013) investigated the detection limits of DLS for the characterisation of polydisperse nanoparticle colloids. To make a controlled, artificial polydisperse colloid, the authors mixed known concentrations of standardly produced and characterised 10nm, 55nm and 80nm Ag nanoparticles, confirming their measurements with AFM and TEM. They found that the polydispersity of the colloids was problematic to the measurement of the true colloid size, as the light scattering intensity from the larger NPs masked out the smaller particles. The authors concluded that as low as a 5% presence of larger NPs in the sample population was enough to mask the detection of the smaller nanoparticle colloid, making up 95% of the sample population [198]. This highlights the sensitivity of DLS measurements to highly polydisperse populations, skewing measurement results. This leads to possible problems monitoring colloids containing aggregates.

Horechyy et al. (2017) used in-situ DLS to monitor the growth of silica core shells on co-polymers. The authors used disposable DLS cuvettes to hold the co-polymer mixture. Silica sol was added to PS-b-P4VP micelles and mixed for 2 mins before placing the cuvette into the Malvern Zetasizer Nano S and starting Z measurements at 2 min intervals. The refractive index and fluid viscosity was set for standard methanol. Each 100 s measurement utilising ten auto-correlations with a 10 s scan speed. The data was averaged using Dispersion Technology Software (DTS). Using this technique, the authors observed five distinct stages in silica shell formation [204]. Time dependent particle diameter for the initial stage after the addition of SiO2 is illustrated in figure 2.32. The authors found that TEM and DLS

measurements of the growths stages showed contradictory trends, where within the first hour a dramatic decrease in particle size was observed on the DLS, and not so much with the TEM. Also after several days there was an observed increase in the DLS particle size measurement, not evident from TEM analysis. After further inspection the cause of these discrepancies was determined as follows:

1. The increasing density of the silica shell lead to a reduction in the hydrodynamic particle size observed by the DLS.
2. After several days, the hydrodynamic particle size increased due to changes in the fluid viscosity, but the shell growth was substantially smaller.

In this work the authors utilised in-situ DLS measurement, concluding that in-situ monitoring was a useful tool in understanding the full growth profile of silica shell nanoparticles.
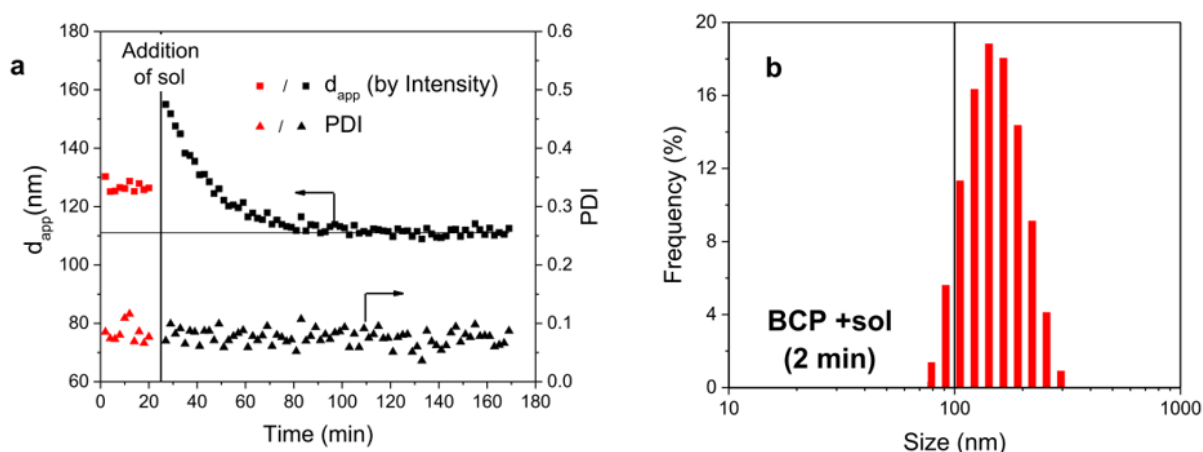
Figure 2.32: (a) Apparent particle size (squares) and PDI (triangles) of PS-b-P4VP co-polymer before (red) and after the addition of SiO2 (black) over time showing silica shell evolution; and (b) intensity of particle size distribution, 2 mins after the addition of SiO2 [204].

2.5 Measurement of nanostructures internal geometries

2.5.1 Transmission Electron Microscope (TEM)

TEM is an established characterisation technique, which can provide both image mode and diffraction mode information from a single sample [205]. It is regarded as one of the main techniques for nanomaterials characterization, largely due to its high lateral spatial

resolution, in the region of 0.08 nm [206]. A feature of nanomaterials is that specific properties, for example, colour, can be related to a particles size. Agglomeration of nanoparticles, or failure to isolate individual nanostructures is likely to result in anomalous property characterisation. Characterising the elastic or mechanical properties of individual nanoparticle/ nanotube/nanofibers is a challenge to many existing testing and measurement techniques. It is difficult to pick up samples and difficult to clamp samples, in order to test for tensile strength or creep, for example [207].

Multi-stage condenser lens systems enable recording of secondary and backscattered electrons. This has advantages for imaging thick or crystalline specimens and for recording secondary electrons and backscattered electrons. The inhomogeneity in cathodoluminescence can also be recorded using complex multistage condenser lens systems for correlation with structural defects [208]. This microscopy technique is useful for characterization in a number of fields related to optoelectronics, energy, geology, cellular biology, and healthcare [209]. Traditionally Scanning Electron Microscopy (SEM) has been used to study the cathodoluminescence of bulk samples. However the lower resolution of SEM (max 20 nm for the most advanced systems) restricts the use of SEM for microstructure correlation. Therefore high resolution cathodoluminescence microscopy is possible using TEM [210]–[213].

TEM case studies

TEM has shown itself to be capable of meeting such challenges. It is commonly used specifically for its ability to isolate and examine individual nanoparticles. This approach reduces the potential for agglomeration which can be a problem with wet-based laser scattering techniques. Nanoparticles of various materials produced by different techniques have also been imaged, with remarkable clarity [214]–[217]. TEM's electron imaging and diffraction options allow property-structure relationships of nano-structures to be understood. It has the resolution to differentiate between nanotubes with subtle nano-scale structural patterns. Interlayer distances of about 0.34 nm have been measured and imaged with impressive clarity, consistent with the (002) plane lattice parameter of graphited carbon [218].

The phase transformation and degradation in the nanostructure of the Si during the lithiation process in the lithium ion batteries results in Si amorphization to Li_xSi phase. The detailed mechanism of this process is not yet fully understood and in-situ nano-characterization techniques are required to investigate the charging and discharging processes. TEM provides a unique characterization platform to investigate the fine details of complex mechanisms, impossible to study otherwise. Wang et. al reported the characteristics of the phase transformation and the variations in the microstructure properties of amorphous Si- coated hollow carbon nanofiber (CNF) composites [35]. The silicon/carbon nanofiber composite was used to coat the interior and exterior of a nanobattery anode. The in-situ TEM charging and discharging of the carbon nanofiber composites was performed. The spontaneous crystallisation of $Li_{15}Si_4$ from the amorphous Li_xSi was observed. Contrary to classic nucleation and growth progress the corresponding phase transition process was observed without phase separation or large-scale atomic motion. The coating of an amorphous Si layer on the CNF was strong in the starting charge/discharge cycles without any structural defects. However, with increasing charge/discharge cycles, the bond between amorphous Si and CNF weakens as the surface roughness is increased, see figure 2.33. This degradation of the nanostructure observed by in-situ TEM eventually reduces the capacity of the composite anode over an extended period of charge/discharge cycles.
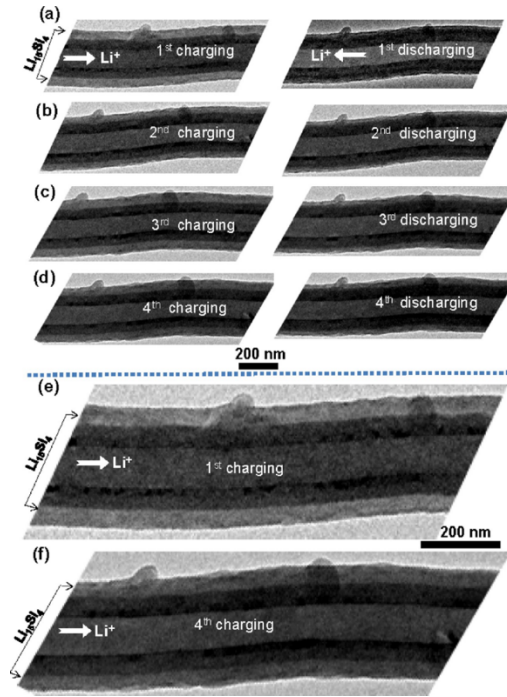
Figure 2.33: TEM images showing the structural evolution of Si-CNF during the cyclic charging and discharging, showing (a−d), the left column is charged and the right column is discharged; and (e) a high magnification image of (a); and (f) a high magnification image of (d).

Note that with cyclic charging and discharging, the surface of the coating layer is gradually crumpling. The two particles shown in this CNF are pre-existing particles. With a very limited number of in situ cycling in the TEM column, the change of the coating layer is not significant. However, as a general trend, it is noted that even with a limited number of charging and discharging cycles, the surface begins to become rougher. To illustrate this point, the images in Figure 2.33 (a & d) are shown magnified in Figure 2.33 (e & f). Note the slightly increased surface roughness in (f) as compared with (e) [219]. The in-situ observations of other nanostructures and nanoparticles have been extensively studied using TEM to highlight the fine details of many complex nano-scale mechanisms and processes [220]–[225].

2.6 Summary

The requirement for nanomaterials has risen steadily over the last ten years, to a point where there are major economic markets for nanomaterials, with nanoparticles holding the most

significant share. Nanoparticles have been applied to diverse fields of science and engineering due to their unique mechanical, optical and electrochemical properties. They have been successfully employed as sensors in the food, drug and biomedical industries. They have been utilized as drug delivery systems or as direct disease treatment themselves. Nps can reduce the usage of anti-biotics with their applications as anti-microbial materials. A significant amount of research today is directed towards applying Nps to conductive inks, miniaturizing circuits and fabricating flexible circuits and sensors. To-date chemical synthesis has dominated as the primary commercial fabrication technique. However, exploratory research has shown that laser-based synthesis could in the future outperform chemical synthesis in terms of cost of production if high-efficiency laser systems can be yielded to continuously produce high value Nps. Therefore, it's expected that with development, LASiS will become a significant Nps synthesis technique in coming years. This wide adaption of nanomaterials places increasing requirements on technology to adapt and enable characterisation of the nanomaterials both in their raw and final product forms. Technology must respond to meet these demands. In this chapter, various approaches to meeting these requirements have been discussed, and with each characterisation technique it is seen that higher resolutions, larger viewing sizes and quicker scanning times are being achieved.

2.7 References

[1]   A. Navrotsky, "Thermochemistry of nanomaterials," *Rev. Mineral. Geochemistry*, vol. 44, no. 1997, pp. 73–103, 2001.

[2]   S. A. A. Rizvi and A. M. Saleh, "Applications of nanoparticle systems in drug delivery technology," *Saudi Pharm. J.*, vol. 26, no. 1, pp. 64–70, 2018.

[3]   M. P. Navas and R. K. Soni, "Laser-Generated Bimetallic Ag-Au and Ag-Cu Core-Shell Nanoparticles for Refractive Index Sensing," *Plasmonics*, vol. 10, no. 3, pp. 681–690, 2015.

[4]   J. K. Pi, H. C. Yang, L. S. Wan, J. Wu, and Z. K. Xu, "Polypropylene microfiltration membranes modified with TiO2 nanoparticles for surface wettability and antifouling property," *J. Memb. Sci.*, vol. 500, pp. 8–15, 2016.

[5]   K. Balasubramanian, "Challenges in the use of 1D nanostructures for on-chip biosensing and diagnostics: A review," *Biosens. Bioelectron.*, vol. 26, no. 4, pp. 1195–1204, 2010.

[6]   M. Tonezzer, T. T. Le Dang, N. Bazzanella, V. H. Nguyen, and S. Iannotta, "Comparative gas-sensing performance of 1D and 2D ZnO nanostructures," *Sensors Actuators, B Chem.*, vol. 220, pp. 1152–1160, 2015.

[7]   F.-K. Liu, "Analysis and applications of nanoparticles in the separation sciences: A case of gold nanoparticles.," *J. Chromatogr. A*, vol. 1216, no. 52, pp. 9034–47, Dec. 2009.

[8]   J.-B. Park, K.-H. Lee, Y.-J. Jeon, S.-H. Lim, and S.-M. Lee, "Si/C composite lithium-ion battery anodes synthesized using silicon nanoparticles from porous silicon," *Electrochim. Acta*, vol. 133, pp. 73–81, 2014.

[9]   Y.-H. Yu *et al.*, "Electrical, morphological, and electromagnetic interference shielding properties of silver nanowires and nanoparticles conductive composites," *Mater. Chem. Phys.*, vol. 136, no. 2, pp. 334–340, 2012.

[10]   K. Bagga, R. McCann, M. Wang, a. Stalcup, M. Vázquez, and D. Brabazon, "Laser assisted synthesis of carbon nanoparticles with controlled viscosities for printing applications," *J. Colloid Interface Sci.*, vol. 447, pp. 263–268, 2015.

[11]   S. M. Haidary, E. P. Córcoles, and N. K. Ali, "Nanoporous silicon as drug delivery systems for cancer therapies," *J. Nanomater.*, vol. 2012, 2012.

[12]   J. J. Ramsden, "Global Nanotechnology," *Appl. Nanotechnol.*, pp. 245–254, 2018.

[13]   E. Commission, *Commission Staff Working Paper: Types and uses of nanomaterials,*

indcluding safety aspects. 2012.

[14] C. Santos *et al.*, "Industrial Applications of Nanoparticles - A Prospective Overview," *5th Int. Conf. Adv. Nano Mater.*, vol. 00, no. JULY, pp. 0–000, 2014.

[15] C. Rehbock, V. Merk, L. Gamrad, R. Streubel, and S. Barcikowski, "Size control of laser-fabricated surfactant-free gold nanoparticles with highly diluted electrolytes and their subsequent bioconjugation," *Phys. Chem. Chem. Phys.*, vol. 15, no. 9, pp. 3057–3067, 2013.

[16] F. Mafuné, J. Kohno, Y. Takeda, T. Kondow, and H. Sawabe, "Structure and Stability of Silver Nanoparticles in Aqueous Solution Produced by Laser Ablation," *J. Phys. Chem. B*, vol. 104, no. 35, pp. 8333–8337, 2002.

[17] N. G. Semaltianos *et al.*, "Silicon nanoparticles generated by femtosecond laser ablation in a liquid environment," *J. Nanoparticle Res.*, vol. 12, no. 2, pp. 573–580, 2010.

[18] K. K. Kim, D. Kim, S. K. Kim, S. M. Park, and J. K. Song, "Formation of ZnO nanoparticles by laser ablation in neat water," *Chem. Phys. Lett.*, vol. 511, no. 1–3, pp. 116–120, 2011.

[19] L. T. Zhen Guo, *Fundamentals and Applications of Nanomaterials*. Boston, MA: 009 ARTECH HOUSE 685 Canton Street Norwood, MA 02062, 2009.

[20] N. Komoda, M. Nogi, K. Suganuma, K. Kohno, Y. Akiyama, and K. Otsuka, "Printed silver nanowire antennas with low signal loss at high-frequency radio," *Nanoscale*, vol. 4, no. 10, p. 3148, 2012.

[21] E. Balliu, H. Andersson, M. Engholm, T. Öhlund, H. E. Nilsson, and H. Olin, "Selective laser sintering of inkjet-printed silver nanoparticle inks on paper substrates to achieve highly conductive patterns," *Sci. Rep.*, vol. 8, no. 1, pp. 2–10, 2018.

[22] K. Rajan, I. Roppolo, A. Chiappone, S. Bocchini, D. Perrone, and A. Chiolerio, "Nanotechnology, Science and Applications Dovepress Silver nanoparticle ink technology: state of the art," *Nanotechnol. Sci. Appl.*, vol. 9, pp. 1–13, 2016.

[23] L. Sydanheimo, J. Virkki, L. Ukkonen, and Y. Ren, "Optimisation of manufacturing parameters for inkjet-printed and photonically sintered metallic nanoparticle UHF RFID tags," *Electron. Lett.*, vol. 50, no. 21, pp. 1504–1505, 2014.

[24] M. Chien Dang, T. M. Dung Dang, and E. Fribourg-Blanc, "Silver nanoparticles ink synthesis for conductive patterns fabrication using inkjet printing technology," *Adv. Nat. Sci. Nanosci. Nanotechnol.*, vol. 6, no. 1, 2015.

[25] B. Calderón-Jiménez, M. E. Johnson, A. R. Montoro Bustos, K. E. Murphy, M. R. Winchester, and J. R. Vega Baudrit, "Silver Nanoparticles: Technological Advances, Societal Impacts, and Metrological Challenges," *Front. Chem.*, vol. 5, no. February, pp. 1–26, 2017.

[26] J. Weber, R. Singhal, S. Zekri, and A. Kumar, "One-dimensional nanostructures: fabrication, characterisation and applications," *Int. Mater. Rev.*, vol. 53, no. 4, pp. 235–255, 2008.

[27] M. Ahmad, J. Kiely, R. Luxton, M. Jabeen, and M. Khalid, "Facile aqueous growth of 150 nm ZnO nanowires for energy harvester: Enhanced output voltage using Pt sputtered electrode," *Sens. Bio-Sensing Res.*, vol. 7, no. June, pp. 141–145, 2016.

[28] M. Ahmad, M. A. Iqbal, J. Kiely, R. Luxton, and M. Jabeen, "Enhanced output voltage generation via ZnO nanowires (50 nm): Effect of diameter thinning on voltage enhancement," *J. Phys. Chem. Solids*, vol. 104, no. January, pp. 281–285, 2017.

[29] S. Sahay and M. J. Kumar, "Diameter Dependence of Leakage Current in Nanowire Junctionless Field Effect Transistors," *IEEE Trans. Electron Devices*, vol. 64, no. 3, p. 1330, 2017.

[30] E. C. Dreaden, A. M. Alkilany, X. Huang, C. J. Murphy, and M. A. El-Sayed, "The golden age: Gold nanoparticles for biomedicine," *Chem. Soc. Rev.*, vol. 41, no. 7, pp. 2740–2779, 2012.

[31] W. Haiss, N. T. K. Thanh, J. Aveyard, and D. G. Fernig, "Determination of size and concentration of gold nanoparticles from UV-Vis spectra," *Anal. Chem.*, vol. 79, no. 11, pp. 4215–4221, 2007.

[32] Y. Li, Z. Wang, L. Sun, L. Liu, C. Xu, and H. Kuang, "Nanoparticle-based sensors for food contaminants," *TrAC - Trends Anal. Chem.*, vol. 113, pp. 74–83, 2019.

[33] A. El-Ansary and L. M. Faddah, "Nanoparticles as biochemical sensors," *Nanotechnol. Sci. Appl.*, vol. 3, pp. 65–76, 2010.

[34] K. S. Lee and M. A. El-Sayed, "Gold and silver nanoparticles in sensing and imaging: Sensitivity of plasmon response to size, shape, and metal composition," *J. Phys. Chem. B*, vol. 110, no. 39, pp. 19220–19225, 2006.

[35] R. Sharma, K. V. Ragavan, M. S. Thakur, and K. S. M. S. Raghavarao, "Recent advances in nanoparticle based aptasensors for food contaminants," *Biosens. Bioelectron.*, vol. 74, pp. 612–627, 2015.

[36] J. Deng, P. Yu, Y. Wang, L. Yang, and L. Mao, "Visualization and quantification of

neurochemicals with gold nanoparticles: Opportunities and challenges," *Adv. Mater.*, vol. 26, no. 40, pp. 6933–6943, 2014.

[37] A. Bigdeli *et al.*, "Nanoparticle-based optical sensor arrays," *Nanoscale*, vol. 9, no. 43, pp. 16546–16563, 2017.

[38] D. Liu, Z. Wang, and X. Jiang, "Gold nanoparticles for the colorimetric and fluorescent detection of ions and small organic molecules," *Nanoscale*, vol. 3, no. 4, pp. 1421–1433, 2011.

[39] X. Y. Chen, W. Ha, and Y. P. Shi, "Sensitive colorimetric detection of melamine in processed raw milk using asymmetrically PEGylated gold nanoparticles," *Talanta*, vol. 194, no. October 2018, pp. 475–484, 2019.

[40] C. W. Lam *et al.*, "Diagnosis and spectrum of melamine-related renal disease: Plausible mechanism of stone formation in humans," *Clin. Chim. Acta*, vol. 402, no. 1–2, pp. 150–155, 2009.

[41] M. Ramezani, N. Mohammad Danesh, P. Lavaee, K. Abnous, and S. Mohammad Taghdisi, "A novel colorimetric triple-helix molecular switch aptasensor for ultrasensitive detection of tetracycline," *Biosens. Bioelectron.*, vol. 70, pp. 181–187, 2015.

[42] M. J. Ruedas-Rama, J. D. Walters, A. Orte, and E. A. H. Hall, "Fluorescent nanoparticles for intracellular sensing: A review," *Anal. Chim. Acta*, vol. 751, pp. 1–23, 2012.

[43] J. Xu *et al.*, "A facile aptamer-based sensing strategy for dopamine through the fluorescence resonance energy transfer between rhodamine B and gold nanoparticles," *Dye. Pigment.*, vol. 123, pp. 55–63, 2015.

[44] T. Konduru, G. C. Rains, and C. Li, "A customized metal oxide semiconductor-based gas sensor array for onion quality evaluation: system development and characterization," *Sensors (Basel).*, vol. 15, no. 1, pp. 1252–1273, 2015.

[45] I. K. Cigić and H. Prosen, "An overview of conventional and emerging analytical methods for the determination of mycotoxins," *Int. J. Mol. Sci.*, vol. 10, no. 1, pp. 62–115, 2009.

[46] R. Vargas-Bernal, E. Rodrguez-Miranda, and G. Herrera-Prez, "Evolution and Expectations of Enzymatic Biosensors for Pesticides," *Pestic. - Adv. Chem. Bot. Pestic.*, no. June, 2012.

[47] N. Yusoff, A. Pandikumar, R. Ramaraj, H. N. Lim, and N. M. Huang, "Gold

nanoparticle based optical and electrochemical sensing of dopamine," *Microchim. Acta*, vol. 182, no. 13–14, pp. 2091–2114, 2015.

[48] C. R. Raj, T. Okajima, and T. Ohsaka, "Gold nanoparticle arrays for the voltammetric sensing of dopamine," *J. Electroanal. Chem.*, vol. 543, no. 2, pp. 127–133, 2003.

[49] S. M. F. Cruz, L. A. Rocha, and J. C. Viana, "Printing Technologies on Flexible Substrates for Printed Electronics," in *Flexible Electronics*, IntechOpen, 2018.

[50] L. Nayak, S. Mohanty, S. K. Nayak, and A. Ramadoss, "A review on inkjet printing of nanoparticle inks for flexible electronics," *J. Mater. Chem. C*, vol. 7, no. 29, pp. 8771–8795, 2019.

[51] Y. Gao, R. Liu, X. Wang, J. Liu, and Q. Fang, "Flexible RFID Tag Inductor Printed by Liquid Metal Ink Printer and Its Characterization," *J. Electron. Packag.*, vol. 138, no. 3, p. 031007, 2016.

[52] P. Kopyt *et al.*, "Graphene-based dipole antenna for a UHF RFID tag," *2015 IEEE MTT-S Int. Microw. Symp.*, vol. 1, no. 7, pp. 1–3, 2015.

[53] T. Leng, X. Huang, K. Chang, J. Chen, M. A. Abdalla, and Z. Hu, "Graphene Nanoflakes Printed Flexible Meandered-Line Dipole Antenna on Paper Substrate for Low-Cost RFID and Sensing Applications," *IEEE Antennas Wirel. Propag. Lett.*, vol. 15, pp. 1565–1568, 2016.

[54] J. Matyas, L. Munster, R. Olejnik, K. Vlcek, and P. Slobodian, "Antenna of silver nanoparticles mounted on a flexible polymer substrate constructed using inkjet print technology Antenna of silver nanoparticles mounted on a fl exible polymer substrate constructed using inkjet print technology," vol. 13.

[55] S. Jeong *et al.*, "Stable aqueous based Cu nanoparticle ink for printing well-defined highly conductive features on a plastic substrate," *Langmuir*, vol. 27, no. 6, pp. 3144–3149, 2011.

[56] J. F. Duval and H. M. Herr, "FlexSEA: Flexible, Scalable Electronics Architecture for wearable robotic applications," *Proc. IEEE RAS EMBS Int. Conf. Biomed. Robot. Biomechatronics*, vol. 2016-July, pp. 1236–1241, 2016.

[57] M. Y. Cheng, C. L. Lin, and Y. J. Yang, "Tactile and shear stress sensing array using capacitive mechanisms with floating electrodes," *Proc. IEEE Int. Conf. Micro Electro Mech. Syst.*, vol. 2, pp. 228–231, 2010.

[58] C. C. Chiang, C. C. K. Lin, and M. S. Ju, "An implantable capacitive pressure sensor for biomedical applications," *Sensors Actuators, A Phys.*, vol. 134, no. 2, pp. 382–

388, 2007.

[59]   K. Kim, B. Kim, and C. H. Lee, "Printing Flexible and Hybrid Electronics for Human Skin and Eye-Interfaced Health Monitoring Systems," *Adv. Mater.*, vol. 1902051, pp. 1–22, 2019.

[60]   H. He, L. Sydänheimo, J. Virkki, and L. Ukkonen, "Experimental Study on Inkjet-Printed Passive UHF RFID Tags on Versatile Paper-Based Substrates," vol. 2016, pp. 1–9, 2016.

[61]   B. Chen, Y. Jiang, X. Tang, Y. Pan, and S. Hu, "Fully Packaged Carbon Nanotube Supercapacitors by Direct Ink Writing on Flexible Substrates," *ACS Appl. Mater. Interfaces*, vol. 9, no. 34, pp. 28433–28440, 2017.

[62]   P. Chandra, J. Singh, A. Singh, A. Srivastava, R. N. Goyal, and Y. B. Shim, "Gold Nanoparticles and Nanocomposites in Clinical Diagnostics Using Electrochemical Methods," *J. Nanoparticles*, vol. 2013, pp. 1–12, 2013.

[63]   R. Intartaglia, K. Bagga, and F. Brandi, "Study on the productivity of silicon nanoparticles by picosecond laser ablation in water: towards gram per hour yield.," *Opt. Express*, vol. 22, no. 3, p. 3117, 2014.

[64]   R. Ranjbarzadeh, A. Moradikazerouni, R. Bakhtiari, A. Asadi, and M. Afrand, "An experimental study on stability and thermal conductivity of water/silica nanofluid: Eco-friendly production of nanoparticles," *J. Clean. Prod.*, vol. 206, pp. 1089–1100, 2019.

[65]   S. Taufik, A. Barfidokht, M. T. Alam, C. Jiang, S. G. Parker, and J. J. Gooding, "An antifouling electrode based on electrode–organic layer–nanoparticle constructs: Electrodeposited organic layers versus self-assembled monolayers," *J. Electroanal. Chem.*, vol. 779, pp. 229–235, 2016.

[66]   A. Nguyen, L. Zou, and C. Priest, "Evaluating the antifouling effects of silver nanoparticles regenerated by TiO2 on forward osmosis membrane," *J. Memb. Sci.*, vol. 454, pp. 264–271, 2014.

[67]   C. M. Kirschner and A. B. Brennan, "Bio-Inspired Antifouling Strategies," *Annu. Rev. Mater. Res.*, vol. 42, no. 1, pp. 211–229, 2012.

[68]   B. Yu, K. M. Leung, Q. Guo, W. M. Lau, and J. Yang, "Synthesis of Ag-TiO2 composite nano thin film for antimicrobial application," *Nanotechnology*, vol. 22, no. 11, 2011.

[69]   V. J. Schacht *et al.*, "Effects of silver nanoparticles on microbial growth dynamics,"

J. Appl. Microbiol., vol. 114, no. 1, pp. 25–35, 2013.

[70]   H. L. Yang, J. C. Te Lin, and C. Huang, "Application of nanosilver surface modification to RO membrane and spacer for mitigating biofouling in seawater desalination," *Water Res.*, vol. 43, no. 15, pp. 3777–3786, 2009.

[71]   I. Sondi and B. Salopek-Sondi, "Silver nanoparticles as antimicrobial agent: A case study on E. coli as a model for Gram-negative bacteria," *J. Colloid Interface Sci.*, vol. 275, no. 1, pp. 177–182, 2004.

[72]   C. Marambio-Jones and E. M. V. Hoek, "A review of the antibacterial effects of silver nanomaterials and potential implications for human health and the environment," *J. Nanoparticle Res.*, vol. 12, no. 5, pp. 1531–1551, 2010.

[73]   P. V. AshaRani, G. L. K. Mun, M. P. Hande, and S. Valiyaveettil, "Cytotoxicity and genotoxicity of silver nanomaterials," *ACS Nano*, vol. 3, no. 2, pp. 279–290, 2009.

[74]   C. N. Lok *et al.*, "Silver nanoparticles: Partial oxidation and antibacterial activities," *J. Biol. Inorg. Chem.*, vol. 12, no. 4, pp. 527–534, 2007.

[75]   L. Zhang *et al.*, "Mechanistic investigation into antibacterial behaviour of suspensions of ZnO nanoparticles against E. coli," *J. Nanoparticle Res.*, vol. 12, no. 5, pp. 1625–1636, 2010.

[76]   H. Qin *et al.*, "In vitro and in vivo anti-biofilm effects of silver nanoparticles immobilized on titanium," *Biomaterials*, vol. 35, no. 33, pp. 9114–9125, Nov. 2014.

[77]   X. Qu and P. J. J. Alvarez, "Applications of nanotechnology in water and wastewater treatment," *Water Res.*, vol. 47, no. 12, pp. 3931–3946, Aug. 2013.

[78]   P. J. Lu, W. L. Cheng, S. C. Huang, Y. P. Chen, H. K. Chou, and H. F. Cheng, "Characterizing titanium dioxide and zinc oxide nanoparticles in sunscreen spray," *Int. J. Cosmet. Sci.*, vol. 37, no. 6, pp. 620–626, Dec. 2015.

[79]   D. H. Jo, J. H. Kim, T. G. Lee, and J. H. Kim, "Size, surface charge, and shape determine therapeutic effects of nanoparticles on brain and retinal diseases," *Nanomedicine Nanotechnology, Biol. Med.*, vol. 11, no. 7, pp. 1603–1611, 2015.

[80]   S. Report, "Annual Epidemiological Report for 2015 Surgical site infections," no. December, 2017.

[81]   J. Wang *et al.*, "Silver-nanoparticles-modified biomaterial surface resistant to staphylococcus: new insight into the antimicrobial action of silver.," *Sci. Rep.*, vol. 6, no. August, p. 32699, Dec. 2016.

[82]   R. Huang, Y. Han, and S. Lu, "Enhanced osteoblast functions and bactericidal effect

of Ca and Ag dual-ion implanted surface layers on nanograined titanium alloys," *J. Mater. Chem. B*, vol. 2, no. 28, p. 4531, 2014.

[83]   J. S. Kim *et al.*, "Antimicrobial effects of silver nanoparticles," *Nanomedicine Nanotechnology, Biol. Med.*, vol. 3, no. 1, pp. 95–101, 2007.

[84]   T. Hamouda, A. Myc, B. Donovan, A. Y. Shih, J. D. Reuter, and J. R. Baker, "A novel surfactant nanoemulsion with a unique non-irritant topical antimicrobial activity against bacteria, enveloped viruses and fungi," *Microbiol. Res.*, vol. 156, no. 1, pp. 1–7, 2001.

[85]   J. Bogovic, R. Rudolf, and B. Friedrich, "The Controlled Single-Step Synthesis of Ag/TiO2 and Au/TiO2 by Ultrasonic Spray Pyrolysis (USP)," *JOM*, vol. 68, no. 1, pp. 330–335, Jan. 2016.

[86]   Y. K. Jo *et al.*, "Surface-independent antibacterial coating using silver nanoparticle-generating engineered mussel glue," *ACS Appl. Mater. Interfaces*, vol. 6, no. 22, pp. 20242–20253, 2014.

[87]   P. J. P. Espitia, N. de F. F. Soares, J. S. dos R. Coimbra, N. J. de Andrade, R. S. Cruz, and E. A. A. Medeiros, "Zinc Oxide Nanoparticles: Synthesis, Antimicrobial Activity and Food Packaging Applications," *Food Bioprocess Technol.*, vol. 5, no. 5, pp. 1447–1464, 2012.

[88]   S. Decelis, D. Sardella, T. Triganza, J. P. Brincat, R. Gatt, and V. P. Valdramidis, "Assessing the anti-fungal efficiency of filters coated with zinc oxide nanoparticles," *R. Soc. Open Sci.*, vol. 4, no. 5, pp. 1–9, 2017.

[89]   A. Sirelkhatim *et al.*, "Review on zinc oxide nanoparticles: Antibacterial activity and toxicity mechanism," *Nano-Micro Lett.*, vol. 7, no. 3, pp. 219–242, 2015.

[90]   N. Musee, M. Thwala, and N. Nota, "The antibacterial effects of engineered nanomaterials: implications for wastewater treatment plants.," *J. Environ. Monit.*, vol. 13, no. 5, pp. 1164–1183, 2011.

[91]   C. Rode *et al.*, "Antibacterial Zinc Oxide Nanoparticle Coating of Polyester Fabrics," *J. Text. Sci. Technol.*, vol. 1, no. August, pp. 65–74, 2015.

[92]   K. S. Siddiqi, A. ur Rahman, Tajuddin, and A. Husen, "Properties of Zinc Oxide Nanoparticles and Their Activity Against Microbes," *Nanoscale Res. Lett.*, vol. 13, 2018.

[93]   F. Elmi *et al.*, "The use of antibacterial activity of ZnO nanoparticles in the treatment of municipal wastewater," *Water Sci. Technol.*, vol. 70, no. 5, pp. 763–770, 2014.

[94]   C. de la Torre and V. Ceña, "The delivery challenge in neurodegenerative disorders: The nanoparticles role in alzheimer's disease therapeutics and diagnostics," *Pharmaceutics*, vol. 10, no. 4, 2018.

[95]   M. M. Wen *et al.*, "Nanotechnology-based drug delivery systems for Alzheimer's disease management: Technical, industrial, and clinical challenges," *J. Control. Release*, vol. 245, pp. 95–107, 2017.

[96]   S. Cunha, M. Amaral, J. Lobo, and A. Silva, "Therapeutic Strategies for Alzheimer's and Parkinson's Diseases by Means of Drug Delivery Systems," *Curr. Med. Chem.*, vol. 23, no. 31, pp. 3618–3631, 2016.

[97]   Y. Xiao, K. Shi, Y. Qu, B. Chu, and Z. Qian, "Engineering Nanoparticles for Targeted Delivery of Nucleic Acid Therapeutics in Tumor," *Mol. Ther. - Methods Clin. Dev.*, vol. 12, no. March, pp. 1–18, 2019.

[98]   P. Singh, S. Pandit, V. R. S. S. Mokkapati, A. Garg, V. Ravikumar, and I. Mijakovic, "Gold nanoparticles in diagnostics and therapeutics for human cancer," *Int. J. Mol. Sci.*, vol. 19, no. 7, 2018.

[99]   Y. Hui *et al.*, "Role of Nanoparticle Mechanical Properties in Cancer Drug Delivery," *ACS Nano*, vol. 13, no. 7, pp. 7410–7424, 2019.

[100] D. R. Lewis, K. Kamisoglu, A. W. York, and P. V. Moghe, "Polymer-based therapeutics: Nanoassemblies and nanoparticles for management of atherosclerosis," *Wiley Interdiscip. Rev. Nanomedicine Nanobiotechnology*, vol. 3, no. 4, pp. 400–420, 2011.

[101] D. J. Bharali *et al.*, "Organically modified silica nanoparticles: A nonviral vector for in vivo gene delivery and expression in the brain," *Proc. Natl. Acad. Sci. U. S. A.*, vol. 102, no. 32, pp. 11539–11544, 2005.

[102] X. Huang and M. A. El-Sayed, "Plasmonic photo-thermal therapy (PPTT)," *Alexandria J. Med.*, vol. 47, no. 1, pp. 1–9, 2011.

[103] M. R. K. Ali, Y. Wu, and M. A. El-Sayed, "Gold-Nanoparticle-Assisted Plasmonic Photothermal Therapy Advances Toward Clinical Application," *J. Phys. Chem. C*, vol. 123, no. 25, pp. 15375–15393, 2019.

[104] J. Golab, M. Korbelik, D. Russell, D. Preise, A. Scherz, and Y. Salomon, "Photochemical & Photobiological Sciences Targeted photodynamic therapy of breast cancer cells using," 2011.

[105] M. E. Napier and J. M. DeSimone, "Nanoparticle drug delivery platform," *Polym.*

Rev., vol. 47, no. 3, pp. 321–327, 2007.

[106] M. Liu, W. Song, and L. Huang, "Drug delivery systems targeting tumor-associated fibroblasts for cancer immunotherapy," *Cancer Lett.*, vol. 448, no. October 2018, pp. 31–39, 2019.

[107] K. Bagga *et al.*, "Laser-assisted synthesis of Staphylococcus aureus protein-capped silicon quantum dots as bio-functional nanoprobes," *Laser Phys. Lett.*, vol. 10, no. 6, p. 065603, 2013.

[108] P. Chewchinda and T. Tsuge, "Laser Wavelength Effect on Size and Morphology of Silicon Nanoparticles Prepared by Laser Ablation in Liquid," *Jpn. J. Appl. Phys.*, vol. 52, p. 120699, 2013.

[109] T. Baati *et al.*, "Ultrapure laser-synthesized Si-based nanomaterials for biomedical applications: in vivo assessment of safety and biodistribution," *Sci. Rep.*, vol. 6, no. April, p. 25400, 2016.

[110] E. Bagheri *et al.*, "Silica based hybrid materials for drug delivery and bioimaging," *J. Control. Release*, vol. 277, pp. 57–76, 2018.

[111] S. Yang, W. Cai, H. Zhang, X. Xu, and H. Zeng, "Size and Structure Control of Si Nanoparticles by Laser Ablation in Different Liquid Media and Further Centrifugation Classification," *J. Phys. Chem. C*, vol. 113, no. 44, pp. 19091–19095, 2009.

[112] R. Intartaglia, K. Bagga, M. Scotto, A. Diaspro, and F. Brandi, "Luminescent silicon nanoparticles prepared by ultra short pulsed laser ablation in liquid for imaging applications," vol. 2, no. 5, pp. 510–518, 2012.

[113] H. Kobayashi, P. Chewchinda, H. Ohtani, O. Odawara, and H. Wada, "Effects of Laser Energy Density on Silicon Nanoparticles Produced Using Laser Ablation in Liquid," *J. Phys. Conf. Ser.*, vol. 441, p. 012035, 2013.

[114] R. Intartaglia *et al.*, "Bioconjugated silicon quantum dots from one-step green synthesis," *Nanoscale*, vol. 4, no. 4, pp. 1271–1274, 2012.

[115] B. Bahrami *et al.*, "Nanoparticles and targeted drug delivery in cancer therapy," *Immunol. Lett.*, vol. 190, no. July, pp. 64–83, 2017.

[116] F. Y. Kong, J. W. Zhang, R. F. Li, Z. X. Wang, W. J. Wang, and W. Wang, "Unique roles of gold nanoparticles in drug delivery, targeting and imaging applications," *Molecules*, vol. 22, no. 9, 2017.

[117] G. Ajnai, A. Chiu, T. Kan, C. C. Cheng, T. H. Tsai, and J. Chang, "Trends of Gold

Nanoparticle-based Drug Delivery System in Cancer Therapy," *J. Exp. Clin. Med.*, vol. 6, no. 6, pp. 172–178, 2014.

[118] Y. H. Chen *et al.*, "Methotrexate conjugated to gold nanoparticles inhibits tumor growth in a syngeneic lung tumor model," *Mol. Pharm.*, vol. 4, no. 5, pp. 713–722, 2007.

[119] M. E. Wechsler, J. E. Vela Ramirez, and N. A. Peppas, " 110th Anniversary : Nanoparticle Mediated Drug Delivery for the Treatment of Alzheimer's Disease: Crossing the Blood–Brain Barrier ," *Ind. Eng. Chem. Res.*, vol. 58, pp. 15079–15087, 2019.

[120] P. Han, W. Martens, E. R. Waclawik, S. Sarina, and H. Zhu, "Metal Nanoparticle Photocatalysts: Synthesis, Characterization, and Application," *Part. Part. Syst. Charact.*, vol. 35, no. 6, pp. 1–16, 2018.

[121] B. Wiley, Y. Sun, B. Mayers, and Y. Xia, "Shape-controlled synthesis of metal nanostructures: The case of silver," *Chem. - A Eur. J.*, vol. 11, no. 2, pp. 454–463, 2005.

[122] S. Iravani, H. Korbekandi, S. V. Mirmohammadi, and B. Zolfaghari, "Synthesis of silver nanoparticles: Chemical, physical and biological methods," *Res. Pharm. Sci.*, vol. 9, no. 6, pp. 385–406, 2014.

[123] M. M. Oliveira, D. Ugarte, D. Zanchet, and A. J. G. Zarbin, "Influence of synthetic parameters on the size, structure, and stability of dodecanethiol-stabilized silver nanoparticles," *J. Colloid Interface Sci.*, vol. 292, no. 2, pp. 429–435, 2005.

[124] P. Zhao, N. Li, and D. Astruc, "State of the art in gold nanoparticle synthesis," *Coord. Chem. Rev.*, vol. 257, no. 3–4, pp. 638–665, 2013.

[125] J. Turkevich, P. C. Stevenson, and J. Hillier, "A study of the nucleation and growth processes in the synthesis of colloidal gold," *Discuss. Faraday Soc.*, vol. 11, no. c, pp. 55–75, 1951.

[126] G. Frens, "Controlled Nucleation for the Regulation of the Particle Size in Monodisperse Gold Suspensions," *Nat. Phys. Sci.*, vol. 241, pp. 20–22, 1973.

[127] K. R. Brown, A. P. Fox, and M. J. Natan, "Morphology-dependent electrochemistry of cytochrome c at Au colloid-modified SnO2 electrodes," *J. Am. Chem. Soc.*, vol. 118, no. 5, pp. 1154–1157, 1996.

[128] A. Roy, O. Bulut, S. Some, A. K. Mandal, and M. D. Yilmaz, "Green synthesis of silver nanoparticles: Biomolecule-nanoparticle organizations targeting antimicrobial

activity," *RSC Adv.*, vol. 9, no. 5, pp. 2673–2702, 2019.

[129] S. Jendrzej, B. Gökce, M. Epple, and S. Barcikowski, "How Size Determines the Value of Gold: Economic Aspects of Wet Chemical and Laser-Based Metal Colloid Synthesis," *ChemPhysChem*, vol. 18, no. 9, pp. 1012–1019, 2017.

[130] A. K. Mittal, Y. Chisti, and U. C. Banerjee, "Synthesis of metallic nanoparticles using plant extracts," *Biotechnol. Adv.*, vol. 31, no. 2, pp. 346–356, 2013.

[131] X. Li, H. Xu, Z. S. Chen, and G. Chen, "Biosynthesis of nanoparticles by microorganisms and their applications," *J. Nanomater.*, vol. 2011, 2011.

[132] A. D. Dwivedi and K. Gopal, "Biosynthesis of silver and gold nanoparticles using Chenopodium album leaf extract," *Colloids Surfaces A Physicochem. Eng. Asp.*, vol. 369, no. 1–3, pp. 27–33, 2010.

[133] M. H. Magnusson, K. Deppert, J. O. Malm, J. O. Bovin, and L. Samuelson, "Gold nanoparticles: Production, reshaping, and thermal charging," *J. Nanoparticle Res.*, vol. 1, no. 2, pp. 243–251, 1999.

[134] K. Okuyama and I. Wuled Lenggoro, "Preparation of nanoparticles via spray route," *Chem. Eng. Sci.*, vol. 58, no. 3–6, pp. 537–547, Feb. 2003.

[135] M. Gao, L. Sun, Z. Wang, and Y. Zhao, "Controlled synthesis of Ag nanoparticles with different morphologies and their antibacterial properties," *Mater. Sci. Eng. C*, vol. 33, no. 1, pp. 397–404, Jan. 2013.

[136] S. Stopic, P. Dvorak, and B. Friedrich, "Synthesis of spherical nanosized silver powder by ultrasonic spray pyrolysis," *Metall*, vol. 60, no. 6, pp. 377–382, 2006.

[137] K. C. Pingali, D. A. Rockstraw, and S. Deng, "Silver Nanoparticles from Ultrasonic Spray Pyrolysis of Aqueous Silver Nitrate," *Aerosol Sci. Technol.*, vol. 39, no. 10, pp. 1010–1014, Oct. 2005.

[138] S.-Y. Yang and S.-G. Kim, "Characterization of silver and silver/nickel composite particles prepared by spray pyrolysis," *Powder Technol.*, vol. 146, no. 3, pp. 185–192, Sep. 2004.

[139] C. H. Lo, T. T. Tsung, and H. M. Lin, "Preparation of silver nanofluid by the submerged arc nanoparticle synthesis system (SANSS)," *J. Alloys Compd.*, vol. 434–435, no. SPEC. ISS., pp. 659–662, 2007.

[140] J. K. Lung *et al.*, "Preparation of gold nanoparticles by arc discharge in water," *J. Alloys Compd.*, vol. 434–435, no. SPEC. ISS., pp. 655–658, 2007.

[141] L. L. Wang and J. Sen Jiang, "Preparation of α-Fe2O3 nanoparticles by high-energy

ball milling," *Phys. B Condens. Matter*, vol. 390, no. 1–2, pp. 23–27, 2007.

[142] P. Pimpang, W. Sutham, N. Mangkorntong, P. Mangkorntong, and S. Choopun, "Effect of stabilizer on preparation of silver and gold nanoparticle using grinding method," *Chiang Mai J. Sci.*, vol. 35, no. 2, pp. 250–257, 2008.

[143] R. Arbain, M. Othman, and S. Palaniandy, "Preparation of iron oxide nanoparticles by mechanical milling," *Miner. Eng.*, vol. 24, no. 1, pp. 1–9, 2011.

[144] C. Knieke, C. Steinborn, S. Romeis, W. Peukert, S. Breitung-Faes, and A. Kwade, "Nanoparticle production with stirred-media mills: Opportunities and limits," *Chem. Eng. Technol.*, vol. 33, no. 9, pp. 1401–1411, 2010.

[145] M. Baláž *et al.*, "Plant-Mediated Synthesis of Silver Nanoparticles and Their Stabilization by Wet Stirred Media Milling," *Nanoscale Res. Lett.*, vol. 12, no. 1, 2017.

[146] S. Barcikowski and G. Compagnini, "Advanced nanoparticle generation and excitation by lasers in liquids.," *Phys. Chem. Chem. Phys.*, vol. 15, no. 9, pp. 3022–6, 2013.

[147] A. De Giacomo *et al.*, "Cavitation dynamics of laser ablation of bulk and wire-shaped metals in water during nanoparticles production," *Phys. Chem. Chem. Phys.*, vol. 15, no. 9, pp. 3083–3092, 2013.

[148] A. H. Hamad, "Effects of Different Laser Pulse Regimes (Nanosecond, Picosecond and Femtosecond) on the Ablation of Materials for Production of Nanoparticles in Liquid Solution," *High Energy Short Pulse Lasers*, 2016.

[149] M. Dell'Aglio, R. Gaudiuso, O. De Pascale, and A. De Giacomo, "Mechanisms and processes of pulsed laser ablation in liquids during nanoparticle production," *Appl. Surf. Sci.*, vol. 348, pp. 4–9, 2015.

[150] W. Lauterborn and T. Kurz, "Physics of bubble oscillations," *Reports Prog. Phys.*, vol. 73, no. 10, 2010.

[151] R. Petkovšek and P. Gregorčič, "A laser probe measurement of cavitation bubble dynamics improved by shock wave detection and compared to shadow photography," *J. Appl. Phys.*, vol. 102, no. 4, 2007.

[152] I. Akhatov, O. Lindau, A. Topolnikov, R. Mettin, N. Vakhitova, and W. Lauterborn, "Collapse and rebound of a laser-induced cavitation bubble," *Phys. Fluids*, vol. 13, no. 10, pp. 2805–2819, 2001.

[153] J. Lam *et al.*, "γ-Al2O3 nanoparticles synthesised by pulsed laser ablation in liquids:

A plasma analysis," *Phys. Chem. Chem. Phys.*, vol. 16, no. 3, pp. 963–973, 2014.

[154] H. Zeng *et al.*, "Nanomaterials via laser ablation/irradiation in liquid: A review," *Adv. Funct. Mater.*, vol. 22, no. 7, pp. 1333–1353, 2012.

[155] P. Wagener *et al.*, "High productive and continuous nanoparticle fabrication by laser ablation of a wire-target in a liquid jet," *Appl. Surf. Sci.*, vol. 403, pp. 487–499, 2017.

[156] S. Ibrahimkutty, P. Wagener, A. Menzel, A. Plech, and S. Barcikowski, "Nanoparticle formation in a cavitation bubble after pulsed laser ablation in liquid studied with high time resolution small angle x-ray scattering," *Appl. Phys. Lett.*, vol. 101, no. 10, 2012.

[157] A. V. Kabashin and M. Meunier, "Synthesis of colloidal nanoparticles during femtosecond laser ablation of gold in water," *J. Appl. Phys.*, vol. 94, no. 12, pp. 7941–7943, 2003.

[158] J. P. Sylvestre, A. V. Kabashin, E. Sacher, and M. Meunier, "Femtosecond laser ablation of gold in water: Influence of the laser-produced plasma on the nanoparticle size distribution," *Appl. Phys. A Mater. Sci. Process.*, vol. 80, no. 4, pp. 753–758, 2005.

[159] L. Gamrad, C. Rehbock, J. Krawinkel, B. Tumursukh, A. Heisterkamp, and S. Barcikowski, "Charge balancing of model gold-nanoparticle-peptide conjugates controlled by the peptide's net charge and the ligand to nanoparticle ratio," *J. Phys. Chem. C*, vol. 118, no. 19, pp. 10302–10313, 2014.

[160] G. Marzun, J. Nakamura, X. Zhang, S. Barcikowski, and P. Wagener, "Size control and supporting of palladium nanoparticles made by laser ablation in saline solution as a facile route to heterogeneous catalysts," *Appl. Surf. Sci.*, vol. 348, pp. 75–84, 2015.

[161] S. S. Mao, X. Mao, R. Greif, and R. E. Russo, "Initiation of an early-stage plasma during picosecond laser ablation of solids," *Appl. Phys. Lett.*, vol. 77, no. 16, pp. 2464–2466, 2000.

[162] A. Plech, V. Kotaidis, M. Lorenc, and M. Wulff, "Thermal dynamics in laser excited metal nanoparticles," *Chem. Phys. Lett.*, vol. 401, no. 4–6, pp. 565–569, 2005.

[163] C. Y. Shih *et al.*, "Two mechanisms of nanoparticle generation in picosecond laser ablation in liquids: The origin of the bimodal size distribution," *Nanoscale*, vol. 10, no. 15, pp. 6900–6910, 2018.

[164] R. Fabbro, J. Fournier, P. Ballard, D. Devaux, and J. Virmont, "Physical study of laser-produced plasma in confined geometry," *J. Appl. Phys.*, vol. 68, no. 2, pp. 775–

784, 1990.

[165] R. Streubel, S. Barcikowski, and B. Gökce, "Continuous multigram nanoparticle synthesis by high-power, high-repetition-rate ultrafast laser ablation in liquids," *Opt. Lett.*, vol. 41, no. 7, p. 1486, 2016.

[166] G. C. Messina *et al.*, "Pulsed laser ablation of a continuously-fed wire in liquid flow for high-yield production of silver nanoparticles," *Phys. Chem. Chem. Phys.*, vol. 15, no. 9, pp. 3093–3098, 2013.

[167] S. Barcikowski, A. Meńndez-Manjón, B. Chichkov, M. Brikas, and G. Račiukaitis, "Generation of nanoparticle colloids by picosecond and femtosecond laser ablations in liquid flow," *Appl. Phys. Lett.*, vol. 91, no. 8, 2007.

[168] D. Zhang, B. Gökce, and S. Barcikowski, "Laser Synthesis and Processing of Colloids: Fundamentals and Applications," *Chem. Rev.*, vol. 117, no. 5, pp. 3990–4103, 2017.

[169] N. Bärsch, J. Jakobi, S. Weiler, and S. Barcikowski, "Pure colloidal metal and ceramic nanoparticles from high-power picosecond laser ablation in water and acetone," *Nanotechnology*, vol. 20, no. 44, 2009.

[170] C. L. Sajti, R. Sattari, B. Chichkov, and S. Barcikowski, "Ablation efficiency of α-Al2O3 in liquid phase and ambient air by nanosecond laser irradiation," *Appl. Phys. A Mater. Sci. Process.*, vol. 100, no. 1, pp. 203–206, 2010.

[171] A. Schwenke, P. Wagener, S. Nolte, and S. Barcikowski, "Influence of processing time on nanoparticle generation during picosecond-pulsed fundamental and second harmonic laser ablation of metals in tetrahydrofuran," *Appl. Phys. A Mater. Sci. Process.*, vol. 104, no. 1, pp. 77–82, 2011.

[172] N. Bärsch, "Improving Laser Ablation of Zirconia by Liquid Films: Multiple Influence of Liquids on Surface Machining and Nanoparticle Generation," *J. Laser Micro/Nanoengineering*, vol. 4, no. 1, pp. 66–70, 2009.

[173] Y. Jiang, P. Liu, Y. Liang, H. B. Li, and G. W. Yang, "Promoting the yield of nanoparticles from laser ablation in liquid," *Appl. Phys. A Mater. Sci. Process.*, vol. 105, no. 4, pp. 903–907, 2011.

[174] T. T. P. Nguyen, R. Tanabe-Yamagishi, and Y. Ito, "Impact of liquid layer thickness on the dynamics of nano- to sub-microsecond phenomena of nanosecond pulsed laser ablation in liquid," *Appl. Surf. Sci.*, vol. 470, no. July 2018, pp. 250–258, 2019.

[175] S. Barcikowski, V. Amendola, G. Marzun, and C. Rehbock, "Handbook of Laser

Sintheshis," no. April, 2016.

[176] T. Tsuzuki, "Commercial scale production of inorganic nanoparticles," *Int. J. Nanotechnol.*, vol. 6, no. 5–6, pp. 567–578, 2009.

[177] S. Barcikowski *et al.*, "HANDBOOK OF LASER SYNTHESIS OF COLLOIDS," 2016.

[178] M. C. Sportelli *et al.*, "The pros and cons of the use of laser ablation synthesis for the production of silver nano-antimicrobials," *Antibiotics*, vol. 7, no. 3, 2018.

[179] F. Beshkar, O. Amiri, and Z. Salehi, "Synthesis of ZnSnO 3 nanostructures by using novel gelling agents and their application in degradation of textile dye," *Sep. Purif. Technol.*, vol. 184, pp. 66–71, 2017.

[180] A. Mohammadkhani, M. Malboubi, C. Anthony, and K. Jiang, "Characterization of surface properties of ordered nanostructures using SEM stereoscopic technique," *Microelectron. Eng.*, vol. 88, no. 8, pp. 2687–2690, 2011.

[181] E. Buhr *et al.*, "Characterization of nanoparticles by scanning electron microscopy in transmission mode," *Meas. Sci. Technol.*, vol. 20, no. 8, p. 84025, 2009.

[182] A. O'Shea, J. Wallace, M. Hummel, L. H. Strauss, and T. E. Kidd, "Enhanced detection of nanostructures by scanning electron microscopy using insulating materials," *Micron*, vol. 52–53, pp. 57–61, 2013.

[183] Y. Jusman, S. C. Ng, and N. A. Abu Osman, "Investigation of CPD and HMDS sample preparation techniques for cervical cells in developing computer-aided screening system based on FE-SEM/EDX," *Sci. World J.*, vol. 2014, pp. 1–11, 2014.

[184] D. D. Vaughn, O. D. Hentz, S. Chen, D. Wang, and R. E. Schaak, "Formation of SnS nanoflowers for lithium ion batteries," *Chem. Commun.*, vol. 48, no. 45, p. 5608, 2012.

[185] J.-G. Kang, J.-G. Park, and D.-W. Kim, "Superior rate capabilities of SnS nanosheet electrodes for Li ion batteries," 2010. doi: 10.1016/j.elecom.2009.12.025.

[186] Y. Wang *et al.*, "CdS and SnS2 nanoparticles co-sensitized TiO2 nanotube arrays and the enhanced photocatalytic property," *J. Photochem. Photobiol. A Chem.*, vol. 325, pp. 55–61, 2016.

[187] H. Kafashan, R. Ebrahimi-Kahrizsangi, F. Jamali-Sheini, and R. Yousefi, "Effect of Al doping on the structural and optical properties of electrodeposited SnS thin films," *Phys. Status Solidi*, vol. 213, no. 5, pp. 1302–1308, 2016.

[188] H. Kafashan, F. Jamali-Sheini, R. Ebrahimi-Kahrizsangi, and R. Yousefi, "Influence

of growth conditions on the electrochemical synthesis of SnS thin films and their optical properties," *Int. J. Miner. Metall. Mater.*, vol. 23, no. 3, pp. 348–357, Mar. 2016.

[189] U. Chalapathi, B. Poornaprakash, and S.-H. Park, "Chemically deposited cubic SnS thin films for solar cell applications," *Sol. Energy*, vol. 139, pp. 238–248, 2016.

[190] T. Sall, M. Mollar, and B. Marí, "Substrate influences on the properties of SnS thin films deposited by chemical spray pyrolysis technique for photovoltaic applications," *J. Mater. Sci.*, vol. 51, no. 16, pp. 7607–7613, Aug. 2016.

[191] S. Li, X. Gu, Y. Zhao, Y. Qiang, S. Zhang, and M. Sui, "Enhanced visible-light photocatalytic activity and stability by incorporating a small amount of MoS2 into Ag3PO4 microcrystals," *J. Mater. Sci. Mater. Electron.*, vol. 27, no. 1, pp. 386–392, Jan. 2016.

[192] R. V. Kashid, P. D. Joag, M. Thripuranthaka, C. S. Rout, D. J. Late, and M. A. More, "Stable Field Emission from Layered MoS2 Nanosheets in High Vacuum and Observation of 1/f Noise," *Nanomater. Nanotechnol.*, vol. 5, p. 1, 2015.

[193] Y. M. Chen, X. Y. Yu, Z. Li, U. Paik, and X. W. (David) Lou, "Hierarchical MoS2 tubular structures internally wired by carbon nanotubes as a highly stable anode material for lithium-ion batteries," *Sci. Adv.*, vol. 2, no. 7, 2016.

[194] S. Wang *et al.*, "A Facile One-Pot Synthesis of a Two-Dimensional MoS2/Bi2S3 Composite Theranostic Nanosystem for Multi-Modality Tumor Imaging and Therapy," *Adv. Mater.*, vol. 27, no. 17, pp. 2775–2782, May 2015.

[195] Y. Wang, L. Yu, and X. W. D. Lou, "Synthesis of Highly Uniform Molybdenum-Glycerate Spheres and Their Conversion into Hierarchical MoS $_2$ Hollow Nanospheres for Lithium-Ion Batteries," *Angew. Chemie Int. Ed.*, vol. 55, no. 26, pp. 7423–7426, Jun. 2016.

[196] H. Kafashan, M. Azizieh, and H. Nasiri Vatan, "Ultrasound-assisted electrodeposition of SnS: Effect of ultrasound waves on the physical properties of nanostructured SnS thin films," *J. Alloys Compd.*, vol. 686, pp. 962–968, 2016.

[197] K. Bagga *et al.*, "Nanoparticle functionalized laser patterned substrate: an innovative route towards low cost biomimetic platforms," *RSC Adv.*, vol. 7, no. 13, pp. 8060–8069, 2017.

[198] E. Tomaszewska *et al.*, "Detection limits of DLS and UV-Vis spectroscopy in characterization of polydisperse nanoparticles colloids," *J. Nanomater.*, vol. 2013,

2013.

[199] K. Takahashi, H. Kato, T. Saito, S. Matsuyama, and S. Kinugasa, "Precise measurement of the size of nanoparticles by dynamic light scattering with uncertainty analysis," *Part. Part. Syst. Charact.*, vol. 25, no. 1, pp. 31–38, 2008.

[200] S. Bhattacharjee, "DLS and zeta potential - What they are and what they are not?," *J. Control. Release*, vol. 235, pp. 337–351, 2016.

[201] U. Nobbmann and A. Morfesis, "Light scattering and nanoparticles," *Mater. Today*, vol. 12, no. 5, pp. 52–54, 2009.

[202] P. J. Freud, "Nanoparticle Sizing : Dynamic Light Scattering Analysis in the Frequency Spectrum Mode Provided By :," *Instrumentation*.

[203] S. K. Brar and M. Verma, "Measurement of nanoparticles by light-scattering techniques," *TrAC - Trends Anal. Chem.*, vol. 30, no. 1, pp. 4–17, 2011.

[204] A. Horechyy *et al.*, "In-situ monitoring of silica shell growth on PS-b-P4VP micelles as templates using DLS," *Polym. (United Kingdom)*, vol. 107, 2016.

[205] C. R. Brundle, C. A. Evans, and S. Wilson, *Encyclopedia of materials characterization : surfaces, interfaces, thin films*. 1992.

[206] D. K. Schroder, *Semiconductor Material and Device Characterization: Third Edition*. 2005.

[207] Z. . L. Wang, P. Poncharal, and W. . A. de Heer, "Measuring physical and mechanical properties of individual carbon nanotubes by in situ TEM," *J. Phys. Chem. Solids*, vol. 61, no. 7, pp. 1025–1030, 2000.

[208] S. K. Lim, M. Brewster, F. Qian, Y. Li, C. M. Lieber, and S. Gradečak, "Direct Correlation between Structural and Optical Properties of III−V Nitride Nanowire Heterostructures with Nanoscale Resolution," *Nano Lett.*, vol. 9, no. 11, pp. 3940–3944, Nov. 2009.

[209] V. Barbin, "Application of cathodoluminescence microscopy to recent and past biological materials: a decade of progress," *Mineral. Petrol.*, vol. 107, no. 3, pp. 353–362, Jun. 2013.

[210] F. Bertram *et al.*, "Nanoscale Imaging of Structural and Optical Properties Using Helium Temperature Scanning Transmission Electron Microscopy Cathodoluminescence of Nitride Based Nanostructures," *Microsc. Microanal.*, vol. 22, no. S3, pp. 600–601, 2016.

[211] E. White, A. Howkins, and C. Williams, "Investigating the Origin of Luminescence

in Zinc Oxide Nanostructures With STEM-Cathodoluminescence," *Microsc.*, 2015.

[212] G. Hanna *et al.*, "Texture and electronic activity of grain boundaries in Cu(In,Ga)Se 2 thin films," *Appl. Phys. A Mater. Sci. Process.*, vol. 82, no. 1 SPEC. ISS., pp. 1–7, 2006.

[213] D. den Engelsen *et al.*, "Ultraviolet and blue cathodoluminescence from cubic Y_2O_3 and Y_2O_3:Eu^{3+} generated in a transmission electron microscope," *J. Mater. Chem. C*, vol. 4, no. 29, pp. 7026–7034, 2016.

[214] J. Wu, S. Helveg, S. Ullmann, Z. Peng, and A. A. T. Bell, "Growth of encapsulating carbon on supported Pt nanoparticles studied by in situ TEM," *J. Catal.*, vol. 338, pp. 295–304, 2016.

[215] J. Wu, S. Helveg, S. Ullmann, Z. Peng, and A. Bell, "Growth of encapsulating carbon on supported Pt nanoparticles studied by in situ TEM," *J. Catal.*, 2016.

[216] D. Buttry, "High Resolution TEM Study on Phase Transformations in Redox Active Silver Nanoparticles," *PRiME 2016/230th ECS Meet. (October 2-7, 2016)*, 2016.

[217] S. W. Chee, D. Loh, Z. Baraissov, P. Matsudaira, and U. Mirsaidov, "Hopping Diffusion of Gold Nanoparticles Observed with Liquid Cell TEM," *Microsc. Microanal.*, vol. 22, no. S3, pp. 750–751, 2016.

[218] C. He, N. Zhao, C. Shi, J. Li, and H. Li, "Magnetic properties and transmission electron microscopy studies of Ni nanoparticles encapsulated in carbon nanocages and carbon nanotubes," *Mater. Res. Bull.*, vol. 43, no. 8, pp. 2260–2265, 2008.

[219] C. M. Wang *et al.*, "In situ TEM investigation of congruent phase transition and structural evolution of nanostructured silicon/carbon anode for lithium ion batteries," *Nano Lett.*, vol. 12, no. 3, pp. 1624–1632, Mar. 2012.

[220] C. Huiqun, Z. Meifang, and L. Yaogang, "Decoration of carbon nanotubes with iron oxide," *J. Solid State Chem.*, vol. 179, no. 4, pp. 1208–1213, Apr. 2006.

[221] J.-P. Salvetat *et al.*, "Mechanical properties of carbon nanotubes," *Appl. Phys. A Mater. Sci. Process.*, vol. 69, no. 3, pp. 255–260, Sep. 1999.

[222] M. V. Jose *et al.*, "Morphology and mechanical properties of Nylon 6/MWNT nanofibers," *Polymer (Guildf).*, vol. 48, no. 4, pp. 1096–1104, 2007.

[223] C. R. Musil, J. L. Bartelt, and J. Melngailis, "Focused ion beam microsurgery for electronics," *IEEE Electron Device Lett.*, vol. 7, no. 5, pp. 285–287, May 1986.

[224] C. Boit, "New physical techniques for IC functional analysis of on-chip devices and interconnects," *Appl. Surf. Sci.*, vol. 252, no. 1, pp. 18–23, 2005.

[225] R. Schlangen, U. Kerst, C. Boit, T. Malik, R. Jain, and T. Lundquist, *Microelectronics and reliability.*, vol. 47. Pergamon Press, 1964.

Chapter 3: LASiS development towards continuous production

3.1 Introduction

Throughout the last decade, many advances have been made in the field of nanomaterial synthesis via Laser Ablation Synthesis in Solution (LASiS). In this technique, a solid target is ablated using high intensity pulsed laser irradiation while immersed in a liquid. This "green" technique allows ligand-free nanoparticles to be fabricated without the need for environmentally harmful solvents. This technique also allows for a range of single-step and post-production functionalizations enabling its use in areas such as chemical separation, bio-sensing, cellular labelling, display technology. Despite these advances, the challenge of production scale-up and transfer from batch to continuous production has yet to be realized which is necessary for this technique to compete commercially with wet-chemical techniques. In this study, the laser synthesis of silicon nanoparticles via LASiS was performed using solid-state Nd:YAG lasers with various laser wavelengths and power ranges to study their effect on nanoparticle production. Nanoparticle size, size dispersion and nanoparticle yield were studied via Dynamic Light Scattering (DLS). The optical properties and surface chemistry of the produced particles was analyzed via UV-vis and IR spectroscopy respectively. Transmission Electron Microscopy (TEM) was performed to examine nanoparticle morphology.

This work builds upon the existing batch LASiS technique developed in the DCU I-Form Advanced Manufacturing Research Centre [1]–[3]. This chapter presents the characterization of the existing laboratory LASiS technique towards silicon nanoparticle production, while framing the discussion around the current production capabilities toward scale-up compared with initial trials of a newly developed liquid flow-based method. Initial steps towards production scale-up are examined utilizing an initial continuous flow prototype. This continuous flow regime was compared to the standard static-flow batch processing with nanoparticle yield and quality examined.

3.2 Experimental setup

3.2.1 Laser Ablation Setup

For the results presented, two laser systems were used for the creation of nanoparticle colloids. Continuous flow ablation studies were carried out with a picosecond pulsed diode-pumped solid state (DPSS) neodymium-doped yttrium aluminium garnet (Nd:YAG) laser (BrightSolutions WEDGH HF 1064 nm, Italy), operating at a laser pulse duration (τ_p) of 700 ps and pulse repetition frequency of 10 kHz. The sample position was maintained in the laser beam-waist using a nano-position stage (PI-404-3PD, PI) and for this work a spot diameter of 103 µm was attained. The beam profile was measured by a WinCamD-LCM, 1" CMOS Beam Profiler ($\pm 1\,\mu$m working accuracy of interpolated diameters, $55\,\mu$m min beam size measurement by pixel, [4]). Beam diameter was determined using the $1/e^2$ definition, assuming a gaussian beam profile. The beam M^2 factor was calculated to be 2.01 which indicates a high quality beam for an ND: YAG laser system with the beam divergence half-angle calculated to be 13.7 mrad and a beam parameter product (BPP) of 0.68 mm rad. The laser beam was rastered using a 2D scanning galvanometer (SS-12, Raylase) at a speed of 2 mm/s moving in an Archimedean spiral pattern over the top surface of the target.

Wavelength ablation response tests were carried out using a Continuun Surelite flash lamp-pumped Nd:YAG laser, $\tau_p = 5$ ns at 10 Hz repetition rate. The wavelength was selectable at 1064 nm, 532 nm or 355 nm, and the pulse-width and pulse repetition rate was fixed at 6 ns and 10 Hz respectively. For the ablation experiments described, the beam position was fixed, and the target rotated at an off-centre position at a speed of 2 mm/s to attain a circular raster pattern on the surface of the target. The laser beam was focused to a spot diameter of 426 µm.

3.2.2 Nanoparticle Generation

The target material used for both static and dynamic production techniques was silicon rod (99.998% metals basis, Alfa Aesar) with a diameter of 8.28 mm and thickness of 6 mm. For batch production (Figure 3.1. (a)), the target was immersed in 6 ml and 11 ml of ultrapure DI water in two different glass vials such that there was 4 mm of DI water above the top of the target.
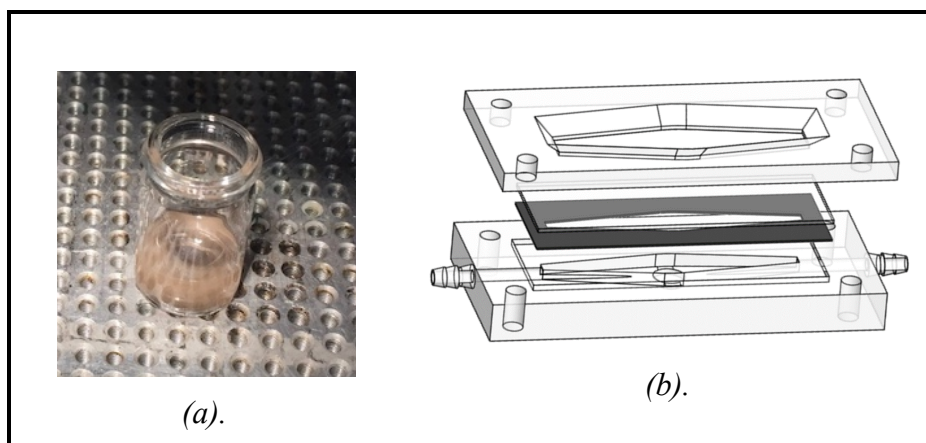
Figure 3.1: (a). 6 ml batch LASiS production glass vial and (b) continuous LASiS production flow cell.

For continuous liquid flow production, the target was mounted within the center of the flow reactor cell (Figure 3.1(b)), with a solvent reservoir feeding a pump, with another reservoir collecting the colloid, as illustrated in Figure 3.2. The flow reactor was designed to ensure uniform flow conditions in order to reduce the effects of the cavitation bubble [5], plume occlusion [6] and particle aggregation at the ablation site [7],[8]. Continuous flowrate was maintained at 100 ml/min.
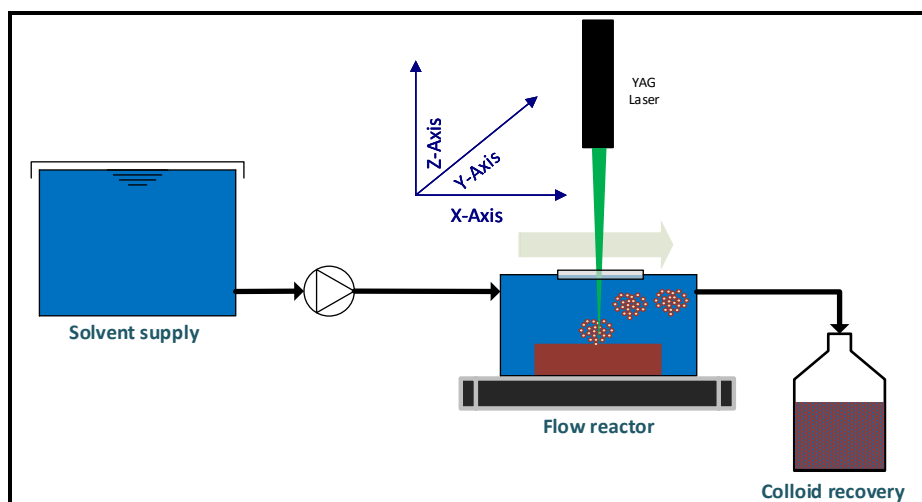
Figure 3.2: Schematic of the flow reactor cell containing the target material for ablation

3.2.3   Metrology

To determine the size distribution of the produced nanoparticle colloids, both transmission election microscopy (TEM) and dynamic light scattering (DLS) techniques were utilized.

The TEM used was an FEI Titan with Field Emission Gun and spherical aberration corrector system (Cs-corrector) of the objective lens operated at 300 kV. Analysis was performed using a copper mesh TEM grid with 40 µl of sample applied and allowed to evaporate at room temperature. The DLS used was a NanoFlex (Microtrac), with analysis performed on 2 ml of sample. The optical properties of the produced nanoparticles were characterized using UV-vis-NIR spectroscopy, Cary 50 (Varian), with a scanning range of 200 – 800 nm at a rate of 20 nm/s with solvent background correction applied. Nanoparticle surface chemistry was analyzed using Attenuated Total Reflectance Fourier Transform Infrared Spectroscopy (ATR-FTIR), Spectrum 100 (Perkin Elmer), with 4 acquisitions averaged for each sample at a resolution of 4 cm^{-1}. To analyze ablation efficiency, high magnification 3D optical microscopy was performed on the ablation targets using a Keyence VHX-2000 variable focus scanning profilometer, scanning at 1 µm increments.

3.3   Results and discussion

3.3.1   Batch production - size, morphology and surface chemistry

A SiNps colloid was synthesized using 1064 nm wavelength irradiation at a maximum operating laser fluence of 1.83 J/cm^2 for 10-minute ablation. The nanoparticles (Nps) size and morphology were analyzed via DLS and TEM respectively.
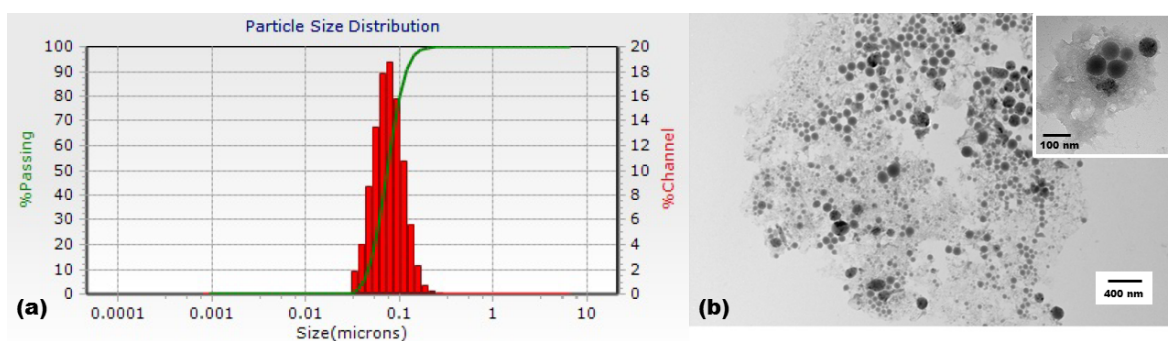
Figure 3.3: (a) DLS nanoparticle size distribution (peak dia. = 90 nm ± 70 nm) and (b) TEM images of SiNPs with scale bars of 400 nm and for (b) inset of 100 nm for SiNPs generated using nanosecond ablation at a wavelength of 1064 nm with a fluence of 1.83 J/cm^2.

TEM revealed that the produced nanoparticles are spherical with a peak diameter of approximately 80 nm. DLS showed a nanoparticle size distribution ranging from 10 nm –

160 nm, with the distribution peaking at 90 nm. The disparity between the TEM and DLS measurements is due to the hydrodynamic diameter [9] of the nanoparticles in suspension being larger than that of their true, dry diameter [10]. Though DLS is a fast, non-destructive technique, this highlights the continuing need for TEM analysis for any studies involving nanoparticles. The particle size distributions is similar to that produced via LASiS in literature using an ultrafast femtosecond Ti:Sapphire laser (pulse width of 110 fs centered at 800 nm) [11].

Fourier-transform infrared spectroscopy (FTIR) spectroscopy was performed to study the surface chemistry of the 1064 nm fabricated Nps. The IR transmission spectra of the produced SiNps are shown in *Figure 3.4*. The spectra showed the presence of a broad peak centered at 2120 cm^{-1} which is indicative of O_x-Si-H bonds and two peaks at 1645 cm^{-1} and 3300 cm^{-1} which were a result of H_2O and OH respectively, resulting from the aqueous nature of the colloid [12]. Also present was a large absorbance band from 1500 cm^{-1} to 1050 cm^{-1} which is a result of various Si-OH, Si-H and Si-O bonding [13], [14]. The large extinction below 1000 cm^{-1} is from O-Si-O and Si-O-Si bonds [12]. This extinction being the most prominent spectral feature indicates that oxygen passivated silicon is the predominant material in the colloid.
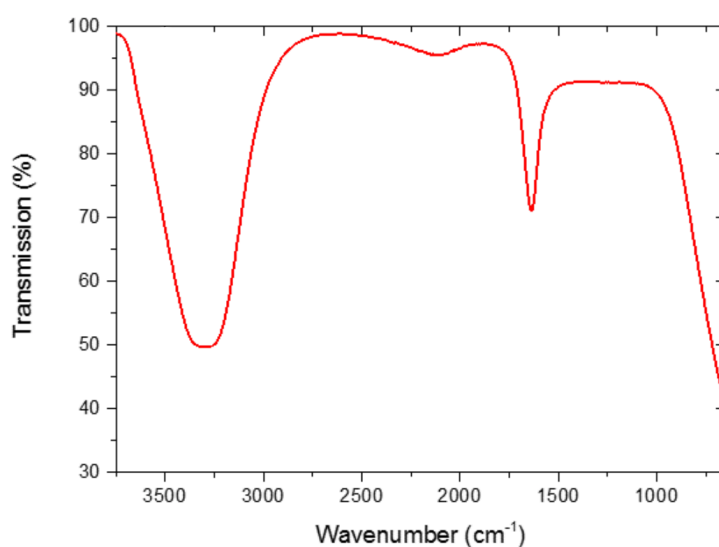
Figure 3.4: ATR-FTIR spectra of the produced SiNPs produced. All colloids were produced by the 1064 nm laser, fluence = 1.83 J/cm2 and RR = 10 kHz.

3.3.1.1 Time dependent batch production

Time dependence productivity of batch production was investigated, ablating silicon targets in triplicate at time intervals from 3 mins to 20 mins. The ablation rate was calculated from gravimetrical measurements of the targets pre and post-ablation. Initial tests were performed with a 6 ml batch volume, resulting in a logarithm decline (*Adj.* $R^2 = 0.83$) in the SiNps production rate over the 20 minute production period. A maximum cumulative productivity of 7.8 mg/h was seen to reduce to 1.7 mg/h after 20 minutes. This log decline is indicative of particle occlusion at the ablation site [15]. Such occlusion effects would reduce the transmission of laser power to the target surface, which is in agreement with the Beer-Lambert law. According to the *Beer-Lambert Law*, any Nps in the pathlength of laser radiation will reduce the laser fluence at the surface of the target [7], [10]. In order to mitigate this, a larger volume test was carried out with 11 ml of solvent. The final productivity was increased to 2.5 ± 0.5 mg/h due to a lower concentration of occluding particles, however the log decline was still observed (*Adj.* $R^2 = 0.94$) as illustrated in *Figure 3.5*. It's clear from these results that increasing the batch volume alone would not produce a scalable, steady-state production process necessary for larger scale production.
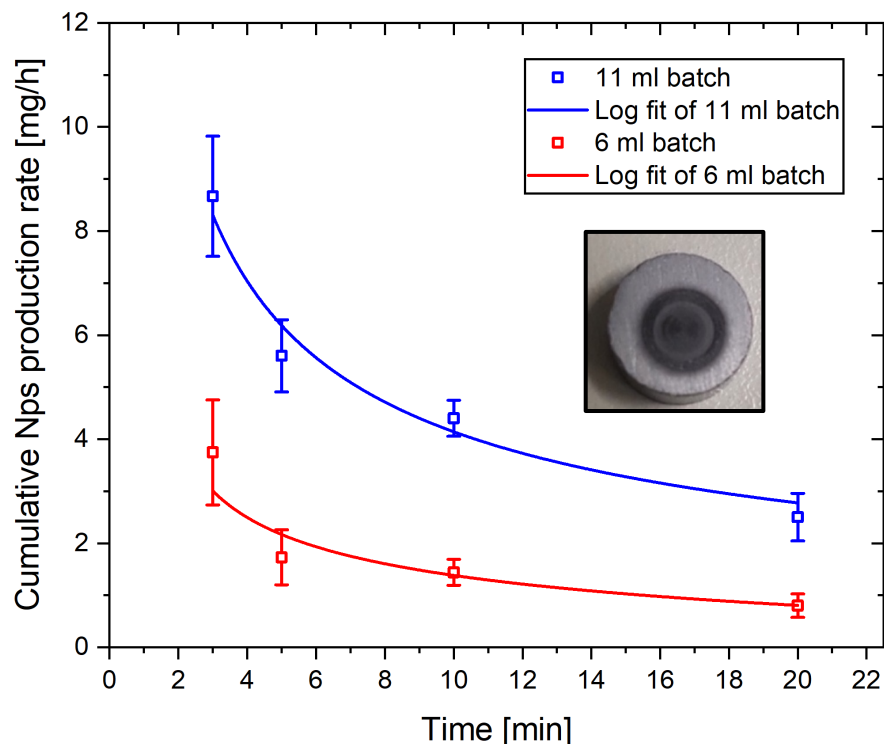
Figure 3.5: Cumulative ablation rate of 6 ml and 11 ml batch production using a 1064 nm laser. A log reduction was observed; Adj. R^2 = 0.83, and Adj. R^2 = 0.94, Prod.$_{11ml}$ = -5.6*ln(0.21*ln(x)). Insert: displays the ablation crater and heating on the target after 20 mins ablation.

UV-vis absorption spectra of the colloids produced are displayed in Figure 3.6. The spectra is characteristic of silicon nanoparticles produced in literature with a shoulder indicated between 200 - 400 nm [11]. The UV-vis spectra is in agreement with the gravimetrical results presented in *Figure 3.5*, with the relative rate of increase in absorption reducing with time. The Nps size distribution of each colloid produced was measured via DLS, as displayed in Figure 3.7.
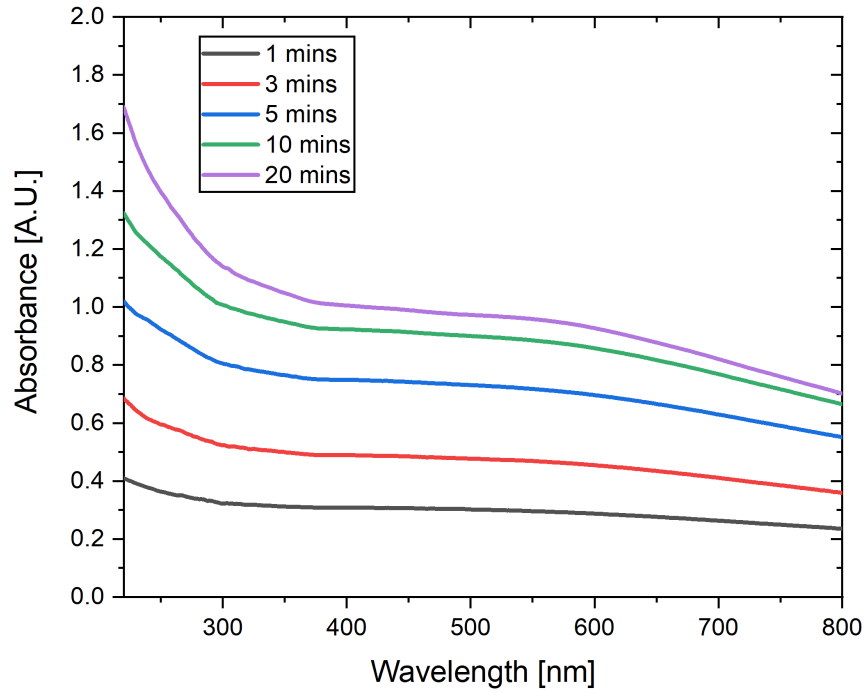
Figure 3.6: UV-vis spectra of 11 ml SiNps colloid produced by 1064 nm laser at 1.83 J/cm² under increasing ablation (n=3).

The Nps peak diameter was seen to increase over time from 57.2 nm to 79.3 nm. Also, the Nps size population width was seen to widen over time, with an increase of 20 nm in the width from the measured peak diameter. This increase in Nps size is possibly due to thermal effects on the target where prolonged ablation would incur heating of the target, promoting fragmentation of larger particles [10]. Also its possible that particle-reirradiation is occurring, and rather than promoting photo-fragmentation, and size reduction, the increased heating of particles (especially in the cavitation bubble) is promoting particle aggregation [9], [16].
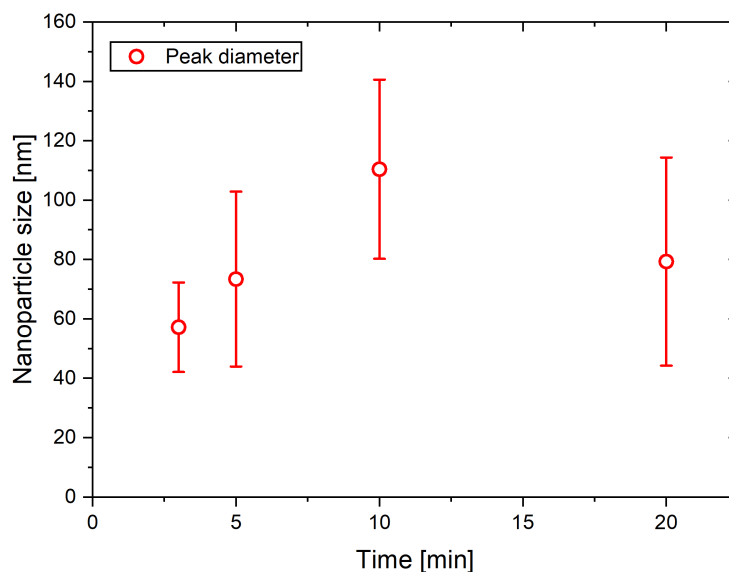
Figure 3.7: SiNps peak diameter and distribution width (± σ from the peak dia. with n=3) showing enlargement of particles over time from 57.2 ± 15.1 at 3-minute ablation to 70.1 ± 35.05 after 20 mins ablation. SiNps produced under 1.83 J/cm² fluence, 11 ml volume, 1064 nm laser system.

3.3.1.2   Fluence dependent batch production

The effect of fluence in batch production (11 ml solvent) was determined under 5-minute ablation trials. The ablation rate increased linearly with fluence (Adj. R^2 = 0.86), but a high process variation from the mean was observed (24 %) within the tests as shown in Figure 3.8.
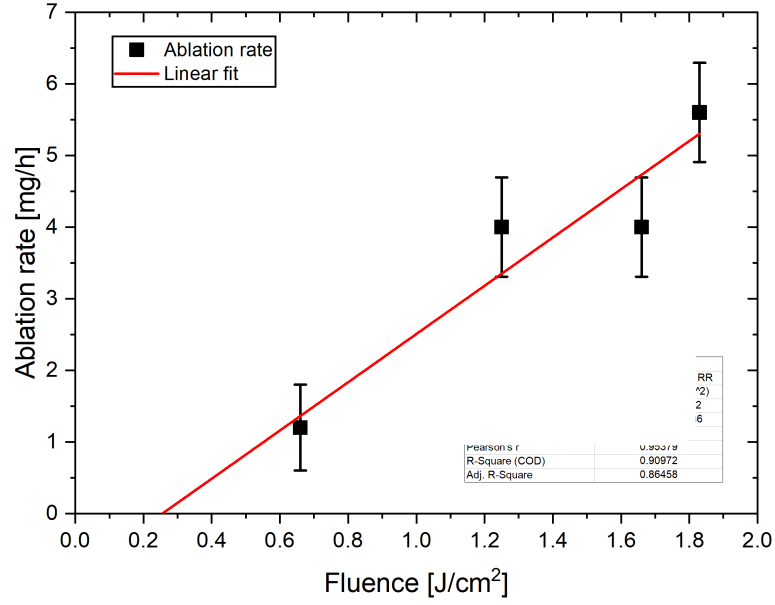
Figure 3.8: Nps productivity after 5 min ablation at increasing fluence levels (RR = 10kHz, 11 ml batch), fluence threshold from extrapolation = 0.28 J/cm² (n=3).

The linear fit allowed for the target fluence threshold to be determined as 0.28 J/cm², however given the large process error bars and low fit correlation, this should be taken as an estimate. The UV-vis absorbance spectra of the collected colloids were in agreement with the gravimetrical measurements of Nps production with the average absorbance spectra displayed in Figure 3.9.
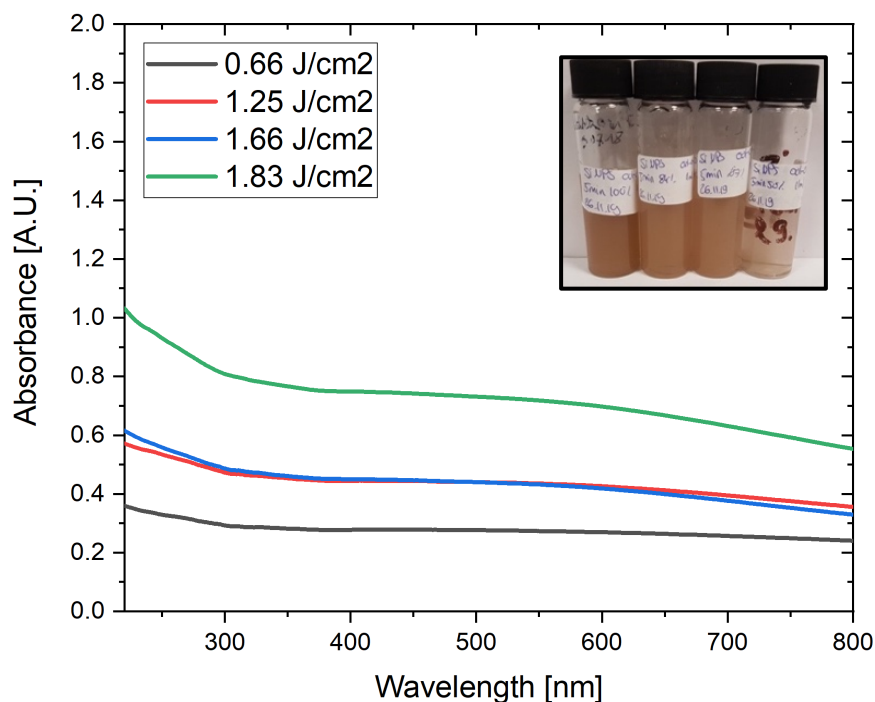
Figure 3.9: Average UV-vis absorbance spectra illustrating the effect of laser fluence on colloid concentration (n=3), insert shows colloids produced at decreasing fluence levels left to right.

3.3.1.3 *Effect of laser wavelength on batch production*

Ablation tests with varied laser wavelengths were carried out using a Continmun Surelite ns laser at 10 Hz repetition rate. Figure 3.10 (b) illustrates the UV-vis spectra of the SiNPs produced via three differing laser wavelengths (1064nm, 532nm, 355nm) at a constant fluence of 0.16 J/cm^2. Irradiation at 532 nm was seen to produce the highest measured ablated mass at all fluence levels tested between 0.04 - 0.16 J/cm^2, as illustrated in Figure 3.10 (a).
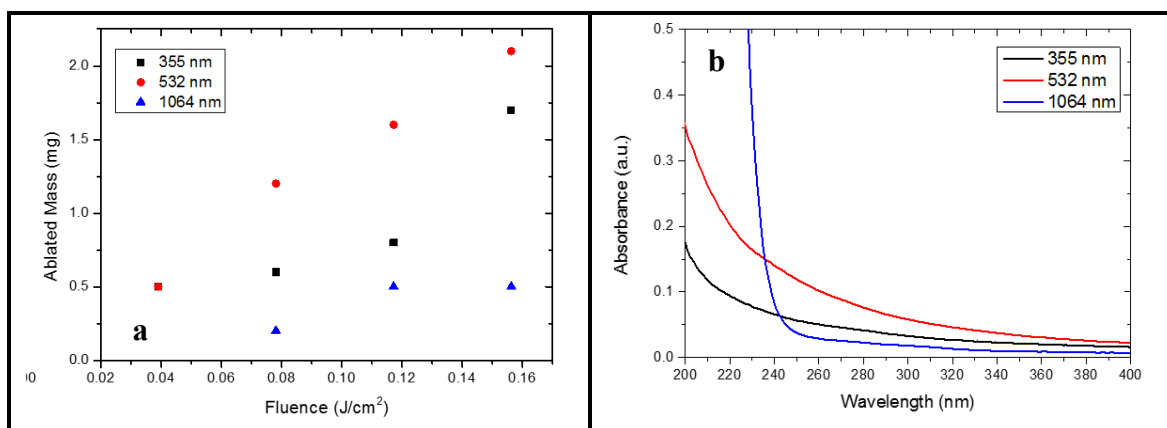
Figure 3.10: (a) Ablated mass for 10-minute ablation tests at 355 nm, 532 nm, and 1064 nm batch ablation over increasing fluences (n=1); (b) Optical absorbance spectra of SiNps produced at 0.16 J/cm².

UV-vis absorbance spectra in Figure 3.10 (b) reflects the gravimetrical tests with the 532 nm produced Nano colloid resulting in the highest absorption at 400 nm. The UV-vis spectra response of 355 nm and 532 nm wavelengths is in agreement with results reported in literature for SiNps fabricated using a similar laser system [17]. The UV-vis spectra suggest that larger particles may be present in the colloid produced at 1064 nm. This is indicated by the higher UV-vis absorbance of the colloid between 220 nm and 240 nm which indicates the presence of microparticles, as reported in literature [18]. The absorption coefficient (α) of silicon is lower at 1064 nm (α = 50 cm^{-1}) compared with 532 nm (α = 10000 cm^{-1}) leading to less photofragmentation occurring within the batch process, explaining the presence of microparticles produced via 1064 nm (ns), while not at 532 nm (ns). [19].

A series of 10-minute ablation tests were carried out at higher fluences levels using a 532 nm laser wavelength. The optical spectra attained is illustrated in Figure 3.11. A fluence of 0.32 J/cm² produced the most dense colloid. Its startling that the highest fluence tested produced the lowest colloid concentration. This result may be due to heating or optical breakdown of the water over the 10 minute period, also plume and particle occlusion early in the ablation process may have been major factors reducing the nanoparticle fabrication productivity [17].

89
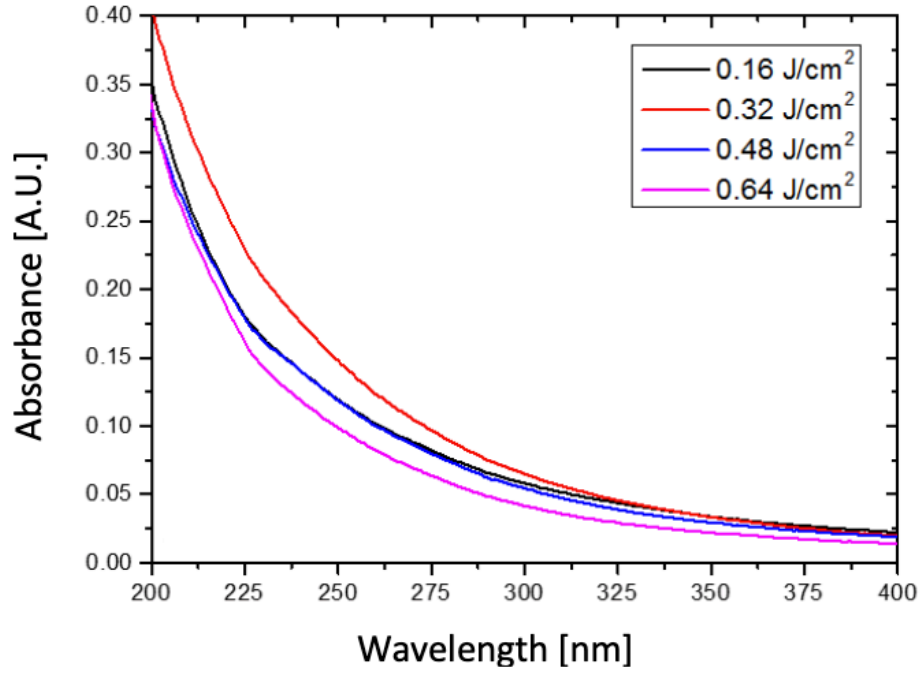
Figure 3.11: UV-vis absorption spectra of SiNps produced for 10 minutes at 532 nm at 10 Hz, with τp = 5ns, (n=1).

3.3.2 *Continuous ablation: towards Np fabrication scale-up*

Continuous flow laser ablation of the target allows for continuous colloid production, with nanoparticle colloid volumes only limited by target material availability and laser operating time. Continuous production offers the promise of removing occluding Nps from the ablation site, mitigating the absorption related problems discussed with batch production, promising higher yields and a steady-state production process. A description of the continuous production process developed is shown in *Figure 3.12*. Initial ablation tests were carried out for 20 minutes runs in triplicate. The size distribution and absorbance spectra of the SiNps colloids produced are displayed in Figure 3.13 and Figure 3.14 respectively. The size distribution revealed nanoparticles similar to those produced via batch production, with a peak diameter of 140 nm ± 65 nm, while a spherical morphology was also observed in Figure 3.18(b).
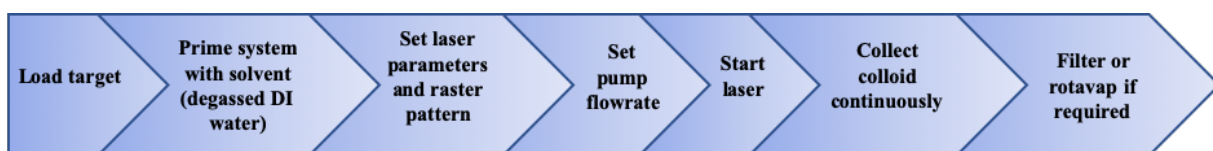
Figure 3.12: Process flow diagram of the continuous production process.

The larger peak diameter can be attributed the continuously produced particles not undergoing "0-D ablation"[10] whereby Nps in the static colloid can interact with the laser irradiation and possibly fragment into smaller diameters Nps. The optical absorbance (Figure 3.13 (b)) of the continuously produced colloid was comparable with that produced via batch production with no new spectral features present.
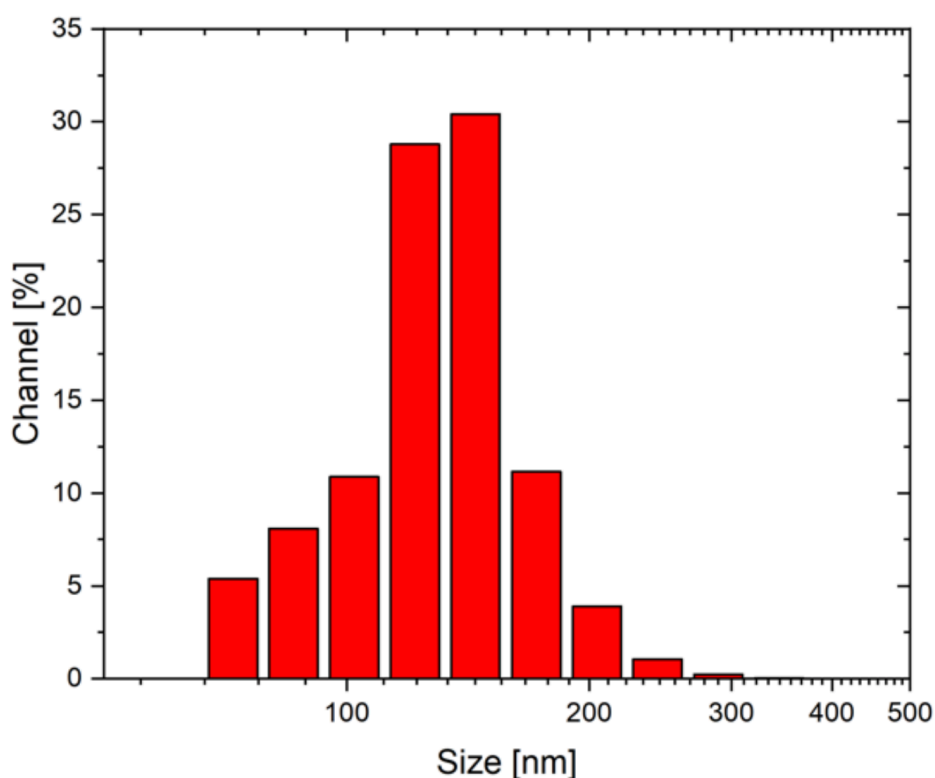
Figure 3.13: Nanoparticle size distribution (140 ± 65 nm) and (b) optical absorbance of continuous flow synthesized SiNps.

91
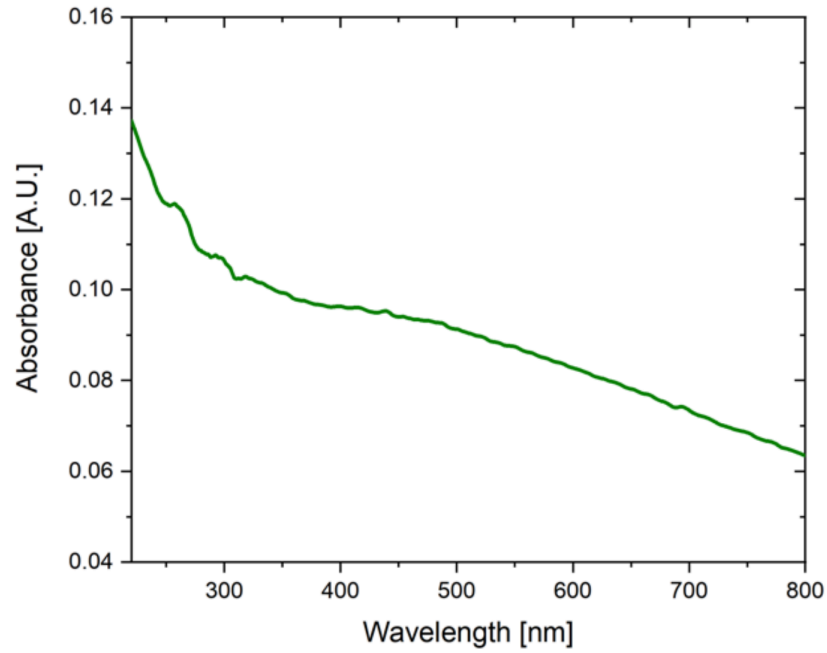
Figure 3.14: Optical absorbance of SiNps fabricated via continuous flow.

3.3.2.1 Time dependent continuous production

Tests were performed to determine if the production-rate changed with ablation time in continuous production mode. UV-vis absorbance measurement was used to indicate colloid concentration and hence infer Nps production rate. A target was ablated continuously for 35 mins with colloid samples taken at regular time intervals. Triplicate tests were performed at 70 ml/min liquid flowrate, with the laser operating at 20 kHz repetition rate and 1.63 J/cm^2 fluence. Average UV-vis spectra results are illustrated in Figure 3.15, showing that the highest colloid concentration was produced after 5 mins ablation with Absorbance at 400 nm reaching values of 0.111A.U., σ = 0.012 A.U. The absorbance measurement at 400 nm for each ablation is illustrated in Figure 3.16. It indicates that the absorbances are within 1σ of the mean for the samples taken after 15-minutes ablation, indicating a statistically similar Nps production rate within the 15-minute to 35-minute ablation window. This suggests that marginally higher ablation rates may be achieved during the first 5-minute window, after which the ablation rate stabilises. The flow conditions are at steady state for the test and there is no indication of a consistent reduction in ablation efficiency, indicative of ablating outside of the beam's focus. Therefore, its proposed that the target surface roughness plays a role in ablation efficiency, as the initial ablations are performed on a polished target surface.
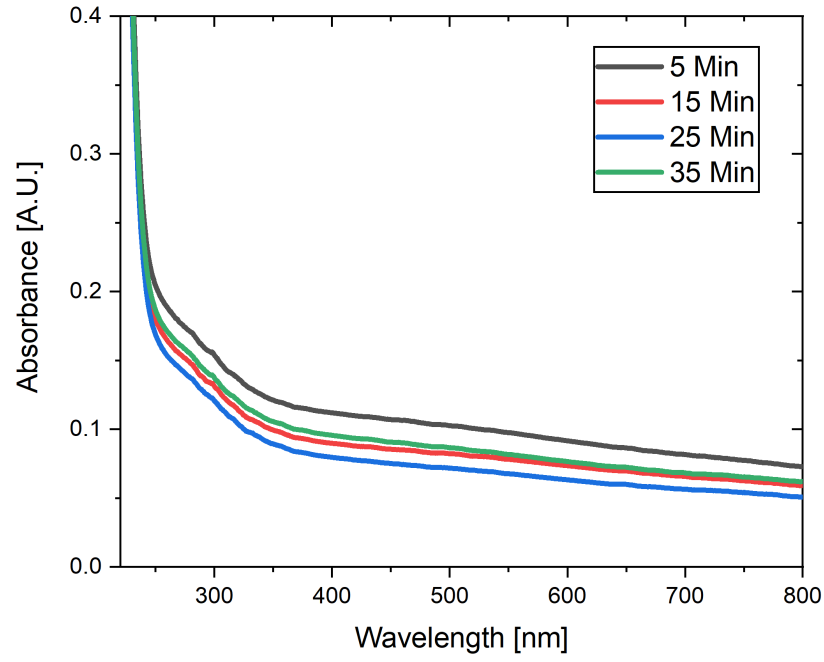
Figure 3.15: Average UV-vis spectra for continuous Nps production over time, operating at 70 ml/min flowrate, RR = 20 kHz RR, F = 1.63 J/cm2 (n=3).
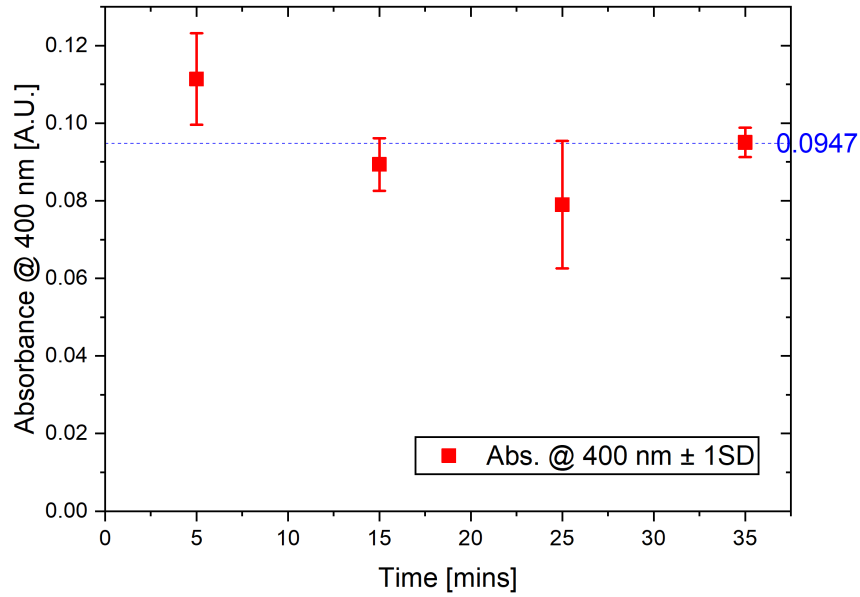
Figure 3.16: Average absorbance at 400 nm for continuous Nps production over time (including ± 1σ), operating at 70 ml/min flowrate, 20 kHz RR, 1.63 J/cm2 Fluence (n=3).

3.3.2.2   Effect of batch and continuous ablation on the target surface

Silicon targets post-ablation were analyzed via 3D optical profilometry and are shown in Figure 3.17. For the static ablation, a shallow ablation crater of 199 μm was observed. For

continuous ablation, a much deeper and well-defined ablation crater was found with a depth of 1050 μm. This demonstrates the increased efficiency of ablation under continuous flow, indicating that occluding material is being removed from the ablation site.
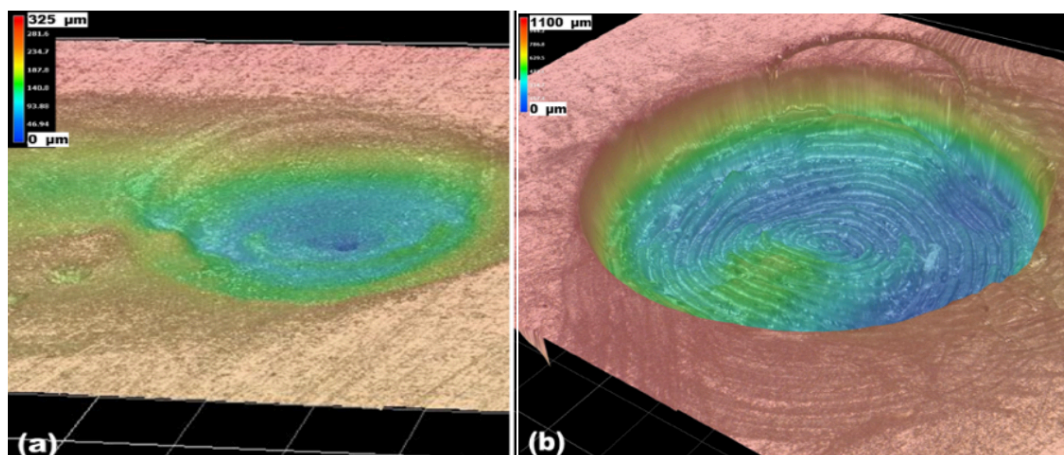
Figure 3.17: 3D optical measurements of the target under (a) 6 ml batch ablation and (b) continuous ablation.

Compared to the batch process, the continuous process resulted in a much higher yield of nanoparticles (*Figure 3.18*). For ablation over a 20-minute window, batch production was seen to generate Np yields of 2.5 ± 0.5 mg/h within a colloid volume of 11 ml while the continuous process resulted in yields of 17 ± 0.7 mg/h in 1000 ml of colloid, showing lower production process variation. Although the colloid produced was lower in concentration due to the liquid flow, with development it should be possible to increase the concentration through the use of re-circulation of the colloid during ablation (semi-batch mode) prior to collection and filtering. The increased ablation efficiency and relative uniformity of the continuous ablated target surface demonstrates that the occluding material such as particles and the generated plume were significantly by-passed during ablations, signifying that the flow cell design shows promise for future work.
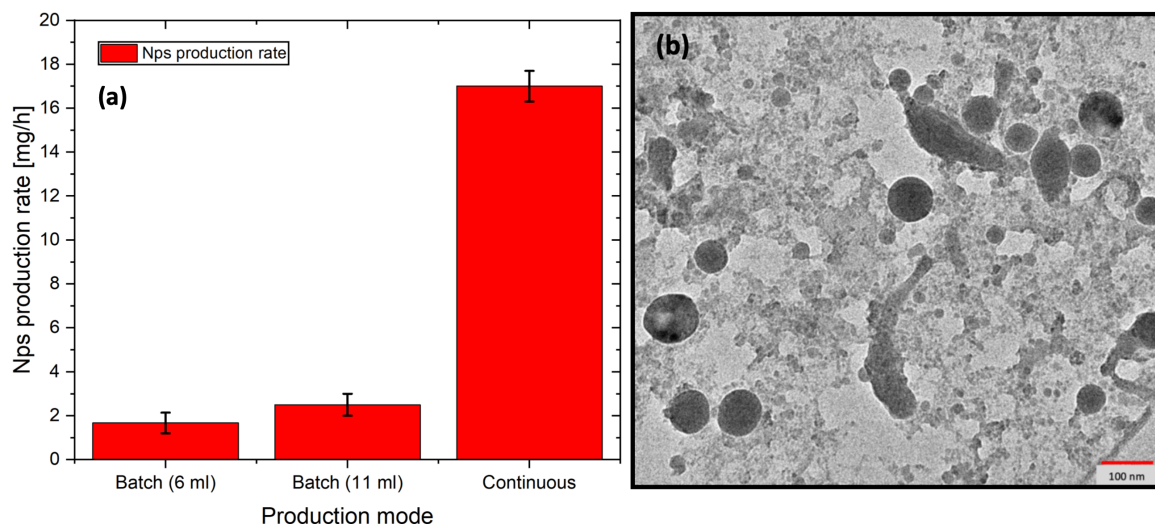
Figure 3.18: (a) Per-hour production rates extrapolated from 20-minute tests and (b) TEM image of SiNps produced via continuous LASiS with 100 nm scale bar.

3.4   Conclusions

In this chapter, the first steps towards the development of an in-house, continuous flow nanoparticle system are presented. The results suggest that appropriate selection of laser conditions, such as wavelength, and fluence for a given material can lead to highly optimized Np production. It was identified that for the production of SiNps, 532 nm ablation proved the most efficient. Under continuous production, similar Nps sizes and morphology was seen compared with the standard batch technique. However, larger variations in peak size and size distribution were seen due to slight variation in the ablation conditions. Ultimately, the continuous flow ablation showed promise in producing large, scalable volumes of nanoparticles more efficiently than batch production, and at a steady production rate. Though further work is required to integrate all the identified improvements into a single system, the process shows tremendous promise towards increasing ablation efficiency with existing lasers and towards realizing high yield laser generated industrial-scale nanoparticles.

3.5   References

[1]   K. Bagga, R. McCann, M. Wang, a. Stalcup, M. Vázquez, and D. Brabazon, "Laser assisted synthesis of carbon nanoparticles with controlled viscosities for printing applications," *J. Colloid Interface Sci.*, vol. 447, pp. 263–268, 2015.

[2]   K. Bagga *et al.*, "Laser-assisted synthesis of ultrapure nanostructures for biological sensing applications," in *Proceedings of SPIE*, Sep. 2016, p. 99280O, doi: 10.1117/12.2237147.

[3]   K. Bagga *et al.*, "Nanoparticle functionalized laser patterned substrate: an innovative route towards low cost biomimetic platforms," *RSC Adv.*, vol. 7, no. 13, pp. 8060–8069, 2017.

[4]   "DataRay WinCamD datasheet." https://www.dataray.com/products/wincamd-lcm-cmos-beam-profiler (accessed Jul. 01, 2020).

[5]   P. Wagener, A. Schwenke, B. N. Chichkov, and S. Barcikowski, "Pulsed laser ablation of zinc in tetrahydrofuran: Bypassing the cavitation bubble," *J. Phys. Chem. C*, vol. 114, no. 17, pp. 7618–7625, 2010.

[6]   S. Barcikowski and F. Mafuné, "Trends and current topics in the field of laser ablation and nanoparticle generation in liquids," *J. Phys. Chem. C*, vol. 115, no. 12, p. 4985, 2011.

[7]   S. Barcikowski *et al.*, "Handbook of Laser Synthesis of Colloids," 2016.

[8]   R. Streubel, S. Barcikowski, and B. Gökce, "Continuous multigram nanoparticle synthesis by high-power, high-repetition-rate ultrafast laser ablation in liquids," *Opt. Lett.*, vol. 41, no. 7, p. 1486, 2016.

[9]   S. Barcikowski, V. Amendola, G. Marzun, and C. Rehbock, "Handbook of Laser Sintheshis," no. April, 2016.

[10]   D. Zhang, B. Gökce, and S. Barcikowski, "Laser Synthesis and Processing of Colloids: Fundamentals and Applications," *Chem. Rev.*, vol. 117, no. 5, pp. 3990–4103, 2017.

[11]   R. Intartaglia, K. Bagga, M. Scotto, A. Diaspro, and F. Brandi, "Luminescent silicon nanoparticles prepared by ultra short pulsed laser ablation in liquid for imaging applications," vol. 2, no. 5, pp. 510–518, 2012.

[12]   K. Mandel, M. Straßer, T. Granath, S. Dembski, and G. Sextl, "Surfactant free superparamagnetic iron oxide nanoparticles for stable ferrofluids in physiological solutions," *Chem. Commun.*, vol. 51, no. 14, pp. 2863–2866, 2015.

[13]   R. Bywalez, H. Karacuban, H. Nienhaus, C. Schulz, and H. Wiggers, "Stabilization of mid-sized silicon nanoparticles by functionalization with acrylic acid," *Nanoscale Res. Lett.*, vol. 7, no. 1, p. 76, 2012.

[14]   A. S. Heintz, M. J. Fink, and B. S. Mitchell, "Silicon nanoparticles with chemically

tailored surfaces," *Appl. Organomet. Chem.*, vol. 24, no. 3, pp. 236–240, Mar. 2010.

[15]   R. Intartaglia, K. Bagga, and F. Brandi, "Study on the productivity of silicon nanoparticles by picosecond laser ablation in water: towards gram per hour yield.," *Opt. Express*, vol. 22, no. 3, p. 3117, 2014.

[16]   S. Barcikowski and G. Compagnini, "Advanced nanoparticle generation and excitation by lasers in liquids.," *Phys. Chem. Chem. Phys.*, vol. 15, no. 9, pp. 3022–6, 2013.

[17]   P. Chewchinda and T. Tsuge, "Laser Wavelength Effect on Size and Morphology of Silicon Nanoparticles Prepared by Laser Ablation in Liquid," *Jpn. J. Appl. Phys.*, vol. 52, p. 120699, 2013.

[18]   Y. Wang *et al.*, "CdS and SnS2 nanoparticles co-sensitized TiO2 nanotube arrays and the enhanced photocatalytic property," *J. Photochem. Photobiol. A Chem.*, vol. 325, pp. 55–61, 2016.

[19]   H. Wang, X. Liu, and Z. M. Zhang, "Absorption coefficients of crystalline silicon at wavelengths from 500 nm to 1000 nm," *Int. J. Thermophys.*, vol. 34, no. 2, pp. 213–225, 2013.

Chapter 4: Real-time monitoring and control towards high-efficiency autonomous laser fabrication of nanoparticles

4.1 Introduction

This chapter builds on the initial continuous flow development in chapter 3, aiming to combine process engineering techniques with laser processing to produce a proof-of-concept on-the-bench nanoparticle fabrication system, towards commercial viability in industrial environments such as biopharma.

The production of nanomaterials, and nanoparticles (Nps) in particular, has become a topic of great interest recently, with these nanomaterials finding application in areas such as biosensing [1],[2], drug delivery [3], in vitro toxicity tests [4], environmental testing [5] and nano-medicine [6], [7], [8]. Current commercial synthesis of nanomaterials relies on chemical reduction methods which are highly cost-effective for bulk production. However, these chemical techniques use environmentally harmful solvents and reagents, and with a shift in focus towards environmentally green and sustainable approaches, alternative routes for Nps synthesis are actively being explored by many research groups. Also, they are not ideal for the biomedical or biopharma industries, where surface purity is an essential requirement [9]. One potential solution to this challenge is the move towards physical techniques such a Laser Ablation Synthesis in Solution (LASiS) [10]. The LASiS technique involves the use of a high-power laser for the ablation of a solid target immersed in a liquid. Compared with chemical synthesis techniques, LASiS produces bare, ligand-free nanoparticles. This allows the produced NPs to be functionalized in single-step post-production, or with a functionalization step incorporated into the LASiS process. Recently, our group has reported the use of these laser synthesized nanomaterials for use in biomimetic surfaces [11] and biological sensing applications [12].

These advantages of LASiS over competing techniques would allow the targeted, cost-effective on-demand production of Nps for R&D environments. However, several challenges need to be met before LASiS can be adopted by the bio-pharmaceutical and bio-medical R&D and production environments, namely:

1. Production efficiency improving toward chemical synthesis efficiencies of scale [10].
2. Process validation and monitoring to meet the Food and Drug Administration's (FDA) [13] via a Quality-by-Design (QbD) frame work [9].

In this work, a starting point towards addressing these process challenges is proposed. Firstly advantage can be taken from the extensive development work in the field to date, namely improved LASiS efficiency by moving towards a continuous production process [14]–[17]. This work is focused toward optimising low-power laser systems which would prove the principle for scaling of the technique and provide a suitable method for providing a turn-key, on-the-bench solution to the provision of NPs for R&D laboratories such as in the biopharma industry. Secondly, for LASiS to become an accepted Np production process in regulated environments, such as the biopharma industry, it must meet regulations such as the Food and Drug Administration's (FDA) PAT guidelines and Quality by Design (QbD) frameworks. A major component of the QbD framework is to monitor the critical process parameters (CPPs) in a timely fashion and enact process change in order to ensure the process stays within specifications and control [9].

LASiS as a technique is still developing and has only recently breached the chemical production parity barrier [17], but to date few commercial PAT tools have been integrated into production systems, leading to slow process characterisation. This poses questions on the readiness for adoption of the technique within regulated industries. Also, from a material development point of view, integrated process monitoring would offer the ability to monitor and change these variables at speed, allowing for rapid process characterisation and Np development. Off-line process characterisation remains the research field's main option that has been implemented for process validation, with off-line analysis via DLS, TEM, SEM, XRD and UV-vis spectroscopy and ATR. Recently some initial tests on implementing on-line monitoring via remotely controlled systems applying colorimetric monitoring were

tested [18], but the monitoring technique remains in its infancy. Laser capital costs would be a factor in developing an on-the-bench production device. Therefore avoiding electron-phonon relaxation [19] by using femtosecond (fs) laser systems would not be possible with the current market costs. Pico-second (ps) lasers offer a good compromise between capital cost, low pulse duration and average laser power.

In this work, a new integrated LASiS nanoparticle manufacturing system is presented. The system incorporates in-situ process characterization integrated with process variables control, paving the way towards rapid manufacturing and single-step product validation. These PAT tools include 180° Dynamic Light Scattering (DLS) to monitor particle sizing and UV-vis Spectroscopy to estimate colloid concentration and monitor stability. Modern additive manufacturing techniques were employed to develop the Np synthesis flow cell reactor, optimising Np production efficiency. The ability to characterise the process in real-time while applying process control should help the LASiS to meet QbD requirements to ensure high reproducibility, process accuracy, product stability and increased process efficiency.

The system was trialled in two regimens: continuous and semi-batch/recirculation production. The results of these trials are described and discussed in terms of Np productivity and quality via on-line measurements from the UV-vis and DLS systems, and as a means of instrument validation and off-line Nps morphology tests via TEM.

4.2   Description of the system

4.2.1   Laser system

The laser system employed for development constitutes a low-power micro-machining picosecond Nd: YAG laser [WEDGE HF 1064, BrightSolutions, Italy, (E-1, Figure 4.1], its specifications is detailed in Table 4.1.

Table 4.1 Bright solutions HF 1064 laser specifications

Wavelength	*[nm]*	*1064*
Average max power	[W]	<6
Max pulse energy	[µJ]	250
Pulse duration	[ps]	500 – 3,000
Repetition rate	[Hz]	10k - 100k
Spot diameter	[µm]	100

The laser beam was rastered using a 2D scanning galvanometer [Raylase SS-12, (E-2)] at variable linear speeds moving in an Archimedean spiral pattern over the surface of the target material. The target was maintained in the beam-waist via an M-404 4PD 1D-nanopositioning stage [PI, Germany, (E-4)], controlling the spot size at 100 µm in diameter. The beam profile is Gaussian, exhibiting a near TEM_{00} mode (ellipticity 0.97) via an F-theta lens.

4.2.2 Nanoparticle fabrication system

The autonomous nanoparticle fabrication system developed is described in Figure 4.1. The custom-designed 3D-printed flow cell (E-3) was fixed horizontally onto the micro-stage. The complete laser system was mounted on an 80 mm diameter Thorlabs optical breadboard.

The reservoir [2l borosilicate glass bottle, Fisherbrand, (E-11)] was filled with degassed solvent pressurized via a remotely controlled variable speed peristaltic pump [Isamatic MCPV510 with XX80EL005 head (Millipore Ltd, (E-5)] under varying flow-rates from 10 ml/min to 400 ml/min. A rotameter (Vogtlin TypV100, (E-6)) calibrated the pump speed (rpm) to volumetric flow (l/min) and was removed during Np manufacture under recirculation flow. Operating pressure in the flow cell was controlled using a Hoffman tubing clamp (V-10) mounted at the exit of the flow cell. Gauge pressure (bar) was measured via an analogue pressure gauge (E-7).
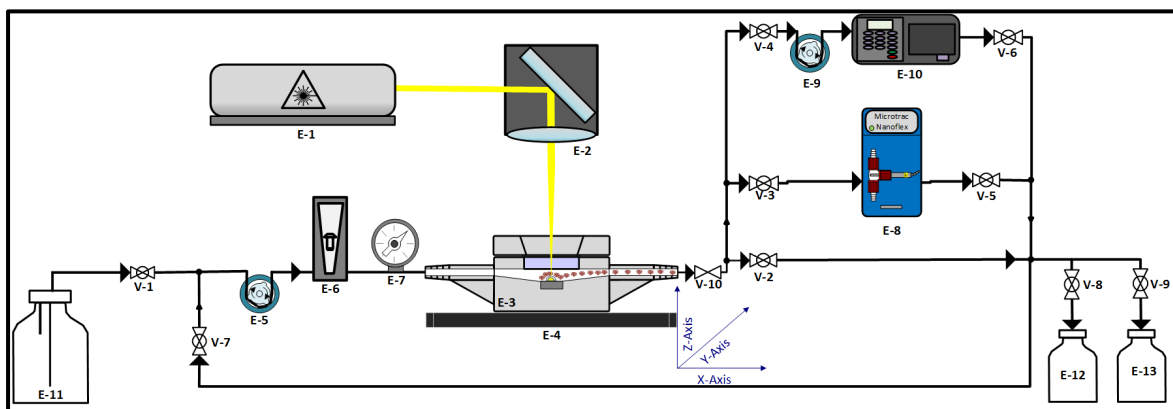
Figure 4.1: Autonomous Np fabrication system

Fluid flow in the system was controlled via ten remotely operated 1/4" Stainless Steel 2-way solenoid valves (12 VDC) with EPDM seals (ACL Ltd. E110BE35///, (V-1 to V10)). The main flow circuit tubing consisted of 2 mm ID PTFE piping. Additional Tygon tubing [rated for 3 bar] was used at the peristaltic pump head and at flow cell hose-tail connections. High pressure rated push-fit connectors (Metalwork Pneumatic Ltd., UK) were employed for the flow circuit. Colloids were collected in a glass bottle (E-12), a waste reservoir (E-13) was employed for system cleaning in place (CIP) and degassing. Valves were selected as "fail-open" in order to guard against over-pressurization of the system. Software safety interlocks were implemented to monitor and manage laser operating status, safe valve actuation and pump operation. Pump actuation was permitted only after user confirmation of the manual clamp valve being in an open state (V-10).

The pipe network was designed to accommodate selectable semi-batch or continuous production, allowing for different production modes and fluid conditions to be tested automatically. Considerations were made to minimize the flow network volume, so that nano-colloid production response measurements could be taken after short ablation times in semi-batch mode, ensuring that the colloid density would be above the limit of detection for the DLS and UV-vis instruments.

4.2.3   Flow cell design evolution

The ablation flow cell was designed to scale production from small volumes (ml) to multi-litre colloids. The design enables laminar flow conditions at the ablation site, and helps to reduce masking effects of the cavitation bubble [20], plume occlusion [21] and particle

102

aggregation [22], [17] by removing masking components from the ablation site and reducing the formation of eddy currents [23].
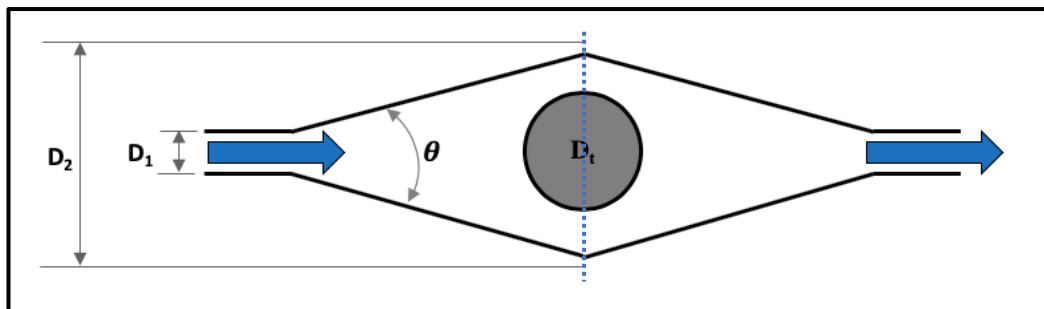
Figure 4.2: Flow cell design geometry overview - diffuser-nozzle layout, featuring target diameter (D_t), inlet pipe diameter (D_1), internal flow cell diameter at target (D_2) and diffuser angle(θ).

An iterative design process was performed using additive manufacturing via 3D printing to rapidly produce new flow-cell prototypes. A series of five designs were produced before the optimum design was achieved. The design methodology considered the following mechanical and chemical requirements: liquid flow performance, hermetically sealing of the flowcell, fluid pressure resistance, laser resistance, low Nps adhesion to flow cell surface, and minimisation of the internal wetted volume to allow for measurable Nps concentrations and high flow velocities if required.

The flow cell prototypes were designed in SolidWorks 2016 3D CAD software and fabricated using a Stratasys Connex1 3D printer employing dual material print with VeroWhitePlus (RGD835) photopolymer (65 shore D)[24] selected for the chamber structure due to its comparable material properties to Teflon PTFE (hardness 55 shore D) [25], and soft photopolymer TangoBlack (FLX973) used for the top-plate gasket ensuring a hermetic seal for the system.

A starting specification for the flow cell design was to ensure laminar flow at the ablation site. A secondary concern was to minimize the volume in the flow network surrounding the flow-cell by minimizing the inlet pipe diameter to the flow cell (D_1, Figure 4.2). This would contribute to a lower dilution factor of nano colloid in the solvent. This should help ensure that the Np colloid provides a signal above the limit of detection (LOD) of the at-line PAT,

during general operation in continuous and semi-batch modes. A minimum dimension for the flow-cell inner diameter (D_2, Figure 4.2) at the ablation site was defined by the target material geometry selected. Due to cost, availability and laser scanning considerations, material rods with an outer diameter (D_t) of 8.5 mm were chosen.

A starting point for the flow-cell geometry was a diffuser-nozzle design, shown in Figure 4.2. Given the dimensional specifications stated above, the angle of the diffuser cone (θ) would be critical to producing a developed, laminar flow. Venturi nozzle geometry specifications were chosen as a design template for the flow cell due to the streamlined flow and low-pressure losses exhibited, during venturi nozzle operation. They specify a cone angle in the range of 5°-15°[26] to produce streamlined flow within the nozzle. It should be noted that the venturi nozzle is an approximation as the wetted area in the ablation cell is a rectangular duct, rather than a cylinder. Flow velocities and Reynolds numbers were calculated for a typical flow cell with inlet pipe diameter (D_1=3 mm) and rectangular hydrodynamic dynameter (D_2=D_{hyd}= 5.7 mm), at the flow ranges reported in literature (10-500 ml/min). The resulting Reynolds number (Figure 4.3) indicates laminar conditions at flow rates up to 500 ml/min at the ablation site. But flowrate should be limited to 280 ml/min to avoid turbulent conditions in the inlet pipe.
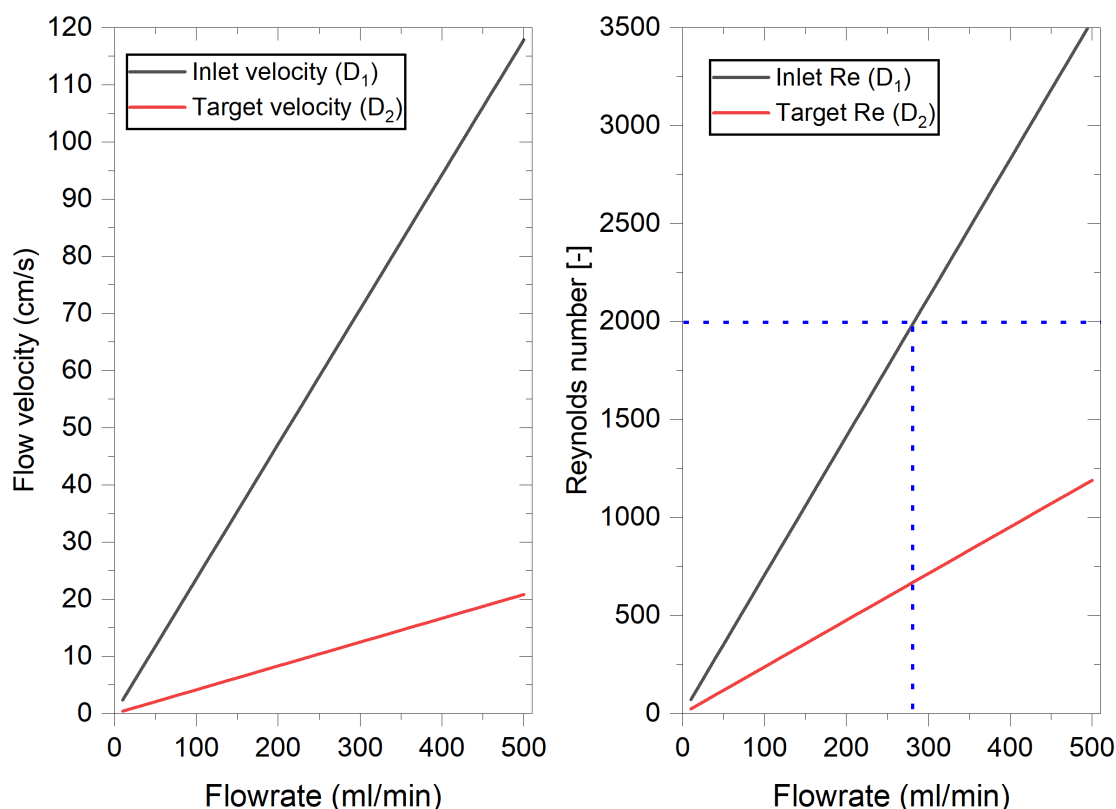
Figure 4.3: Flow conditions at the flow cell inlet and the target position.

The fluid layer height between the target and glass laser window was optimized at 4 mm, minimizing energy losses due to absorption of the solvent while ensuring no plume/glass interaction [23], as illustrated in Figure 4.12. The beam depth of focus (<1.5 mm) was such that there was no possibility of laser-window ablation. The window was positioned at an angle offset from the normal (3°) to account for beam back reflections. The initial flow-cell design can be seen in Figure 4.4. All flow cell designs were composed of three main components:

1. The base, including integrated 3mm inner diameter hose-tail connections, to allow for easy connection to Tygon tubing.
2. A laser window.
3. Top-plate including an integrated gasket seal.
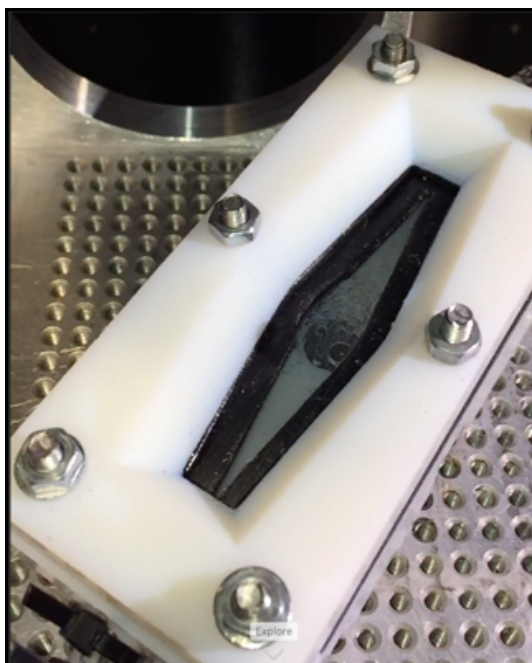
Figure 4.4: Prototype 1 flow cell in use with Si target installed, note bubble adhesion to the laser window.

Prototype 1 seen in Figure 4.4 included a 2 mm quartz glass microscope (>82% transmission @ 1064 nm) slide acting as a laser window. Under testing it was seen that bubbles adhered to the glass and interfered with ablation, even after plasma pre-cleaning of the glass. The slide offered limited resistance to fluid flow under pressure, had a low laser damage threshold and absorbed laser irradiation energy. These were inefficiencies of the design that needed to be improved.

The major details of the design iterations are described below:

Prototype 2 updates;

- Sapphire glass laser window microscope (4mm, >85% transmission @ 1064 nm).
- Geometry redesign to accommodate square sapphire glass laser window.

Prototype 3 updates;

- A Thorlabs laser window was include; this reduced energy absorption, increased laser damage threshold, increased fluid pressure resistance and reduced bubble adhesion to the wetted side of the laser window. The borosilicate-crown optical glass included an AR coating: 523 nm - 532 nm & 1047 nm - 1064 nm, High damage

threshold (10 J/cm^2) and low laser absorption (>92% transmission @ 532 & 1064 nm).

- The chamber geometry was redesigned to accommodate the Thorlabs window.
- Top-plate was redesigned for the Thorlabs laser window.

Prototype 4 updates;

- To allow for operation at higher liquid pressures (>4 bar) a commercial EPDM O-ring was included. The O-ring also offered better chemical resistance to solvent than the Tango black gaskets.
- Geometry redesign was performed to reduce the diffuser cone angle to 16°, in alignment with the venturi nozzle design guidelines.
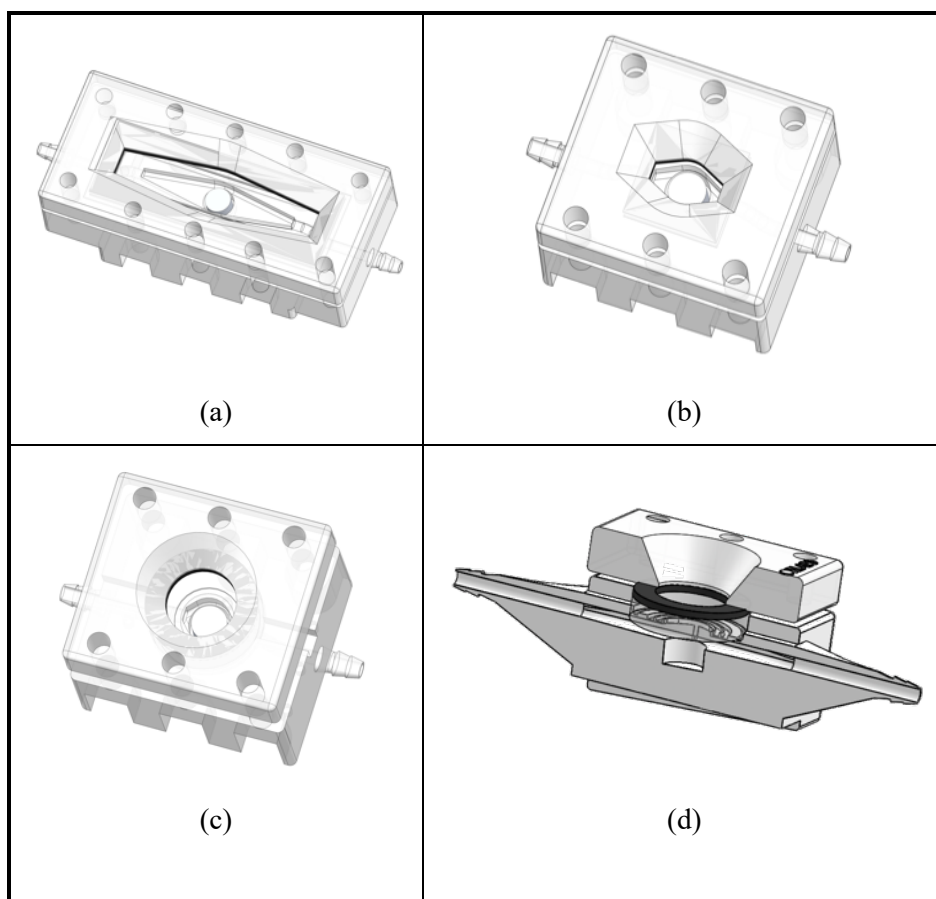
Figure 4.5: Flow cell prototype design evolution, from (a) prototype 1 to (d) prototype 4.
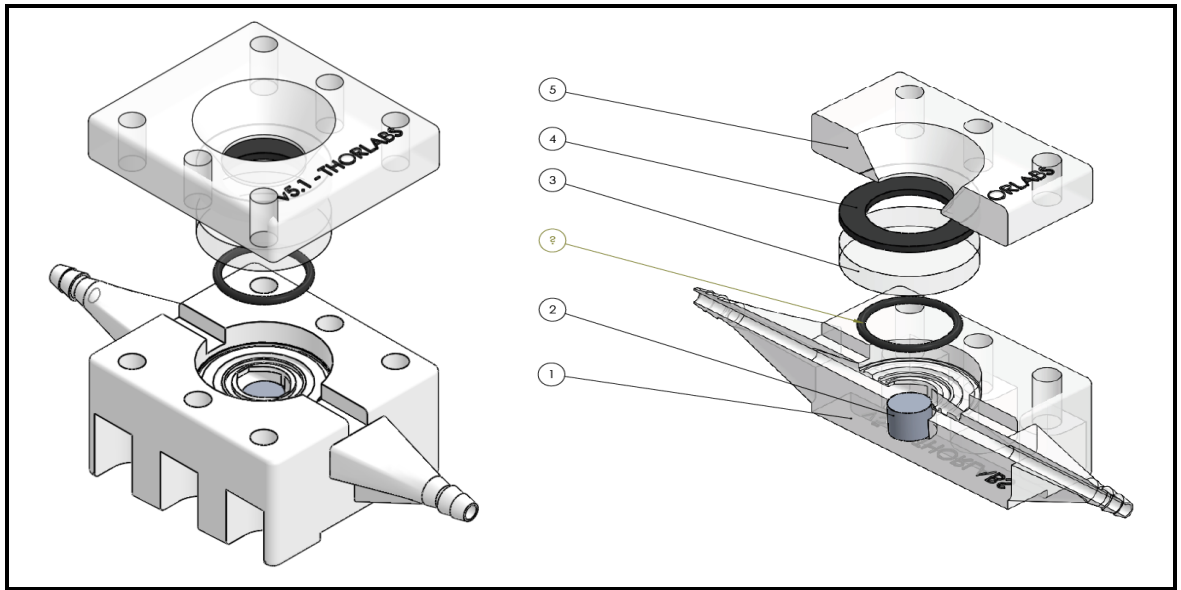
Figure 4.6: Image of final NP fabrication flow cell design (version 4) comprising of Base (1.), Target material (2.), O-ring (3.), laser window (4.), gasket (5.) and top-plate (6.).
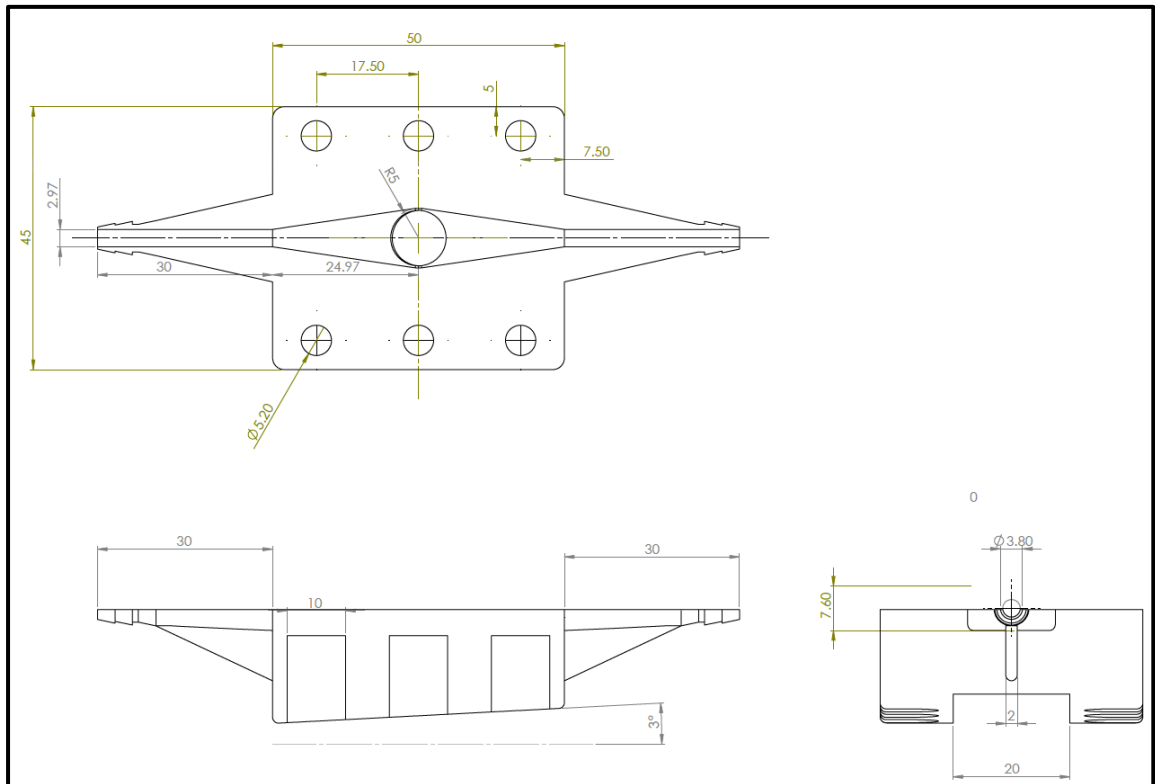
Figure 4.7: Schematic of final prototypes liquid flow surface geometry

4.2.4   *Autonomous platform development*

Control and monitoring software was developed in the National Instruments LabVIEW 2017 programming environment. "Bloomy controls" [27] & National Instruments style guidelines [28] were incorporated into the design methodology of the user interface and code development. The user interface design is seen in Figure 4.8; all instrumentation can be controlled directly in the software or via automatic test scripts. Test scripts are uploaded to the program via comma separated variable (CSV) tables, with options for selecting test times, production configuration (continuous/semi-batch), process variables, monitoring to be performed and test sequencing. The program architecture incorporates a queued message handler including an observer loop. This modular design offers scalability of code and ease of error management. A full set of equipment drivers (equipment in Figure 4.9) was developed within the LabView platform. The software process flow and architecture are included in Appendix B.

A range of process parameters were controlled directly by the software including laser fluence, repetition rate, solvent flow-rate, stage height and fabrication mode (continuous or semi-batch). Individual operational system states were selectable including: Np production, measurement, clean-in-place, solvent-fill and data post-processing. Other parameters were manually controlled with user commands and confirmation requests sent by the program such as: beam scan-speed, raster pattern, flow-cell pressure and laser wavelength (laser system dependent). Data files acquired (.csv) contained process variables data for each run, run timing, colloid UV-vis absorption spectra, and colloid Np size distribution.

All data files were collated and summarized automatically at the end of each run with the final files uploaded to Google Drive File Stream, allowing remote analysis. Remote access was available via TeamViewer, allowing remote monitoring and control of the Nps manufacture. The software process-flow is described in the Appendix B.

a.

b.
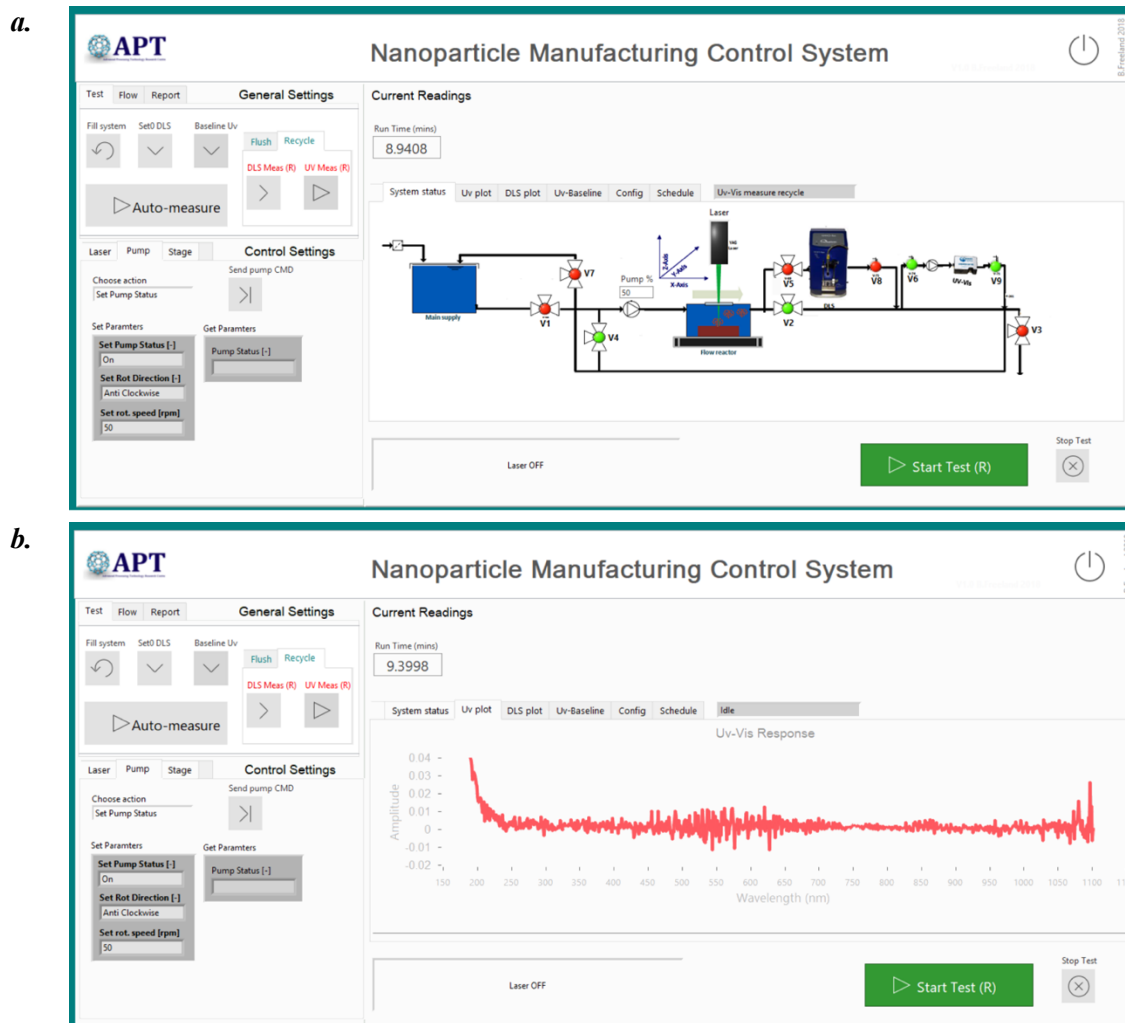
Figure 4.8: NPs manufacturing control system front panel,(a) controlling valves for UV-vis measurement and (b) displaying spectra.

4.2.5 Hardware connectivity

The connectivity described in Figure 4.9 is composed of a USB 2.0 hub (Belkin, USA) linking the control PC to the UV-vis, micro-position stage, laser system and DLS control. A National Instruments CompactRIO (cRIO-9041) industrial controller managed the fluid control valves and the pump control while an industrial Ethernet switch (Beckhoff Gmbh, Germany) managed data connectivity with the DLS data files along with PC connection to the NI CompactRIO.
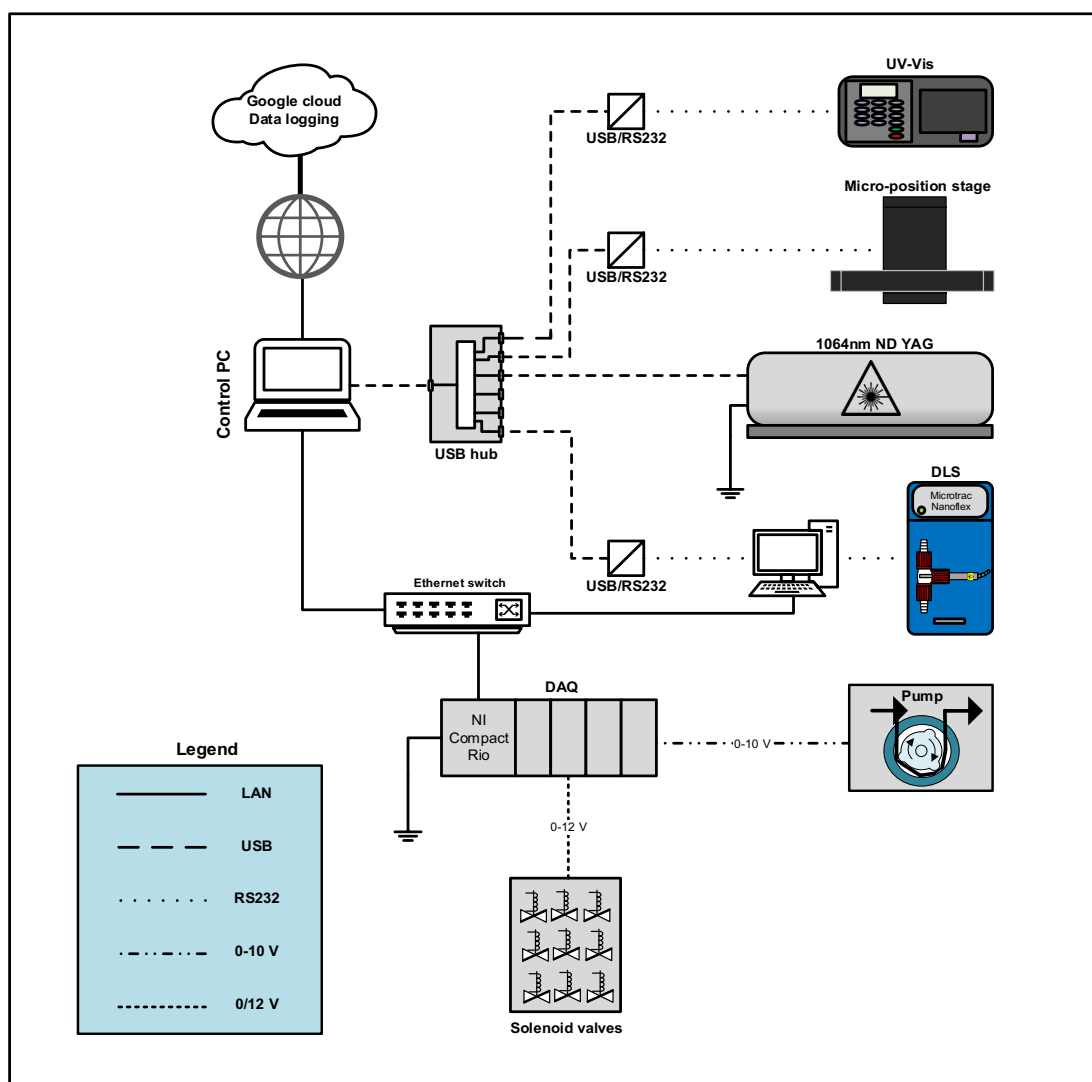
Figure 4.9: Nanoparticle manufacturing control platform consisting of production and monitoring hardware connected via serial (RS232), digital (USB and Ethernet) and analogue protocols (0-10, 0/24 VDC).

4.2.6 In-situ monitoring tools

At-line dynamic light scattering was implemented [NANO-flex® 180° DLS Size, Microtrac Ltd, (E-8)] via a by-pass loop as DLS measurements must be taken under static fluid conditions, i.e. fluid movement only due to Brownian motion [29]. During measurement, the by-pass loop was isolated from the main loop by closing valves (V-3 & V-5). A time delay of thirty seconds was implemented to ensure that the colloid had stabilized prior to measurement. During Np fabrication, continuous mixing was performed between the by-pass loop and the main loop by alternating the control valves to enable near real-time measurement of a homogenous colloid. A glass (inert, low-surface adhesion) flow-cell,

illustrated in Figure 4.10 was designed in-house and manufactured by Eirglass Ltd (Dublin 11).

The flow cell included an EPDM o-ring with a compression fit PTFE sealing the probe. The probe was mounted at an angle of 90° to the vertical to mitigate bubble adhesion on the probe tip. This ensured that during the fluid stabilization period, bubbles present in the by-pass loop would be held in the static volume after the probe tip, not affecting measurement.
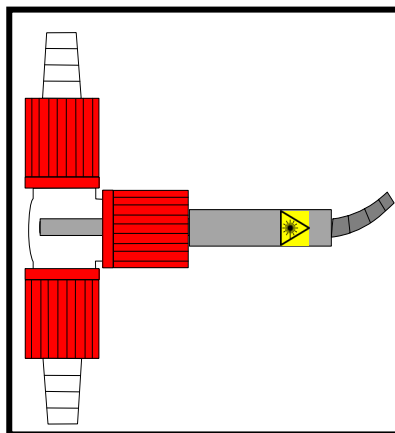
Figure 4.10: DLS glass flow cell with DLS probe inserted.

UV-vis measurement was implemented via a Libra S22 UV-vis Spectrophotometer (Biochrom Inc., USA, (E-10)) including an 80µl quartz flow cell cuvette (10 mm, Biochrom Inc., USA) and in-line peristaltic pump sipper system (Biochrom Inc., USA (E-9)). Automatic CIP flush cycles were performed on both measurement loops at process initialization during the liquid fill stage and post-Np fabrication. Base-line measurements were taken at test initialisation for both instruments.

4.3 Validation Study

4.3.1 Overview

Silicon was chosen as the development material for the fabrication system due to its availability, biocompatibility and its applications towards the biomedical and biopharma industries including drug delivery [30] and biosensing [31]. A gold target was utilized to allow comparison with state of the art LASiS production. As a means to thoroughly test the applicability of the production system in different modes and determine the effectiveness of at-line process monitoring, trials were performed in continuous and semi-batch modes. All continuous and semi-batch tests performed were scheduled via the developed software. Experimental parameters including ablation time, laser power, repetition rate, fluid flowrate and pressure, and measurement timing were loaded into the program from a comma-separated variable file (.CSV) experiment initialisation file. Batch tests were performed with manual interaction with the software.

4.3.2 Materials and Methods

The parameters used for all Si tests are described in Table 4.2. Continuous and semi-batch Np production modes were tested and compared with the standard batch technique.

Table 4.2: Experimental laser parameters utilised for LASiS system testing.

Fluence	**[J/cm^2]**	**1.83**
Average pulse energy	[μJ]	147
Pulse duration	[ps]	500
Repetition rate	[Hz]	10k
Spot diameter	[μm]	100
Spot area	[cm^2]	8.01 x10^{-5}
Liquid flowrate	[ml/min]	10-170
Scan speed	[mm/s]	2

Under batch configuration, the target was placed in a glass vial with 4 mL of deionized (DI) water. During continuous ablation, the target was placed in a custom-designed flow cell with fresh, de-gassed DI water flowing over the ablation site. Also, the semi-batch (re-circulation flow), comprised of a closed-loop piping system where piping contained an internal process volume of 83 ml of liquid continuously recirculated within the flow cell for a set time. All tests were performed in triplicate.

(a)   (b)   (c)
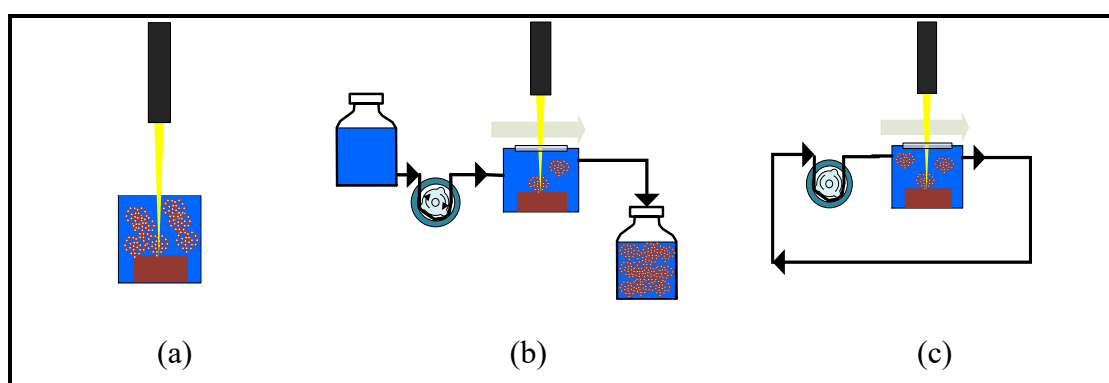
Figure 4.11. Schematic of the system used for nanoparticle synthesis via LASiS under (a) batch, (b) continuous and (c) semi-batch production modes.

4.3.2.1 Target Selection and preparation

Silicon rods (99.998% metals basis, Alfa Aesar, Ø=8.5 mm) were cut into 4 mm slices using a diamond saw-blade. Si and gold plate (99.998% metals basis, Alfa Aesar) targets were mechanically polished using P1200 silicon carbide abrasive sheets before each test.

For batch production, the target was immersed in 4 ml of ultrapure degassed DI water in a glass vial such that there was 4 mm of DI water above the top of the target. Initial tests confirmed that the liquid height above the target was sufficient to avoid liquid breakdown effects. For continuous and semi-batch ablation, the target was mounted within the centre of the flow cell reactor with the top of the target surface parallel to the flow cell base as described in Figure 4.12. There was a constant flow of degassed DI water above the target.
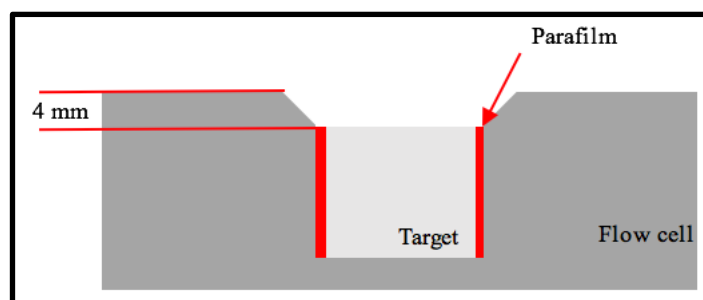
Figure 4.12: Position of the target within the flow cell

4.3.2.2 Nanoparticle characterisation

Dynamic light scattering was used as the primary Np size characterisation technique, solvent background correction was employed and the SiNps particles were assumed to be spherical with a refractive index of 1.46. Each measurement displayed was an average of three 180 s acquisitions with a 10 s pause between acquisitions. As a means of validating the DLS measurements, transmission electron microscopy (TEM) analysis was performed. The TEM used was a FEI Titan with Field Emission Gun and spherical aberration corrector system (Cs-corrector) of the objective lens operated at 300 kV. Analysis was performed using a copper mesh TEM grid with 40 µl of sample applied and allowed to evaporate at room temperature.

Optical properties of the colloids were characterized using UV-vis-NIR spectroscopy, with a scanning range of 200 – 900 nm at a rate of 20 nm/s with solvent background correction applied.

4.3.2.3 Focus determination

Experiments were conducted to identify the stage height for optimum beam waist diameter with the new flow-cell. Initially, tests were carried out in air, using the flow cell with its top plate removed and a silicon target installed. The stage height was varied at a speed of 2 mm/s until the peak laser irradiation on the target surface was visually and aurally observed, noted by a higher amplitude ablation noise [22]. Following these sighting trials, LASiS efficiency tests were performed. The tests were carried out in triplicate with a laser fluence of 1.83 J/cm^2, a 10k Hz repetition rate and beam scan speed of 2 mm/s, a liquid flow rate 100 ml/min, gauge pressure of 0.5 bar and an ablation time of 15 mins with the system in continuous mode. It was determined from Figure 4.13 that maximum ablation efficiency centred around

47.5mm stage height, with a 1.5 mm tolerance in beam width, where no significant reduction of efficiency was observed.
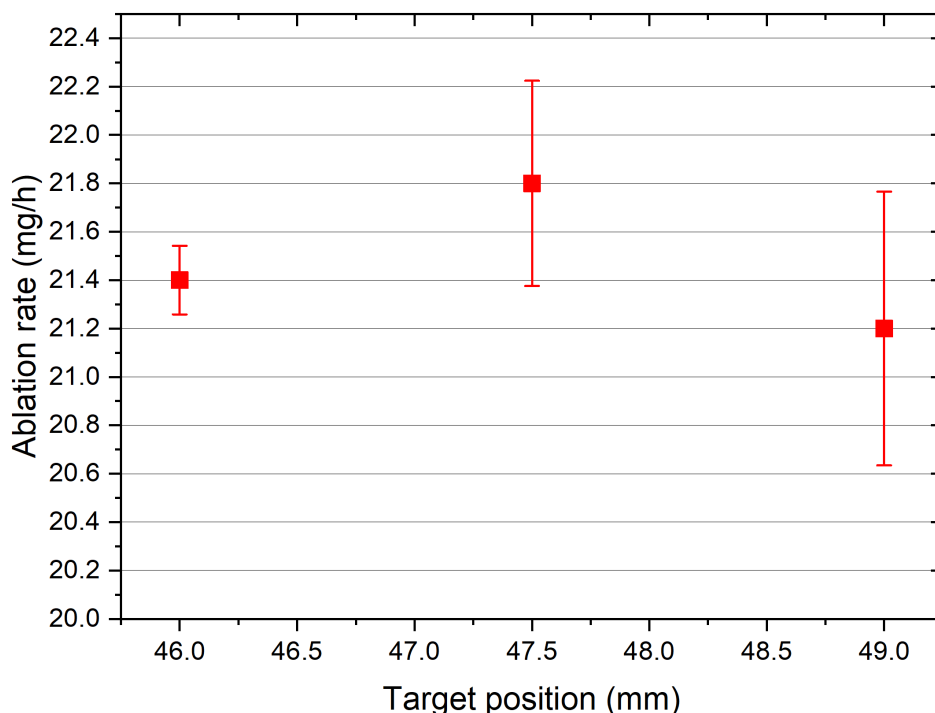
Figure 4.13: Nps production rate at different stage heights (continuous production, n=3, spot ⌀ = 100 μm).

4.4   Continuous Production results

Continuous mode Np fabrication was evaluated in terms of productivity, efficiency, quality of colloids produced, and measurement reliability of the at-line PAT tools installed. As expected, continuous mode provides substantially higher (x5) Np productivity (19.1 mg/h) compared with batch mode (3.5 mg/h). Continuous production (Figure 4.14) proved to have a low process variation, with a 95% confidence interval of 1.2 mg/h from the mean for the 15 min tests. The drawback of the continuous flow system is a reduction in SiNps concentration in the colloid to 6.8 mg/L. However, this is an acceptable concentration for most biomedical applications such as DNA tagging [31], allowing the application to be used in single step functionalization for biomarker development. An example of SiNps production within the flow-cell is illustrated in Figure 4.16, with the 1.8 *l* colloid manufactured shown in Figure 4.19.
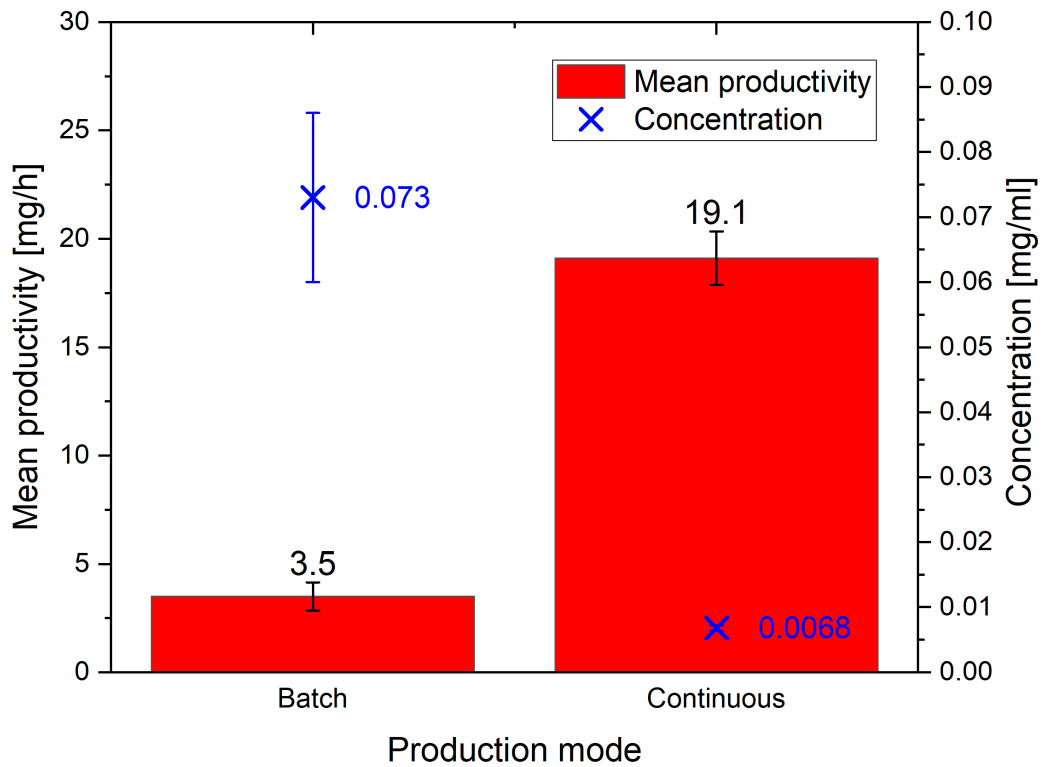
Figure 4.14: Productivity of the system for SiNps in batch and continuous modes, 50ml/min flow rate 0.5 bar gauge pressure, gravimetrical measurements (n=3).

4.4.1 Comparison with state-of-the-art production efficiency

The efficiency of LASiS processes is described by the 'power-specific productivity' (mg/Wh), which was determined as 12.9 mg/Wh for the Si tests described. The state of the art research productivity and efficiencies are reported with gold, where Kohsakowski et al.(2017) [32], reported a yield of 16.92 mg/Wh, using a 32W ns laser system at the fundamental wavelength for 60 mins, and recently by Dittrich et al.(2019) [15] who reported a productivity of 37.8 mg/h and an efficiency of 6 mg/Wh for a short test (linear extrapolation of a 10 s test) using a similar power laser system (<10W, 1064nm) described in this work. The Si test results are a promising start to system development, as they approach the current high production efficiencies reported for a material that possesses a lower absorption coefficient than gold at 1064 nm [33]. To benchmark the system against literature, initial tests were performed with a gold target, the results of which can be seen in Figure 4.15.

To aid parity of comparison with Dittrich et al. (2019) the average laser power was increased to 2.65 W by adjusting the repetition rate to 20 kHz. The liquid flow rate was set at 140 ml/min for the 5 min tests which were performed in triplicate. A process productivity of 66.7 (± 2.8) mg/h and power-specific productivity of 25.19 mg/Wh was achieved at a colloid concentration of 11 mg/l. These are encouraging results, providing higher Np production efficiencies compared with the best-in-class medium power micromachining laser system reported to date.
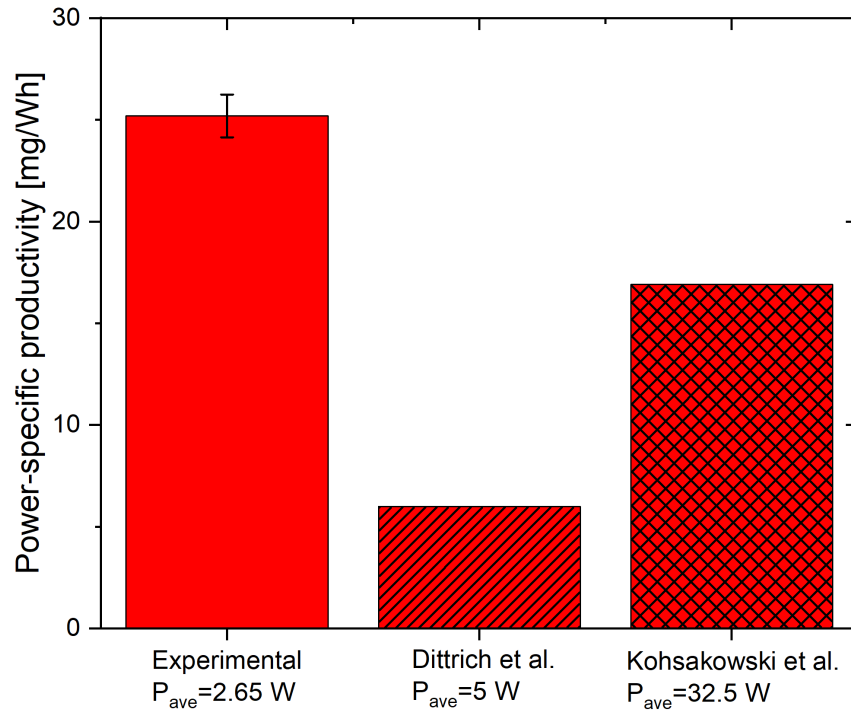
Figure 4.15: Best in class power-specific productivity for micromachining laser systems.

The efficiency of the system can be attributed to a number of factors, firstly the removal of shielding effects due to efficient removal of nanoparticles, microbubbles and debris from the irradiation site– as a result of efficient laminar flow within the flow cell [32]. The continuous liquid flow reduces the possibility of liquid breakdown and bubble accumulation due to thermal build-up in the colloid [22], [34]. No liquid breakdown was seen during the tests. A test in progress is shown in Figure 4.16. Temporal avoidance of the cavitation bubble occurred due to low pulse overlap at 10 kHz & 20 kHz repetition rate [32], leading to more efficient ablation. The cavitation bubble lifecycle is reported to range between 150 and 300 µS [35], depending on pulse energy. The time-span for the primary bubble collapse to occur can be less than 100µs [32]. Thus at 10 kHz repetition rate temporal avoidance of the

cavitation bubble lifecycle, or at least the primary bubble may be occurring. This would contribute to unrestricted irradiation of the target, hence high production efficiency.
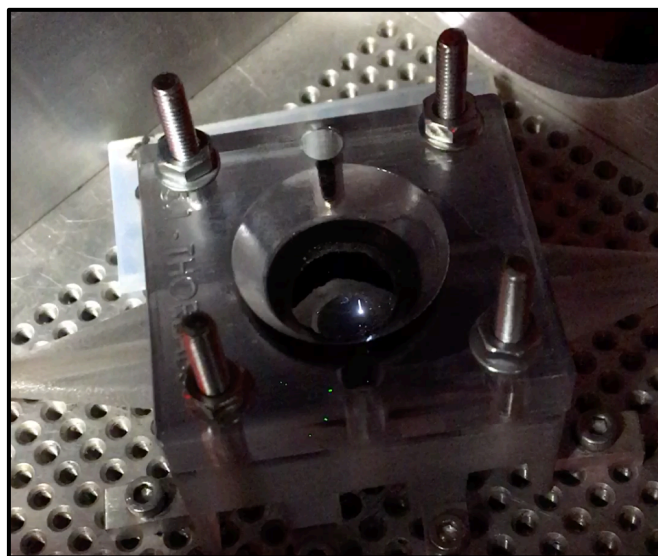
Figure 4.16: LASiS SiNps continuous production in the 3D printed flow cell

Another contributing factor to high production efficiencies was the relatively low colloid concentration the process was operating at. The low concentration would reduce the possibility for Np concentration gradients at the ablation site [15], thereby reducing colloid masking effects. Also, thermal effects may be contributing to ablation efficiency. Increasing the bulk temperature of silicon increases its linear absorption coefficient at 1064 nm [36] and in doing so, reduces the ablation threshold of picosecond laser systems [36], [37]. It has been seen that the silicon lattice will increase in temperature upwards of 400°C by ps irradiation (> 2 ps) as a small inter-pulse distance (0.2μm) was employed, beam overlap will occur. Due to this overlap, it is expected that local heating of the target material would arise, lowering the ablation threshold for the next pulse, increasing the material mass removal rate.

4.4.2   *Process monitoring & product characterisation*

In the future, the Np manufacturing system will be utilised as a testbed for Np production with various target materials under several process conditions. Flowrate is one such condition that may be altered. Changing the flowrate affects the concentration of the colloid and, possibly could change productivity by using liquid flow to remove masking agents from the ablation site, as discussed previously. A range of flowrates have been implemented in literature (10 ml/min to 500 ml/min), depending on the application and laser power [15],

[38], [39]. To this end, the viability of UV-vis spectroscopy as a monitoring tool under a selection of DI water flowrates was evaluated while producing SiNps, as illustrated in Figure 4.17. As expected, the highest absorption, thus colloid concentration, was attained at 10 ml/min flowrate (0.3 A.U. abs. at 400nm), with the highest flowrate tested producing the lowest concentration colloid (170 ml/min, 0.05 abs. @ 400 nm). The absorbance spectra acquired are in agreement with results from Bagga et al. (2013), as representative of a SiNps colloid immersed in DI water. Thus, for the pulse energy (147 mJ) and fluid flow rates (10-170 ml/min) tested, at-line UV-vis measurement can characterise colloids produced without the need for prior concentration steps.
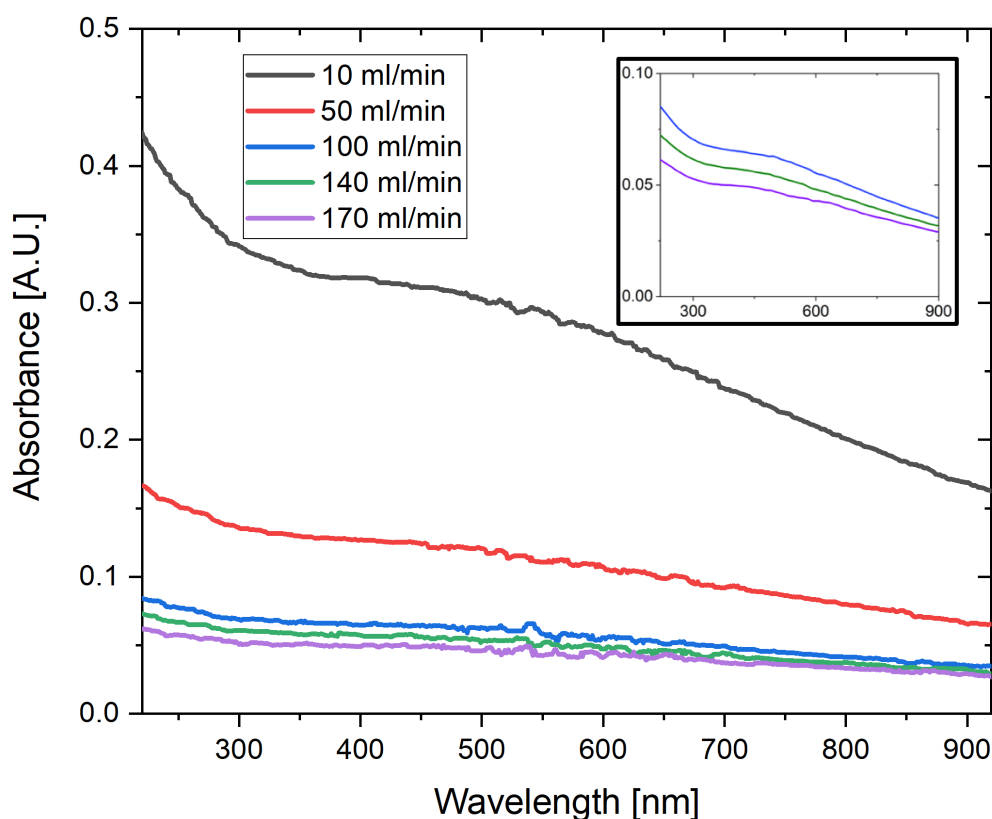
Figure 4.17: UV-vis spectra of a continuously produced SiNps colloids at increasing fluid flow rates, insert: zoom window of the more dilute colloid concentrations.

As a demonstration of the production suitability, the colloid size distribution was measured with DLS both during production (at-line) and post-filtration (off-line). The results of the measurement are displayed in Figure 4.18. Off-line samples were filtered via 0.2 μm Millipore vacuum disk filters. The at-line samples displayed a bi-modal peak, possibly due to macro-particles remaining in suspension due to recirculation flow prior to measurement.

This off-line filtered sample possesses a size distribution peak at 74.6 nm ± 40 nm, (2σ). The DLS measurement is in agreement with the TEM analysis presented in Figure 4.25. The SiNps size distributions reported in this work are similar to those published by Intartaglia et al. (2011& 2012)[40], [41] displaying a shoulder at 500 nm and a broad continuous band within the range of 220 nm to 900 nm. Thus, it can be demonstrated that in continuous mode, the manufacturing system produced SiNps colloids in agreement with those published in literature.

(a)   (b)
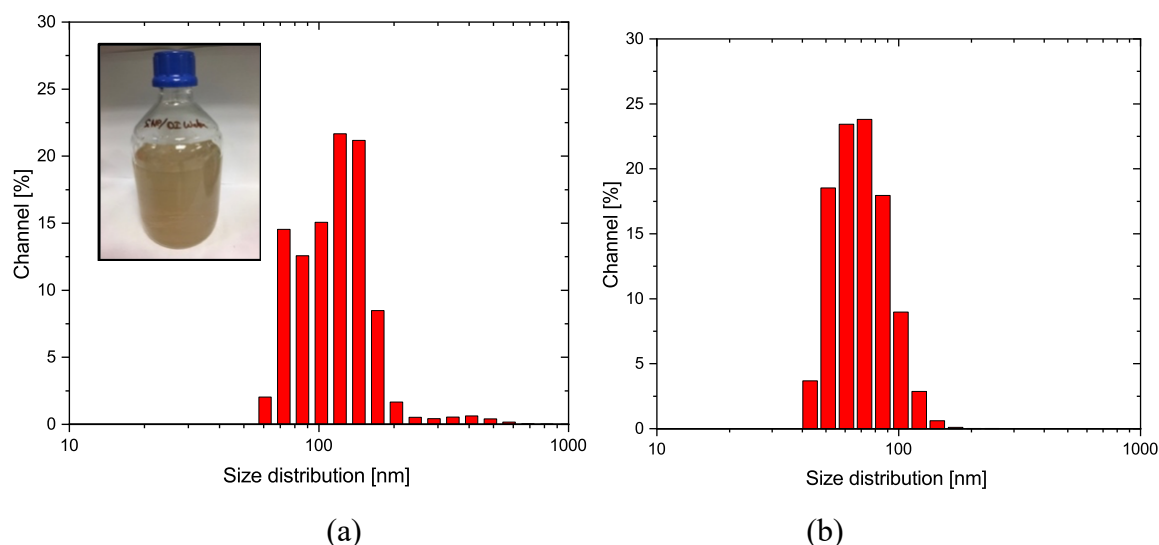
Figure 4.18: (a) At-line DLS monitoring of SiNps displaying a bi-modal distribution, peak 1 at 119 ± 51 nm, (74% colloid volume) and peak 2 at 70 ± 15 nm (26% colloid volume). (b) Off-line 0.2 μm filtered DLS colloid, peak at 74.6 nm ± 40 nm.

Optical analysis of the AuNps colloid was performed in order to validate the production process. The UV-vis spectrum (Figure 4.19) is characteristic of gold Nps, with a surface plasmon resonance (SPR) peak at 522 nm. Off-line DLS measurement (see Figure 4.20) revealed a peak diameter of 2.6 nm ± 0.7 nm. Previously it has been reported that AuNps SPR wavelength was size-dependent, where Nps with a similar diameter (9 nm) displayed an SPR at 517 nm [42], with larger particles (22nm) producing an SPR at 540 nm (approximately) [18]. The optical response and size distribution of SiNps and AuNps produced in this work are in agreement with those reported in literature.

121
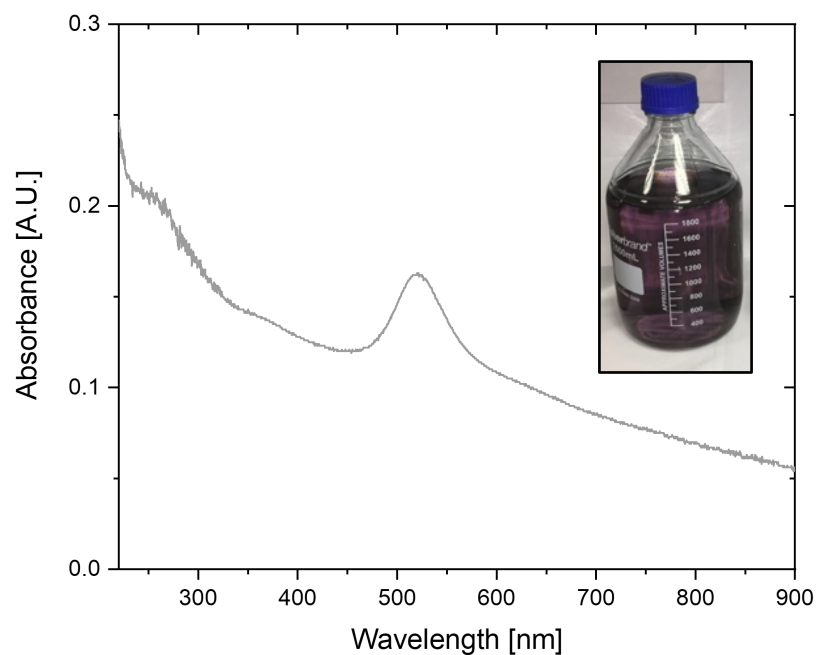
Figure 4.19: Off-line UV-vis spectra (insert.1.8L colloid produced) AuNps colloid.
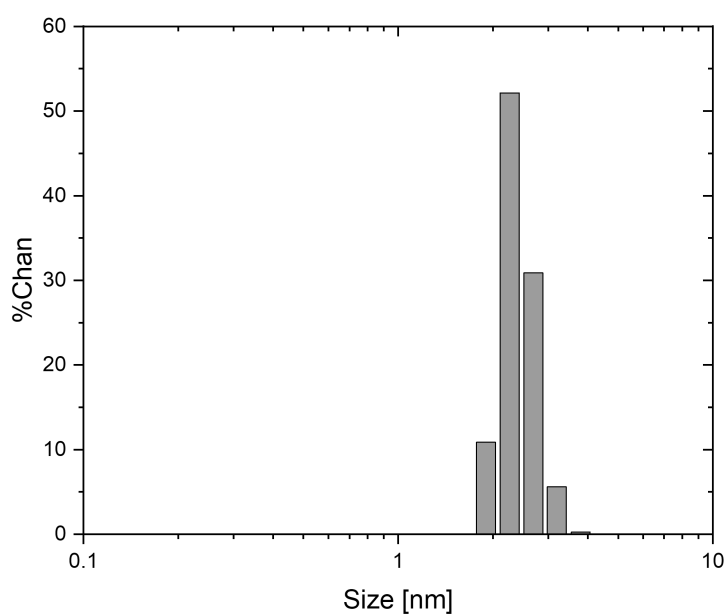
Figure 4.20: Off-line DLS size distribution AuNps colloid, peak diameter at 2.6 ± 0.7 nm.

4.5 Recirculation production

The recirculation/semi-batch mode could be used to produce colloids to high concentrations allowing for "concentration on-demand" production. The semi-batch mode also acts as a testing ground for laser parameter selection, as recirculation time can be increased in order to provide an acceptable measurement resolution for the at-line measurement tools.

Additionally, as the flow-cell ensures laminar flow at the irradiation site, particle photo fragmentation can be studied in semi-batch mode. Firstly, the productivity performance of recirculation (semi-batch) and continuous modes were evaluated. Figure 4.21 shows the triplicate results for a series of semi-batch production tests, up to 60 mins in length. As the semi-batch mode is closed-loop, no samples can be taken until the end of the test. Therefore, tests were stopped after 1, 7, 15, 30 and 60 mins with gravimetrical ablated mass measurements taken at the end of the test. A recirculation solvent flow rate of 140 ml/min was selected for all tests. A low process variance was observed for the productivity, with confidence intervals ranging between 7.03 mg/h to 0.31 mg/h from the mean. The process productivity is in agreement with the Beer-Lambert law; as the Nps production rate decreases logarithmically with time due to particles occluding the beam. Thus, the productivity is subject to a logarithmic decline from initial high production rates of 34 mg/h to 7 mg/h (Bradley model, $y = -13.21*\ln(0.14*\ln(x))$ adjusted R^2 of 0.995) as seen in Figure 4.21.
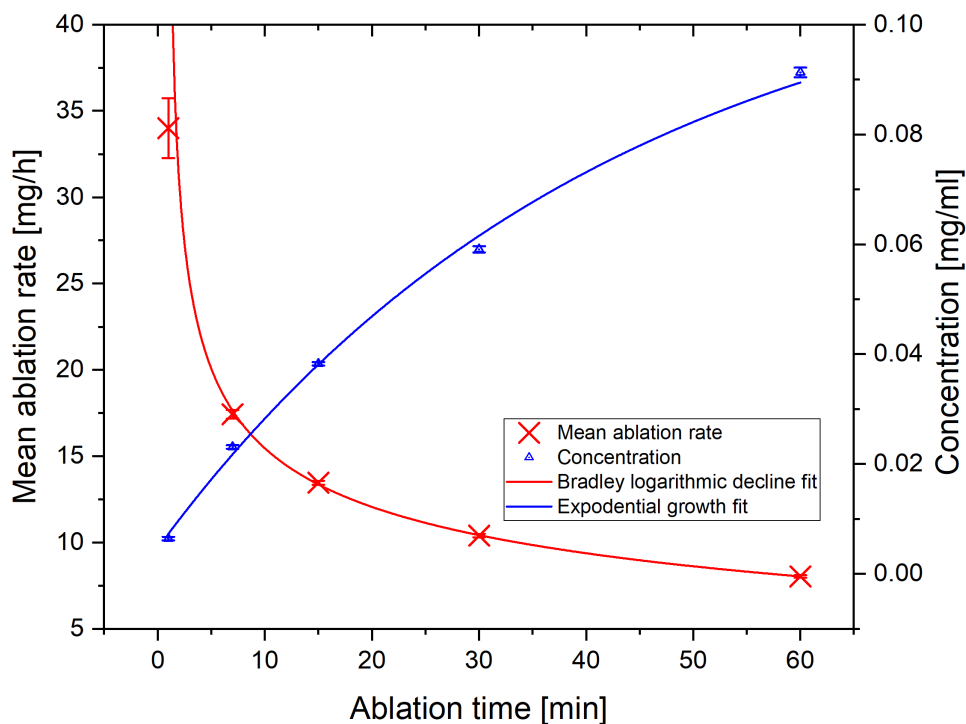
Figure 4.21: SiNps production rate and colloid concentration over 60 mins recirculation, (n=3).

At the start of the batch ablation, with low colloid concentrations, no irradiation shielding is taking place. Thus, the process is similar to continuous production mode. Its seen after 1 min ablation high productivity was achieved, offering power-specific productivity of 23 mg/Wh,

123

higher than efficiencies developed in section 4.4. This indicates that high solvent flow rates in continuous mode may infer higher production yields. However, this result requires a 60x extrapolation, so further continuous flow testing would be required to validate the claim.
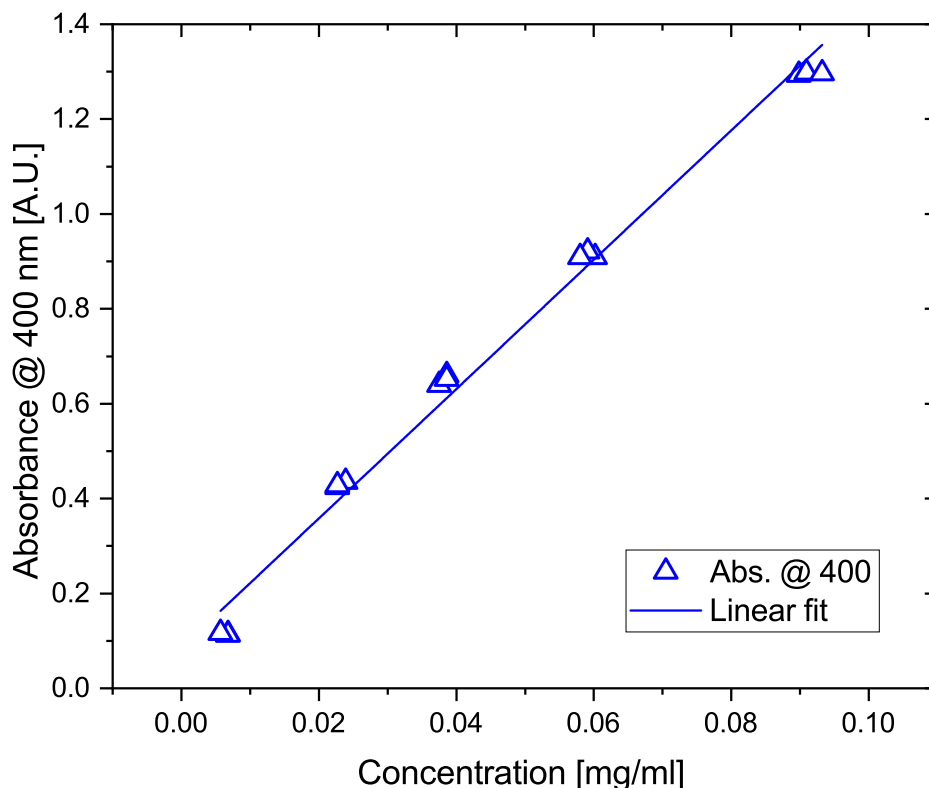
Figure 4.22: UV-vis absorbance versus colloid concentration showing a linearly fit (adjusted R2= 0.989, n=3). Conc$_{Pred}$ =0.07258*(Abs.)-0.00576.

The semi-batch tests show a capacity for the process to produce 83 ml of SiNps colloid with a selectable concentration up to 91 ± 4 mg/L in 60 min, displaying a process variation of only 4%. This concentration production compares with 6.8 mg/l produced via continuous production at 50 ml/min liquid flow, at the expense of production efficiency The concentrations produced compare well with colloids produced by Kobayashi et al.(2013) who achieved 30 mg/l using a similar power laser systems (fluence = 0.6 J/cm^2) on Si targets in batch mode [43]. This operational mode provides for small volume (<100 ml), high concentration Nps production, suitable for the generation of thin-films towards biosensing and Nps inks applications.

4.5.1   At-line colloid monitoring

At-line UV-vis monitoring should offer numerous process advantages when monitoring the state of the process in real-time. Its applications as a PAT tool could vary from on-line estimates of colloid concentration, indications of colloid quality, test for solvent and surfactant suitability, identify if the ablation is within control limits, determination of the impact of changing process conditions, and act as early fault diagnosis. To determine at-line UV-vis suitably to meet the requirement set out above, 60 min triplicate tests were carried out, measuring UV-vis spectra at-line. The result of an at-line optical analysis can be seen in Figure 4.23. The spectra are seen to be representative of SiNps; the absorbance is observed to increase with increasing processing time, indicating higher colloid concentrations.
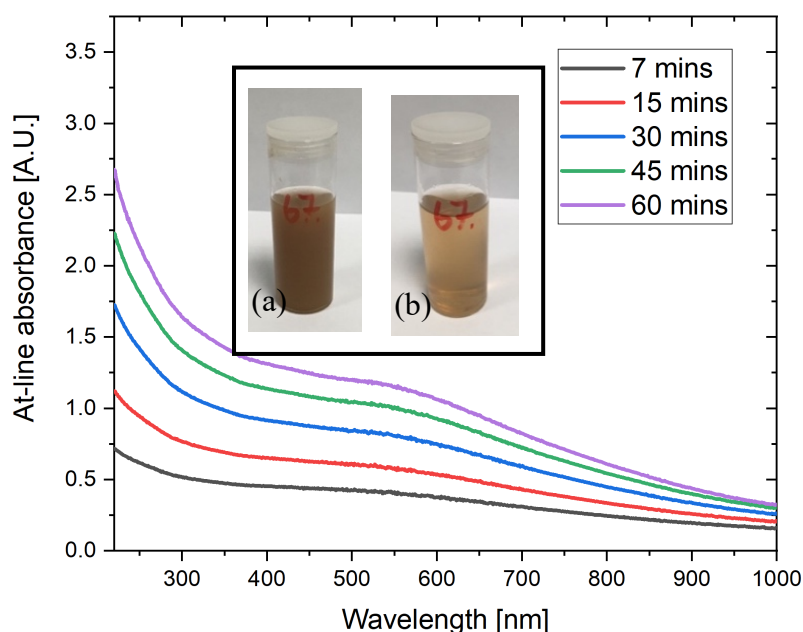
Figure 4.23: At-line UV-vis absorbance spectra for SiNps recirculation production (n=3), insert shows colloid produced after 60 mins, pre filtration and post filtration (0.2μ).

An example of 30 ml of 83 mg/L SiNps colloid pre and post-filtration is displayed in Figure 4.23 (a & b). The prefiltered colloid is cloudy, indicating the presence of macro-particles, possibility due to thermal effects on the target, where the ablation threshold is lowered, and larger particles formed. The UV-vis absorbance at 400 nm was employed to represent SiNps concentration as that wavelength possesses the lowest absorption coefficient for DI water [5]. Therefore, any absorption increase should be due solely to SiNps. An absorbance estimate based on the off-line linear fit of gravimetrical concentration data developed in Figure 4.22 was employed for the triplicate at-line tests, the process results are shown in

Table 4.3, where a low process variation is observed and an estimate of in-process concentration developed.

Table 4.3 At-line UV-vis absorption summary for triplicate semi-batch production tests, final concentration measured gravimetrically - 0.9 mg/ml (n=3)

Time	Mean absorbance	SD	Mean predicted concentration	SD
[Mins]	[A.U]	[A.U.]	[mg/ml] *	[mg/ml]
7	0.4558	0.0094	0.0273	0.0007
15	0.6563	0.0087	0.0419	0.0006
30	0.9141	0.0065	0.0606	0.0005
45	1.1242	0.0127	0.0758	0.0009
60	1.2958	0.0023	0.0883	0.0002

A selected at-line DLS measurement taken at the end of a 15 min semi-batch ablation is shown in Figure 4.24, and compared with a 4 ml sample of the colloid analysed off-line, pre and post-filtration. The at-line measurement is bi-modal with peak 1 at 72.9 nm ± 40 nm (65% of *vol.*) and peak 2 at 198 nm ± 94 nm (35% of vol.), whereas both off-line samples are unimodal with off-line peak at 70 nm ± 32 nm and filtered at 53 nm ± 22 nm. The at-line results indicate that macro-particle formation is taking place in the process, this is not seen in the off-line measurements, possibility due to the time-delay allowing large particle sedimentation to take place. The macro-particle peak displayed in the at-line measurement may not contribute to 35% of the population volume as described by the DLS data, as with the heterodyne measurement process it is usual for larger particles to mask smaller ones and in doing so, the instrument reports a larger size population weighting [44].
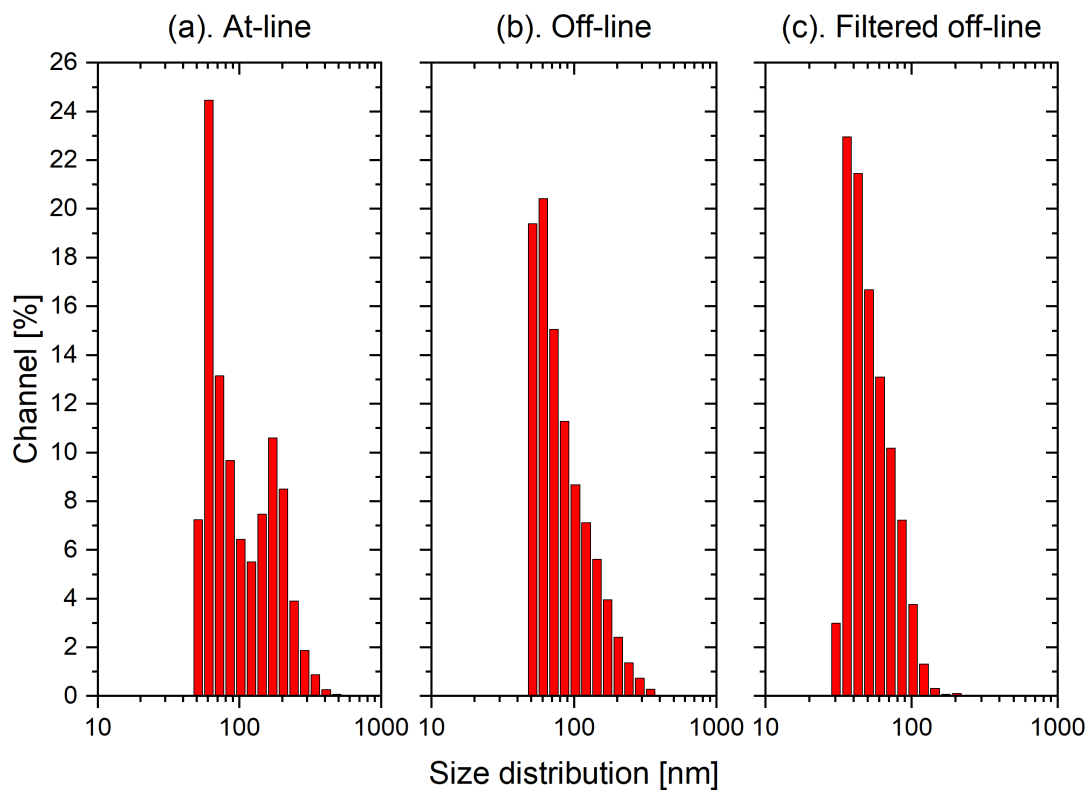
Figure 4.24: DLS measurements of SiNPs in DI water after 15 minutes of recirculation production (a) at line, (b) off-line, and (c) filtered off-line.

The primary peak at 70 nm is seen in all measurements and validated by TEM imaging seen in *Figure 4.25* (15-minute semi-batch ablation). The image was analysed using ImageJ software [45], the peak diameter was observed at 70 nm ± 90 nm (Full-width-half-max), this is slightly higher than that of the filtered off-line DLS measurement, due to the difference in measurement techniques and the DLS analysis would sample a larger representative colloid volume.
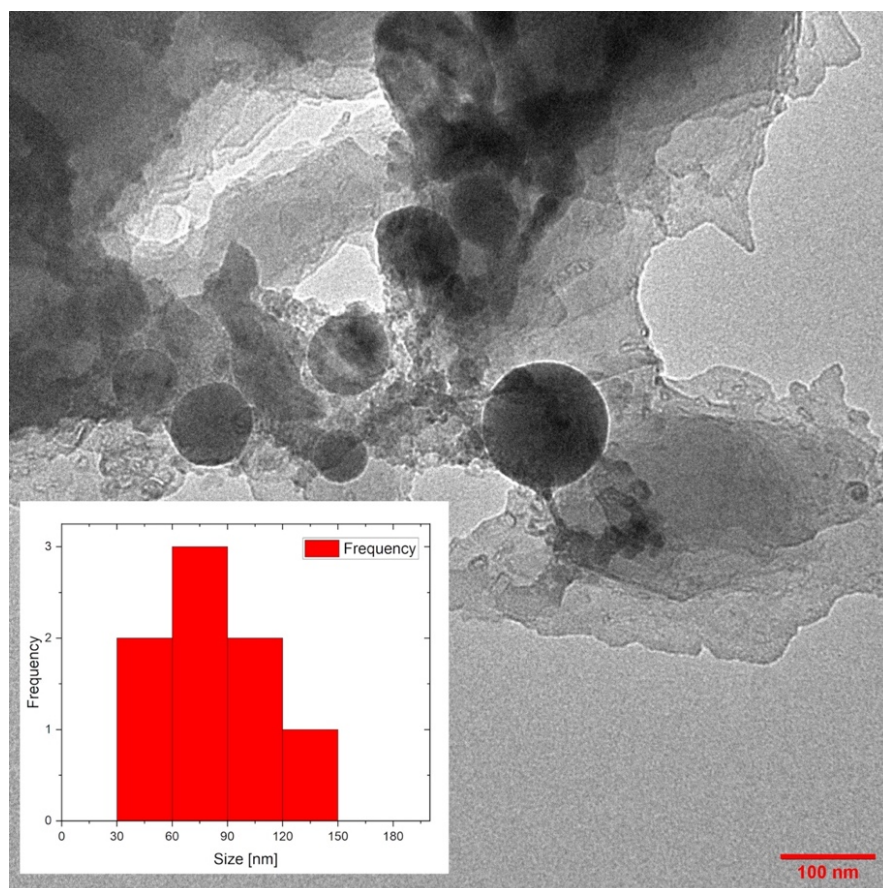
Figure 4.25: TEM analysis of LASiS produced SiNps (recirculation mode).

4.6   Validation of Process analytical technology (PAT)

4.6.1   At-line UV-vis spectroscopy validation

UV-vis spectroscopy is a common nano-colloid optical characterisation method, performed in the majority of the LASiS literature discussing colloid quality. In this work the application of an at-line measurement approach is discussed. Now the efficiency of its measurement against a larger data set (n=27) is examined, covering different operational modes (semi-batch/continuous) and colloid concentrations. The at-line measurement is compared with the standard off-line approach. A linear correlation between at-line measurement and off-line was observed with an adjusted R^2 of 0.993. There was a slight offset of 0.00089 A.U., explained by the difference in the quartz flow cell compared with the cuvette. The absorbance slope displayed almost parity of measurement (1.070). A 90% confidence interval of the predication (at-line) was applied to the linear fit. All at-line measurements are

deemed to be in control and representative of the off-line, falling within the 90% confidence interval (t-*distribution*) of the linear fit.
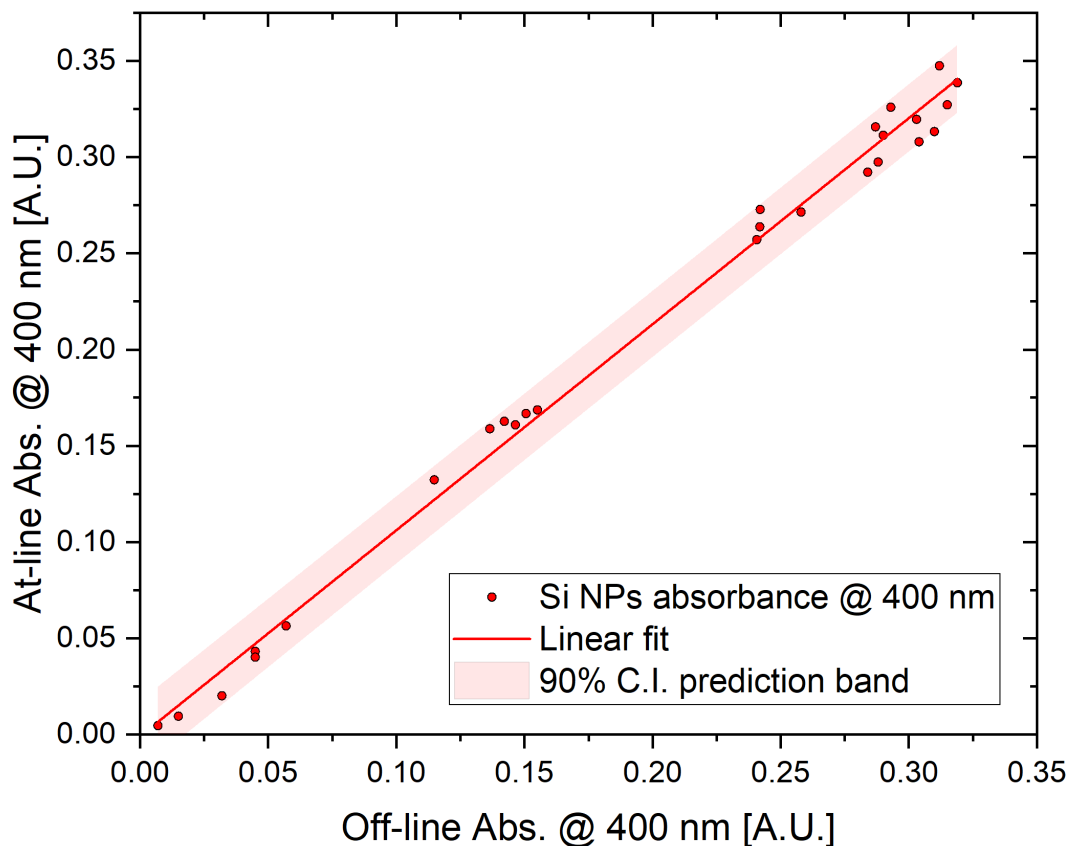
Figure 4.26: Plot of at-line vs off-line UV-vis measurements for a data set (n=27), adjusted R^2= 0.993, offset = 0.00089, slope = 1.070 (t-dist.).

4.6.1.1   At-line DLS validation

To validate the at-line DLS process monitoring, a series of semi-batch experiments illustrated in Figure 4.22 were implemented with at-line DLS measurement performed after laser irradiation was complete, allowing comparison of at-line, off-line and filtered measurements. The result of the peak diameter process means is displayed in Figure 4.27, where a 1σ overlap of at-line and off-line is observed. A student t-test performed on the data showed with a 90% confidence level, the at-line and off-line means showed no significant difference (standard error on the mean = 8 nm). Consequently, using the null hypothesis, it can be assumed that at-line size analysis can be implemented and is representative of the conventional off-line DLS analysis.
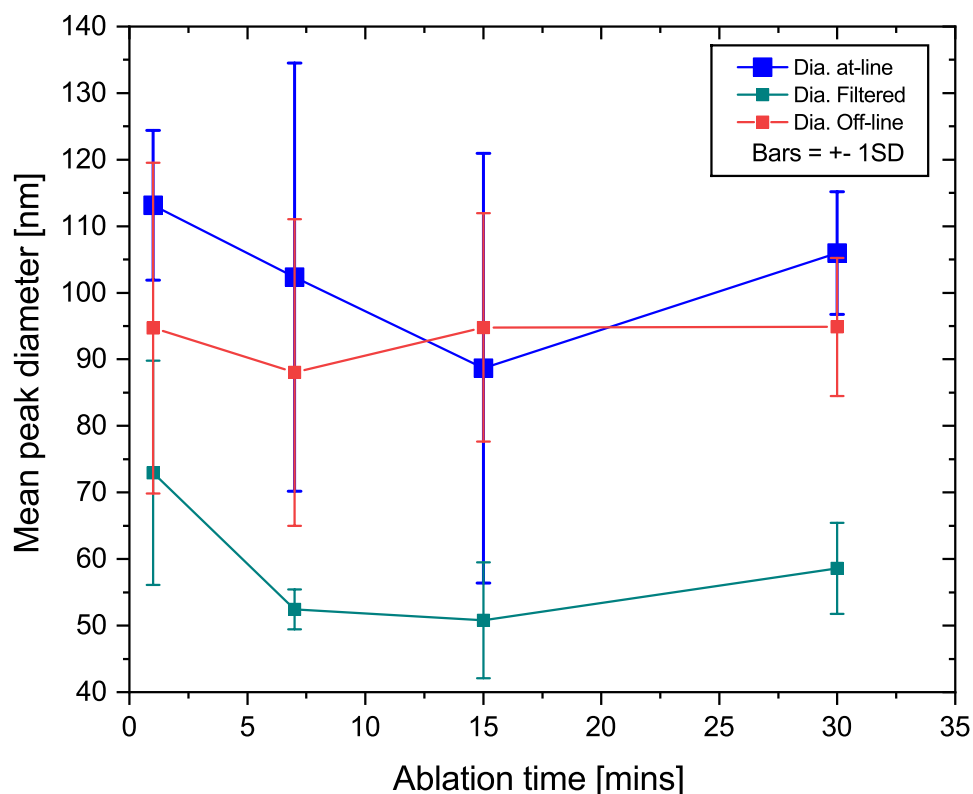
Figure 4.27: DLS peak diameter measured at-line, off-line and off-line-filtered (0.2 microns). The bars signify ±1σ of mean peak diameter (n=3).

It should be noted that from the individual size distribution measurement in Figure 4.24 and the mean process data in Figure 4.27 the at-line measurement displays larger peak diameters compared with off-line, with the difference in measurement reducing after 7 mins. It is likely that during the initial Np production processes, a low concentration of larger Nps are produced that sediment prior to the off-line analysis, hence are only observed at-line.
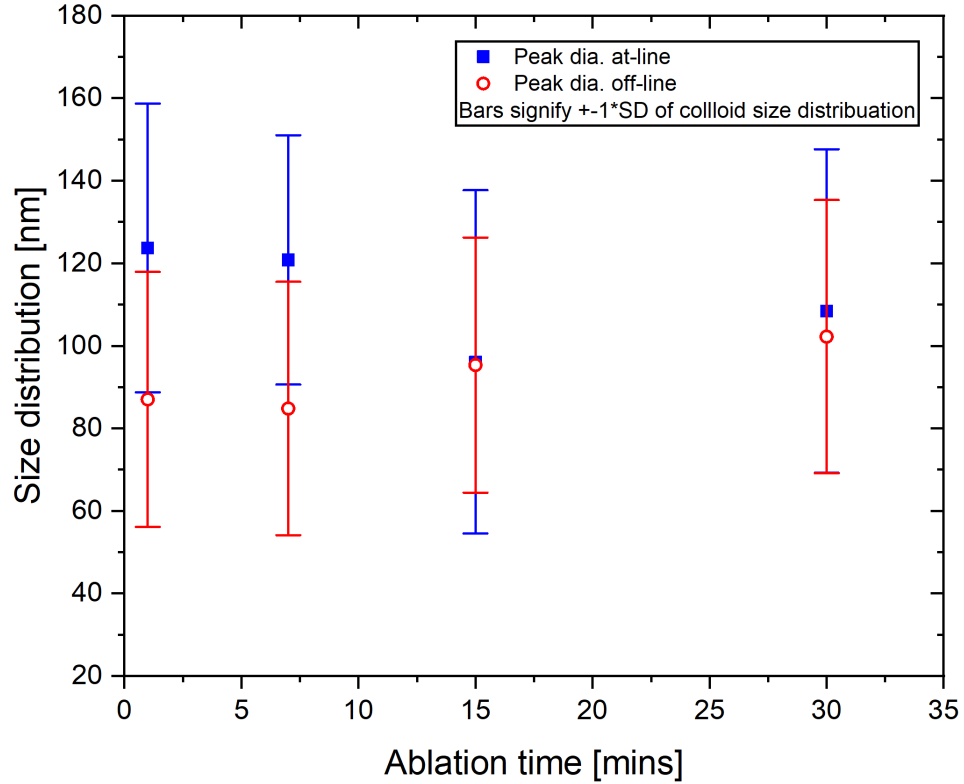
Figure 4.28: At-line and off-line DLS measurements of Nps peak diameters including size population width (±1σ) for ablation times.

4.6.1.2 At-line semi-batch size monitoring

To utilise the DLS as an at-line monitoring tool, 60-minute triplicate tests were performed monitoring the SiNps size at-line, beginning at 7 mins ablation. The individual colloid peak diameter and distribution width (2σ) is illustrated in Figure 4.29, and plotted alongside the process mean ($\bar{x}$=103 nm) and process standard deviation (Σ=24 nm), for the three runs. For the tests the peak diameters are largely within 1σ of the process mean for the majority of measurements taken, indicating that the ablation process is in control. However, a process change is indicated at the 15 – 30 minute ablation time, where the peak diameters approach or cross the 1σ control limit. This process change may be due to thermal effects on the target or colloid settling taking place. Lower concentration colloids may also be more susceptible to machine vibrations interfering with the measurement. Nanoparticle size has been previously seen to be a function of laser fluence [46] and pulse overlap [47] as the laser conditions remained constant for the tests performed and the resultant peak diameter stayed within 1σ from the mean it can be assumed that there was no significant change in the process conditions during the test.
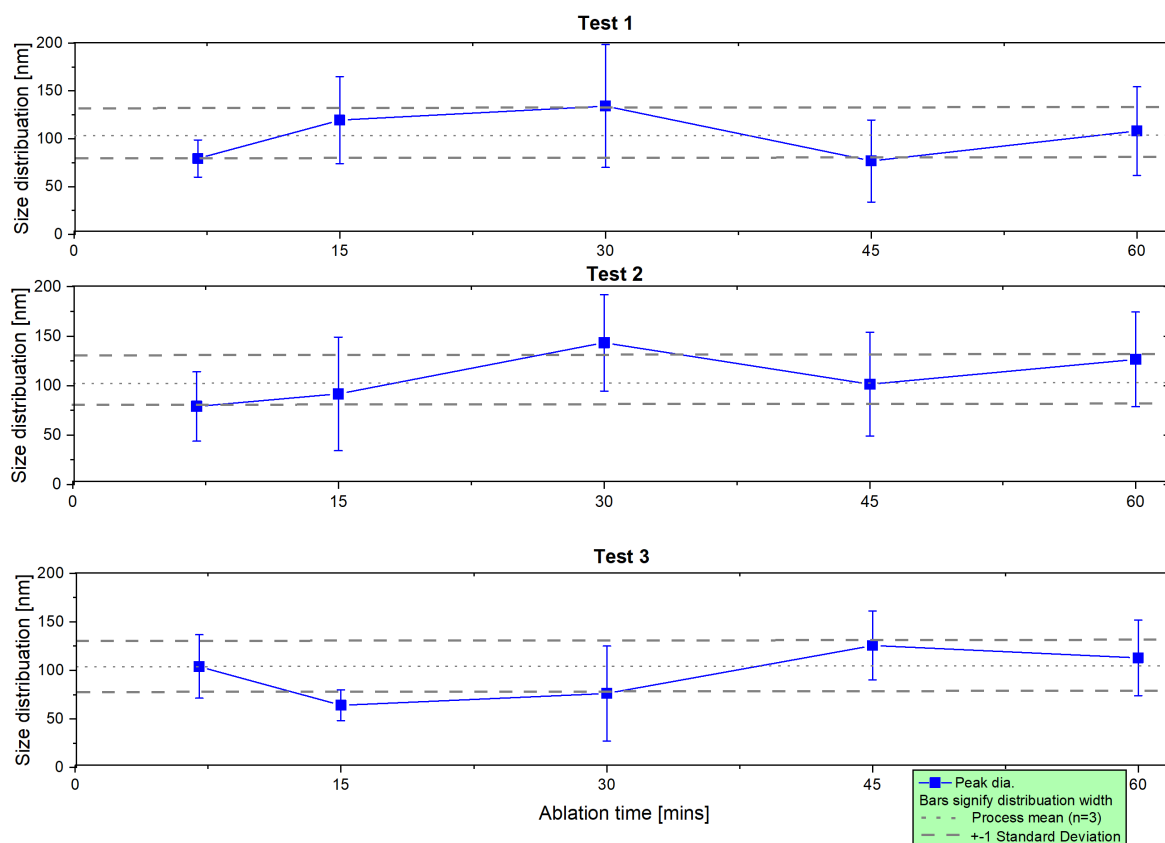
Figure 4.29: At-line DLS measurement of Nps size distribution (±1) for recirculation production up to 60 minutes, (DLS measurement, n=3).

Given that the process recirculates the Nps colloid within the flow cell, the possibility of photofragmentation should be considered, however a trend of size reduction with time is not observed. This observation is in alignment with the hypothesis that minimal photofragmentation of the SiNps should occur under 1064nm irradiation [23], [48] as SiNps excitation is relatively low at the fundamental wavelength when compared with, for example a 532nm [36] where the absorption coefficient is two orders of magnitude greater. This analysis demonstrates that Si colloids can be manufactured to repeatable size distributions independent of colloid concentration and process time. As discussed previously it is expected that the at-line measurements will measure slightly higher than off-line measurement, but the at-line monitoring can prove a useful insight into the process, and in the future could act as the primary colloid validation step.

4.7 Conclusions

With increasing advances in nanoparticle applications in biosensing and biotherapeutics, nanotechnology is fast becoming a significant research tool for biological and medical fields. For interdisciplinary research to adopt laser-based production as their chosen nanoparticle production technique, the LASiS community must make strives to compete with chemical synthesis in terms of productivity while taking advantage of LASiS benefits in terms of "green-synthesis" and single-step functionalization.

To improve nanoparticle fabrication productivity, this work has focused on implementing highly efficient Nps production. Rapid prototyping was implemented to produce a laminar flow environment, that successfully removed occluding material from the ablation site, offering best-in-class productivity for Gold nanoparticles published to date.

A secondary component to aid the adoption of LASiS by other research fields is to reduce the operational complexity of the nanoparticle production process and apply PAT tools to offer in-situ nanoparticle characterisation. To this end, a user-friendly software platform was developed, allowing manual and fully automated scheduled production. The software offered direct control over the production and monitoring tools, providing flexibility for an expert user and automated nanoparticle production for standard processes.

Two commercially available monitoring tools were integrated into the production system and tested under several production conditions for silicon nanoparticle production. It was seen that UV-vis spectroscopy could monitor the colloid effectively in continuous mode under flow conditions up to 170 ml/min. It was shown that colloid concentration can be altered by solvent flow in continuous mode or by production time in semi-batch mode. For the first time in a laser-based Np production process, at-line dynamic light scattering monitoring was implemented successfully. It was determined to offer comparative and statistically similar measurements compared with off-line monitoring and provided a new insight into the production process. This provided an option in the future for testing Np stability with solvent and surfactant suitability during processing. This initial work points to a promising future for the adoption of the LASiS techniques across several research fields.

4.8   References

[1]   E. Bagheri *et al.*, "Silica based hybrid materials for drug delivery and bioimaging," *J. Control. Release*, vol. 277, pp. 57–76, 2018.

[2]   F. Fathi, M.-R. Rashidi, and Y. Omidi, "Talanta Ultra-sensitive detection by metal nanoparticles-mediated enhanced SPR biosensors," *Talanta*, vol. 192, no. September 2018, pp. 118–127, 2018.

[3]   A. Silva, M. Amaral, J. Sousa Lobo, and C. Lopes, "Lipid Nanoparticles for the Delivery of Biopharmaceuticals," *Curr. Pharm. Biotechnol.*, vol. 16, no. 999, pp. 1–1, 2016.

[4]   C. Rehbock *et al.*, "Current state of laser synthesis of metal and alloy nanoparticles as ligand-free reference materials for nano-toxicological assays," *Beilstein J. Nanotechnol.*, vol. 5, no. 1, pp. 1523–1541, 2014.

[5]   M. Vasiliev and K. Alameh, "Photonic nano-structures for water quality monitoring," *19th Int. Conf. Opt. Fibre Sensors*, vol. 7004, no. April, p. 70045E, 2008.

[6]   V. M. Petriev *et al.*, "Nuclear nanomedicine using Si nanoparticles as safe and effective carriers of 188 Re radionuclide for cancer therapy," *Sci. Rep.*, vol. 9, no. 1, pp. 1–10, 2019.

[7]   A. S.D. *et al.*, "Electrophoretic deposition of ligand-free platinum nanoparticles on neural electrodes affects their impedance in vitro and in vivo with no negative effect on reactive gliosis," *J. Nanobiotechnology*, vol. 14, no. 1, pp. 1–11, 2016.

[8]   D. A. Mahvi, R. Liu, M. W. Grinstaff, Y. L. Colson, and C. P. Raut, "Local Cancer Recurrence : The Realities , Challenges , and Opportunities for New Therapies," pp. 488–505, 2018.

[9]   C. for D. E. and Research, "About the Center for Drug Evaluation and Research - OPS Process Analytical Technology - (PAT) Initiative," no. September, 2004.

[10]   S. Jendrzej, B. Gökce, M. Epple, and S. Barcikowski, "How Size Determines the Value of Gold: Economic Aspects of Wet Chemical and Laser-Based Metal Colloid Synthesis," *ChemPhysChem*, vol. 18, no. 9, pp. 1012–1019, 2017.

[11]   K. Bagga *et al.*, "Nanoparticle functionalized laser patterned substrate: an innovative route towards low cost biomimetic platforms," *RSC Adv.*, vol. 7, no. 13, pp. 8060–8069, 2017.

[12]   K. Bagga *et al.*, "Laser-assisted synthesis of ultrapure nanostructures for biological sensing applications," in *Proceedings of SPIE*, Sep. 2016, p. 99280O, doi:

10.1117/12.2237147.

[13] FDA, "Guidance for Industry Process Validation : General Principles and Practices Guidance for Industry Process Validation : General Principles and Practices," 2011.

[14] D. Cenide, R. Streubel, N. Bärsch, and S. Barcikowski, "Advanced liquid flow reactor design for laser ablation in liquid Motivation : Task : Continuous Fabrication of Nanoparticles State of the art : Stationary ablation Task : Properties : Production Chamber : Laser Bio-conjugation Chamber," vol. 115, no. May, pp. 6–7, 2012.

[15] S. Dittrich, R. Streubel, C. McDonnell, H. P. Huber, S. Barcikowski, and B. Gökce, "Comparison of the productivity and ablation efficiency of different laser classes for laser ablation of gold in water and air," *Appl. Phys. A Mater. Sci. Process.*, vol. 125, no. 6, pp. 1–10, 2019.

[16] R. Streubel, G. Bendt, and B. Gökce, "Pilot-scale synthesis of metal nanoparticles by high-speed pulsed laser ablation in liquids," *Nanotechnology*, vol. 27, no. 20, 2016.

[17] R. Streubel, S. Barcikowski, and B. Gökce, "Continuous multigram nanoparticle synthesis by high-power, high-repetition-rate ultrafast laser ablation in liquids," *Opt. Lett.*, vol. 41, no. 7, p. 1486, 2016.

[18] S. Crivellaro, A. Guadagnini, D. M. Arboleda, D. Schinca, and V. Amendola, "A system for the synthesis of nanoparticles by laser ablation in liquid that is remotely controlled with PC or smartphone," *Rev. Sci. Instrum.*, vol. 90, no. 3, 2019.

[19] P. E. Hopkins, J. C. Duda, B. Kaehr, X. W. Zhou, C. Y. Peter Yang, and R. E. Jones, "Ultrafast and steady-state laser heating effects on electron relaxation and phonon coupling mechanisms in thin gold films," *Appl. Phys. Lett.*, vol. 103, no. 21, pp. 0–5, 2013.

[20] P. Wagener, A. Schwenke, B. N. Chichkov, and S. Barcikowski, "Pulsed laser ablation of zinc in tetrahydrofuran: Bypassing the cavitation bubble," *J. Phys. Chem. C*, vol. 114, no. 17, pp. 7618–7625, 2010.

[21] S. Barcikowski and F. Mafuné, "Trends and current topics in the field of laser ablation and nanoparticle generation in liquids," *J. Phys. Chem. C*, vol. 115, no. 12, p. 4985, 2011.

[22] S. Barcikowski *et al.*, "Handbook of Laser Synthesis of Colloids," 2016.

[23] S. Barcikowski, V. Amendola, G. Marzun, and C. Rehbock, "Handbook of Laser Sintheshis," no. April, 2016.

[24] Stratasys Polyjet Technology, "VeroWhite Plus Datasheet," p. 2015, 2016.

[25]   Dupont, "Teflon PTFE," *Prop. Handb.*, pp. 1–38, 1996.

[26]   W. Boyes, *Instrumentation Reference Book (Fourth Edition)*, 4th ed. Butterworth-Heinemann, 2010.

[27]   P. A. Blume, U. S. River, N. J. Boston, and I. San, "Colorr G aller y."

[28]   D. Guidelines, "Development Guidelines," no. 321393, 2003.

[29]   P. E. Plantz, "Explanation of Data Reported by Microtrac Instruments," *Microtrac Appl. Note*, pp. 1–7, 2008.

[30]   S. M. Haidary, E. P. Córcoles, and N. K. Ali, "Nanoporous silicon as drug delivery systems for cancer therapies," *J. Nanomater.*, vol. 2012, 2012.

[31]   K. Bagga *et al.*, "Laser-assisted synthesis of ultrapure nanostructures for biological sensing applications," in *Proceedings of SPIE*, Sep. 2016, p. 99280O, doi: 10.1117/12.2237147.

[32]   P. Wagener *et al.*, "High productive and continuous nanoparticle fabrication by laser ablation of a wire-target in a liquid jet," *Appl. Surf. Sci.*, vol. 403, pp. 487–499, 2017.

[33]   M. N. Polyanskiy, "Refractive index database." .

[34]   D. Zhang, B. Gökce, and S. Barcikowski, "Laser Synthesis and Processing of Colloids: Fundamentals and Applications," *Chem. Rev.*, vol. 117, no. 5, pp. 3990–4103, 2017.

[35]   S. I. Kudryashov *et al.*, "Nanosecond-laser generation of nanoparticles in liquids: From ablation through bubble dynamics to nanoparticle yield," *Materials (Basel).*, vol. 12, no. 2, pp. 1–15, 2019.

[36]   A. A. Brand, F. Meyer, J. F. Nekarda, and R. Preu, "Reduction of picosecond laser ablation threshold and damage via nanosecond pre-pulse for removal of dielectric layers on silicon solar cells," *Appl. Phys. A Mater. Sci. Process.*, vol. 117, no. 1, pp. 237–241, 2014.

[37]   J. Thorstensen and S. Erik Foss, "Temperature dependent ablation threshold in silicon using ultrashort laser pulses," *J. Appl. Phys.*, vol. 112, no. 10, 2012.

[38]   S. Barcikowski, B. Gökce, and G. Marzun, "Process-stable , highly pure nanomaterials for energy research made by scalable , continuous laser production," vol. 3022, no. 2013, p. 11928, 2016.

[39]   S. Reich *et al.*, "Pulsed laser ablation in liquids: Impact of the bubble dynamics on particle formation," *J. Colloid Interface Sci.*, vol. 489, pp. 106–113, 2017.

[40]   R. Intartaglia *et al.*, "Optical properties of femtosecond laser-synthesized silicon

nanoparticles in deionized water," *J. Phys. Chem. C*, vol. 115, no. 12, pp. 5102–5107, 2011.

[41]   R. Intartaglia *et al.*, "Bioconjugated silicon quantum dots from one-step green synthesis," *Nanoscale*, vol. 4, no. 4, pp. 1271–1274, 2012.

[42]   S. Link and M. A. El-Sayed, "Size and temperature dependence of the plasmon absorption of colloidal gold nanoparticles," *J. Phys. Chem. B*, vol. 103, no. 21, pp. 4212–4217, 1999.

[43]   H. Kobayashi, P. Chewchinda, H. Ohtani, O. Odawara, and H. Wada, "Effects of Laser Energy Density on Silicon Nanoparticles Produced Using Laser Ablation in Liquid," *J. Phys. Conf. Ser.*, vol. 441, p. 012035, 2013.

[44]   E. Tomaszewska *et al.*, "Detection limits of DLS and UV-Vis spectroscopy in characterization of polydisperse nanoparticles colloids," *J. Nanomater.*, vol. 2013, 2013.

[45]   C. A. Schneider, W. S. Rasband, and K. W. Eliceiri, "NIH Image to ImageJ: 25 years of image analysis," *Nat. Methods*, vol. 9, no. 7, pp. 671–675, 2012.

[46]   A. V. Kabashin and M. Meunier, "Synthesis of colloidal nanoparticles during femtosecond laser ablation of gold in water," *J. Appl. Phys.*, vol. 94, no. 12, pp. 7941–7943, 2003.

[47]   S. Barcikowski, A. Hahn, A. V. Kabashin, and B. N. Chichkov, "Properties of nanoparticles generated during femtosecond laser machining in air and water," *Appl. Phys. A Mater. Sci. Process.*, vol. 87, no. 1, pp. 47–55, 2007.

[48]   R. Intartaglia, K. Bagga, and F. Brandi, "Study on the productivity of silicon nanoparticles by picosecond laser ablation in water: towards gram per hour yield.," *Opt. Express*, vol. 22, no. 3, p. 3117, 2014.

Chapter 5:   High efficiency nanoparticle production via liquid flow optimization

5.1   Introduction

This chapter builds on the rig developed in chapter 4, now focusing on understanding how process parameters affect ablation efficiency and determining ways of maximising ablation rates and Np yield. Particular attention is taken towards liquid conditions including solvent flowrate and pressure within the flow cell. Silicon is the chosen target material as in chapter 4. Prior to performance testing, a method to define Np production process efficiency from the literature is introduced. This efficiency grading allows the experimental laser system used in this work to be placed within power and efficiency categories agreed in the literature, allowing for the experimental process developed to be compared with "best in class" production rates published to date [1].

There is a high complexity in the mechanisms involved for Np formation within liquids. The process depends on interactions between the laser parameters on the target materials, the resultant plasma interaction in the liquid environment, followed by the interactions between the cavitation bubble with the liquid environment and the next laser pulse [2], [3]. The nano and meso particles formed during each pulse can have significant impact on the subsequent laser pulses; absorbing and deflecting laser energy aided by photo-fragmentation [4], [5] and occlusion. Secondary effects such as the resultant shockwaves produced interact with plasma production and bubble collapse [6]. Target surface topology, liquid conditions and material transition layers (liquid-air/ liquid-glass-air) can all affect Np production by diffracting the beam. Also significant are transient effects including plasma lifetime and cavitation bubble life-cycle interaction with the liquid and target [6]–[8]. It is clear that this is a highly complex and difficult-to-model process with several interacting process variables. In recent times steps have been taken to develop highly complex computer-based molecular models [9],[10],[11],[12] to understand the underlying mechanisms in more detail. However to date, the field has been relying primarily on experimental results from high-speed imaging [13]–[16] such as temporally resolved shadowgraphy [17]. Shadowgraphy has imaged the

resultant plasma from laser irradiation in liquids, along with the lifecycle of the cavitation bubble, its interaction with liquid and the solid target and output of Nps. The responses of the cavitation bubble to varied process conditions has been reported, these include changes to laser parameters, material properties and environmental fluid conditions [2].

As a precursor to experimental performance studies, a SiNps LASiS production model based on work by Intartaglia et al. (2014) is adapted. The goal of applying the model is two-fold; firstly to help understanding of the experimental data by relating known laser mechanisms and parameters to the experimental results studied in this chapter. And secondly, to enable prediction of laser power requirements for pilot scale SiNps production. The model is altered to better represent a micro-machining laser system operating under continous Np production. The existing model, while cited widely [18]–[21] suffers from overestimating productivity capabilities due to a very large extrapolation from its experimetal fit data, which was performed at very low productivities and colloid concentrations within a batch production mode. The new model developed is proposed to offer better prediction for pilot scale LASiS production compared with litrature.

5.1.1 Categorisation and comparison of Nanoparticle fabrication productivity

In order to determine the effectiveness of the Np production system it should be compared against the reported best-in-class. A problem arises of how to compare production efficiencies from lasers systems of varying costs and output powers. The field has determined power-specific productivity (mg/Wh) as the best method to compare laser systems. The metric is based on a gravimetrical measurement of the total amount of ablated target material, it assumes 100% of the ablated material is converted to nanoparticles. This metric assumes that laser power is in general linked to capital costs, and indeed running costs of the system [6], as discussed in chapter 2. Hence it is also useful for assessing the commercial viability of each process. However, the metric has limitations as a comparison tool as an ultra-low power (sub 0.5W) laser system could achieve high power-specific productivity but produce a very low, and non-scalable quantity of Nps. To combat this, Ditterch et al. [1] proposed categorizing laser systems into different power groups. They discussed three average output power classes that laser system should fall into, as described in Table 5.1.

Table 5.1: Comparison of the experimental laser systems parameters with the laser classes defined by *Ditterch et al (2019).

Description	Unit	Compact class CryLaS DSS-1064-Q4	Middle class Rofin Powerline E20	High-end class Amphos flex 500	Experimental system Bright solutions Wedge HF 1064
Wavelength	[nm]	1064	1064	1030	1064
Average max power	[W]	0.15	<10	500	<6
Max pulse energy	[µJ]	128	403	100	250
Pulse duration	[ps]	1k	5k-10k	3	500 – 3,000
Repetition rate	[Hz]	1-1.2k	20 - 200k	$(1.2\text{-}40)$ $\times10^6$	10k - 100k
Spot diameter	[µm]	61	70	148	101
Fluid flowrate	[ml/min]	5	5	510	15 - 140

The pulse energies and wavelengths of each system selected were similar, with average power output offering the difference in laser class. Power ranges started at 0.15 W for the compact class to <10W for the medium class and 500 W for the high-end class. The laser system used for the productivity testing falls within the medium class with an average output power of <6W. There are still concerns when using the productivity metric as a neutral comparison between systems given that the ablation test time is not defined. It has been suggested that under continuous flow conditions productivity will remain constant with time [7], but the process may take several minutes to reach steady state [22] and ablation mass measurements from tests of several seconds may not scale well to production runs. Best-fit models were used to extrapolate productivity from 10s tests by Ditterch et al. (2019). Rather than gravimetrical measurements, these productivities achieved during a test of several seconds in duration may not scale to several minutes or hours of production. Many factors may affect the long-term operation of an ablation process and its steady-state operation such as laser power fluctuation [22], target heating [23], bubble formation, bubble trapping in the flow cell [7], [24], [25], inconsistent fluid flow and varying target beam waist position [6]. These factors may contribute to the fact that several power specific productivities reported are conducted for production tests less than 1 minute in duration.

5.1.2   *State of the art production*

As LASiS is a relatively new technique, still in the development phase, the majority of publications on the topic surround the properties and functionality of the nanomaterials produced, rather than focusing on productivity of fabrication. Thus, the field is lacking in productivity research data, or at very least in publishing the productivity rates achieved under testing. Lab-scale nanomaterial characterization such as TEM and XPS require low quantities of colloids for characterization (< 1 mg/ml concentrations), compared with larger quantities utilized in commercial material production of catalysts, inks [26]–[29] and solar panels [30], [31]. Generally, the LASiS processes reported in the literature operate for time periods from seconds to minutes, typically producing low volumes of Np colloids. These processes are not representative of a production process capable of meeting industry demands. These short, low productivity ablation processes are typically performed in batch-mode and are not configured to handle target surface temperature increases [23], bubble accumulation, colloid saturation and supply of fresh solvent, problems that need to be addressed for pilot-scale manufacture [6], [7], [22].

However, in the last five years, as nanomaterials have found more applications, there has been a marked increase in interest towards LASiS production optimisation. Consistent developments have been made as documented in the Table 5.2, which reports the highest yields (production rate) to date, almost all under liquid flow conditions. Under this development, there has been a goal of progressing the technique towards cost-parity with chemical synthesis, as discussed in the literature review in chapter 2. The highest production efficiency published to date was obtained by Ditterch et al., (2019) utilising a low-power compact class system ablating a solid gold target mounted in a flow cell. They achieved high efficiencies by spatially bypassing the cavitation bubble using high-speed beam rastering. However, as discussed previously, both the test times conducted, and colloid quantities produced were very low when compared with requirements of a scaled process.

The highest productivity yields have been reported using gold targets in DI water [1], [32] under continuous liquid flow. The highest productivity found using time periods that could relate to a production process was achieved by Streubel et al. (2016), with a ablation time of 15 minutes. They obtained a production efficiency of 16.9 mg/Wh using a 1D gold wire target [32] fed into a liquid stream under high power laser irradiation (32 W). Silver has also

141

developed as a chosen "high productivity" material [33], [34]. The highest production efficiencies reported for silicon is 3.63 mg/Wh, being observed in batch mode using a high powered 1070 nm $Yb^{3}+$ fibre laser system producing pulse energies of 1 mJ at 20 kHz RR. In that work the authors suggest more productivity increases would be possible with the application of liquid flow and laser optimisation. However, the productivity stated is extrapolated from an ablation rate determined by a single pulse. Therefore this result should be taken with caution to scale towards hour-long productivity values.

From Table 5.2, it can be seen that large production and efficiency increases are yielded from using high-power laser systems. High pulse energies (>1mJ)[35] applied on target material yield exponential ablated mass responses [18], [24], [25], compared with a linear ablation response from lower pulse energies [5]. High pulse energies utilise mechanisms such as a phase explosion at the ablation site [36], [37] along with additional effects such as material heating, lowering the fluence threshold [23], and pulse interactions with the cavitation bubble collapse, directing more energy back into the material compared with low pulse energies [24], [25]. All these factors combine to suggest that the primary route towards an efficiency-scalable LASiS production process is to apply a high-end laser system and benefit from this exponential productivity response to energy. However, this work strives to investigate the possibility of using a medium-class laser system and low pulse energies (in terms of micro-machining) that will not promote that exponential ablation response, but by utilising flow conditions to produce a more efficient and scalable LASiS process. It is the author's view that the route towards cost-parity with chemical synthesis is not just a matter of using higher power ablation, and as a consequence higher cost laser system to yield higher quantities of Np, but to combine middle-class laser systems with high-efficiency flow environments, thus reducing the capital cost which is a major contributing factor towards the expense of LASiS production.

Table 5.2: Current state-of-the-art LASiS production efficiencies reported using continuous flow systems for a range of common materials, ranked in terms of power specific productivity.

Target	Laser system	Laser system class [1]	Process time (mins)	Productivity (mg/h)	Power specific productivity (mg/Wh)	Year	Ref
Au	1064 nm, 0.15 W, 1.2 kHz, 1000 ps	Compact	0.17	6.12	42.5	2019	[1]
AI_2O_3	1047 nm, 70 W, 15kHz, 20 ns	High-end	5	600	31.5	2010	[25]
Au	1064 nm, 5kHz, 32 W, 10 ns	High-end	15	550	16.9	2017	[32]
Au	1030 nm, 5MHz, 500 W, 3 ps	High-end	0.17	5760	14	2019	[1]
Ag	1064 nm, 100Hz, 25 W, 10 ns	High-end	-	317	12.7	2013	[33]
Au	1064 nm, 5 W, 15kHHz, 5k ps	Middle	0.17	39.6	6.5	2019	[1]
Ag	1030nm, 10MHz, 500W, 3ps	High-end	60	1900	3.8	2016	[34]
Si	1070nm Yb^3+ fiber, E_0=1 mJ, 120 ns, 20kHz, 20 W	High-end laser. Batch mode. Extrapolation based on single pulse, 120 ns.		72	3.6	2018	[35]

5.1.3 Silicon ablation prediction model

In terms of planning for Np production scale-up, a representative model of the process would be beneficial in estimating the laser power required for large scale production and also help to identify the underlying effects seen in experimental data. To date several deterministic and statistical models have been developed to estimate Nps ablation rates [6], [38],[5], [39]. Intartaglia et al. (2014) developed a model to calculate maximum possible SiNp productivity (Yield$_{max}$) for a 1064 nm picosecond laser system similar to that used in this work. Due to its target material and laser system applicability, this model was chosen for further investigation and development. The model developed by Intartaglia et al. (2014) is described as follows:

$$Productivity_{max} = (1.7 \times 10^{-5}) \times E_0 \times RR \text{ , [g/s]} \qquad \text{(Eq. 5.1.)}$$

Where the laser Nps productivity was found to be a function of a new ablation efficiency coefficient (η) determined to be 1.7 x 10^{-5} g J^{-1}, the laser pulse energy (E$_0$) and the laser repetition rate (RR). η was derived from a logarithmic fit of experimental data based the following equation:

$$\eta = (\rho \times k)/(e \times F_{th}^{app}) \text{, [g/J]} \qquad \text{(Eq. 5.2)}$$

Eq. 5.2 included the material bulk density (ρ) and Eulers constant (e). The "apparent fluence threshold" (F$_{th}$^{app}) and the laser energy penetration depth (k) were determined experimentally from batch LASiS testing. k is understood to account for the absorption depth of the laser energy into the bulk target material, including the thermal diffusion distance (D$_{th}$) into that material, which is a function of the thermal diffusivity (D$_i$) of the material (0.85 cm^2 s^{-1} for Si) and pulse the pulse duration;

$$D_{th} = 2\sqrt{D_i \times \tau_p} \qquad \text{(Eq. 5.2.b.) [40]}$$

Intartaglia *et al.* (2014) observed that there was a linear increase of ablated mass, proportional to the average laser power in the NIR range, while incorporating the presence of particle occlusion and photo-fragmentation into the model parameters. This linear assumption is in agreement with other articles published, generally in the range of fluences up to 3 J/cm^2 [24] and offers a good base to conservatively estimate possible ablation efficiencies from higher power laser systems. Their study produced Nps with a mean diameter of 42 nm using a 1064 nm laser with a pulse width of 60 ps, repetition rate of 20

Hz (which would have allowed for partial cavitation bubble temporal avoidance) with applying laser fluence up to 2.7 J/cm^2.

The laser pulse duration used in this model is similar to that of general ps machining laser systems, where electron-phonon coupling is taking place, ie. heating of the lattice structure in the material occurs as there is relaxation time between the pulses for electron-phonon coupling to take place. The electron-phonon response for silicon is below 2 ps. The authors predicted a potential productivity of 6 g/h SiNp using a 100 W laser system operating at 100 kHz RR. If this prediction was experimentally validated it would produce the highest yield reported to date.

Using Eq. 5.1 to solve for the experimental setup, assuming maximum fluence of 1.83 J/cm^2 and a repetition rate of 10 kHz, the expected maximum theoretical Np productivity would be 90 mg/h, with an efficiency of 61 mg/Wh. This is substantially higher than data published to date, and it's expected that the model overestimates production rates, as the experimentally fit parameters are developed based on experimental productivity of just 0.4 mg/h [5], requiring a large extrapolation [6]. Operating at such low productivity and colloid concentrations would mitigate several factors that limit productivity such as Np colloid masking effects, liquid breakdown, target heating plume occlusion and cavitation bubble occlusion, the latter being avoided by the low repetition rate employed in the work. This argument is confirmed by the low fluence threshold 0.18 J/cm^2 observed in the experimentation, which is significantly lower than those reported in other papers for silicon ablation threshold in air, 0.35 J/cm^2 for ps 1064nm YAG lasers [23]. These issues would indicate that currently the model is not suitable for prediction of medium-to-high through-put laser systems. Clearly η experimentally derived by Intartaglia *et al. is* overestimating the potential efficiency of a production-scale LASiS process. However, the model is a good starting point to develop a correlation for such applications.

5.1.3.1   *Model redevelopment*

In order to find new experimental values for η, F_{th} and k, the model must be redeveloped to reflect the experimental setup. An explanation of the model development follows. The expected ablated mass (M_a) per pulse is a function of the bulk material density (ρ), the laser beam cross sectional area (s) and the depth of material removed per pulse (T).

$$M_a = \rho \times s \times T \hspace{3cm} (Eq.\ 5.3.)$$

Assuming the absorbed energy into the bulk material reduces exponentially with distance from the material's surface, using the standard logarithmic ablation law for pulsed laser ablation a value for T can be found as follows;

$$T = k \times ln \left({F_t}/{F_{th}} \right) \qquad\qquad (Eq.\ 5.4.)\ [41]$$

where T is a function of the energy penetration depth (k), the applied fluence on the target in air (F_t) and material fluence threshold (F_{th}). Now using Eq. 5.3 and substituting in for T gives:

$$M_a = \rho \times s \times k \times ln \left({F_t}/{F_{th}} \right) \qquad\qquad (Eq.\ 5.5.)$$

Given that the pulsed ablation process is occurring on a target submerged in a liquid, we must take account of the energy absorbed by the liquid and the energy lost to the plume and particle occlusion. Therefore, we do not know the fluence applied to the target directly (F_t), but only the fluence provided by the laser (F_0). The fluence threshold of the material due to laser irradiation in air (F_{th}) is not useful for the model, but the "process" or "apparent" fluence threshold in the liquid environment (F_{th}^{app}) quantifies the reaction of the material to laser irradiation confined within a liquid. So, we substitute the fluence threshold of the material in air with the process threshold in liquid;

$$M_a = \rho \times s \times k \times ln \left({F_0}/{F_{th}^{app}} \right) \qquad\qquad (Eq.\ 5.6.)$$

Now, in order to ensure the model is useful for laser system prediction, the model needs to be laser system independent and scale linearly with pulse energy provided by the laser (E_0). Therefore, replacing s as follows;

$$F_0 = \frac{E_0}{s_0}, \qquad\qquad (Eq.\ 5.7.)$$

Now replacing for s in Eq. 5.6 with Eq. 5.7;

$$M_a = \rho \times \frac{E_0}{F_0} \times k \times ln \left({F_0}/{F_{th}^{app}} \right) \qquad\qquad (Eq.\ 5.8.)$$

Assuming maximum possible ablated mass, M_a is maximized following the natural log laws as follows;

$$y = \frac{ln(x)}{x}, y_{max} = \frac{1}{e} \qquad\qquad (Eq.\ 5.9.)$$

Rearranging for the maximum ablated mass;

$$M_a = \left(\frac{\rho \times k \times E_0}{F_0} \right) \times \left(\frac{F_0}{F_{th}^{app}} \right) \times \frac{ln\left({F_0}/{F_{th}^{app}} \right)}{\left(\frac{F_0}{F_{th}^{app}} \right)} \qquad\qquad (Eq.\ 5.10.)$$

Simplifying;

$$M_{a_{max}} = \frac{\rho \times k}{e \times F_{th}^{app}} \times E_0, \text{ [g]} \qquad\qquad (Eq.\ 5.11.)$$

Then providing a repetition rate-based prediction per hour;

$$M_{a_{max}} = \frac{\rho \times k}{e \times F_{th}^{app}} \times E_0 \times RR \times 3600, \text{ [g/h]} \qquad (Eq.\ 5.12.)$$

To make the model of practical use that would represent a scaled-up process better, we need to determine new correlations for k and F_{th}^{app}. The process fluence threshold may be found experimentally, assuming a linear correlation of fluence to ablated mass as discussed later and illustrated in Figure 5.1. The energy absorption depth (k) can be found by rearranging *Eq. 5.4* for the LASiS process as follows;

$$k = \frac{T}{ln\left(\frac{F_t}{F_{th}}\right)} \qquad\qquad (Eq.\ 5.13.)$$

F_t was decoupled from the k term by the division of an approximation of F_t using: $ln(F_0/F_{th}^{app})$ as an estimate [5], [41].

$$k = \frac{T}{ln\left(\frac{F_0}{F_{th}^{app}}\right)} \text{ (nm)} \qquad\qquad (Eq.\ 514.)$$

T can be determined experimentally, where A is the area of the ablation crater, as follows;

$$T = \frac{M_a}{\rho \times A}, \text{ (nm)} \qquad\qquad (Eq.\ 5.15.)$$

The model is based on a linear relationship of productivity with pulse energy and repetition rate, this relationship is not true in all cases. Under high pulse energies phase explosion may occur promoting exponential response to laser power [25], thus this model may offer a conservative estimate of productivity, useful when specifying laser requirements to meet specific productivity goals.

5.2   Materials and methods

The same ND: YAG 1064 laser system (WEDGE HF 1064) employed in chapter 4 is used for the development work in this chapter, along with the integrated Np production rig. Process variables used for the productivity tests is summarized in   Table 5.3, where the experimental system is directly compared with the middle class system described in [1]. The experimental system has a lower average laser power and pulse energy compared with the middle class system noted in [1] but operates at similar repetition rates. A liquid flow regime

is tested including examining the effects of high flow rates (15- 450 ml/min) including controlled pressure within the flow cell (1-3 bar gauge pressure). Silicon targets were prepared as described in chapter 4. The profiles of the ablation craters were examined using a VHX-2000 (Keyence) 3D Optical Microscope. Ablation craters were also analysed via a scanning electron microscopy (SEM) using an EVO LS15 (Zeiss) with LaB6 filament, accelerating voltage of 3 kV, and a beam current intensity of 25 pA.

*Table 5.3: Process parameters employed for tests to determine highest nanoparticle production efficiencies compared with a typical middle-class laser system described by Ditterch et al. * experimental laser pulse duration changes linearly from 500 ps at 10k RR to 3ns at 100k RR.*

Factors	Unit	Middle class*	Experimental
Average laser power	[W]	5	1.47 @ 10 kHz, 2.65 @ 20 kHz
Max absorbed Fluence	[J/cm^2]	6.7	1.83 @ 10 kHz, 1.65 @ 20 kHz
Pulse energy	[μJ]	330	147 @ 10 kHz, 133 @ 20 kHz
Repetition rate	[kHz]	15	10 - 50
Pulse duration	[ps]	5000	500-1250*
Beam diameter	[μm]	70	102
Inter-pulse distance	[μm]	670	<1
Scan speed	[mm/s]	10,000	2-10, 9000
Liquid Flow rate	[ml/min]	5	15 - 450
Flow velocity	[cm/s]	0.4	11.6 @ 140 ml/min
Cell pressure	[bar]	-	1, 2, 3

5.3   Results and discussion

5.3.1   Prediction Model development

To alter the model developed by Intartaglia et al. (2014) so that it provides a more relevant estimation of long-term production for a micro-machining scale laser systems such as the one developed in Chapter 4, new values for F_{th}^{app} and k must be determined that better capture the process conditions of continuous Np manufacture. As the existing model does not account for changes in pulse duration with repetition rate, a feature of the experimental

laser system, a parameter for pulse duration (τ_p) is integrated into the new model, detailed in section 5.3.1.3.

Firstly, the ablation fluence threshold was determined for the process under continuous liquid flow conditions, $F_t = 1.05 - 1.83$ J/cm^2, RR = 10 kHz, flowrate = 140 ml/min, SS = 2 mm/s, ablation time = 15 mins. A linear fit (Adj. $R^2 = 0.93$) of pulse ablation efficiency to fluence applied was determined, as seen in Figure 5.1(a), the linear response is in accordance with literature for fluences under 3 J/cm^2 [25]. The x-axis intercept determined the process fluence threshold [5], [23] to be 0.35 J/cm^2, similar to the values found by Thorstensen et. al. (2012), for a ns laser system ablating Si in air [23].
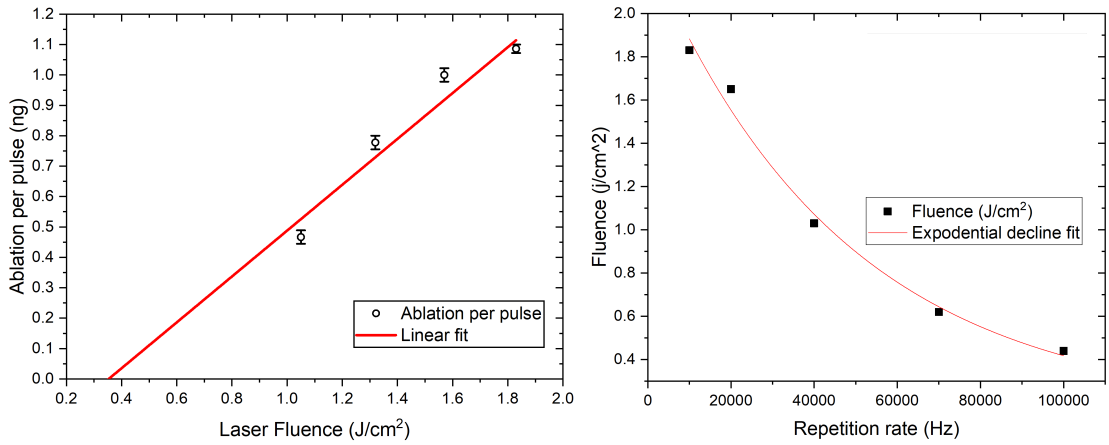
Figure 5.1 (a) Pulse ablation efficiency of a silicon target under various fluences, RR=10kHz, the material fluence threshold was linearly extrapolated (y = -9.59+27.15x) to be 0.35 J/cm^2, adjusted $R^2 = 0.93$, n=3. (b) The maximum operating fluence of the experimental laser system reduces exponentially with increasing repetition rate (adjusted R^2=0.98, n=3).

It has been reported that ablation productivity increases linearly with repetition rate [5], [25], as the energy applied per second increases for fixed pulse energies. However, this is only true for laser system's that can provide constant pulse energies (E_0) and pulse durations (τ_p) over their operational repetition rate range. We already know the experimental laser systems pulse duration increases linearly; from 500 ps at 10 kHz RR to 3000 ps at 100 kHz RR. From Figure 5.1(b), the maximum fluence available, and thus pulse energy of the laser system decreases exponentially with increasing repetition rates, this poses problems as to how to model the system.

As the pulse duration increases towards the ns range the electron lattice temperature reaches equilibrium [42] and conduction becomes the primary heat transfer mechanism [1],[43],[44]. As described in Eq. 5.2b, the thermal penetration depth, heat affected zone (HAZ) and total energy penetration into the bulk target material (k) increases with $\sqrt{\tau_p}$ [1],[43],[44]. Therefore, to produce a more representative model of the experimental laser system, k was fitted to the range of operable pulse durations. The process parameters for tests conducted is described in Table 5.4, with T determined using Eq. 5.14 and experimental ablated mass per pulse date of 0.9 ng ± 0.1 @ 10kHz as illustrated in Figure 5.3.

Table 5.4: Experimental parameters for determining k.

Repetition rate (kHz)	Pulse duration (ps)	Pulse energy (µJ)	Flowrate (ml/min)	Scan speed (mm/s)
10	500	147	140	2
20	692	133	140	2
30	972	98	140	2
50	1534	71	140	2
70	2096	50	140	2

k was calculated as per Eq. 5.14, where values for T (Figure 5.2) and F_{th}^{app} (Figure 5.1(a)) were determined experimentally as described above. The fluence applied on the material surface (F_t) was a component of the T value determined, as it would contribute to M_a. Therefore, the reduction in E_o with increased τ_p is accommodated in the model as F_t in Eq. 5.14, the log reduction of k illustrated (Adj. $R^2 = 0.99$) must be indicative of thermal effects as an outcome of increasing τ_p as described in Eq. 5.2. b.
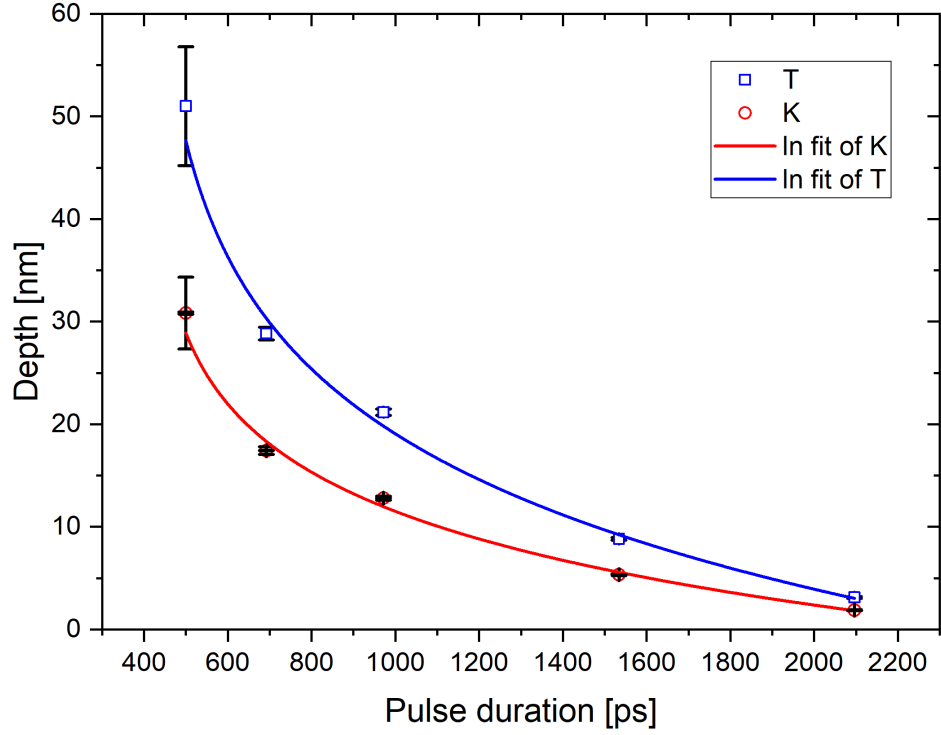
Figure 5.2: (a) Log fit of ablation depth (T) and energy absorption depth (k) per pulse compared with pulse durations (RR=10 − 70 kHz), k=70.28-9.21*ln(τp-410.74), Adj. R^2= 0.99, n=3.

The ablation coefficients determined from the log fits are in agreement with literature for similar systems; at 10 kHz RR, T = 51 ± 6 nm and k = 31 ± 4 nm. Pulse ablation depth found in this work is similar to the values achieved by McCann et al. for a similar 1064 nm ND:YAG laser system (1.83 J/cm^2, 10 kHz RR), who ablated a polymer target in air and achieved values for T between 20 nm - 70 nm [45]. The values also correspond well with the work by Schütz et al. that discussed an ablation depth per pulse range of 10 nm – 100 nm for a 1064 nm laser system operating between 1 and 2 J/cm^2 fluence [38] . The value of k is in agreement with that found by Intartaglia et al.(2014) who achieved k = 36 nm, also operating at 10 kHz RR using a 1064 nm Nd:YAG laser system.
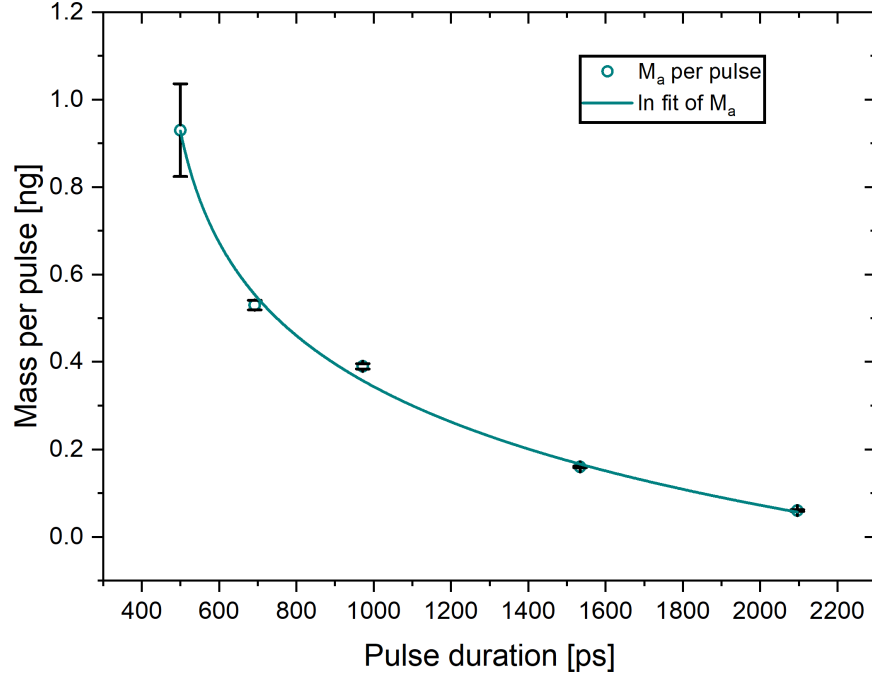
Figure 5.3: Log fit of ablated mass per pulse over the same varied pulse durations, Adj. R^2 0.98 (n=3).

5.3.1.1   Optical profilometry

Optical profilometry was performed on a selected ablation crater as a secondary validation of gravimetric measurements and the ablation depth value found from Figure 5.2 (based on ablated mass). An example of the surface analysis is seen in Figure 5.4. For the 15-minute ablation time, the average crater depth was 182 μm, estimated ablated mass of 7.8 mg, compared with 6.8 mg measured gravimetrically. The estimate for ablation depth per pulse was 47 nm, within one standard deviation of the fitted value. Also, to note, the optical profilometry analysis also shows that ablation was even over the entire crater spiral.

Profilometry analysis	
Crater diameter	4870 μm
Average depth of crater	182 μm
Volume	0.49 cm³
Volume est. of ablated mass	7.8 mg
T estimate	47 nm
Ablated mass meas.	6.8 mg
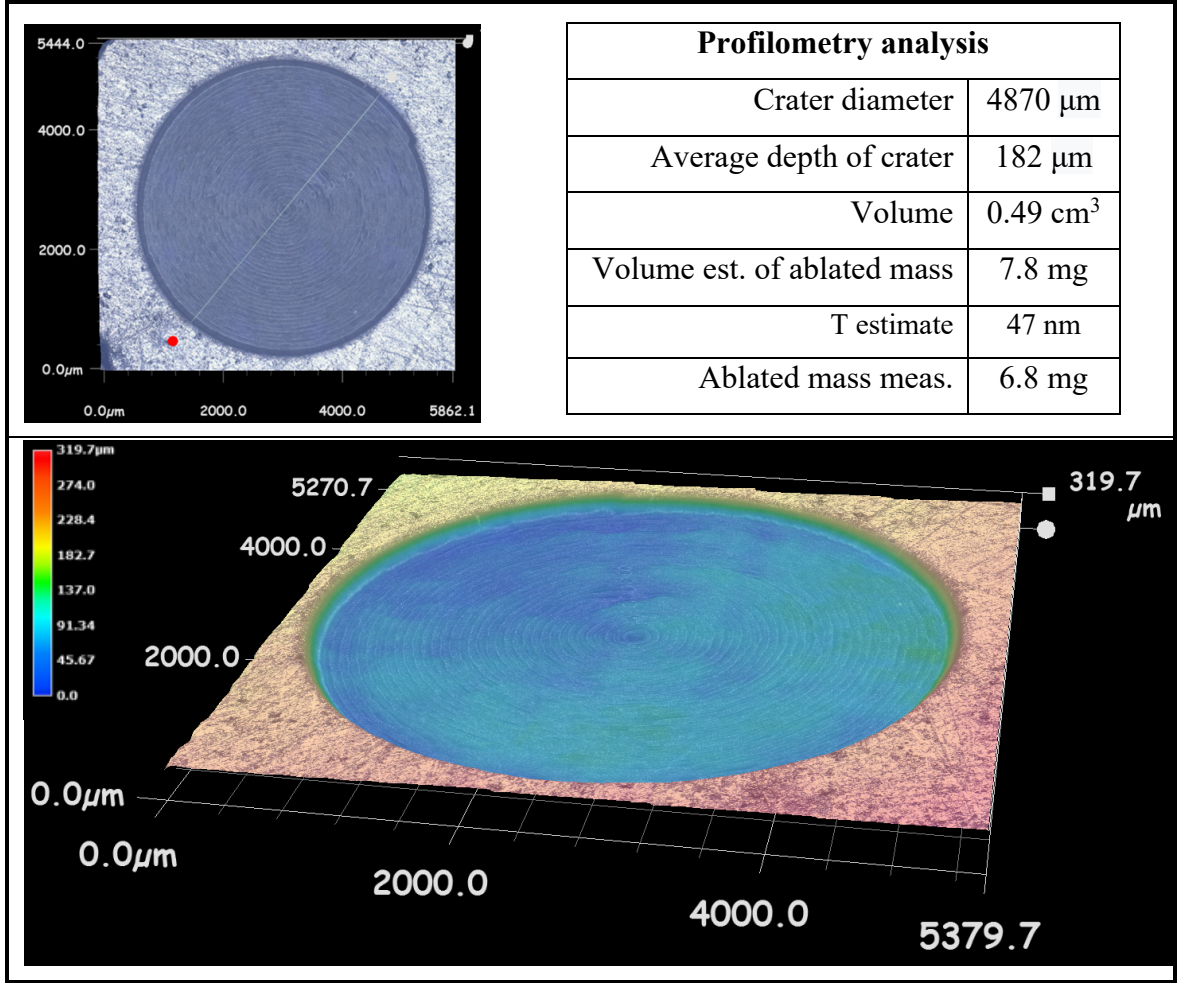
Figure 5.4 Typical ablation profile of Si target under the following conditions: 1.83 J/cm, 10 kHz RR, 2 mm/s SS, 140 ml/min liquid flowrate, 15 minute ablation (slice 11).

5.3.1.2 Models including pulse duration

A possible way to simplify the modelling of pulse duration to lattice-heating effects has been suggested in the past [1],[43],[44], rather than changing k over pulse duration, a more straight-forward assumption that fluence threshold changes with pulse duration was implied; $F_{th}^{app} \propto \sqrt{\tau_p}$. A new model was developed based on this relationship, calculating F_{th}^{app} as a function of the changing pulse duration as follows;

$$F_{th}^{app}{}_{@\tau_p} = \left(\frac{\sqrt{\tau_p}}{\sqrt{500}}\right) \times F_{th}^{app}{}_{@\ 500\ pS} \qquad (Eq.\ 5.16.)$$

For the laser operational range, F_{th}^{app} was observed to increase from 0.35 J/cm² at 10 kHz RR ($\tau_p = 500pS$) to 0.73 J/cm² at 70 kHz ($\tau_p = 2096\ pS$) using Eq. 5.16 over the laser operational range.

5.3.1.3 Summary of the developed process models

From the work described in this chapter, three new models are developed with varying levels of complexity, their derived coefficients are described in Table 5.5. A summary of the process conditions achieved in developing the models is described in Table 5.6. The models are described as follows;

Model 1: Includes experimental values of $F_{th}{}^{app}$ and k at 10 kHz RR & $\tau_p = 500\ ps$. $F_{th}{}^{app}$ is in agreement with published values [23], [46]. Both parameters are more representative of pilot-scale, higher colloid concentration process, η is an order of magnitude lower than that used by Intartaglia et al.

$$Productivity_{model\_1} = (7.54{\times}10^{-6}) \times E_0 \times RR, (g/s) \qquad (Eq.\ 5.17)$$

Model 2: Assumes k is constant, using Eq. 5.16. to relate the effect of changing τ_p on the fluence threshold. The breakdown of the model components is detailed in Table 5.5.

$$Productivity_{model\_2} = 0.0017\sqrt{\tau_p}^{-1}{\times}E_0 \times RR , (g/s) \qquad (Eq.\ 5.18)$$

Model 3: Includes experimental value of $F_{th}{}^{app}$ found at 10 kHz RR, and applied the log relationship between k and pulse duration determined in Figure 5.2, adding a τ_p term to the model.

$$Productivity_{model\_3} = \left(1706.54 - 208.72 \times ln(\tau_p - 410.74)\right){\times}E_0 \times RR , (g/s)$$

$$(Eq.\ 5.19)$$

Table 5.5: Parameters required for evaluation of the productivity developed models.

$Productivity_{max} = \eta \times E_0 \times RR$			
Parameter	**Units**	**Model 1[a]**	**Model 2[b]**	**Model 3[c]**
k	[nm]	31	31	$70.28 - 9.21 \times ln(\tau_p - 410.74)$
F_{th}	[J/cm^2]	0.35	$0.0156\sqrt{\tau_p}$	0.35
η	[gJ^{-1}]	7.54×10^{-6}	$\dfrac{(7.18 \times 10^{-6})}{(0.0424\sqrt{\tau_p})}$	$\dfrac{2.33\left(70.28 - 9.21 \times ln(\tau_p - 410.74)\right) \times 10^{-7}}{0.95}$

[a] developed using $\tau_p = 500\ ps$.

[b] developed using $\tau_p = 500 – 3000\ ps$.

[c] developed using $\tau_p = 500 – 3000\ ps$.

Under the assumption of a linear increase in ablated mass with applied laser power, model 1 was compared with the model proposed by Intartaglia et al. (2014) and an experimental data set illustrated in Figure 5.5. Model 1 achieving a mean relative error (MRE) of 7%, compared experimental data, whereas the model developed by Intartaglia et al. (2014) as a scale up estimation tool, and not a specific process estimator achieved 139% MRE. The efficiency parameter for model 1 was determined to be 7.54 x 10^{-6} gJ^{-1}, significantly lower than proposed by Intartaglia et al. (2014), which is in alignment with the assumption a more scalable representative process would contain more ablation limiting factors such as particle occlusion. The maximum productivity predicted by Model 1 for the experimental laser system is 39 mg/h at 10 kHz RR and 72 mg/h at 20kHz RR, it should be noted that this model doesn't account for the loses due to thermal affects associated with increasing τ_p. Model 1 indicates that a 37 W 1064 nm laser system would be required to produce 1 g/h SiNps at 10 kHz RR. Table 5.6 contains a summary of the model development results.

Table 5.6: Model results summary

Parameter	Values (model 1)	Description
T_{fitted}	51 ± 6 nm	Determined @ 10 kHz RR, E_0=147 μJ, 2mm/s scan speed, 140 ml/min liquid flow rate, unregulated chamber pressure.
k_{fitted}	31 ± 4 nm	
F_{th}^{app}	0.35 J/cm^2	
M_a per pulse	0.9 ± 0.1 ng	
η	7.54 x 10^{-6} g/j	
Predicted max productivity	39 mg/h	10 kHz RR & 147 μJ E_0
	72 mg/h	20 kHz RR, 133 μJ E_0
Proposed laser system to meet 1 gram/hour SiNps productivity		37 W, 1064 nm, ps laser system operating at; 10kHz RR, 3.7 mJ E_0
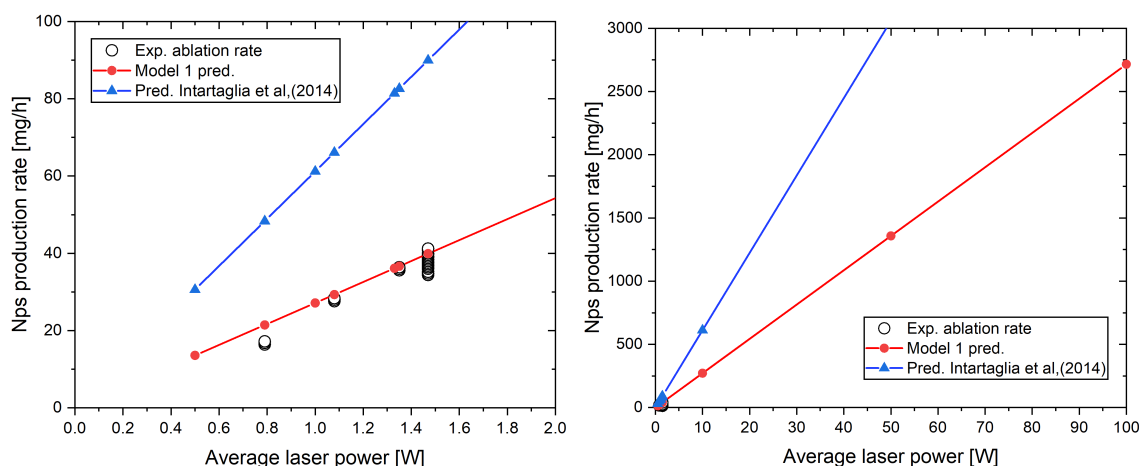
Figure 5.5: Prediction of SiNps productivity for a range of laser output powers. Comparing the Intartaglia et. al. model (Eq. 5.2, $\eta = 1.7 \times 10^{-5}$, k = 36 nm, $f_{th}^{app} = 0.18$ J/cm^2) with Model 1 (Eq. 5.17).

5.3.2 Process development steps

Process development work carried out in this chapter builds upon the development from batch production towards continuous in chapter 3 and flow cell design in chapter 4. In this chapter a range of single-factor optimisation tests were carried out as per Figure 5.6. This testing protocol determined the effects of each process parameter on Np fabrication efficiency with the aim of maximising production.
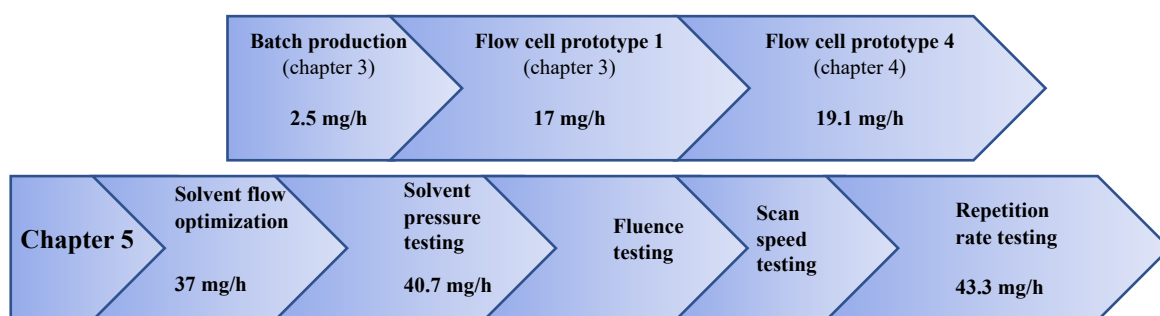
Figure 5.6: Experimental development of SiNps production

5.3.3 Effect of liquid flowrate on productivity

Tests were performed to determine the effect of solvent flowrate on SiNp productivity under the following process conditions: laser fluence set to 1.83 J/cm^2 at 10k RR and beam scan speed of 2 mm/s. The liquid flow varied within a range of 15 to 460 ml/min under unregulated flow cell pressure conditions. Pressure was observed to increase from 0.5 - 1.5 bar with flowrate, due to flow resistance in the flow cell. The flow range is comparable with

Streubel et al. (2016) [34] who tested flowrates of 300 ml/min in an unpressurized flow cell under irradiation by a 500 W, 3 ps laser source. Laszlo et al., (2010) determined that liquid flow significantly removed gas bubbles from the ablation site, with no increase in production efficiency observed above 190 ml/min for ablation of a ceramic target by a 60 W 1064 nm laser [25]. From *Figure 5.7* it can be seen that the Np productivity is a power function of increasing flowrate, adjusted R^2 of 0.95, and all values within 90% confidence interval of the prediction. It is assumed that increasing liquid flow removed occluding particles and gas build-up from the ablation site. Increasing liquid flowrate above 170 ml/min provides a lower relative ablation increases, with insignificant increase in ablation efficiency between 170 ml/min and 300 ml/min, with production error-bars overlapping. A distinct drop-off in efficiency is observed below 140 ml/min. Flow-cell laser window imaging was performed at 240 frames per second (FPS) using an iPhone 6s, see Figure 5.8**.** It was seen that at lower flowrates, (<100 ml/min) significant bubble accumulation occurred on the surface of the laser window within the flow cell. Fluid bubble stripping effects are observed at flowrates above 100 ml/min. Gas bubble presence at the ablation site would have significant detrimental effects on laser ablation efficiency, adding another phase transition for the incident beam to pass through, and also increasing the reflected energy [1]. It should be noted that an adverse effect to increasing flowrates is the logarithmic decline in colloid concentration, so there needs to be a balance struck between efficient flow and colloid concentration production. Going forward, 140 ml/min was chosen as the flowrate to allow for other process parameter tests because at this flowrate no bubble build-up was visible in the flow cell, and productivity performance was within 10% of the steady state values achieved within the 170 - 300 ml/min range, while minimising the dilution effect as much as possible.
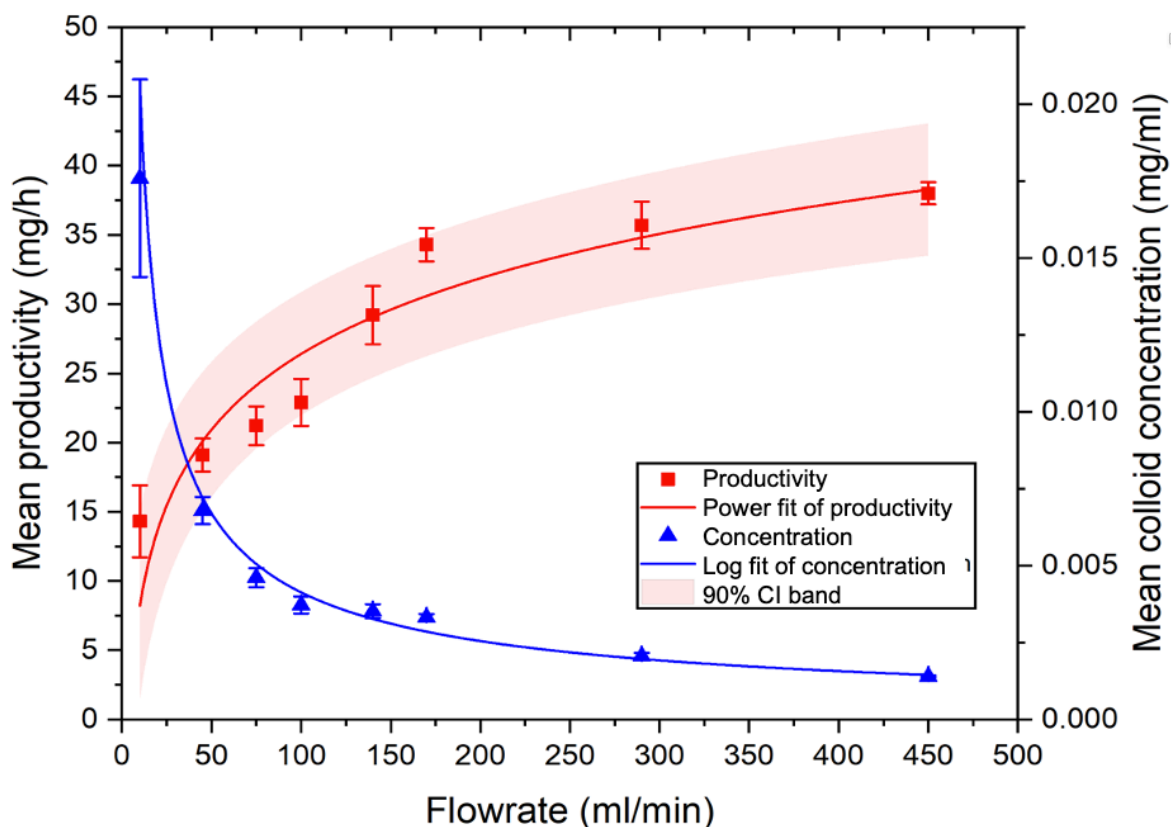
Figure 5.7: SiNps productivity and colloid concentration measurements under varied continuous flow conditions (pressure, observed <1.5 bar). Mean productivity followed a power fit; $y=0.1025*(x)^{-0.6973}$, with concentration following a log decline: $c=7.889*ln(x)-9.9336$, adjusted $R^2=0.93$.

15 ml/min	70 ml/min
100 ml/min	140 ml/min
300 ml/min	450 ml/min
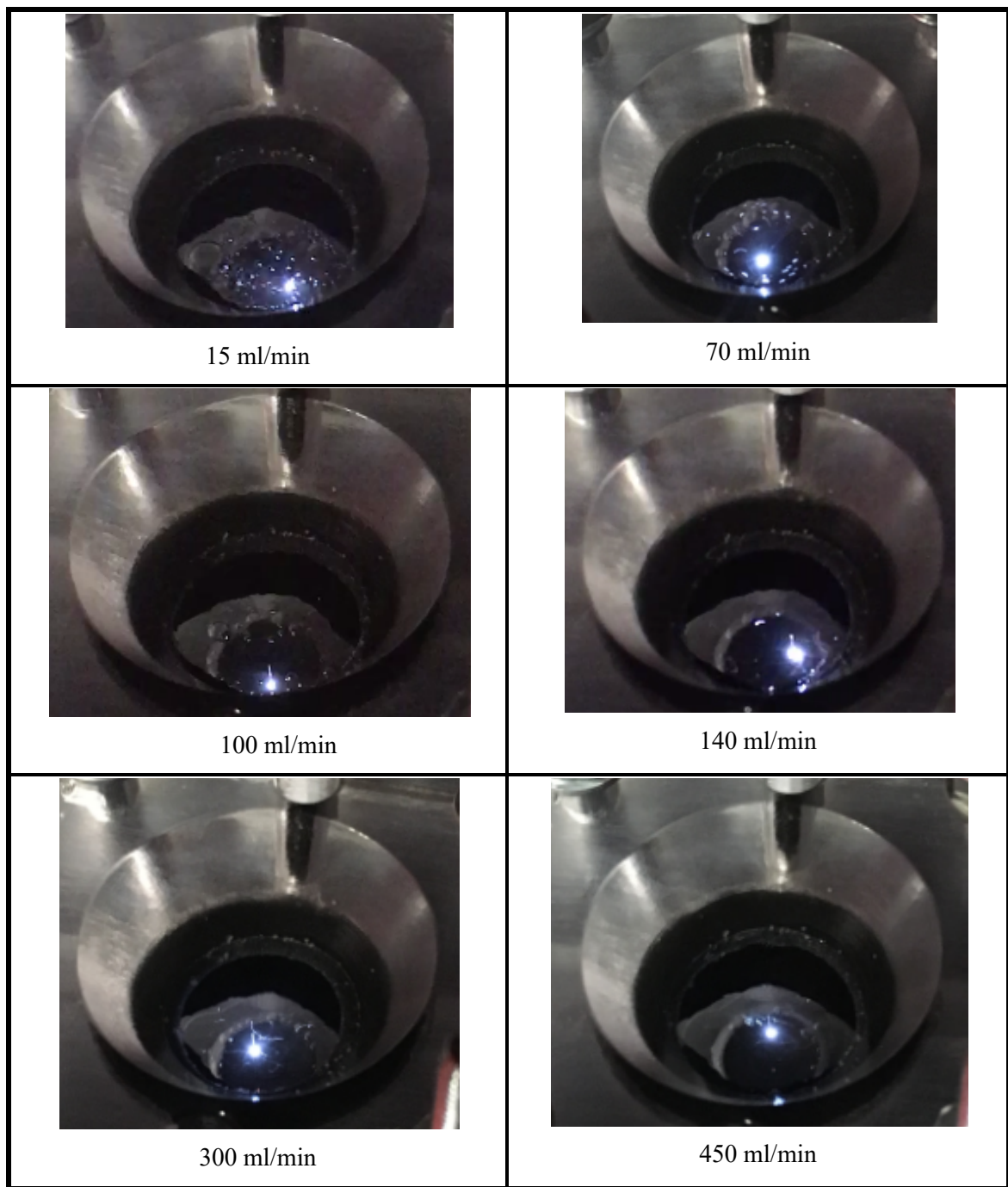
Figure 5.8: Flow conditions within the flow-cell during ablation (photo at time = 60 s, assumed laser steady state ablation), bubble build-up observed in laser window at flowrates up to 70 ml/min.

5.3.4 *Effect of liquid pressure on productivity and Np size*

From Figure 5.8 it can be seen that with high flowrates (>100 ml/min) there is little bubble accumulation in the flow cell. A noticeable increase in productivity is seen in *Figure 5.7*

with flowrates above 100 ml/min, this indicates the impact bubble stripping has on productivity. The productivity increase may be due to fluid flowrate alone, or pressure may be a factor, which has not been controlled. To separate the interaction effects of solvent flowrate and pressure on ablation efficiency, ablation tests were performed at three constant pressure levels (1 - 3 bar), over varied liquid flowrates.

Results from liquid flowrate and pressure tests are illustrated in Figure 5.9. As expected, an increase in ablation efficiency is seen with increasing liquid flowrate under constant pressure conditions. Also, a marked increase in productivity is observed for increasing pressure at a constant flowrate. A maximum productivity of 40.7 mg/h is achieved under 140 ml/min liquid flow at 3 bar pressure, yielding 27.7 mg/Wh, higher than reported in literature for SiNps production. It is assumed that the target material is irradiated by the same fluence level over all pressures tested because the refractven index of water is only marginally affected by increasing pressure [29]. In Figure 5.10 it is seen that by increasing ambient pressure to 2-bar while operating at low flowrates (50 ml/min) the bubble suppression effect is similar to that of 100 ml/min liquid flow with unregulated chamber pressure, where few macro-bubbles are observed. This effect is more than likely due to liquid pressure increasing the gas solubility in the liquid [47].
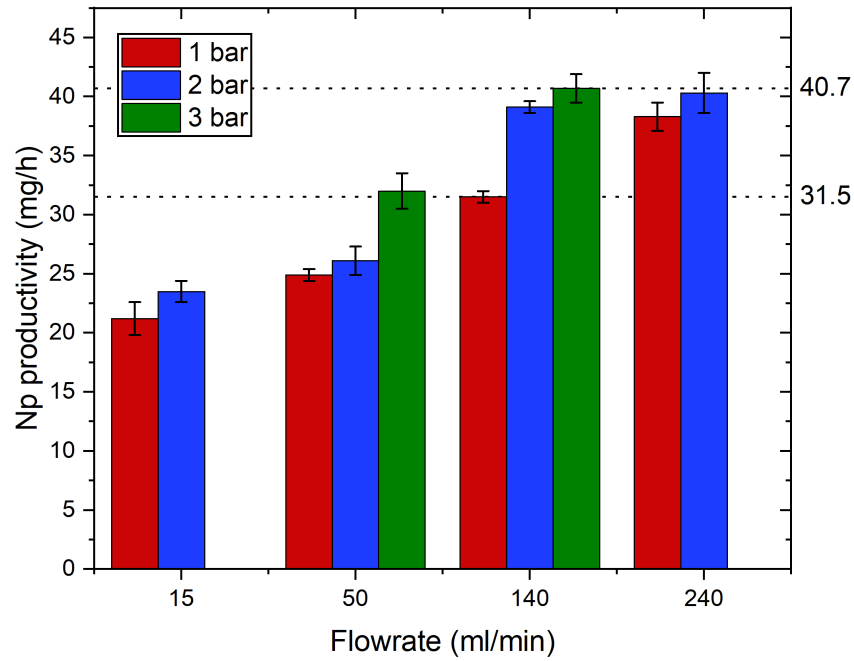
Figure 5.9: Ablation rate at varying fixed flow-cell pressures and flowrates, fluence 1.83 J/cm². repetition rate 10kHz & laser beam scan speed 2mm/s.

| 50 ml/min, pressure controlled @ 2 bar | 240 ml/min, pressure controlled @ 2 bar |
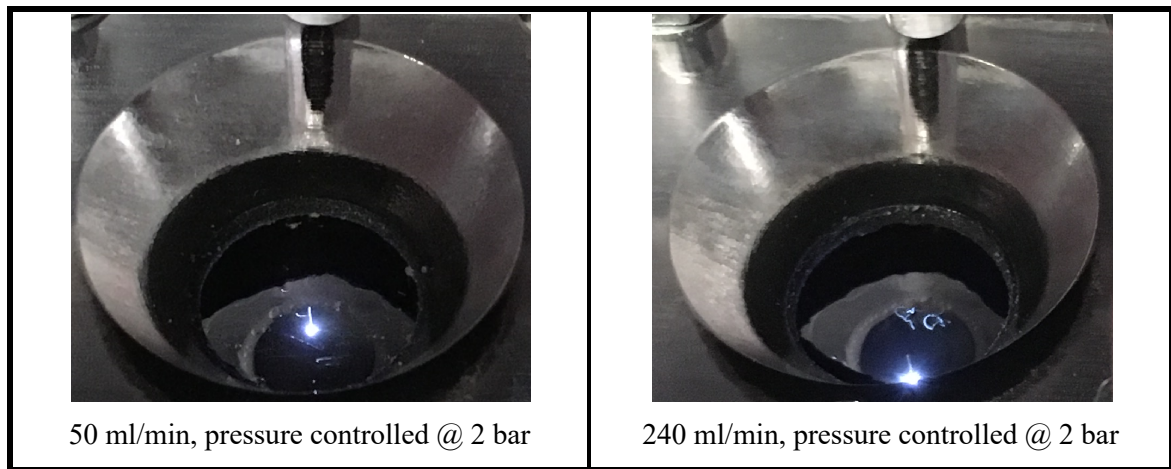
Figure 5.10: Bubble conditions within the flow cell under 2 bar gauge pressure.

Now examining the pressure response at a flowrate of 140 ml/min flowrate, as illustrated in *Figure 5.11*, determines a power relationship between Np productivity and ambient pressure (Adj. $R^2 = 0.96$), indicating that the results are in agreement with literature reporting large relative productivity increases with low relative pressure increases [48], [49] therefore there may not be significant productivity gains in pressurizing the flow cell further.
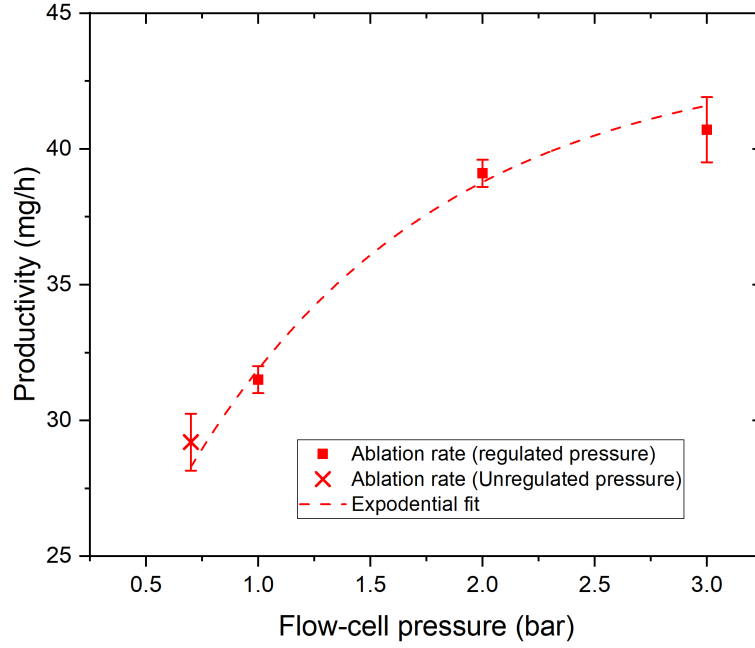
Figure 5.11: Power relationship of SiNps productivity Vs liquid pressure at constant liquid flow rate (Adj. R² = 0.96), Productivity=43.53-28.55*exp(-0.9x), FR=140 ml/min, F=1.83 J/cm², RR=10 kHz, n=3.

When maintaining the pressure at 2 bar and increasing flowrate to 240 ml/min, no bubbles were observed in the flow cell. This suggests the possibility that under the laser conditions tested, at flowrates above 50 ml/min cavitation bubble occlusion [2],[49] and exhausted vapor occlusion [49] are the critical productivity restricting parameters at work, rather than plume and particle occlusion. This conclusion is drawn because it is expected that flowrate would have an effect of removing occluding particles from the ablation site, whereas pressure would not. Therefore, the increase in productivity due to fluid pressure must be as a result of pressure impacting the following;

1. Cavitation bubble dynamics.
2. Plasma generation and material interaction.
3. Solubility of gas bubbles generated due to LASiS process within the liquid.

5.3.5 *Effect of plasma generation*

From the literature it has been discussed that pressurized ablation chambers have been seen to generate confined plasmas [49],[48], reducing the maximum height extension of the plasma [49], [50], while increasing its width along the target, thus directing more of the

plasma energy towards the target [49]. De Giacomo et al. (2017), observed that moderate increases in pressure (1-2 bar) lead to increases in Nps produced [17], as seen in this work. The authors observed that higher operating pressures (30-130 bar) yielded less relative effect on increasing particle production.

Ambient pressure will have little effect on the formation of laser induced plasmas, during irradiation, where the plasma's internal pressure has been reported to be between 10^4 bar to 10^5 bar. Plasma expansion stops when the pressure of the plasma is equal to the pressure of the vapor layer surrounding the plasma, which is affected by the ambient pressure and has been reported to be spatially confined [49]. Under ambient pressures the plasma expansion has been reported to be confined vertically even at pressures between 1 bar and 30 bar, but with more significant effects at higher operating pressures (150 bar) [49].

5.3.6 *Effect of cavitation bubble*

The change in cavitation bubble dynamics may be having a large effect on the Np productivity increase observed. Within the cavitation bubble itself the pressure has been determined from literature to be approximately 0.1 bar [2]. Thus, liquid ambient pressures in the range of 0.67 bar to 3.0 bar could have an effect on the bubble development. Increasing ambient pressure has been seen to reduce the cavitation bubble lifecycle [2] and increase the confined internal pressure within the cavitation bubble [2], [49]. As a result it also increases the temperature of the exhaust vapour to between 1000 - 7000 Kelvin [2] that expels into the liquid during bubble collapse. A model, based on the Rayleigh-Plesset equation for a spherical bubble within an incompressible fluid (as seen in Figure 5.12), developed by Soliman et al. (2010) predicts the change in bubble dynamics with pressure as follows [51]:

$$t_c = 0.915 R_{max} \times \sqrt{\frac{\rho}{p_{amp} - p_v}}, \qquad (Eq.\ 5.20)$$

$where;$
- $t_c = $ time interval between maximum radius extension and bubble collapse.
- ρ = density of liquid.
- p_{amb} = ambient pressure of liquid.
- p_v = cavitation bubble pressure.
- R_{max} = maximum bubble radius.

163
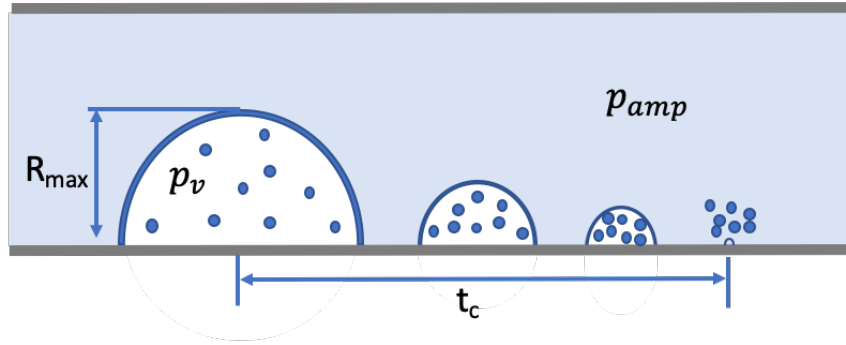
Figure 5.12: Cavitation bubble collapse time (t_c) from maximum bubble extension (R_{max}), indicating bubble vapour pressure (p_v), ambient pressure (p_{amp}) and the expulsion of nanoparticles.

Its is assumed that the experimental bubble behaviour is similar to that observed by Tomko et al. (2017). Where they used optical imaging to examine the cavitation bubble dynamics over a similar pressure range (0.2 bar - 1.6 bar). Therefore the experimental maximum bubble radius (R_{max}) is assumed to decrease at the same rate as a function of hydrodynamic pressure. A summary of the values chosen is described in Table 5.7. Calculations for t_c were performed over an operational liquid ambient pressure range of 0.67 – 3 bar, the resultant prediction values of t_c and R_{max} is described in Table 5.8. The expected bubble lifetime for the primary bubble is approximately 150 µs (as discussed in chapter 4) for the experimental system. Therefore, under ambient pressure of 3 bar, t_c was seen to reduce from 12.1 µs to 1.3 µs, possibly reducing the cavitation bubble lifecycle by 10%.

Table 5.7: Solvent, deionised water, properties for the experimental system.

Description	Assumed values	Units
R_{max}	100	[µm]
ρ_{water}	997	[kg/m^3]
p_{amb}	100 - 300	[kPa]
p_v	10	[kPa]

The reduction in cavitation bubble lifecycle would increase laser beam temporal avoidance of the cavitation bubble, increasing ablation efficiency. Its proposed by this work that increased ambient pressure aids temporal avoidance of the cavitation bubble, along with

increasing heating of the target. Resultant shockwaves from plasma and bubble collapse progress parallel to the target surface [49] and increase the energy acting on the target. This confinement of shockwaves occurs within a pressurised liquid environment, restricting the natural progression of the pulse-induced shockwaves and thermal energy from projecting outward from the target into the liquid, but redirecting some of that energy back into the target [49]. This increase of heating would lower the fluence threshold of the surface of the target [23], allowing for higher ablation efficiency compared with lower ambient pressure conditions.

Table 5.8 Estimates of time interval from R_{max} to bubble collapse, assuming bubble size response with pressure similar to that described by Tomko et. al., (2017).

Ambient pressure (bar)	Assumed R_{max} (μm)	Predicted t_c (μs)
0.67	100	12.1
1	70	6.7
2	50	3.3
3	25	1.3

This proposed thermal effect can be seen in the melt holes and surface texturing of the ablation crater on the Si target apparent in Figure 5.14 (c & d). The resultant crater produced under 2 bar gauge pressure shows signs of melt, but under the same laser conditions and liquid flowrate at 1 bar gauge pressure, no melt is observed on the textured surface. It should be noted that similar melt effects are observed at Figure 5.14 (e & f) where ablation was conducted under 1 bar ambient pressure, but with an increased repetition rate of 30 kHz, and pulse duration increase from 500 ps to 972 ps. The increase in RR would provide higher average power into the bulk material (1.47 W @ 10kHz- 2.66 @ 20 kHz), over a longer pulse duration.

As discussed previously the increased pulse duration will have an effect of heating the lattice structure (Eq. 5.2b), as indicated by the melt displayed in *Figure 5.14*. Similar melt holes and textured surface due to LASiS was observed by Kudryashov et al. (2019), on Si targets.

However, they employed orders of magnitude higher power-densities (0.5 - 1.0 GW/cm^2) than those tested in this work [35]. Similar melt patterns were observed by Neckermann et al. (2010) using a ND:YAG 532 nm, nS laser systems, whose wavelength provides a higher absorption coefficient for silicon than the 1064 laser used in the experiments [52]. This supports the hypothesis that the higher ablation efficiencies achieved under increased liquid ambient pressures is due to increased heating of the target surface. We have seen with the results above that a route toward increased Np productivity lies in avoidance of the cavitation bubble and the particles produced. It has been suggested that the route towards control of Np size lies in controlling the cavitation bubble dynamics also [13].

It would be expected that smaller particles would be formed with increasing pressure, as its been seen to reduce the bubble lifetime, allowing less time for particle nucleation and growth within the bubble [2]. However, within this work no formal conclusions can be made about the effect of pressure on particle size. As illustrated in Figure 5.13, a slight reduction in Nps peak diameter is observed (Peak dia = 75 nm @ 1 bar - 55 nm @ 3 bar). However, the population distribution broadens with pressure (size distribution width = ±15 at 1 bar to ± 35 at 3 bar), in agreement with similar trends of colloid size increase with pressure reported elsewhere [49], [15]. This widening of the size distribution indicates that a possible bi-modal formation may be encouraged to occur with pressure, where nucleation and growth of small Nps within the cavitation bubble is not the sole Np fabrication mechanism, but also some larger particles are formed and ejected into the liquid at the breakdown of the superheated molten metal layer that borders the plasma–liquid interface [11].
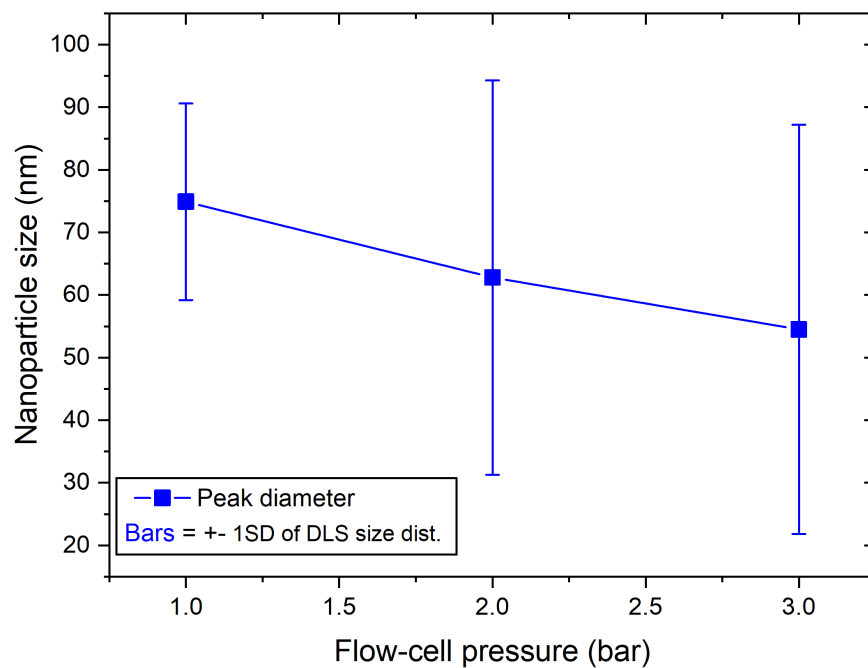
Figure 5.13: Nanocolloid size progression with pressure, lines between points acting as a guide to the eye, F=1.83 J/cm², RR = 10 kHz, SS = 2 mm/s, n=3.
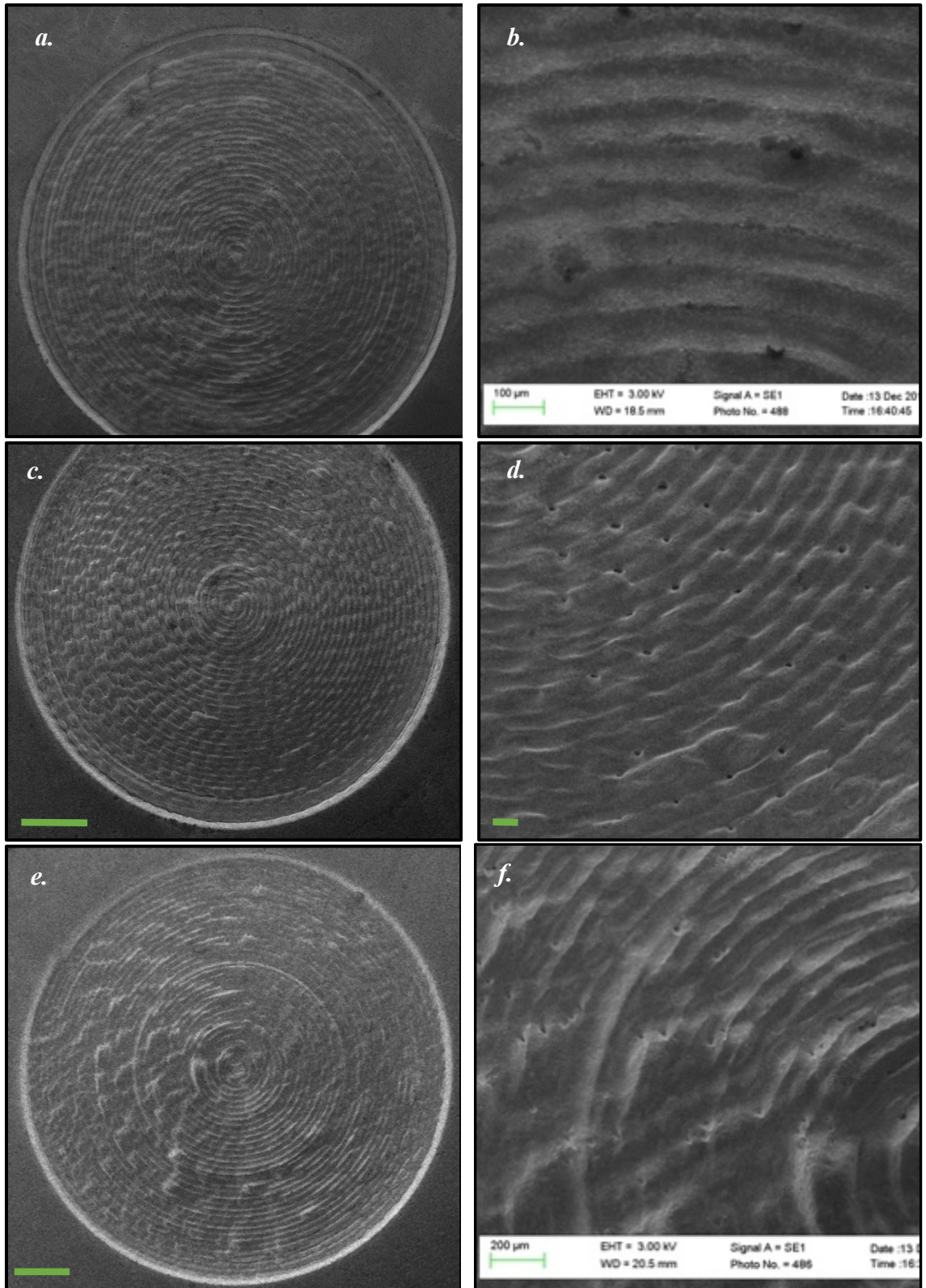
Figure 5.14: SEM images of Si targets after 15 mins continuous ablation, 3 kV, WD=19.5, signal = SE1. (a, b) 10 kHz RR, , τ_p=500 ps, 140 ml/min, 1 bar gauge pressure, (c, d) 10 kHz RR, τ_p=500 ps, 66 ml/min, 2 bar gauge pressure, and (e, f) 30 kHz RR, τ_p= 1056 ps, 140 ml/min, 1 bar gauge pressure.

5.3.7 *Effect of Fluence on Np productivity*

The effect of laser fluence on the ablation efficiency and Np size formation was determined from the ablated mass and DLS size measurements of the resultant colloid. The tests were performed in continuous production mode, with flow conditions maintained constant at 140 ml/min with flow cell pressure at 1 bar. A linear ablation response to fluence (adjusted R^2 of 0.93, as discussed previously) is observed. This correlates well with literature for silicon at similar fluence ranges [5], [53], where a linear ablation response was observed below 3 J/cm^2. It is well known that above F_{th} the initial ablation response is linear, followed by a secondary log-saturation response. The log response is influenced by laser energy absorption and scattering due to occluding particles in the colloid along with laser interactions with F_t dependent plume and cavitation bubble sizes [24],[25],[37].

It is possible that for the experimental work illustrated in Figure 5.5, the drop-off from the linear fit for the highest fluence tested (1.83 J/cm^2) indicates the start of the log ablation response. A log fit of the data provides an adjusted R^2 of 0.97. It is expected that the possible log response would be due to a higher concentration of occluding particles at the ablation site rather than laser induced optical breakdown of the liquid. From the literature a typical pulse intensity threshold for optical breakdown of water was seen to be $4x10^{11}$ W/cm^2 [54], for a 1064 nm laser operating at 6 ns pulse duration. The maximum pulse intensity tested in this work at 10k RR is $1.87x10^4$ W/cm^2, several orders of magnitude lower. However the log-relationship is in agreement with ablation efficiency tests in air performed by McCann et al., [45] on a similar laser system, where ablation rates of polymer in air were determined to be logarithmically dependant on the ratio of the incident to the transmitted laser intensities. However, for the fluence ranges tested with the laser system, it would be imprudent to assume that the ablation response to applied pulse energy is approaching log response when the linear fit has such a high correlation.
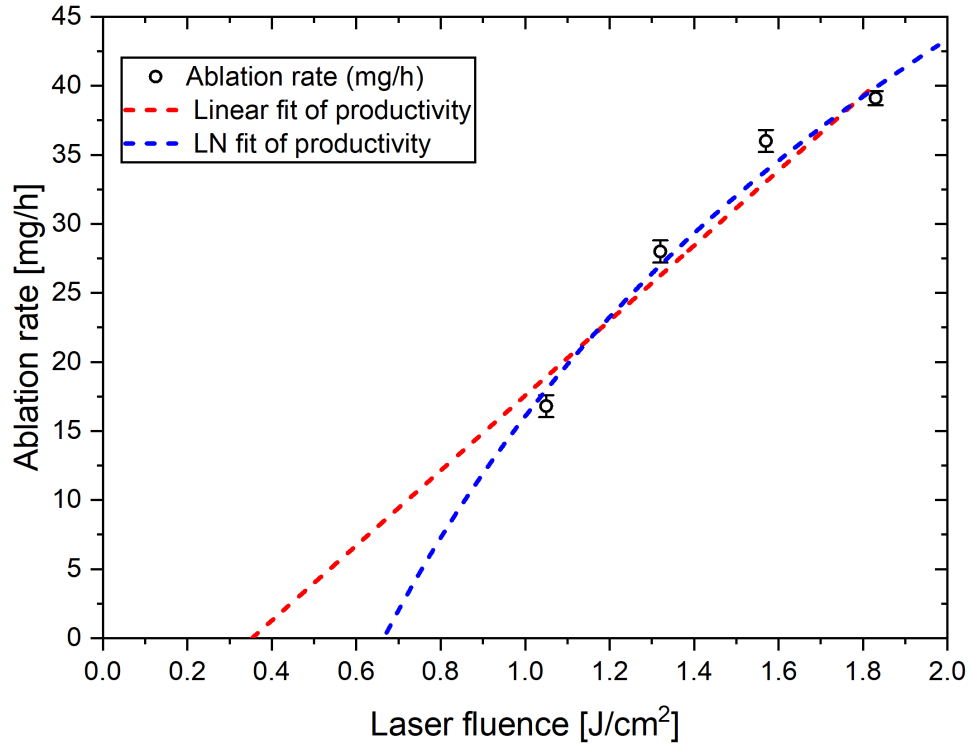
Figure 5.15: Ablation efficiency over a fluence range, a log fit was determined with an apparent fluence threshold (F_{th}^{app}) extrapolated at 0.35 J/cm², y=a*ln(x)+b, adjusted R^2=0.93.

5.3.8 Effect of Fluence on SiNp size

From the literature it has been noted that increasing fluence may increase the Np peak diameter and size distribution [55]. It has been noted that for palladium the mean peak diameter of PdNps increased from 6.98 ± 3.13 nm to 8.9 ± 3.89 nm under increased fluence from 9 J/cm² to 20 J/cm² for a 1064 nm laser system [56]. This is admittedly a small size increase, but the authors conclude that a trend of increasing Np size with fluence is observed. More significant size increases has been reported while operating at higher fluences; it has been reported that raising the applied fluence from 100 J/cm² to 1000 J/cm² for fs irradiation resulted in an AuNps peak diameter increase from 15 nm to 120 nm [55]. There are fewer reports of size increase at lower fluence levels, such as the ones applied in this work, therefore it is difficult to predict the impact of experimental laser fluence on Nps size. Many interacting factors may play a role in determining Nps size. Photofragmentation [4] can lead to smaller particles, particle occlusion can lower the laser fluence on the target, leading to smaller particles. Target melt can produce larger Nps, whereas phase explosions from higher applied fluence levels can produce smaller particles due to the   growth-aggregation

mechanism at play [6]. It can be seen from Figure 5.16 that the smallest Np peak diameter and size distribution of 65 ± 23 nm is produced at 1.05 J/cm^2, the lowest fluence tested with an increase in particle size to 100 ± 42 nm at 1.83 J/cm^2. However, this increase is not observed to be linear, more of a step change with fluence levels higher than 1.05 J/cm^2. These results would indicate that, indeed, lower applied fluence may provide small SiNps. However, reflecting literature findings [6],[56] it can be difficult to conclude a definite relationship between fluence and Np size. Therefore, the experimental test window is too narrow to conclude statistical trends from this data.
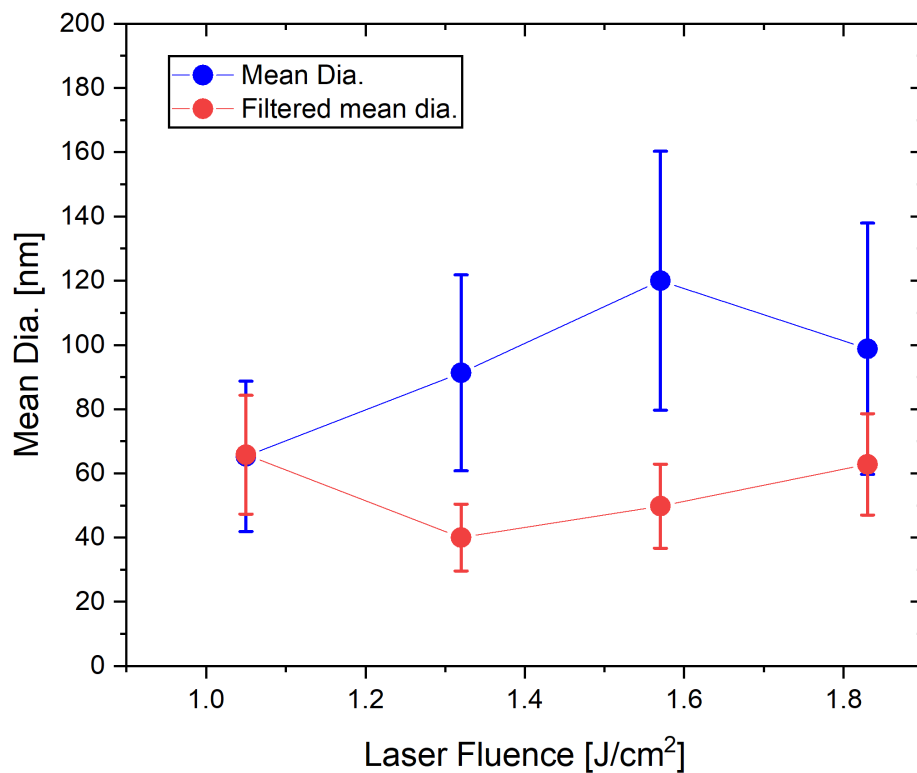
Figure 5.16: Plot of Nps size with applied fluence; mean peak diameter and colloid population distribution width (bars) displayed. Off-line and 0.2 micron filtered colloids presented (n=3).

5.3.9   Scan speed & inter-pulse distance

An optimum beam scan-speed for the system was determined experimentally under continuous flow conditions (140 ml/min) while ablating a silicon target under a fluence of 1.83 J/cm^2 at a repetition rate of 10 kHz. This chapter is focused on developing a "proof of concept" system to provide a roadmap towards on-the-bench manufacture of Nps in Bio-pharmaceutical research laboratories. With that in mind, miniaturization and cost

rationalisation of the equipment is a factor. In meeting these restrictions, scan speeds were selected that would accommodate replacing a high-speed galvanometer scanner with a small form-factor, low-cost micro-position stage in future rig designs. It is noted that polygon scanners are reducing in price and could be an equipment option in later designs. Scan speeds were varied between 2 and10 mm/s and a maximum productivity of 29.9 ± 0.5 mg/h for the speed range tested was achieved at 2 mm/s. A linear reduction in yield (adjusted $R^2 = 0.99$) was observed with increased scan speeds as seen in Figure 5.17.
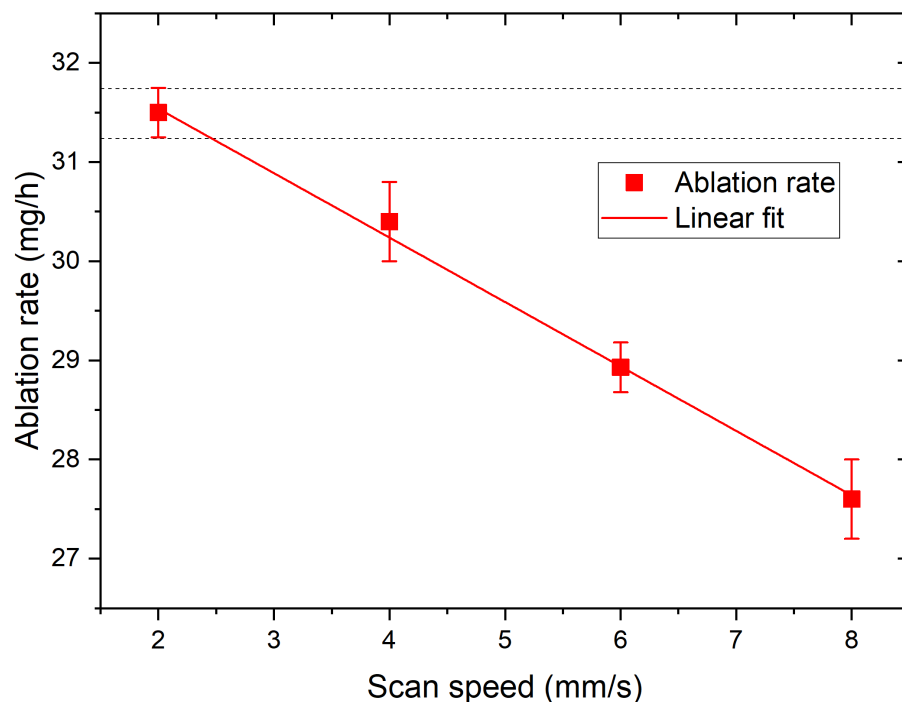
Figure 5.17: Plot of Nanoparticle productivity with respect to beam scan speed. The inter-pulse distance was determined to be ranging from 0.2 μm at 2 mm/s to 0.8 μm at 8 mm/s, ablation parameters used as follows; 10 kHz PRF, 1.83 J/cm², 140 ml/min flow, 0.67 bar flow-cell pressure.

Currently the momentum in the field is directed towards utilizing ultra-high scanning speeds (1,000 - 10,000 mm/s) coupled with high laser repetition rates (100 kHz – 1 MHz) to provide large inter-pulse distances and spatially avoid the cavitation bubble to mitigate efficiency losses. To examine this high-speed option for the experimental system 15-minute triplicate tests were performed at 9000 mm/s, offering an inter-pulse distance of 900 μm per pulse. This would ensure spatial avoidance of the cavitation bubble completely. An Np productivity of 23.4 mg/h ($\sigma = 3.2$) was achieved, significantly lower than that achieved with 2 mm/s

scan speed. This result indicates that temporal avoidance must be the primary laser avoidance mechanism when operating at 10 kHz RR, at a pulse duration of 500 ps for the experimental system tested.

The complete cavitation bubble lifecycle is thought to be 200 µs [32] and the primary bubble collapse is estimated to be in the region of 100 µs [32], where the bubble is estimated to be approximately 100 µm in diameter [57] at maximum expansion. At 10 kHz repetition rate, primary bubble temporal avoidance may be achieved, at 20 kHz the primary bubble may re-irradiated by a single following pulse. while at 30 kHz the bubble is expected to be re-irradiated by three following pulses. The question arises, if there are possible gains to be achieved applying a certain amount re-irradiation. In the literature, a ns pre-pulse was seen to reduce the ablation threshold of a silicon target in an air environment by preheating the surface [46]. A 2 mm/s scan speed was selected as the parameter going forward with the process optimisation, the inter-pulse distance for different repetition rates used during development can be seen in Table 5.9.

Table 5.9: Inter-pulse distances at varying repetition rates for a scan speed of 2 mm/s.

Repetition rate [Hz]	Inter-pulse distance [microns/pulse]
10,000	0.20
30,000	0.07
50,000	0.04
70,000	0.03

5.3.10 Effect of laser repetition rate

From the literature it is known that ablation efficiency should scale linearly with repetition rate [58], [33],[5]. This would be in agreement with the ablation model 1 developed earlier in the chapter. However, this is only true for laser systems that maintain the same pulse duration and pulse energy over the increasing repetition rates. With the experimental laser system used, the pulse duration increases linearly from 500 pS at 10 kHz RR to 2096 ps at 70 kHz RR, with the pulse energy reducing in a log fashion (Adj. $R^2 = 0.95$) from 147 µJ to

55 µJ, with a fluence of 0.62 J/cm², approaching the F_{th}^{app} of 0.35 J/cm². It's clear that the productivity results achieved are a function of several interacting and interconnected parameters, based on the experimental laser system employed. The following interconnected effects are expected to influence the productivity with increased RR:

- Increasing the RR at a constant scan speed will reduce the laser temporal avoidance of the cavitation bubble.
- Increasing the RR will provide a log reduction in E_0.
- Increasing RR will linearly increases τ_p.
  - Increasing τ_p will in turn raise F_{th}^{app} and elevate heating on the target.
- Increase RR will raise average power applied to target per unit time.
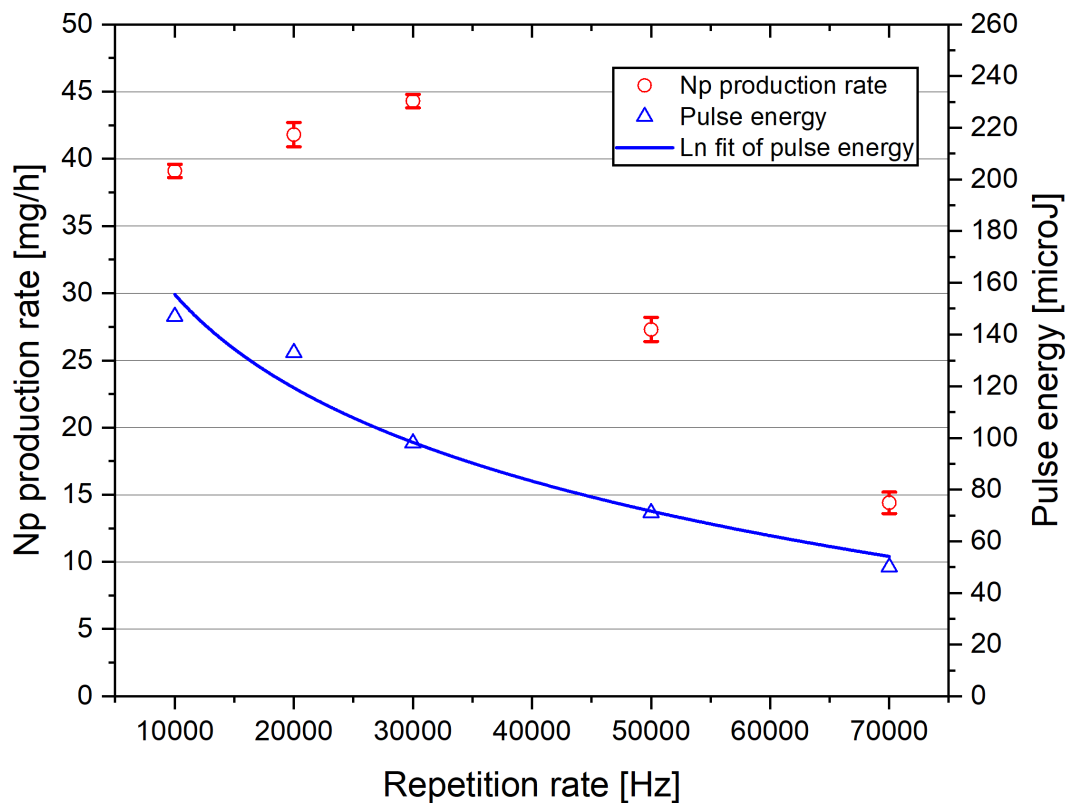
Figure 5.18: Effect of repetition rates on Np productivity, Conditions:2 bar flow cell pressure, 140 ml/min flowrate, laser fluence 1.83 J/cm² & scan speed 2mm/s, 15-minute ablation. Pulse energy log fit with RR, Adj.R²=0.95, E₀=-52.1ln(x)+635.4.

Achieving maximum productivity from the experimental laser system is the main aim of the work therefore the effect of repetition rate on productivity was evaluated for the maximum available E_0 at each RR tested. The highest ablation efficiency reached was 44.3 mg/h at 30

kHz RR, and 98 μJ E_0, as illustrated in *Figure 5.18*, with a confidence interval from the mean of 0.5 mg/h, producing a Np colloid with 75.5 nm peak diameter and Gaussian width of 60 nm pre-filtration (post-filtered peak: 65 nm ± 39 nm). The Nps productivity did not follow the pulse energy log decline response to increasing RR, therefore for this experimental system it can be concluded that E_0 is not the sole parameter effecting productivity. The UV-vis spectra taken after 30 s of each continuous ablation is displayed in Figure 5.19, the absorptions are in alignment with the gravimetrical ablation data, with 30 kHz providing the highest concentration Np colloid.

Looking at ablation craters in Figure 5.14, the increased efficiency must be aided by increased thermal effects at 30 kHz RR, as melt is observed within the ablation crater. This localised heating would also contribute to reducing the ablation fluence threshold at the heated site [23]. At the low scan speeds used in this work, temporal avoidance is aided by fluid flow to remove occluding particles from the ablation site, temporal avoidance of the cavitation bubble is expected to be the primary avoidance mechanism. Thus, increasing RR and τ_p would increase the pulse overlap and occlusion potential of the cavitation bubbles.
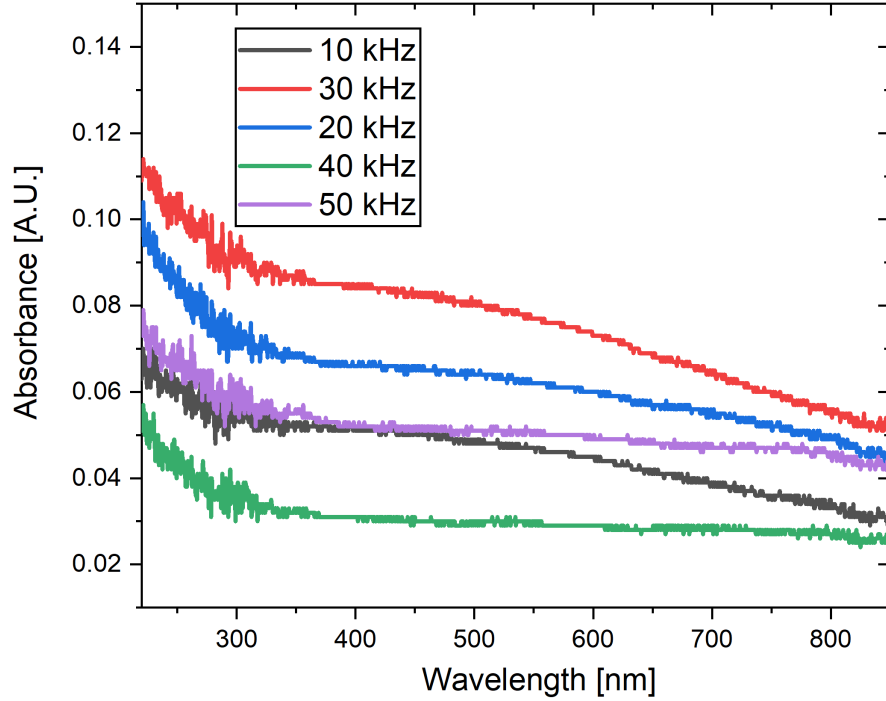
Figure 5.19: UV-vis spectra for SiNps produced in continuous flow mode (140 ml/min), at ablation time, t = 30s, max operational E_0 at each RR. 30 kHz RR, 98 μJ E_0 produced the most concentrated colloid.

Figure 5.20 compares the models developed earlier in the chapter with experimental data. All models include the experimental values for E_0 and RR. Model 1 does not account for changes in τ_p with RR, which can be determined as significant, as the model diverges from experimental values with changing τ_p. Models 2 & 3 include a factor for τ_p, and their prediction performance is closer to experimental data. Both models show a productivity peak between 10 and 30 kHz RR. It is assumed that above 30 kHz, the pulse energy has reduced by a greater degree than the thermal build-up in heat affected zone, which helps to decrease the ablation threshold [23]. Therefore, above 30 kHz RR the balance between E_0, RR, P_{ave}, τ_p and the heat affected zone lowers ablation efficiency. The relative errors (R.E.) and mean relative errors (M.R.E) of all models for the experimental space is described in Table 5.10. Each model predicts 10 kHz well, as expected given that F_{th}^{app} is determined at this RR. Model 2 maintains a MRE of 25.7% up to 30 kHz, after which the model starts diverging from experimental data. Comparatively Model 3 accounts for changing τ_p better, with MRE of 18.3% up to 50 kHz RR, and a MRE for all data points of 26.7%.

At the repetition rates tested the cavitation bubble will be irradiated, as its lifecycle (100-200 μs) is longer than the pulse rates tested (100 μs @ 10 kHz - 14 μs @ 70 kHz). It is expected from the literature that the cavitation bubble is not spatially by-passed at scan speeds tested in this study, given that the bubble radius is assumed to be approximately 100 μm for 1.6 J/cm^2 fluence irradiation [59]. The inter-pulse distance for the tested rep-rates can be seen in Table 5.9. At 10kHz RR and 2mm/s SS, the 100 μm cavitation bubble, with a lifecycle of 100 - 200 μs would be struck once or twice by the laser beam before it has been temporally and spatially by-passed. However it has been noted that pressure can have a significant effect on cavitation bubble lifecycle and diameter [2], reducing the cavitation bubble radius and collapse time. Time resolved OES, shadowgraphy imaging or single pulse ablation tests would be required to investigate the physical parameters in more detail [13].
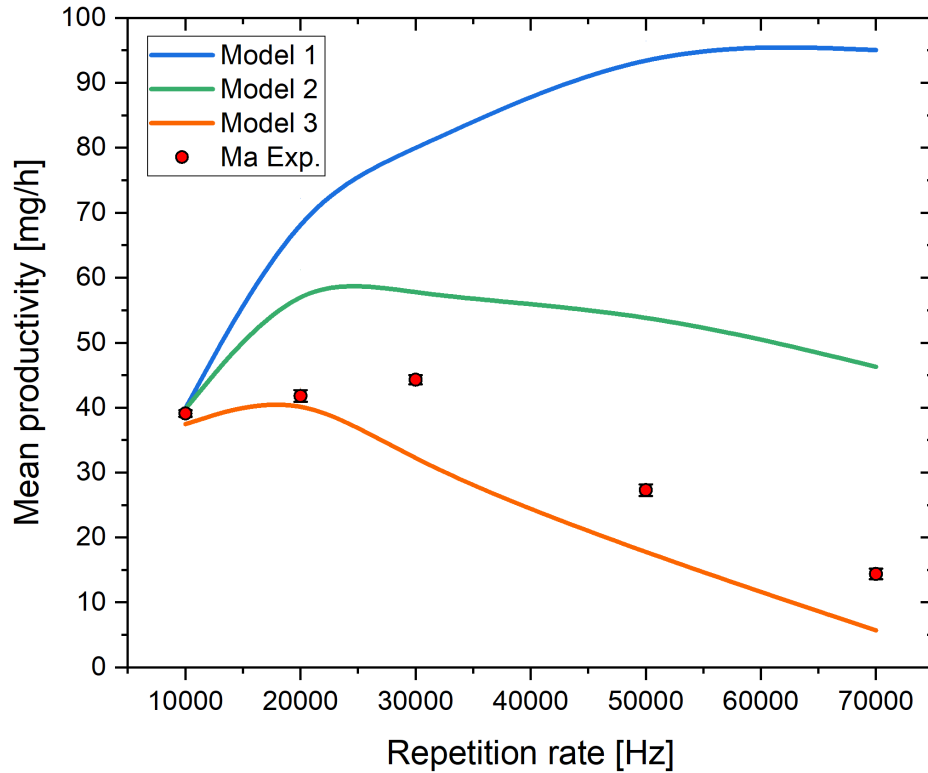
Figure 5.20: Plot of models developed compared with experimental data of productivity for changing repetition rate.

It can be concluded that pulse duration plays a significant role in productivity. In Model 1, τ_p is not accounted for, leading to prediction divergence with increasing RR and τ_p. Models 2 and 3 account for τ_p and provide better prediction of the complex experimental mechanisms including the interacting and interconnected effects of E_0, RR, τ_p and bulk target heating. Both models show a peak response between 15 - 30 kHz with significant reductions

in production after that, which is representative of the experimental data. The assumed relationship between F_{th}^{app} and τ_p in Model 2 overestimates the production ability with increasing RR. Model 3 best fits the experimental data, therefore heating and energy absorption into the bulk material must play a significant role in the ablation mechanism, as they are accounted for in the experimental fit of k. From these tests it is clear that with ablation in liquids is a complex multivariate response system, that would need significant additional work to provide a more accurate model of the system.

Table 5.10: Prediction relative error for models 1, 2 and 3.

RR (Hz)	Model 1 R.E. (%)	Model 2 R.E. (%)	Model 3 R.E. (%)
10000	2.1	1.8	4.2
20000	72.8	46.5	3.0
30000	80.2	28.9	29.9
50000	253.1	101.0	35.9
70000	560.0	221.4	60.3
M.R.E (%)	193.6	79.9	26.7

5.3.11 Repetition rate effect on Np size

Changes in repetition rate have been reported to affect Np size, Menendez et al., (2011) described a reduction in AuNps size dispersion and increase in productivity under increasing repetition rates (0.1 - 6 kHz) using a fs laser system in semi-batch production, they stated the size reduction was due to increased nano colloid photofragmentation [60]. However, it's assumed that due to the high flowrates and the RRs employed in this study including a small laser spot size compared to the flow-cell channel, minimal photofragmentation would occur in the current setup. No significant change after 10 kHz RR was observed over the repetition rate range tested in this work. Colloids produced at 10 kHz possessed a slightly higher (100 nm ± 37 nm) peak diameter compared with those produced at higher repetition rates (80 nm ± 37 nm @ 20kHz RR). This would indicate that either a small population of larger particles are being produced at 10 kHz, possibly as a function of the higher pulse energy. Or it is possible that photo-fragmentation of larger particles (100 - 200 nm approx.) occurs at repetition rates from 20 kHz onwards. Zamiri et al. (2013) reported similar size behaviour

to our findings [61]. Post-filtration (0.2 µm) removed the larger colloids, indicating a similar peak diameter (65 nm ±15) and size distribution throughout the repetition rate range tested. This indicates that the larger particles measured at 10kHz are skewing the size population reported due to the DLS measurement technology.
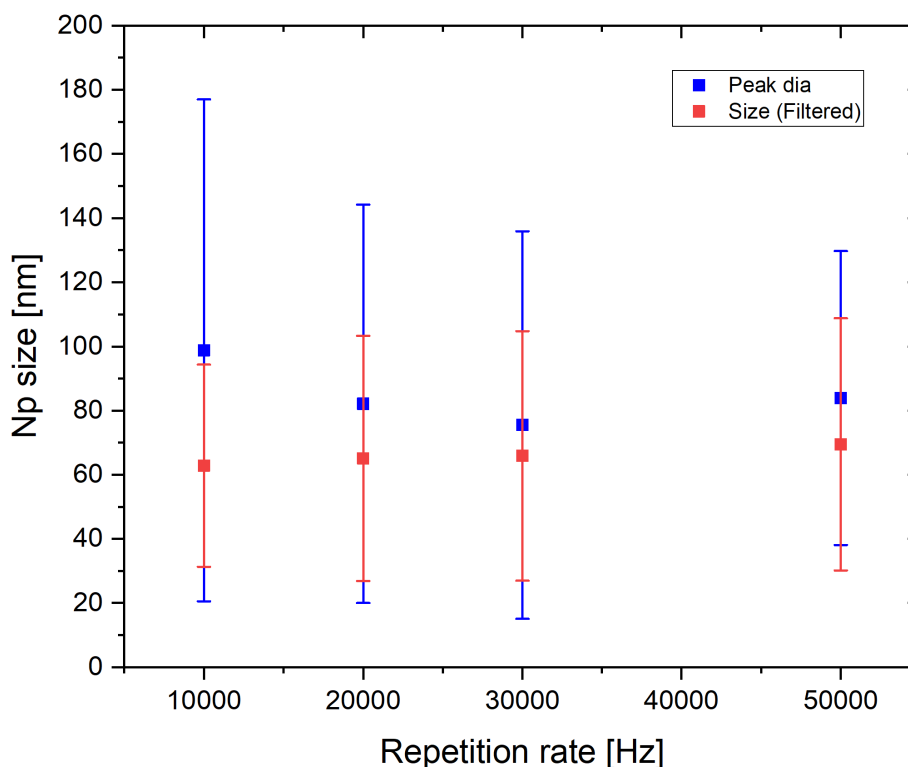
Figure 5.21: Np size dispersion over varied RRs for tests outlined in this section (n=3)

5.3.12 Summary of SiNps size production

Throughout this work a defined range of SiNps have been produced. The solvent has remained constant (no addition of salts) therefore only physical effects from the laser and liquid conditions have impacted the plasma and cavitation bubble, resulting in Nps size changes as illustrated in Figure 5.22. SiNps of diverse size ranges (55 nm to 119 nm) have been fabricated in this work the smallest peak diameter of 55 nm ± 35 nm achieved in batch mode. The smallest size dispersion of a Nano colloid produced in continuous mode was 75 nm ± 15 nm under 1 bar ambient pressure and a liquid flowrate of 140 ml/min with maximum fluence of 1.83 J/cm^2. It was seen that increasing ambient pressure would reduce the peak diameter (55 nm) but also increase the colloid size dispersion. Increasing fluence from 1.05 J/cm^2 to 1.83 J/cm^2 was seen to increase Nps peak diameter by 32 nm. Post-filtration (0.2

μm) is a successful technique to produce colloids of even size dispersion and could reduce the measured peak diameter by up to 40 nm.
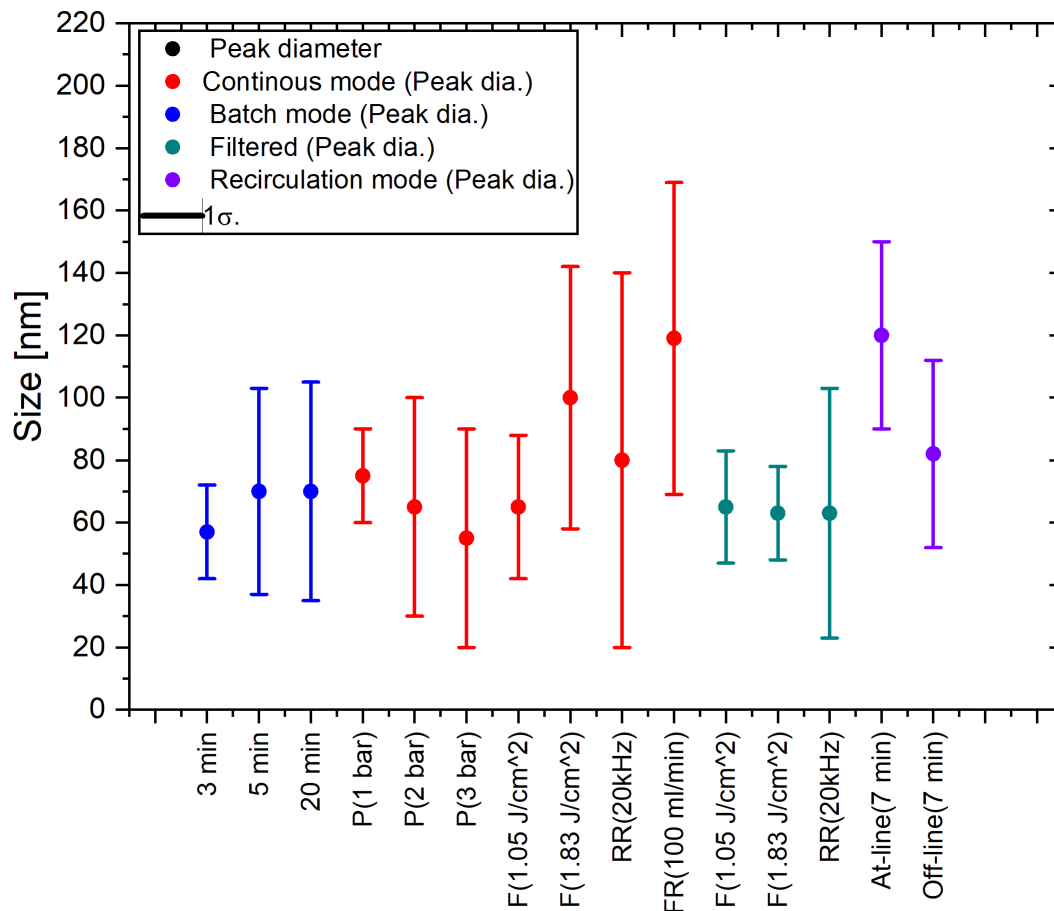
Figure 5.22: Summary of SiNps size dispersions fabricated via LASiS via batch, continuous and recirculation production. The smallest size dispersion was observed under batch production or post-filtration of samples. The largest size dispersion was observed under continuous production at 20 kHz RR and τ_p= 778 ps.

5.3.13 Comparison with best in class

A summary of the highest production values achieved during testing is illustrated in Figure 5.23, The highest productivity of 44.3 mg/h was achieved using the following conditions; F= 1.3 J/cm^2, RR= 30 kHz, 1 bar gauge pressure and 140 ml/min. However, the highest productivity did not yield the highest power-specific productivity, the performance parameter of note for comparison of Np production systems. At 30 kHz RR the laser provides 2.94 W average power compared with 1.47 W at 10 kHz. The highest power-specific productivity of 27.7 mg/Wh was achieved at F = 1.83 J/cm^2, RR= 10 kHz, SS = 2 mm/s, P

= 3 bar, FR = 140 ml/min. This value compares very favourably (×7) with the highest reported for SiNps production as 3.6 mg/W h by Kudryashov et. al. (2019).
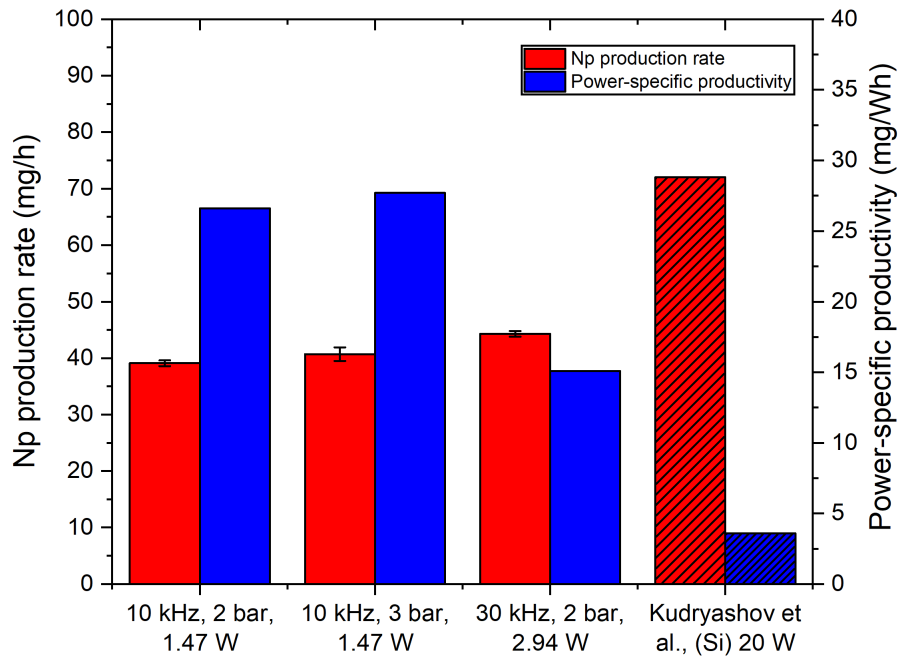
Figure 5.23: Summary graph of the highest performing conditions for SiNps productivity and power-specific productivity compared with best reported for SiNps.

5.4   Rapid multiple material tests

5.4.1   Overview

A series of tests were conducted, producing commonly researched Np materials in order to compare the developed production system with the state of the art reported. In literature Gold has been selected as the performance bench-mark material for LASiS productivity. This is due in-part to its numerous applications in the electronics and medical industry. Zinc and silver were selected as they are some of the most widely applied Nps in commercial use and in research today.

5.4.2   Target selection

Gold plate (99.998% metals basis, Alfa Aesar), silver plate (>99.999% metals basis, Scottsdale bullion silver) and Zinc rods (10 mm, 99.9998% metals basis, Alfa Aesar) were machined and mechanically polished to produce discs of 8 mm outer diameter and 4 mm

thickness. Np size dispersion was measured off-line using the DLS and compared with TEM analysis.

5.4.3   Methods

Continuous production tests were conducted, to identify the optimum operational repetition rate for each material. UV-vis measurements were taken at-line after 30 s ablation at each repetition rate setpoint under standard flow conditions (100 ml/min, 1 bar). The absorption of the UV-vis spectra was considered an indication of the Np colloid concentration and infers the production efficiency of the laser conditions. After initial test were completed, a 15-minute productivity test was conducted for each material (5 minutes for gold due to resource limitations) at their optimum repetition rate under continuous flow conditions of 140 ml/min, 1 bar gauge pressure, unless otherwise stated) and maximum operational pulse energy (E_0) at the chosen repetition rate.

5.4.4   Multiple material results

5.4.4.1   Size, morphology and optical results

Off-line DLS measurements of colloids produced are reported in Table 5.11 and Table 5.12. AgNps were seen to have a peak diameter of 3.1 nm ± 1.2 nm, AuNps possessed a peak diameter of 2.6 nm ± 0.7 nm, produced at 1 bar and no significant measured change in the Nps produced at 2 bar gauge pressure (2.5 ± 0.9 nm). The ZnO Nps produced in DI water contained a larger size distribution with a peak diameter of 77 nm ± 58 nm. A selection of LASiS produced colloids were imaged via TEM as illustrated in Figure 5.25 and all particles were spherical in shape.

At-line measured UV-vis optical spectra for each material are displayed in Figure 5.24. Under high flow conditions, low Np colloid concentrations were produced for each material. A repetition rate of 20 kHz (E_0=133 µJ) was observed to produce the highest concentration Nps colloid for all materials tested. The visual inspection of colloids produced for all tests (inserts pictures in Figure 5.24) are in alignment with the UV-vis absorption results. AgNps colloids displayed in Figure 5.24 (a) indicate a plasmonic peak at 390 nm under 20 kHz RR, similar to LASiS produced Nps reported in literature with SPR at 400 nm and diameter of 10 nm [62]. AuNps contained a plasmonic peak at 520 nm and this is in agreement with

results reported in chapter 4, and those reported previously with a SPR at 517 nm for Np size of 9 nm [63].

The optical absorption spectra of the ZnO displayed a shoulder between 340 - 380 nm, similar to those produced via LASiS by Kim et al., using a 1064 nm laser with DI water as a solvent [64].
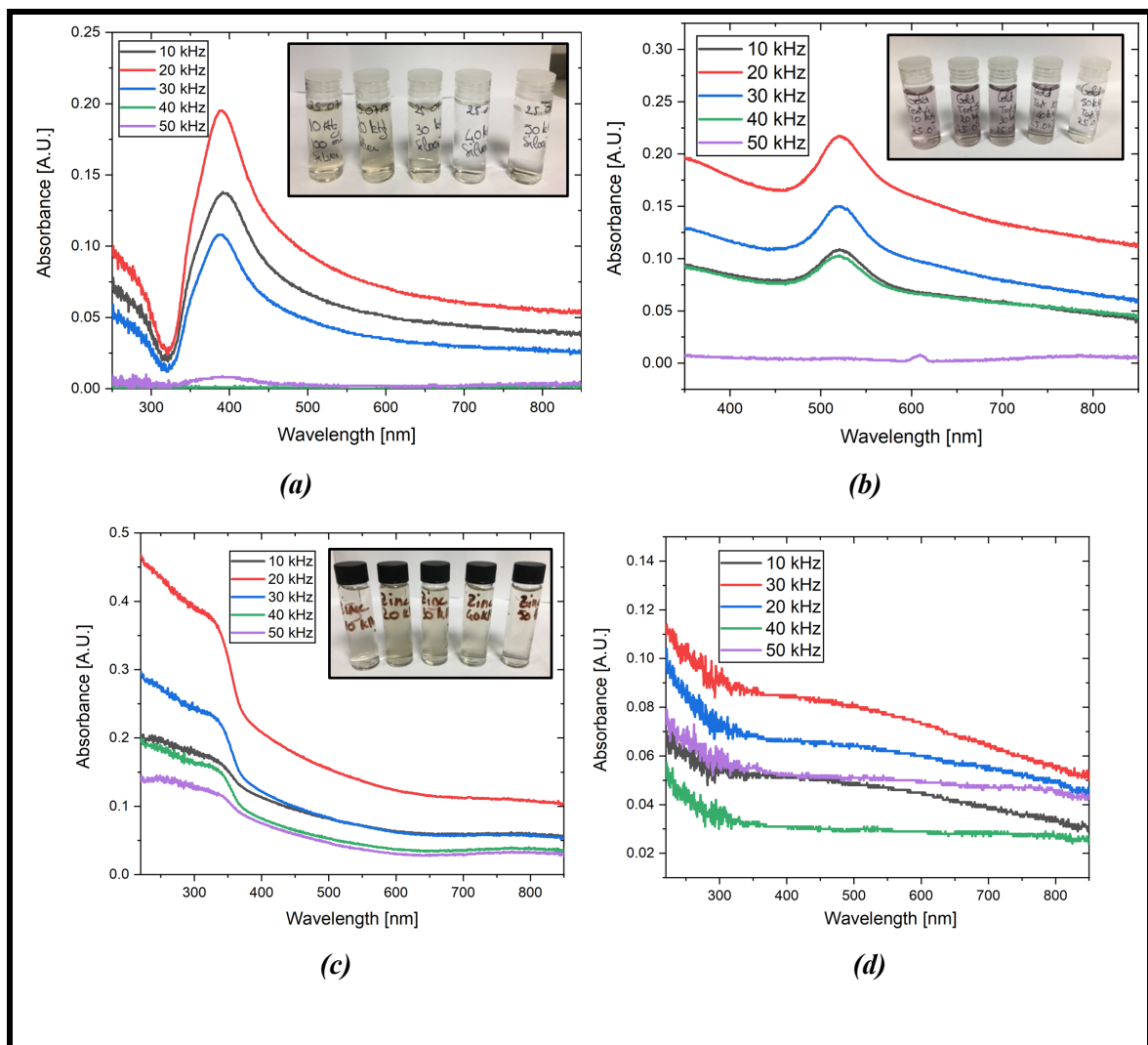
Figure 5.24: UV-vis spectra for Ag (a), Au (b), ZnO (c) and Si (d) Nps, produced in continuous flow mode ((a-c) @100 ml/min, (d)@ 140 ml/min), time = 30 s, max operational E_0 for each RR. 20kHz RR, 133 µJ E_0 produced the most concentrated colloid for all materials tested, n=1.
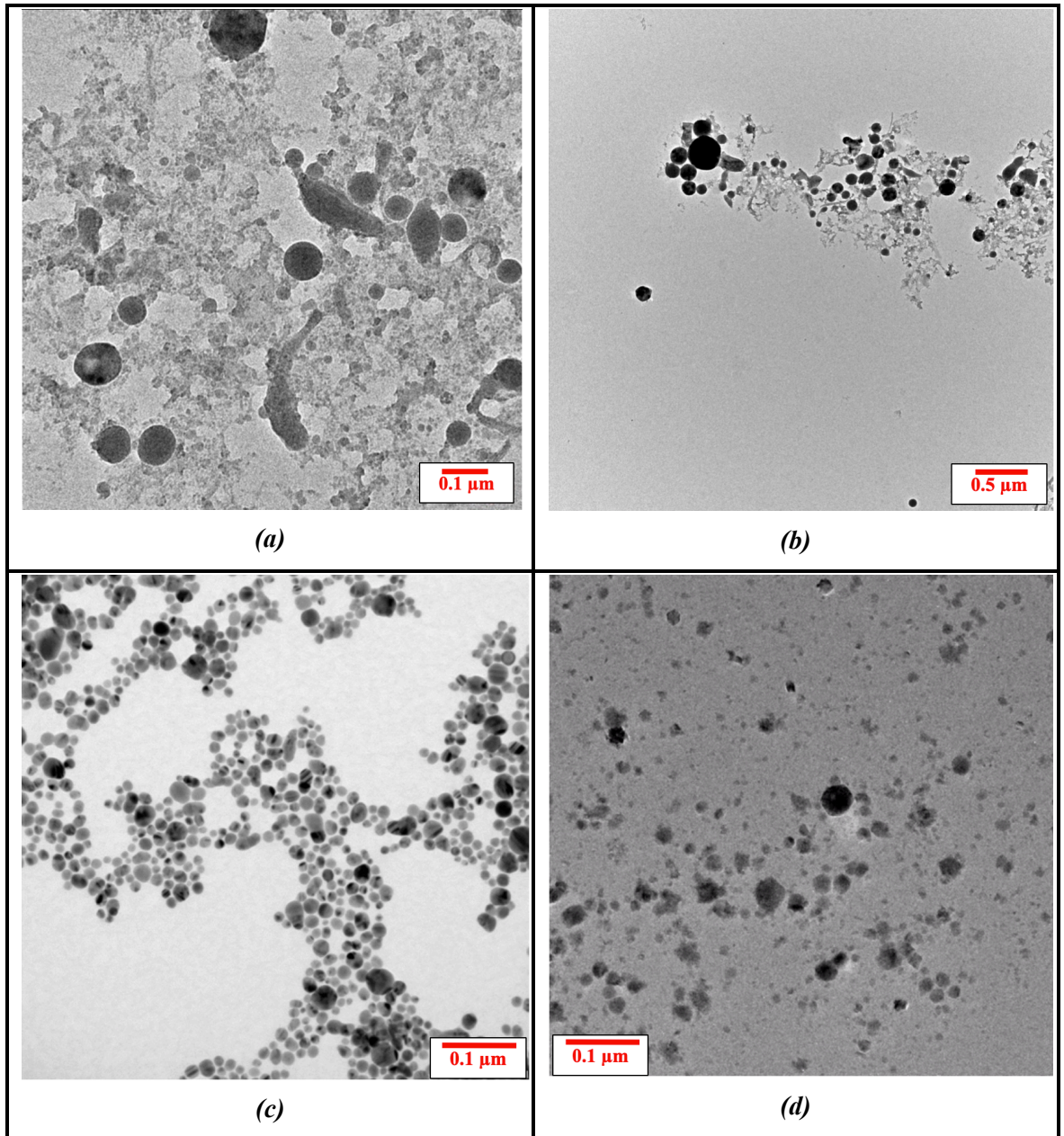
Figure 5.25:TEM images of a selection of Nps produced in this study (a). SiNps produced at 1 bar gauge pressure (30 kHz RR, $E_0 = 98$ µJ, sample 30), (b). SiNps produced at 2 bar gauge pressure, (c). AgNps produced at 20 kHz RR, $E_0 = 133$ µJ, 1 bar gauge pressure and (c.) ZnO Nps produced at 20 kHz, $E_0 = 133$ µJ, in IPA.

5.4.4.2 Productivity results

Productivity results from the optimised ablation tests of Ag, Au and ZnO targets in DI water was compiled and compared against the AuNps production of a "middle class" laser yields of 39.6 mg/h AuNps from Dittrich et. al., (2019). As illustrated in Figure 5.26 the selected highest production rates of SiNps (RR = 10kHz, $E_0 = 147$ µJ & RR = 30 kHz, $E_0 = 98$ µJ),

discussed earlier in the chapter were included for comparison also. All materials tested yielded higher productivity rates than those achieved by Dittrich et. al., (2019), while employing lower average laser powers 1.47 W and 2.9 W compared with 6.1 W [1]. The highest productivity of 151.5 mg/h (SD = 14.4 mg/h) was achieved irradiating a Zinc target, producing a colloid of 13 mg/l as described in Table 5.12.
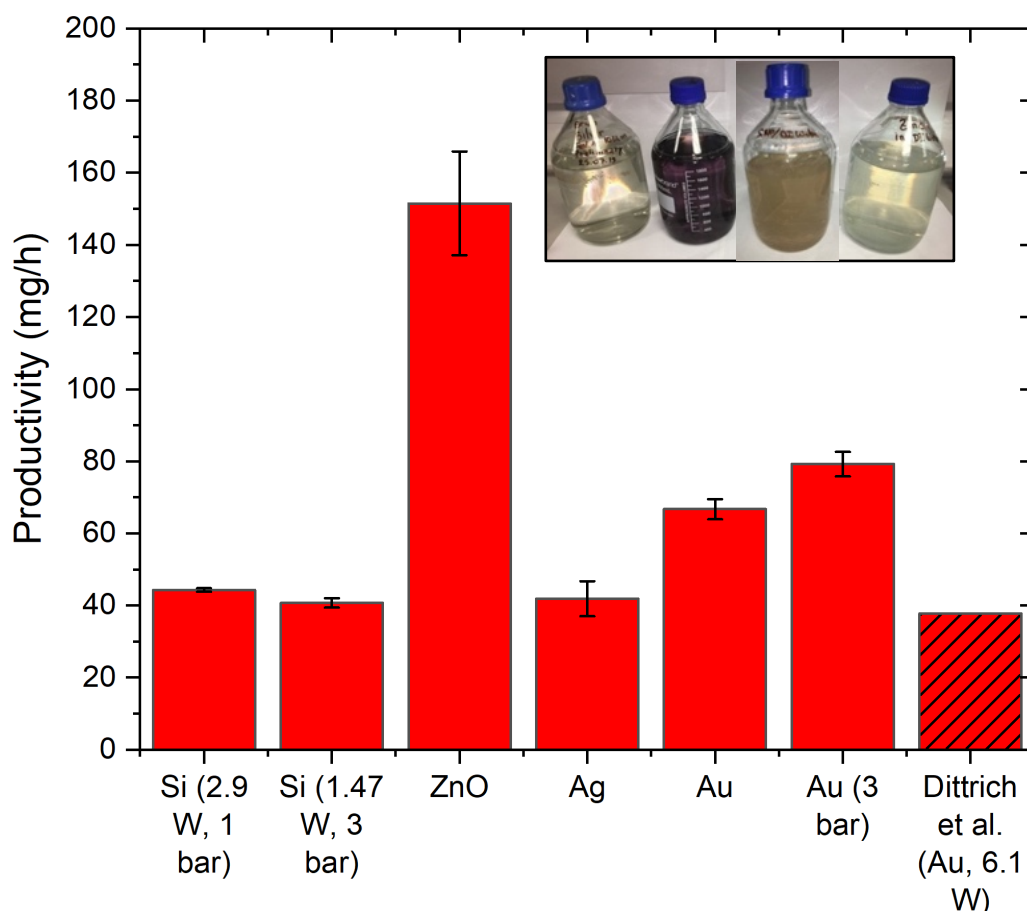
Figure 5.26: (a) Productivity for Si, Ag, Au and ZnO Nps fabrication under continuous flow conditions (140 ml/min) at 1 bar gauge pressure (unless otherwise stated), SiNps 10 kHz & 30 kHz, all other material 20 kHz RR, 2 mm/s scan speed (n=3). Results compared with the best-in-class reported for a medium-class laser system (6 W) tested by Dittrich et. al., 2019. (Insert): 2 litre bottles of Nps colloids produced from Ag, Au, Si and ZnO.

Gold was tested under 1 bar and 2 bar operational pressures. As seen previously for silicon target testing, an increase in chamber pressure resulted in higher production rates, increasing from 66.7 mg/h (SD = 2.8) to 79.2 mg/h (SD = 3.4) at 3 bar, markedly higher than the productivity achieved by Dittrich et. al. (2019) for a 10 s test. For better comparison all productivity results were converted to power-specific-productivity as shown in Figure 5.27.

The highest power-specific productivity was achieved for ZnO Nps production of 57.2 mg/Wh. Gold Nps were produced at 29.9 mg/Wh, the highest recorded efficiencies for a "middle" or "high-end" laser systems reported to date, comparing well with Sajti et al. (2009) who achieved 32.5 mg/Wh ablating AI_2O_3 pressed powder [25], Kohsakowski et. al. (2017) achieving 16.9 mg/Wh for AuNps production and a maximum efficiency of 6.5 mg/W h for a "middle class" system.
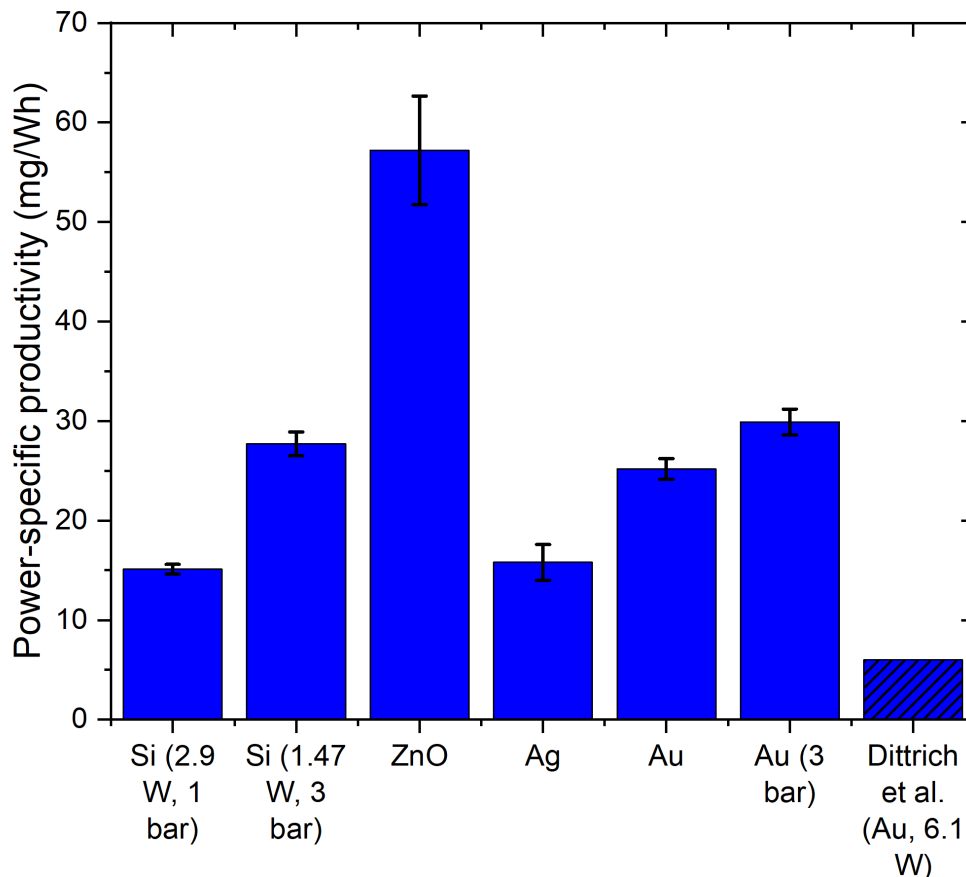
Figure 5.27: Power-specific productivity tested for optimum conditions of Si, Ag, Au and ZnO Nps compared with best-in-class for middle class laser system[1].

These results indicate that the system is performing well, with high efficiencies attained by the removal of occluding particles and bubbles from the ablation site. However, a "compact class" system has reported AuNps production efficiencies of 42.5 mg/Wh, while operating at a low fabrication rate of 6.12 mg/h [1]. This low production rate and low average power output (0.15 W) would provide ablation efficiency advantages due to the low concentration of particles occluding beam irradiation and lower power outputs producing smaller volume cavitation bubbles, and hence a more efficient process. Higher power-specific productivities for AuNps may be possible by operating the experimental laser system at 10 kHz RR rather

than the optimum productivity setpoint of 20 kHz, due to the lower power applied at 10 kHz. However a balance needs to be struck between maximising production yield and production efficiency.

Table 5.11: Np properties of Si and Ag Nps produced at optimum production conditions in continuous mode.
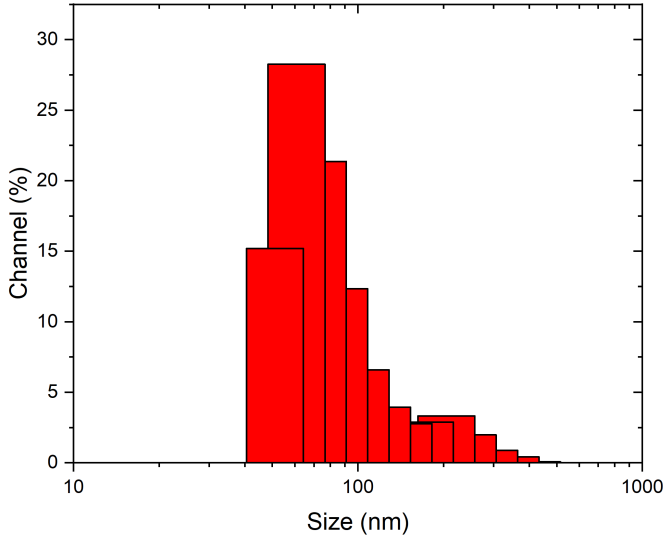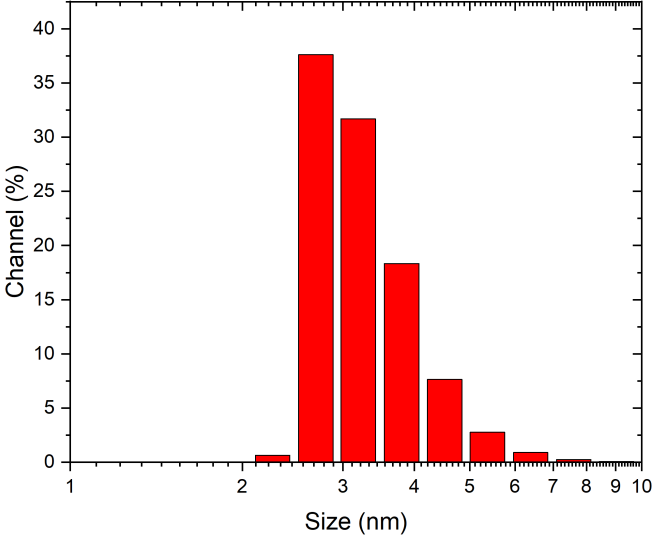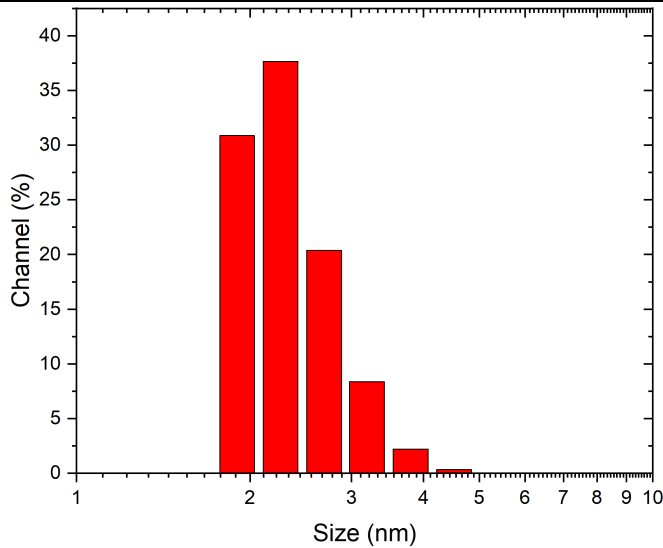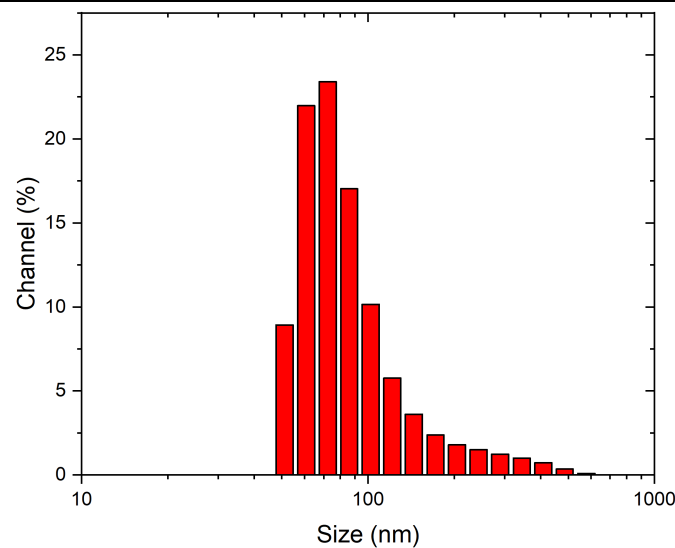
Material	Si Nps	Ag Nps
Np size Off-line DLS measurement (unfiltered, n=3).		
	78 nm ± 60 nm	3.1 nm ± 1.2 nm
Optical/ plasmon response	Characteristic shoulder at 500 nm, with a decline from 200 nm to 800 nm [65].	SPR: 385 nm
Photo- luminescence	E_m: 300 nm	E_m: 488 nm
Concentration	5 mg/l	7 mg/l

Table 5.12: Np properties of Au and ZnO Nps produced at optimum production conditions in continuous mode.

Material	Au Nps	ZnO Nps
Np size Off-line DLS measurement (unfiltered, n=3).		ZnO in H_2O
	2.6 nm ± 0.7 nm @ 1 bar, 2.5 nm ± 0.9 nm @ 3 bars	77 nm ± 58 nm in H_2O, 55 nm ± 47 nm in IPA
Optical/ plasmon response	SPR: 520 nm	No SPR present in ZnO/DI water suspension
Photo- luminescence	E_m: 560 nm	-
Concentration	11 mg/l	13 mg/l

5.4.5 *Commercial outlook*

To assess the commercial outlook of the production system developed the optimised productivity of AuNps was compared with best published to date. The costs were determined based on the reported work of Jendrzej et. al.,(2017) which describe the LASiS total production costs and compare it with a developed chemical synthesis process (Turkevich method). These calculations are described in Appendix 1.a. & 1.b. They include, capital expenses, labour, materials (bulk target), maintenance, depreciation and electrical usage required to produce 1 gram of AuNps. Including Irish labour costs (grade 1 research assistant), it would cost $323.3 to produce 1g of gold nanoparticles. For ease of comparison including USA labour costs documented by Jendrzej et. al.(2017), this equates to $354.5/g AuNps. These costs compare favourably with the reported LASiS production costs of $544.4/g [66] and, more strikingly are lower than high volume estimates for wet chemical synthesis estimated at $373/g. Therefore, by optimising the LASiS productivity of a low-cost laser system this work was able to reach and slightly undercut cost-parity with chemical synthesis of Gold Nano colloid.

5.5 Conclusions

Three new models were developed to predict SiNp production rates during LASiS. Model 1 was based on an existing published model, with new model parameters determined from fits of experimental data. Model 1 achieved an MRE of 7% from the 10 kHz experimental data and predicted that a 37 W laser system would be required produce 1 gram of SiNps. Models 2 and 3 were developed to account for pulse duration, compared with experimental data they followed the trend of production over a range of increasing repetition rates and pulse durations. Model 3 achieving an MRE of 3.6% for experiments conducted between 10 kHz-20 kHz RR, with an overall MRE of 26.7 % from 10 kHz RR to 70 kHz. These results compare favourably with Model 1 that achieved 193% MRE over the same experimental space.

Process parameters such as solvent flow rate, pressure, laser scan speed, fluence and repetition rates were tested in a single factor fashion to yield process understanding and move towards process optimisation. It should be noted that the process response to variables was inferred from a combination of sources including experimental results, theoretical models developed in this chapter and results published literature. To attain a more clear

understanding of the mechanisms of interactions between all the process variables involved, advanced techniques such as nanosecond-imaging, shadowgraphy and optical emission spectroscopy (OES) should be employed to monitor the plasma and cavitation bubble response to process change. This would require a completely new line of research, not within the scope or timescale of this work.

It was seen that changes in process conditions had a major impact on productivity, the effect on size dispersion was less dramatic, producing colloids with size ranges between 75 nm – 119 nm. Research has indicated that lower repetition rates (1 - 5 Hz) can provide different SiNps sizes, but utilising lasers at such low RRs could reduce the Nps production efficiency and was outside the scope of this work. For future work it has been noted in research that salts can have quenching effects on Nps aggregation during the growth phase and produce colloids with distantly smaller peak diameters, also the use of solvents such as EtOH have produce SiNps with smaller sizes, due in part to the physical parameters of the solvent effecting the cavitation bubble and passivation effects on the seeding particles. The application of a new 3D printed flow-cell developed in chapter 4, has resulted in a highly efficient process. The outcome of the process optimisation for silicon nanoparticle production yielded the highest production efficiencies reported to date for the material. The process was also seen to be highly repeatable with productivity offering a variance of 1.1% from the process mean (95% CI).

Based on the optimised process flow conditions, tests were performed on common material targets. Power-specific productivities for zinc oxide, gold and silicon nanoparticles were seen to be higher than published for a "middle-class" and "high-end laser" systems. The efficiency increases resulted in a lower cost production rate for gold Nps, the standard material for production cost comparisons of synthesis techniques. It was concluded that the costs to produce 1 gram of AuNps using the experimental system would be less than other LASiS process published to date and indeed chemical synthesis described in literature. This offers a new route towards production of Nps, rather than applying the approach of utilising a high-power, high-cost laser systems to reach cost-parity with chemical synthesis at high production quantities, a high efficiency, low-cost system can provide a feasible alternative.

5.6   References

[1]   S. Dittrich, R. Streubel, C. McDonnell, H. P. Huber, S. Barcikowski, and B. Gökce, "Comparison of the productivity and ablation efficiency of different laser classes for laser ablation of gold in water and air," *Appl. Phys. A Mater. Sci. Process.*, vol. 125, no. 6, pp. 1–10, 2019.

[2]   J. Tomko *et al.*, "Cavitation bubble dynamics and nanoparticle size distributions in laser ablation in liquids," *Colloids Surfaces A Physicochem. Eng. Asp.*, vol. 522, pp. 368–372, 2017.

[3]   S. Barcikowski *et al.*, "HANDBOOK OF LASER SYNTHESIS OF COLLOIDS," 2016.

[4]   R. Intartaglia *et al.*, "Optical properties of femtosecond laser-synthesized silicon nanoparticles in deionized water," *J. Phys. Chem. C*, vol. 115, no. 12, pp. 5102–5107, 2011.

[5]   R. Intartaglia, K. Bagga, and F. Brandi, "Study on the productivity of silicon nanoparticles by picosecond laser ablation in water: towards gram per hour yield.," *Opt. Express*, vol. 22, no. 3, p. 3117, 2014.

[6]   D. Zhang, B. Gökce, and S. Barcikowski, "Laser Synthesis and Processing of Colloids: Fundamentals and Applications," *Chem. Rev.*, vol. 117, no. 5, pp. 3990–4103, 2017.

[7]   R. Streubel, G. Bendt, and B. Gökce, "Pilot-scale synthesis of metal nanoparticles by high-speed pulsed laser ablation in liquids," *Nanotechnology*, vol. 27, no. 20, 2016.

[8]   D. Cenide, R. Streubel, N. Bärsch, and S. Barcikowski, "Advanced liquid flow reactor design for laser ablation in liquid Motivation : Task : Continuous Fabrication of Nanoparticles State of the art : Stationary ablation Task : Properties : Production Chamber : Laser Bio-conjugation Chamber," vol. 115, no. May, pp. 6–7, 2012.

[9]   L. V. Zhigilei, E. Leveugle, B. J. Garrison, Y. G. Yingling, and M. I. Zeifman, "Computer simulations of laser ablation of molecular substrates," *Chem. Rev.*, vol. 103, no. 2, pp. 321–347, 2003.

[10]   J. Zou, C. Wu, W. D. Robertson, L. V. Zhigilei, and R. J. D. Miller, "Molecular dynamics investigation of desorption and ion separation following picosecond infrared laser (PIRL) ablation of an ionic aqueous protein solution," *J. Chem. Phys.*, vol. 145, no. 20, 2016.

[11]   C. Y. Shih *et al.*, "Two mechanisms of nanoparticle generation in picosecond laser

ablation in liquids: The origin of the bimodal size distribution," *Nanoscale*, vol. 10, no. 15, pp. 6900–6910, 2018.

[12]   C. Y. Shih, C. Wu, M. V. Shugaev, and L. V. Zhigilei, "Atomistic modeling of nanoparticle generation in short pulse laser ablation of thin metal films in water," *J. Colloid Interface Sci.*, vol. 489, pp. 3–17, 2017.

[13]   S. Ibrahimkutty *et al.*, "A hierarchical view on material formation during pulsed-laser synthesis of nanoparticles in liquid," *Sci. Rep.*, vol. 5, pp. 1–11, 2015.

[14]   A. Letzel *et al.*, "Size Quenching during Laser Synthesis of Colloids Happens Already in the Vapor Phase of the Cavitation Bubble," *J. Phys. Chem. C*, vol. 121, no. 9, pp. 5356–5365, 2017.

[15]   S. Ibrahimkutty, P. Wagener, A. Menzel, A. Plech, and S. Barcikowski, "Nanoparticle formation in a cavitation bubble after pulsed laser ablation in liquid studied with high time resolution small angle x-ray scattering," *Appl. Phys. Lett.*, vol. 101, no. 10, 2012.

[16]   S. Reich *et al.*, "Pulsed laser ablation in liquids: Impact of the bubble dynamics on particle formation," *J. Colloid Interface Sci.*, vol. 489, pp. 106–113, 2017.

[17]   A. De Giacomo, A. De Stradis, A. Santagata, G. Valenza, and M. Dell'Aglio, "Study of the Effect of Water Pressure on Plasma and Cavitation Bubble Induced by Pulsed Laser Ablation in Liquid of Silver and Missed Variations of Observable Nanoparticle Features," *ChemPhysChem*, vol. 18, no. 9, pp. 1165–1174, 2017.

[18]   L. Kőrösi *et al.*, "Ultrasmall, Ligand-Free Ag Nanoparticles with High Antibacterial Activity Prepared by Pulsed Laser Ablation in Liquid," *J. Chem.*, vol. 2016, pp. 1–8, 2016.

[19]   R. García-Calzada *et al.*, "Facile laser-assisted synthesis of inorganic nanoparticles covered by a carbon shell with tunable luminescence," *RSC Adv.*, vol. 5, no. 62, pp. 50604–50610, 2015.

[20]   B. Tekcan *et al.*, "A near-infrared range photodetector based on indium nitride nanocrystals obtained through laser ablation," *IEEE Electron Device Lett.*, vol. 35, no. 9, pp. 936–938, 2014.

[21]   A. Barchanski *et al.*, "Bioconjugated gold nanoparticles penetrate into spermatozoa depending on plasma membrane status," *J. Biomed. Nanotechnol.*, vol. 11, no. 9, pp. 1597–1607, 2015.

[22]   S. Barcikowski *et al.*, "Handbook of Laser Synthesis of Colloids," 2016.

[23]   J. Thorstensen and S. Erik Foss, "Temperature dependent ablation threshold in silicon using ultrashort laser pulses," *J. Appl. Phys.*, vol. 112, no. 10, 2012.

[24] C. L. Sajti, R. Sattari, B. Chichkov, and S. Barcikowski, "Ablation efficiency of α-Al2O3 in liquid phase and ambient air by nanosecond laser irradiation," *Appl. Phys. A Mater. Sci. Process.*, vol. 100, no. 1, pp. 203–206, 2010.

[25] C. L. Sajti, R. Sattari, B. N. Chichkov, and S. Barcikowski, "Gram scale synthesis of pure ceramic nanoparticles by laser ablation in liquid," *J. Phys. Chem. C*, vol. 114, no. 6, pp. 2421–2427, 2010.

[26] A. Kosmala, R. Wright, Q. Zhang, and P. Kirby, "Synthesis of silver nano particles and fabrication of aqueous Ag inks for inkjet printing," *Mater. Chem. Phys.*, vol. 129, no. 3, pp. 1075–1080, 2011.

[27] M. Rosa *et al.*, "Zirconia nano-colloids transfer from continuous hydrothermal synthesis to inkjet printing," *J. Eur. Ceram. Soc.*, vol. 39, no. 1, pp. 2–8, 2019.

[28] M. Chien Dang, T. M. Dung Dang, and E. Fribourg-Blanc, "Silver nanoparticles ink synthesis for conductive patterns fabrication using inkjet printing technology," *Adv. Nat. Sci. Nanosci. Nanotechnol.*, vol. 6, no. 1, 2015.

[29] C. Campos-cuerva, M. Zieba, and V. Sebastian, "Screen-printed nanoparticles as anti-counterfeiting tags," 2016.

[30] J.-W. Jeon, S. Yoon, H. Choi, J. Kim, D. Farson, and S.-H. Cho, "The Effect of Laser Pulse Widths on Laser—Ag Nanoparticle Interaction: Femto- to Nanosecond Lasers," *Appl. Sci.*, vol. 8, no. 1, p. 112, 2018.

[31] M. Stafe, A. Marcu, and N. N. Puscas, *Pulsed Laser Ablation of Solids*, vol. 53. 2014.

[32] P. Wagener *et al.*, "High productive and continuous nanoparticle fabrication by laser ablation of a wire-target in a liquid jet," *Appl. Surf. Sci.*, vol. 403, pp. 487–499, 2017.

[33] G. C. Messina *et al.*, "Pulsed laser ablation of a continuously-fed wire in liquid flow for high-yield production of silver nanoparticles," *Phys. Chem. Chem. Phys.*, vol. 15, no. 9, pp. 3093–3098, 2013.

[34] R. Streubel, S. Barcikowski, and B. Gökce, "Continuous multigram nanoparticle synthesis by high-power, high-repetition-rate ultrafast laser ablation in liquids," *Opt. Lett.*, vol. 41, no. 7, p. 1486, 2016.

[35] S. I. Kudryashov *et al.*, "High-throughput laser generation of Si-nanoparticle based surface coatings for antibacterial applications," *Appl. Surf. Sci.*, vol. 470, no. November 2018, pp. 825–831, 2019.

[36] J. Ní Mhurchú and G. Foley, "Dead-end filtration of yeast suspensions: Correlating specific resistance and flux data using artificial neural networks," *J. Memb. Sci.*, vol. 281, no. 1–2, pp. 325–333, 2006.

[37] N. M. Bulgakova and A. V. Bulgakov, "Pulsed laser ablation of solids: Transition from normal vaporization to phase explosion," *Appl. Phys. A Mater. Sci. Process.*, vol. 73, no. 2, pp. 199–208, 2001.

[38] V. Schütz, U. Stute, and A. Horn, "Thermodynamic investigations on the laser ablation rate of silicon over five fluence decades," *Phys. Procedia*, vol. 41, pp. 640–649, 2013.

[39] G. Račiukaitis, M. Brikas, P. Gečys, B. Voisiat, and M. Gedvilas, "Use of high repetition rate and high power lasers in microfabrication: How to keep the efficiency high?," *J. Laser Micro Nanoeng.*, vol. 4, no. 3, pp. 186–191, 2009.

[40] F. Brandi, N. Burdet, R. Carzino, and A. Diaspro, "Very large spot size effect in nanosecond laser drilling efficiency of silicon," *Opt. Express*, vol. 18, no. 22, p. 23488, 2010.

[41] B. Neuenschwander, B. Jaeggi, M. Schmid, and G. Hennig, "Surface structuring with ultra-short laser pulses: Basics, limitations and needs for high throughput," *Phys. Procedia*, vol. 56, no. C, pp. 1047–1058, 2014.

[42] M. Harb, R. Ernstorfer, T. Dartigalongue, C. T. Hebeisen, R. E. Jordan, and R. J. D. Miller, "<Carrier relaxation and lattice heating dynamics in silicon.pdf>," pp. 25308–25313, 2006.

[43] S. Preuss, A. Demchuk, and M. Stuke, "Sub-picosecond UV laser ablation of metals," *Appl. Phys. A Mater. Sci. Process.*, vol. 61, no. 1, pp. 33–37, 1995.

[44] N. N. Nedialkov, S. E. Imamova, and P. A. Atanasov, "Ablation of metals by ultrashort laser pulses," *J. Phys. D. Appl. Phys.*, vol. 37, no. 4, pp. 638–643, 2004.

[45] R. McCann, K. Bagga, R. Groarke, A. Stalcup, M. Vázquez, and D. Brabazon, "Microchannel fabrication on cyclic olefin polymer substrates via 1064 nm Nd:YAG laser ablation," *Appl. Surf. Sci.*, vol. 387, pp. 603–608, 2016.

[46] A. A. Brand, F. Meyer, J. F. Nekarda, and R. Preu, "Reduction of picosecond laser ablation threshold and damage via nanosecond pre-pulse for removal of dielectric layers on silicon solar cells," *Appl. Phys. A Mater. Sci. Process.*, vol. 117, no. 1, pp. 237–241, 2014.

[47] S. L. A. W. Constants and J. Kuiz, "Pii: soo45-6535(98)00212-4," *Science (80-.).*, vol. 38, no. 3, pp. 573–586, 1999.

[48] A. De Giacomo *et al.*, "Cavitation dynamics of laser ablation of bulk and wire-shaped metals in water during nanoparticles production," *Phys. Chem. Chem. Phys.*, vol. 15, no. 9, pp. 3083–3092, 2013.

[49] M. Dell'Aglio, A. Santagata, G. Valenza, A. De Stradis, and A. De Giacomo, "Study of the Effect of Water Pressure on Plasma and Cavitation Bubble Induced by Pulsed Laser Ablation in Liquid of Silver and Missed Variations of Observable Nanoparticle Features," *ChemPhysChem*, vol. 18, no. 9, pp. 1165–1174, 2017.

[50] N. Mirghassemzadeh, M. Ghamkhari, and D. Dorranian, "Dependence of Laser Ablation Produced Gold Nanoparticles Characteristics on the Fluence of Laser Pulse," *Soft Nanosci. Lett.*, vol. 03, no. 04, pp. 101–106, 2013.

[51] W. Soliman, T. Nakano, N. Takada, and K. Sasaki, "Modification of Rayleigh-Plesset theory for reproducing dynamics of cavitation bubbles in liquid-phase laser ablation," *Jpn. J. Appl. Phys.*, vol. 49, no. 11, 2010.

[52] K. Neckermann *et al.*, "Local Structuring of Dielectric Layers on Silicon for Improved Solar Cell Metallization," *Proc. 22nd EPVSEC, Milan*, no. June 2014, pp. 3–6, 2007.

[53] K. Bagga *et al.*, "Laser-assisted synthesis of Staphylococcus aureus protein-capped silicon quantum dots as bio-functional nanoprobes," *Laser Phys. Lett.*, vol. 10, no. 6, p. 065603, 2013.

[54] J. Noack and A. Vogel, "Laser-induced plasma formation in water at nanosecond to femtosecond time scales: calculation of thresholds, absorption coefficients, and energy density," *IEEE J. Quantum Electron.*, vol. 35, no. 8, pp. 1156–1167, 1999.

[55] J. P. Sylvestre, A. V. Kabashin, E. Sacher, and M. Meunier, "Femtosecond laser ablation of gold in water: Influence of the laser-produced plasma on the nanoparticle size distribution," *Appl. Phys. A Mater. Sci. Process.*, vol. 80, no. 4, pp. 753–758, 2005.

[56] J. Kim, D. Amaranatha Reddy, R. Ma, and T. K. Kim, "The influence of laser wavelength and fluence on palladium nanoparticles produced by pulsed laser ablation in deionized water," *Solid State Sci.*, vol. 37, pp. 96–102, 2014.

[57] S. I. Kudryashov *et al.*, "Nanosecond-laser generation of nanoparticles in liquids: From ablation through bubble dynamics to nanoparticle yield," *Materials (Basel).*, vol. 12, no. 2, pp. 1–15, 2019.

[58] P. Wagener, A. Schwenke, B. N. Chichkov, and S. Barcikowski, "Pulsed laser ablation of zinc in tetrahydrofuran: Bypassing the cavitation bubble," *J. Phys. Chem. C*, vol. 114, no. 17, pp. 7618–7625, 2010.

[59] S. Ibrahimkutty *et al.*, "A hierarchical view on material formation during pulsed-laser synthesis of nanoparticles in liquid," *Sci. Rep.*, vol. 5, pp. 1–11, 2015.

[60] A. Menéndez-Manjón and S. Barcikowski, "Hydrodynamic size distribution of gold nanoparticles controlled by repetition rate during pulsed laser ablation in water," *Appl. Surf. Sci.*, vol. 257, no. 9, pp. 4285–4290, 2011.

[61] R. Zamiri *et al.*, "The effect of laser repetition rate on the LASiS synthesis of biocompatible silver nanoparticles in aqueous starch solution," *Int. J. Nanomedicine*, vol. 8, pp. 233–244, 2013.

[62] F. Mafuné, J. Kohno, Y. Takeda, T. Kondow, and H. Sawabe, "Structure and Stability of Silver Nanoparticles in Aqueous Solution Produced by Laser Ablation," *J. Phys. Chem. B*, vol. 104, no. 35, pp. 8333–8337, 2002.

[63] S. Link and M. A. El-Sayed, "Size and temperature dependence of the plasmon absorption of colloidal gold nanoparticles," *J. Phys. Chem. B*, vol. 103, no. 21, pp. 4212–4217, 1999.

[64] K. K. Kim, D. Kim, S. K. Kim, S. M. Park, and J. K. Song, "Formation of ZnO nanoparticles by laser ablation in neat water," *Chem. Phys. Lett.*, vol. 511, no. 1–3, pp. 116–120, 2011.

[65] R. Intartaglia *et al.*, "Bioconjugated silicon quantum dots from one-step green synthesis," *Nanoscale*, vol. 4, no. 4, pp. 1271–1274, 2012.

[66] S. Jendrzej, B. Gökce, M. Epple, and S. Barcikowski, "How Size Determines the Value of Gold: Economic Aspects of Wet Chemical and Laser-Based Metal Colloid Synthesis," *ChemPhysChem*, vol. 18, no. 9, pp. 1012–1019, 2017.

Chapter 6: Stable nano-silver colloid production via Laser Ablation Synthesis in Solution (LASiS) under laminar recirculatory flow

6.1 Introduction

Moving on from development and optimization of the production system in chapters 3, 4 & 5, a more in-depth study of a particular Np manufactured with the production rig is introduced. Silver nanoparticles (AgNps) are among the most widely studied and utilized nanomaterials in the world, with several applications in Engineering and Biotechnology. Due to their possible future applications AgNps were chosen as a test material to develop further.

As stated previously, AgNps are widely used, due to their uptake in applications across fields of electrical engineering, biotechnology and healthcare [1]. However, the established chemical synthesis nanomaterial production technique has a negative environmental impact due in part to its waste by-products. Furthermore, post-production washing steps may be need to remove ligands depending on the surface purity requirements of the application [2]. Polymers bound on the nanoparticle surface can also be present post-production and they have been seen to detrimentally effect the conductivity of nano colloid printed circuits [3] . To combat these issues a "green-synthesis" technique has been developed over the past fifteen years. This technique utilises laser irradiation to ablate a solid material target submerged within a liquid, ejecting Nps from the plasma plume into the surrounding liquid, allowing for ligand free Np production and the potential for single step functionalization. The emergence of LASiS can significantly reduce the amount of post-processing required when compared with chemical production.

However, there are drawbacks with the LASiS technique where high-cost laser systems must be employed to produce colloids of comparable concentrations to those made via commercial wet synthesis [4]. Another potential route for LASiS is the focus on applications which are not well supported by chemical synthesis and which require specific Np properties. This avoids the requirement to meet the large-scale production efficiencies of chemical synthesis and can be achieved through the use of low-powered laser systems, reducing the capital costs and allowing bench-scale production of bespoke nanomaterials. One such use for these nanomaterials is the generation of silver thin-films which are gaining applications in various areas such as amplification of light energy in solar panels [5], localized surface plasma response barcodes [6], cell imaging [7], anti-microbial coatings (sub 40 nm peak diameter, concentration > 0.21 mg/L for cytotoxic effectiveness on Yeast [8] & >0.5 mg/L for E. coli cytotoxicity [9],[10]), food packaging [11] and conductive inks (> 15% *wt*.,70-150 mg/ml) [3],[12],[13]. Thin-film production requires a narrow Np size dispersion and stable colloids at specific, repeatable concentrations. It is expected that LASiS can meet these demands using low power picosecond and femtosecond lasers systems, at relative low capital costs. However, LASiS efficiency problems must be addressed; to-date there has been a transition from "batch" production towards "semi-batch" and "continuous". "Semi-batch" systems have been seen to be advantageous where defined colloid concentrations are required [14], however these system remain sub-optimal as laminar flow at the ablation site is not guaranteed. Near chemical synthesis efficiencies have been reached under certain production conditions [15], but post-production steps to increase the concentration would generally be required in order to obtain useable colloids, when using low power laser systems.

To offer a feasible ink colloid for thin-films printing, colloid quality and stability must be maintained along with increasing LASiS production efficiency. This study examines a new laminar flow semi-batch production process for the production of AgNps in terms of stability and colloid size distribution and the resulting colloid applicability to thin-films printing.

6.2   Experimental setup

Silver nano-colloids were manufactured utilizing a "semi-batch" Laser Ablation Synthesis in Solution (LASiS) technique, described in Figure 1. The developed approach is unique in

terms of other LASiS "semi-batch" processes, such as the one described by Nachev et al. [16], as it ensures uniform laminar flow at the ablation site. The irradiation source used in this work was a picosecond-pulsed WEDGE HF 1064 (BrightSolutions, Italy) Nd:YAG laser with a wavelength of 1064 nm, maximum output power of 1.2 W, a pulse width of 700 ps and a pulse repetition rate of 10 kHz.

The target material selected was silver plate (>99.999% metals basis, Scottsdale bullion silver) machined and mechanically polished to produce discs of 8 mm outer diameter and 4 mm thickness. The target was placed into a custom designed 3-D printed flow cell. De-gassed, de-ionized water was employed as the base colloid solvent for most of the tests, with the addition of 0.86 mg/L NaCl for additional colloid stability tests. The liquid was recirculated continuously over the surface of the target at a rate of 100 mL/min during the tests. The high flow rate solvent regime ensured that efficient Np production was carried out, enabling the removal of possible masking effects from the laser plume, cavitation bubbles or Nps at the ablation site. The colloid was recirculated within a PTFE piping loop (total volume 100 ml) until the end of the test. This setup allowed the production of colloid under the set processing conditions. The laser beam's spot size was controlled at 140 μm and operational fluence was maintained at 1.83 J/cm^2. The beam was scanned in an Archimedean spiral across the target surface at a speed of 2 mm/s. Flow control was performed via automatic valve and peristaltic pump actuation via a developed LabVIEW control program. Productions tests were carried out each with a set duration of 15 minutes each.
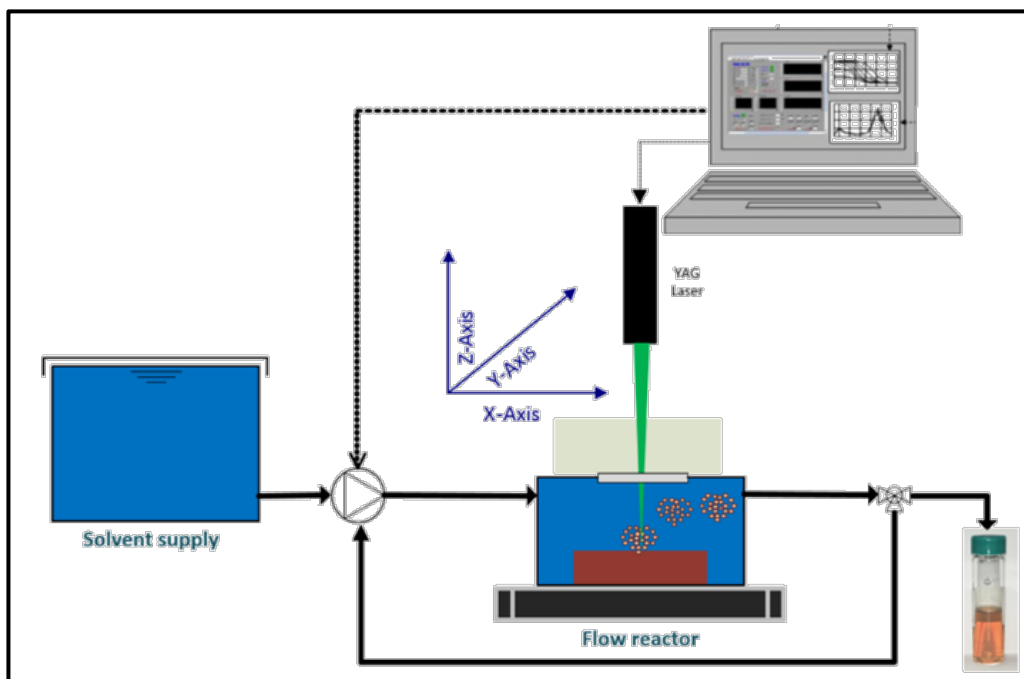
Figure 6.1: Schematic of the LASiS production setup including flow reactor cell containing the target material, solvent reservoir, laser system and control valves.

6.2.1   Metrology

The colloids size and morphology were determined with various analytical techniques. Np size distribution was determined via 180° backscatter dynamic light scattering (DLS) and transmission election microscopy (TEM). The DLS used was a NanoFlex (Microtrac), with analysis performed on 2 mL samples. A 60 s acquisition time was used averaging over a set of five measurements. Background correction was applied with the base colloid solvent, in this cases DI-water. The TEM used was an FEI Titan with Field Emission Gun and spherical aberration corrector system (Cs-corrector) of the objective lens operated at 300 kV. Analysis was performed using a copper mesh TEM grid with 40 µl of sample applied and allowed to evaporate at room temperature.

The Np colloids optical properties were characterized using a Biochrom Libra S22 UV/Vis spectrophotometer, with a scanning range of 200 – 900 nm with DI water background correction applied. For both DLS and UV-vis measurements, a one-in-ten dilution of the colloid was used to mitigate measurement saturation, no post-filtration was performed, ensuring that the DLS and UV-vis characterizations were representative of the production process. A commercial silver Nps colloid (Sigma Aldrich, 10 nm, 25 ml, 0.02 mg/ml, SPR

403 nm, #730785) was compared against the produced colloids. The commercial colloid as measured via the same DLS and UV-vis method as a calibration concentration reference.

6.3   Results and Discussion

The nano-colloid produced under continuous re-circulation conditions compares well with commercially available products prepared via wet chemical synthesis in terms of optical response, concentration and size dispersion. The DLS measurement observed a population size distribution peak at 21 nm, with the distribution ranging from 10 - 50 nm, see Figure 6.2(a). TEM imagining (see result in Figure 6.2(b)) was in agreement with the hydrodynamic size distribution measured via DLS, noted in Fig. 2a.

TEM imagining indicated a small population of larger particles (>50 nm) not observed in the DLS analysis. These particles may be due to aggregation during the TEM grid drop-casting step, or alternatively sedimented during DLS measurement. This alludes to the continuing need for a secondary, direct measurement technique such as TEM when characterizing Nps. The colloids displayed a surface plasmon resonance (SPR) band at 396 nm (Figure 6.3) with a red shift to 402 nm after twelve days stored at room temperature, indicating some aggregation has occurred. This spectrum compares well with those reported in literature for laser produced Nps [17], [18].
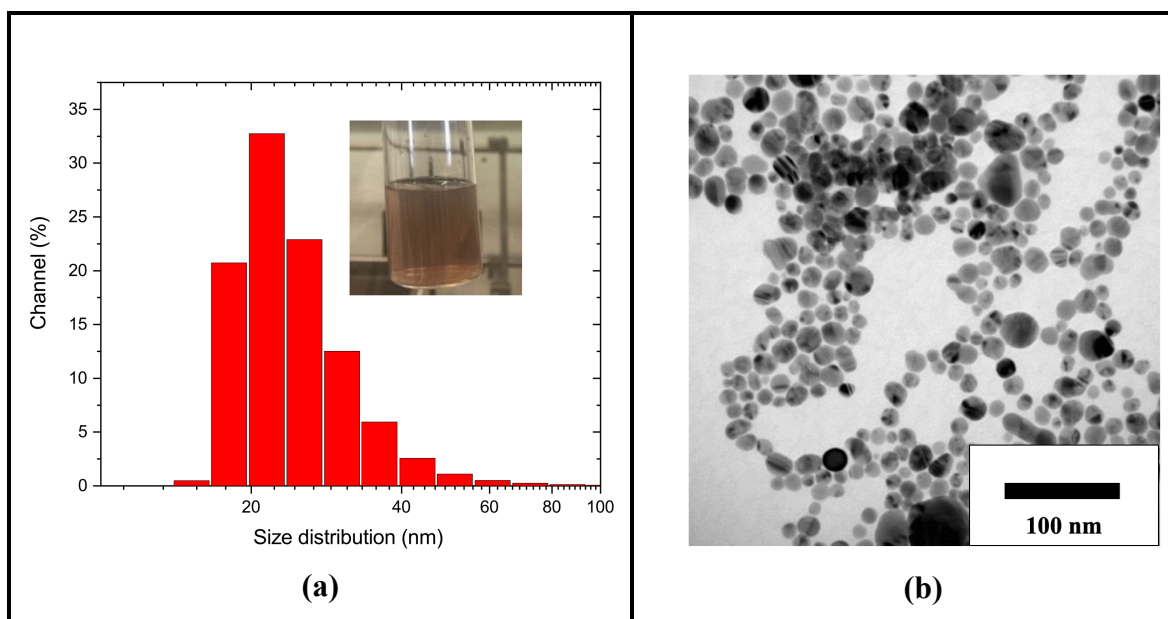
Figure 6.2: (a) DLS Np size distribution analysis, peak dia. = 21 nm and (b) TEM image of AgNPs with scale bar of 100 nm.

The peak intensity changed by 1.7% within twelve days, this is well within the general range of 5% UV-vis absorption reduction typically recorded post production for a stable colloid [19]. Typically, a red shift would indicate aggregation, however this would usually be linked with a higher drop in intensity. The short optical tail corresponds to a red tint in the colloid [20], and supports the assumption of low particle size dispersion present in the colloid. A change of Nps diameter of 1.7 nm after six days (Figure 6.4) was measured, this is less than the 2 nm resolution of the measurement device. No change was observed at day twelve. These results indicate that a highly stable colloid was produced, with similar size and SPR characteristics to the commercial colloid. Due to Np similarities, it allowed for a calibration curve of colloid concentration to absorption to be developed from a series of dilutions of the commercial colloid, starting with a known concentration. From this, it was estimated that LASiS produced colloid possessed a concentration of 0.091 mg/mL after the 15-minute ablation period, at a production efficiency of 21 mg/Wh.
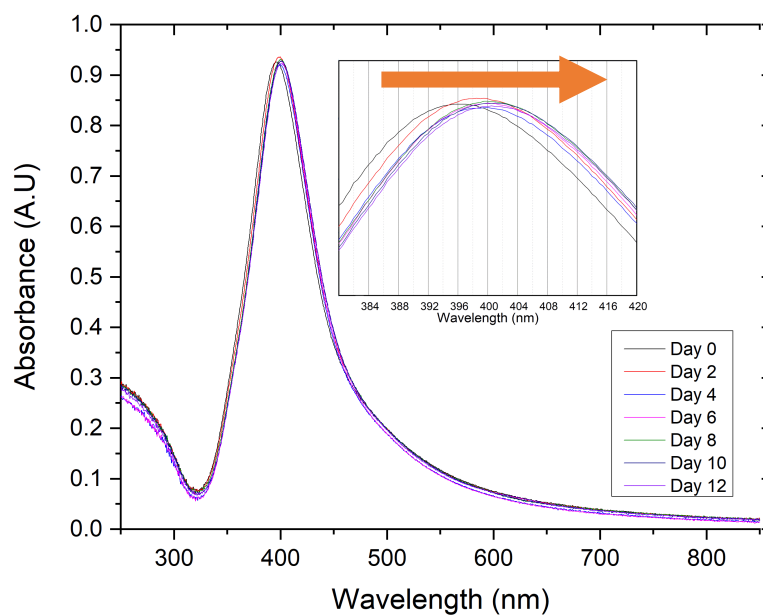
Figure 6.3: Absorption spectrum of AgNps produced, with a plasmonic peak at 396 nm at day 0, and red shifting towards 402 nm at day 12 while showing a small intensity drop.

(a)   **(b)**
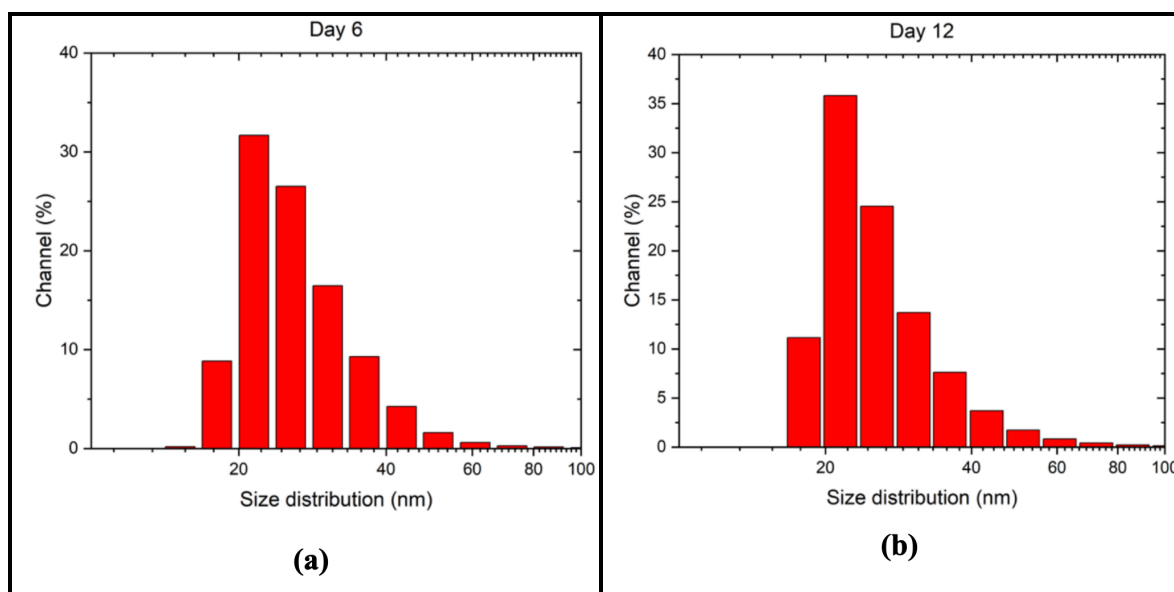
Figure 6.4: DLS analysis of AgNps colloid (a) after six days resting at room temperature, the peak diameter is 22.7 nm ± 11nm (2σ). After twelve days (b) the indicated distribution change is within the accuracy of the measurement device; with a peak diameter of 22 nm ± 12 nm, (n=3).

6.3.1 Electrolytes to aid size reduction

It has been well established that the presence of electrolytes in the ablation liquid can have a size quenching effect on particle formation [21]. The NaCl acts as a stabilizer on initial particles formed within the cavitation bubble. These "primary-particles" are smaller than the general colloid population (sub-10 nm) [22], as they can act as "seeding particles' for Np growth. Therefore if the "primary-particles" are stabilized, the colloid size distribution should exhibit a higher proportion of smaller Nps while lowering the possibility of agglomeration [2]. Other studies have suggested that at low concentrations, NaCl addition can aid Np long-term stability [23], but at higher concentrations act as a destabilizer. In these tests, AgNps formation was tested in the presence of a low concentration ionic liquid environment.
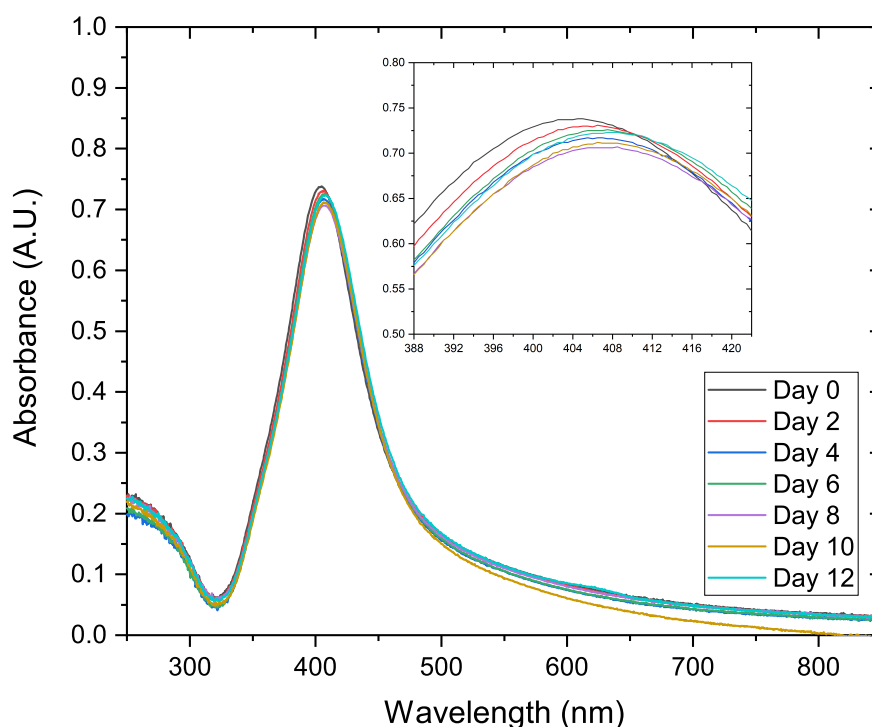
Figure 6.5: Absorption spectrum of AgNps produced in a weak NaCl ionic solvent of 0.86 mg/L. The plasmonic peak was at 404 nm at day 0, and red shifted to 407 nm at day 12. The signal intensity also dropped by 4.3%.

In Figure 6.5 a 3 nm red shift on the SPR can be observed from day 0 to day 12, also the intensity dropped by a higher proportion (4.3%) than the salt free AgNps. As this drop is approaching the limit of 5% allowed deviation of absorbance, it would be expected that the colloid would be unstable over a period of 5 or more weeks [24]. However, size quenching

205

did occur as the peak diameter has reduced from 22 nm when DI water was used to 11 nm when the weak ionic fluid was used. A smaller size distribution of only 5 nm at day 0 was recorded using the weak ionic solution compared to a main peak size distribution of about 12nm when DI water was used. These results indicate that the AgNps size remained constant over the testing period, but some colloid may have fallen out of suspension, leading to the drop-in absorption intensity. This work shows promising results for using varying salts concentrations to adjust AgNps size distribution.
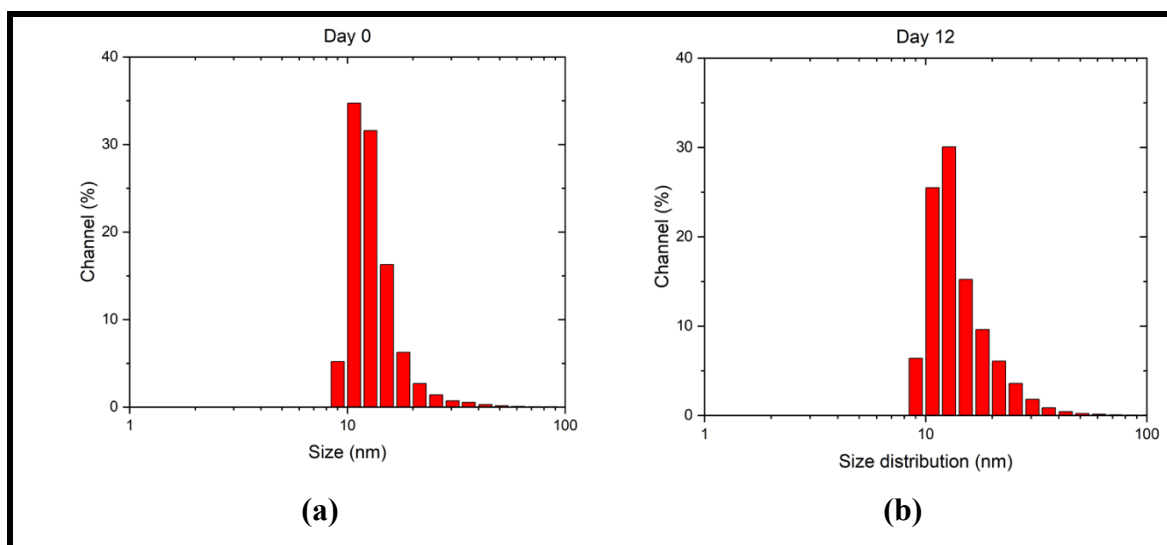
Figure 6.6: DLS measurement of AgNps produced in the presence of 0.86 mg/l NaCl/DI water solution showing (a) the peak diameter of 11.3 nm and a width of 5 nm at day 0, and (b) a peak diameter of 11.9 nm and an increased width of 7 nm at day 12.

6.4   Conclusions

Silver nanoparticles were produced utilising a new laminar flow "semi-batch" production method. The colloids were seen to be comparable with commercially available colloids in terms of optical response, size and stability. The colloids were produced within a 15-minute period and could be directly applied to thin-film printing of anti-microbial surfaces. If applied for the printing of conductive circuits, post colloid production processing would be required to increase their concentration. Using a weak ionic liquid for Nps production was found to provide size quenching, providing a pathway towards increased size control during the production process. However, it was seen to have a more variable effect on colloid stability than when DI water alone was used as the solvent. Electrolyte addition along with its interaction with Nps concentration at the ablation site needs to be studied in more detail to gain a better understanding of maintaining high density, stable colloids. This work

confirms that LASiS is a feasible technique towards commercial low-powered laser-based Ag nano-colloid production.

6.5 References

[1] S. H. Lee and B. H. Jun, "Silver nanoparticles: Synthesis and application for nanomedicine," *Int. J. Mol. Sci.*, vol. 20, no. 4, 2019.

[2] C. Rehbock *et al.*, "Current state of laser synthesis of metal and alloy nanoparticles as ligand-free reference materials for nano-toxicological assays," *Beilstein J. Nanotechnol.*, vol. 5, no. 1, pp. 1523–1541, 2014.

[3] L. Cao *et al.*, "The preparation of Ag nanoparticle and ink used for inkjet printing of paper based conductive patterns," *Materials (Basel).*, vol. 10, no. 9, 2017.

[4] R. Intartaglia *et al.*, "Bioconjugated silicon quantum dots from one-step green synthesis," *Nanoscale*, vol. 4, no. 4, pp. 1271–1274, 2012.

[5] T. D. Dzhafarov, A. M. Pashaev, B. G. Tagiev, S. S. Aslanov, S. H. Ragimov, and A. A. Aliev, "Influence of silver nanoparticles on the photovoltaic parameters of silicon solar cells," *Adv. nano Res.*, vol. 3, no. 3, pp. 133–141, 2016.

[6] C. Campos-cuerva, M. Zieba, and V. Sebastian, "Screen-printed nanoparticles as anti-counterfeiting tags," 2016.

[7] K. S. Lee and M. A. El-Sayed, "Gold and silver nanoparticles in sensing and imaging: Sensitivity of plasmon response to size, shape, and metal composition," *J. Phys. Chem. B*, vol. 110, no. 39, pp. 19220–19225, 2006.

[8] A. Panáček *et al.*, "Antifungal activity of silver nanoparticles against Candida spp.," *Biomaterials*, vol. 30, no. 31, pp. 6333–6340, 2009.

[9] M. Gao, L. Sun, Z. Wang, and Y. Zhao, "Controlled synthesis of Ag nanoparticles with different morphologies and their antibacterial properties," *Mater. Sci. Eng. C*, vol. 33, no. 1, pp. 397–404, Jan. 2013.

[10] D. Lee, R. E. Cohen, and M. F. Rubner, "Antibacterial properties of Ag nanoparticle loaded multilayers and formation of magnetically directed antibacterial microparticles," *Langmuir*, vol. 21, no. 21, pp. 9651–9659, 2005.

[11] M. Carbone, D. T. Donia, G. Sabbatella, and R. Antiochia, "Silver nanoparticles in polymeric matrices for fresh food packaging," *J. King Saud Univ. - Sci.*, vol. 28, no. 4, pp. 273–279, 2016.

[12]   M. Chien Dang, T. M. Dung Dang, and E. Fribourg-Blanc, "Silver nanoparticles ink synthesis for conductive patterns fabrication using inkjet printing technology," *Adv. Nat. Sci. Nanosci. Nanotechnol.*, vol. 6, no. 1, 2015.

[13]   N. C. Raut and K. Al-Shamery, "Inkjet printing metals on flexible materials for plastic and paper electronics," *J. Mater. Chem. C*, vol. 6, no. 7, pp. 1618–1641, 2018.

[14]   D. Zhang, B. Gökce, and S. Barcikowski, "Laser Synthesis and Processing of Colloids: Fundamentals and Applications," *Chem. Rev.*, vol. 117, no. 5, pp. 3990–4103, 2017.

[15]   P. Wagener *et al.*, "High productive and continuous nanoparticle fabrication by laser ablation of a wire-target in a liquid jet," *Appl. Surf. Sci.*, vol. 403, pp. 487–499, 2017.

[16]   P. Nachev *et al.*, "Synthesis of hybrid microgels by coupling of laser ablation and polymerization in aqueous medium," *J. Laser Appl.*, vol. 24, no. 4, p. 042012, 2012.

[17]   F. Mafuné, J. Kohno, Y. Takeda, T. Kondow, and H. Sawabe, "Structure and Stability of Silver Nanoparticles in Aqueous Solution Produced by Laser Ablation," *J. Phys. Chem. B*, vol. 104, no. 35, pp. 8333–8337, 2002.

[18]   J.-W. Jeon, S. Yoon, H. Choi, J. Kim, D. Farson, and S.-H. Cho, "The Effect of Laser Pulse Widths on Laser—Ag Nanoparticle Interaction: Femto- to Nanosecond Lasers," *Appl. Sci.*, vol. 8, no. 1, p. 112, 2018.

[19]   S. Barcikowski *et al.*, "Handbook of Laser Synthesis of Colloids," 2016.

[20]   L. E. Valenti and C. E. Giacomelli, "Stability of silver nanoparticles: agglomeration and oxidation in biological relevant conditions," *J. Nanoparticle Res.*, vol. 19, no. 5, 2017.

[21]   A. Mahmoodi, S. Z. Shoorshinie, and D. Dorranian, "Synthesis and characterization of AgCl nanoparticles produced by laser ablation of Ag in NaCl solution," *Appl. Phys. A Mater. Sci. Process.*, vol. 122, no. 4, pp. 1–10, 2016.

[22]   A. Letzel *et al.*, "Size Quenching during Laser Synthesis of Colloids Happens Already in the Vapor Phase of the Cavitation Bubble," *J. Phys. Chem. C*, vol. 121, no. 9, pp. 5356–5365, 2017.

[23]   C. Rehbock, V. Merk, L. Gamrad, R. Streubel, and S. Barcikowski, "Size control of laser-fabricated surfactant-free gold nanoparticles with highly diluted electrolytes and their subsequent bioconjugation," *Phys. Chem. Chem. Phys.*, vol. 15, no. 9, pp. 3057–3067, 2013.

[24]   S. Barcikowski, V. Amendola, G. Marzun, and C. Rehbock, "Handbook of Laser Sintheshis," no. April, 2016.

Chapter 7: Rapid LASiS process characterization via automated design of experiments (DOE)

7.1 Introduction

Synthesis of nanoparticles is a multi-variate process requiring considerable testing to determine the critical process parameters for optimisation. The development work described previously constituted single-factor experimentation to gain process understanding towards optimising Nps production efficiency. In this chapter, the work moves away from single-factor testing towards a more efficient, design of experiments multi-parameter-based approach.

Design of experiments (DOE) strategies have been used extensively to optimise laser ablation processes. Taguchi based designs have been implemented to optimise laser conditions for ablation of Cyclic olefin polymer (COP) targets [1]. *Loutas et al.* (2019) utilised full-factorial and box-Behnken DOE to investigate the interaction of laser parameters with surface topologies and bonding strength of laminar polymers [2]. DOE has been applied to optimise pulsed laser deposition of PZT on thin-films [3]. Recently DOE has been applied to process-map generation for nanoparticle fabrication techniques. *Khan et al.,(2018)* applied Taguchi orthogonal arrays to investigate the solvent chemistry parameter effect on the aggregation of ZnO Nps, applying response data attained from UV-Vis and FTIR spectroscopy. Plackett-Burman and Taguchi designs were applied to optimise ZnO production via biosynthesis [4]. Full-factorial designs have been implemented to increase the stability and quality of solid lipid Nps [5] and to optimise poly lactic-co-glycolic acid polymer (PLGA) drug formulation to improve the treatment of tumours.

In this study, a new autonomous rapid technique for characterising and producing an optimised Np production rate is presented. The effects of laser parameters such as fluence, repetition rate and beam scan-speed are examined along with liquid conditions, including

solvent flow rate and pressure. Initial experiments were carried out using a Taguchi orthogonal Design of Experiments (DoE) to quickly develop a model towards optimisation of the design space and recommend optimum parameters for Np production, followed on by a reduced parameter, higher-resolution Full Factorial Design (FFD) of a smaller design space. The FFD model offered non-linear modelling capabilities not seen in the limited data collected in the Taguchi DOE. The models were developed with the aim of examining the interaction effects of process parameters on Np ablation efficiency and colloid size dispersion to predict optimum process conditions.

This chapter presents the recirculation flow regime (semi-batch mode) as a rapid test platform predicting the best conditions for continuous flow production. To perform rapid tests, a semi-autonomous design of experiments platform based on the rig developed in chapter 4 were implemented. This reduced the requirement for operator interaction during the experiment and provided a proof-of-concept towards on-the-bench Np rapid manufacturing. Using this method, the effects of varying laser parameters and process conditions on colloid productivity to find a process maximum for productivity is presented below.

7.2 Materials and methods

7.2.1 Experimental setup

The experimental system developed and documented in chapter 4 was implemented for obtaining the results presented in this chapter. In the tests, the process variables (fluence, repetition rate, scan-speed, pressure & flowrate) were altered and two responses were measured at-line, namely Uv-Vis absorption and DLS Nps size distribution. Uv-Vis absorption is used as an indirect measurement of the concentration or quantity of Nps fabricated. For the tests described the system was operated in "re-circulation mode" with the re-circulatory network containing a liquid volume of 88 ml. Test sequencing, machine control and data acquisition was performed via an in-house developed LabVIEW (National Instruments Inc.,) program. An ablation time of five minutes was chosen for the tests, which should allow for an adequately dense colloid to be fabricated, meeting the limit of detection of the at-line measurement devices. The short test time should reduce the interaction effects of Nps occlusion and Np photo fragmentation [6], keeping the process as similar as possible to continuous flow production. The re-circulation mode continuously mixed the DLS by-

pass loop with the main line, ensuring the colloid was homogenous in the system, and measurement was representative of the bulk process fluid.

To allow for rapid characterisation, seven tests were performed on each polished circular silicon target (8.2 mm O.D.) by ablating a 3 mm O.D. Archimedean spirals, which were processed for each test, as shown in *Figure 7.1*. The spirals were designed to mimic the larger 7.5 mm spirals used in the larger scale production tests in chapter 5. A line spacing of 100 µm was used within the spirals as it was previously determined to be the most efficient parameter, in terms of ablation efficiency. From prior testing it was determined that under maximum operational laser fluence for 5 mins ablation, the deepest 3 mm diameter ablation crater would be 0.64 mm which is within the optimal beam width range for the laser optics.
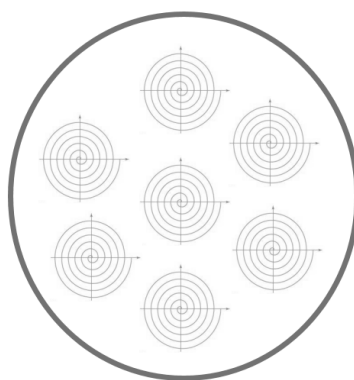
Figure 7.1: Ablation test spirals on Si disc targets

7.2.2 Response characterisation

Uv-Vis absorption measurement was used to determine the ablation rate during testing as absorbance correlates linearly with colloid concentration [7]. Thus ablation rate can be inferred from the colloid concentration achieved. Gravimetrical based ablated mass measurements were not possible as the target was not removed after each spiral ablation. Ablation crater volume and surface topologies were characterised using a VHX-2000 3-dimensional optical profilometer (Keyence, Japan). A scan was performed upwards from the base of the ablation crater in 1 µm increments at a 500x magnification, providing a direct measurement of ablated volume and mass. Nanoparticle colloid size dispersion was monitored at-line and off-line via a Nanoflex Dynamic light scattering instrument (Microtrac Inc.,), and UV-vis response was measured both on-line and off-line with a Libra S22 UV-vis (Biochrom Inc,.) spectrometer.

7.2.3 Test sequencing

The experiments ran semi-autonomously with manual interaction required to load each target and set the flow-cell pressure and spiral location. The total experimental run-time for the 7 spirals on each target, including results acquisition and analysis was under 140 minutes. The test sequencing is described in the Appendix H2.

7.2.4 Productivity experiments: Taguchi orthogonal array

The experimental design chosen for the screening experiments was a Taguchi orthogonal array L_{16} five factors, four levels, detailed in Table 7.1, the test layout is illustrated in Appendix G1.

Table 7.1: Process parameters and levels used

Factors	Symbol	Unit	Level -2	Level -1	Level +1	Level +2	R
Laser power	LP	[%]	61	74.5	87	100	87
Repetition rate	RR	[kHz]	10	30	50	70	10
Scan-speed	SS	[mm/s]	2	4	6	8	2
Flow rate	FR	[ml/min]	15	90	165	240	165
Solvent pressure	P	[bar]	1	1.7	2.3	3	1

Three replicates (R1- R3) were added to the Taguchi design, with one test on each target to test for inter-target normality. Validation tests (V1 - V6) were performed within the design space and model process optimisation tests were performed in triplicate (T1 - T3). The full DOE table is given in Table 7.2.

Table 7.2: Taguchi orthogonal array including replicate tests

Label	Run	FR	P	LP	RR	SS	UV-vis abs @ 400 nm	Np size	Np size (filt.)
[#]	[#]	[ml/min]	[bar]	[%]	[kHz]	[mm/s]	[A.U]	[nm]	[nm]
1	1	-2	+2	+2	+2	+2	0.075	232	29
2	2	+2	-2	+2	-1	1	0.330	257	52.7
3	3	+2	+2	-2	+1	-1	0.014	166	32.4
4	4	+1	-2	+1	+2	-1	0.018	161	53.8
5	5	+1	+1	-2	-1	+2	0.074	200	55.1
6	6	+1	-1	+2	+1	-2	0.245	242	47.6
R1	7	+1	-2	+1	-2	-2	0.286	212	52.5
7	8	+2	+1	-1	+2	-2	0.004	171	55
8	9	-2	+1	+1	+1	+1	0.010	193	50.9
9	10	-1	-2	-1	+1	+2	0.012	188	51
10	11	+1	+2	-1	-2	+1	0.265	325	52.5
11	12	-1	+2	+1	-1	-2	0.360	309	67.2
12	13	-1	-1	-2	+2	+1	0.000	327	40.2
R2	14	+1	-2	+1	-2	-2	0.296	275	74.8
13	15	-1	+1	+2	-2	-1	0.332	251	43.3
14	16	+2	-1	+1	-2	+2	0.319	124.7	46.3
15	17	-2	-2	-2	-2	-2	0.142	268	6.8
16	18	-2	-1	-1	-1	-1	0.050	226	77.3
R3	19	+1	-2	+1	-2	-2	0.305	292	49

The DOE arrays were produced and analysed using Design-Expert 7 (Stat-Ease Inc., USA) and Minitab 19 (LLC., USA) software. The minimum operational fluence was chosen to be above the ablation threshold (0.35 J/cm^2), 61% laser power at 10 kHz RR equates to 1.05 J/cm^2 and 0.62 J/cm^2 at 70 kHz RR. Scan-speeds were chosen to reflect the single factor testing conducted in chapter 5. Repetition rates were selected with the expectation to provide pulse energies above the fluence threshold for ablation and pressure values were chosen concerning equipment limits. From the tests noted in chapter 5, it was seen that flowrates up to 240 ml/min had a significant transient effect on productivity, whereas flowrates above

240 ml/min produced marginal productivity gains. As the experiments here were run in recirculation mode, the flow rate would not have a diluting effect on the colloids produced. A reduced two-factor-interaction (2FI) model was developed for Np colloid UV-vis absorbance prediction using backward elimination to remove insignificant terms. The backward elimination would reduce model complexity while increasing the predicted coefficient of determination (R^2 term). The successful adoption of a 2FI model indicates that only linear interactions between the parameters are observed, i.e. the parameters do not reach maxima within the range chosen. Similarly, a 2FI model was developed for Np size prediction, including backward elimination. A linear model was developed for the filtered colloid Np size estimation.

7.2.5 High-resolution design: Full factorial design (FFD)

A higher resolution full-factorial design was developed to gain more understanding of the process interactions. Fluid flow rate and pressure were removed as process variables to simplify the design space. They were maintained at 180 ml/min and 2 bar gauge pressure respectively. Based on the parameters described in Table 7.3, a reduced quadratic model was developed for colloid absorbance using backward elimination.

Table 7.3: FF reduced design space process parameters and levels used

Factors	Symbol	Unit	Level -1	Level 0	Level +1	R
Laser power	LP	[%]	70	80	100	80
Repetition rate	RR	[kHz]	10	35	60	35
Scan-speed	SS	[mm/s]	1.8	4.8	7.8	4.8

7.3 Results and discussion

7.3.1 Taguchi Design

The DOE results, including colloid absorbance and Nps size measurements, are documented in Table 7.2. A selection of the colloids produced can be seen in *Figure 7.2* which indicates a range of process responses. The mean colloid absorbance was 0.17 ± 0.14 ($1\boldsymbol{\sigma}$), indicating

a large spread in the process response. The average Nps size measured at-line was 232 nm ± 58 nm (1σ). Post-filtration (0.2μ) measurements yielded smaller Nps of 49 nm ± 16 nm.
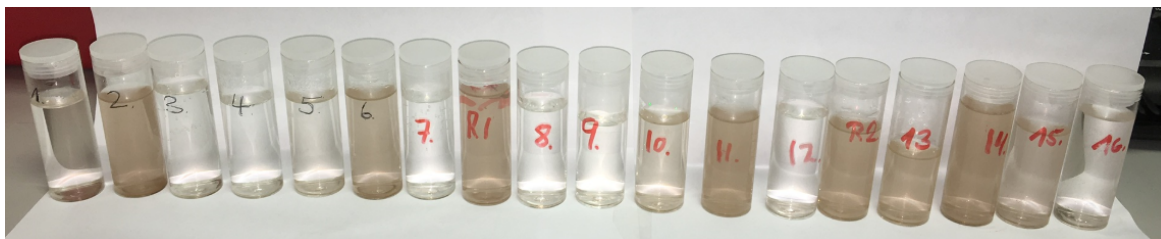
Figure 7.2: Colloids produced directed by the Taguchi screening model

Target ablation (Figure 7.3) displays the range of surface topologies produced with various laser and process parameters, as determined by the Taguchi orthogonal array in Table 7.2. Low laser power (level -2, -1) combined with average repetition rates (level 1) or medium to high scan speeds (level +1, +2) produced only faint surface ablations (spiral #: 3, 7, 12) and low colloid absorbances of 0.014 A.U., 0.004 A.U. & 0.000 A.U. respectively, as shown in Table 7.2. This indicates that the process was operating just above the ablation threshold. Repetition rates of 30 kHz and 50 kHz produced significant melt on the target surface as seen in spiral #: 2 & 6 in Figure 7.3. The craters produced were deep relative to other tests, which implies that heating effects increases the ablation rate in the process, also the resultant colloid concentrations were seen to be high relative to the design space, with values of 0.330 A.U. and 0.245 A.U. Heating of the silicon target has been seen in the past to lower the ablation threshold of an Si target. Replicates (R1 - R3) display similar surface topologies, with each ablation spiral visible, as seen in Figure 7.3 and colloids produced with absorbance of 0.286 A.U., 0.296 A.U. and 0.305 A.U. They possessed an average crater depth of 239 ± 27μm, equating to an ablated mass of 2.1 mg ± 0.25 mg for the 5-minute ablation indicating a target process variability of 12.8 %.
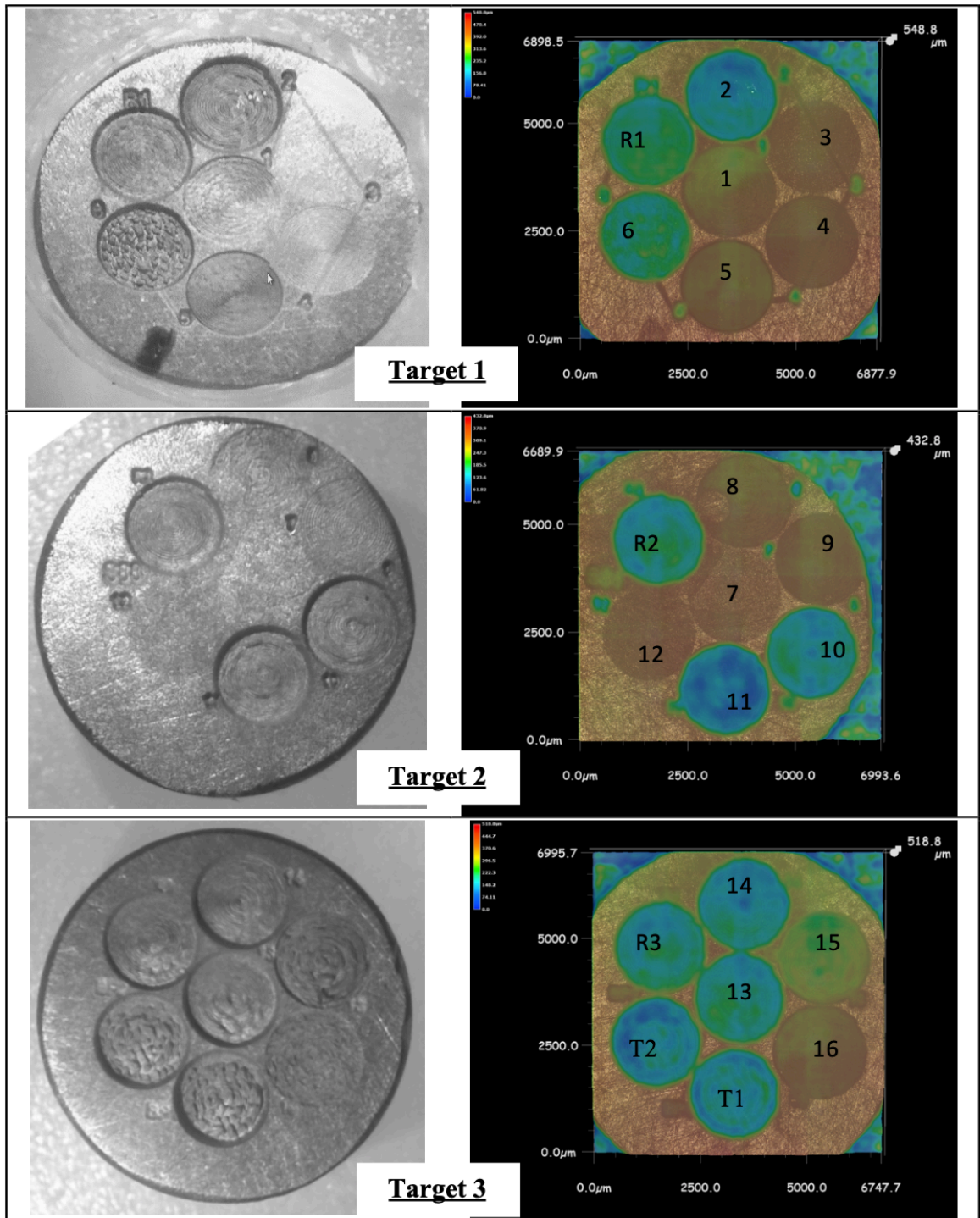
Figure 7.3: Taguchi DOE target surface ablation, (a) target 1 (1-6, R1), (b) target 2 (7-12, R2), (c) target 3 (13-16, R3, R4, T1, T2).
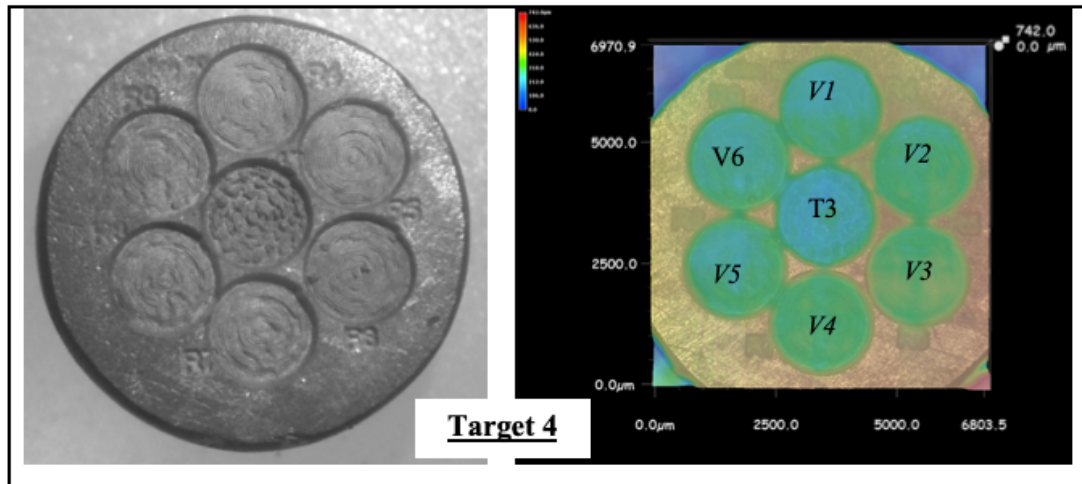
Figure 7.4: Taguchi DOE target surface ablation on target 4 (T3, R4-R9).

7.3.1.1 Full factorial design (FFD) results

The results for the FFD are documented in Table 7.4. The average absorbance measurement was 0.21 A.U. ± 0.11 A.U. A variation of 52 % from the mean was produced within the dataset, indicating a reasonable spread of data. The Nps size data contained a similar range from the mean of 129 nm ± 62 nm.

Table 7.4: *Full factorial design experimental table and results*

Target	Run/label	LP	SS	RR	UV-vis abs @ 400	DLS size
[#]	[#]	[%]	[mm/s]	[kHz]	[-]	[nm]
1	1	0	-1	0	0.2638	68.8
1	2	1	-1	0	0.3271	139.8
1	3	1	1	0	0.3474	129.7
1	4	1	0	-1	0.3196	88.6
1	5	-1	0	-1	0.2100	63.4
1	6	1	1	1	0.1687	174.2
1	7	0	0	0	0.2728	106.7
2	8	0	1	0	0.2802	36.1
2	9	-1	-1	-1	0.2921	117.1
2	10	0	0	-1	0.3157	122.3
2	11	-1	-1	1	0.0202	58.2
2	12	0	-1	1	0.0402	120.8
2	13	1	0	1	0.1589	253.2
2	14	1	1	-1	0.3132	123.0
3	15	0	0	0	0.2300	190.7
3	16	-1	0	1	0.0095	67.5
3	17	-1	1	0	0.1609	235.7
3	18	1	-1	-1	0.3079	110.0
3	19	1	0	0	0.3386	92.8
3	20	0	0	0	0.2974	113.3
4	21	-1	-1	0	0.1627	94.1
4	22	-1	0	0	0.1667	47.3
4	23	-1	1	1	0.0047	126.1
4	24	1	-1	1	0.1324	90.3
4	25	0	0	0	0.2714	212.8
4	26	0	0	1	0.0565	267.8
4	27	-1	1	-1	0.2571	243.2
5	28	0	1	1	0.0432	153.3
5	29	0	-1	-1	0.3259	95.7
5	30	0	1	-1	0.3113	136.0

7.3.2 Signal-to-noise analysis

The signal-to-noise (S/N) ratio was calculated to determine the factors that have the most significant effect on the Taguchi model. There is a need in research for high volumes of uniform-sized SiNps for the semiconductor [8] and bioanalytical industries [9]. Therefore two S/N ratios were chosen for this work, firstly to maximise the colloid concentration produced (absorbance) and secondly to minimise the nanoparticle size. Eq 7.1 and 7.2 describe the S/N definitions used for colloid absorbance and Nps size, respectively.

$$\left(S/N\right)_{Absorbance} = -10log_{10}\left(\Sigma\frac{1/z^2}{n}\right) \qquad \text{(Eq. 7.1)}$$

$$\left(S/N\right)_{Nps\ size} = -10log_{10}\left(\Sigma\frac{y^2}{n}\right) \qquad \text{(Eq. 7.2)}$$

where z is the UV-Vis absorption and the y is the nanoparticle size, and n is the number of responses, 5.

Table 7.5 describes the calculated S/N ratios for the Taguchi experimental design for both colloid absorbance and Nps size response variables. The factors are ranked in terms of a "delta value" which is a calculation of the difference between the process response variables for each factor between level -2 and level 2. For the experimental range, the first-ranked factor was repetition rate which possessed the highest delta value for both colloid absorbance and Nps size. The second-ranked factor was laser power for both responses, followed by laser scan speed. Liquid pressure had the smallest effect on the change in process responses in the range used.

Table 7.5: Responses for signal-to-noise ratio of colloid absorbance and Nps size for Taguchi test.

Response	Factor	Level				Delta	Rank
		-2	**-1**	**1**	**2**		
Absorbance	RR	-12	-16.78	-32.02	-46.11	34.11	1
	LP	-38.77	-31.24	-23.42	-13.48	25.29	2
	FR	-26.37	-33.91	-20.32	-26.32	13.6	3
	SS	-21.67	-26.89	-34.9	-23.46	13.23	4
	P	-25.07	-31.64	-30.21	-20	11.65	5
Nps size	RR	-40.15	-41.36	-40.04	-35.77	5.59	1
	LP	-38.45	-41.9	-36.43	-40.54	5.47	2
	FR	-38.89	-41.41	-40.51	-36.51	4.91	3
	SS	-41.68	-38.36	-39.61	-37.67	4.01	4
	P	-37.89	-39.92	-38.37	-41.15	3.26	5

From the main effects plots illustrated in Figure 7.5 and Figure 7.6 it can be concluded that linear trends exist between laser power, repetition rate and the absorbance signal-to-noise ratio. Increasing laser power and reducing repetition rate will directly increase the signal-to-noise. This observation is in agreement with general research where increasing laser pulse energy will increase Nps productivity. For the experimental laser system tested, increasing the repetition rate has the effect of reducing pulse energy supplied to the target. No clear trend exists for the Nps size signal-to-noise ratio. There is a slight trend observed with increasing repetition rate and flow rate on Nps size signal-to-noise. Indicating that lower pulse energies and lower concentration colloids may contain smaller size distributions, or at least that the smaller sized Nps are not masked by the larger colloid during the DLS measurement.
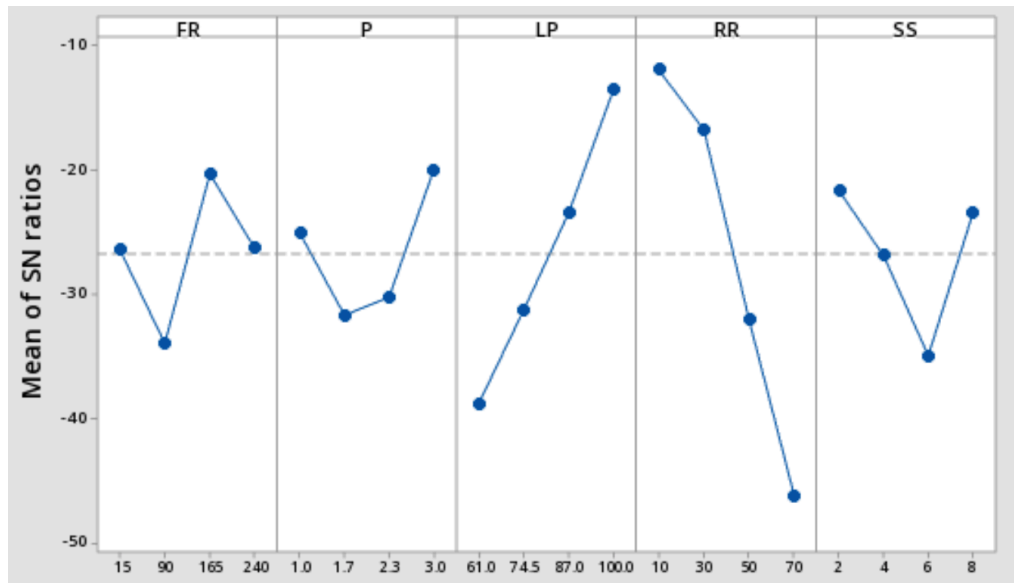
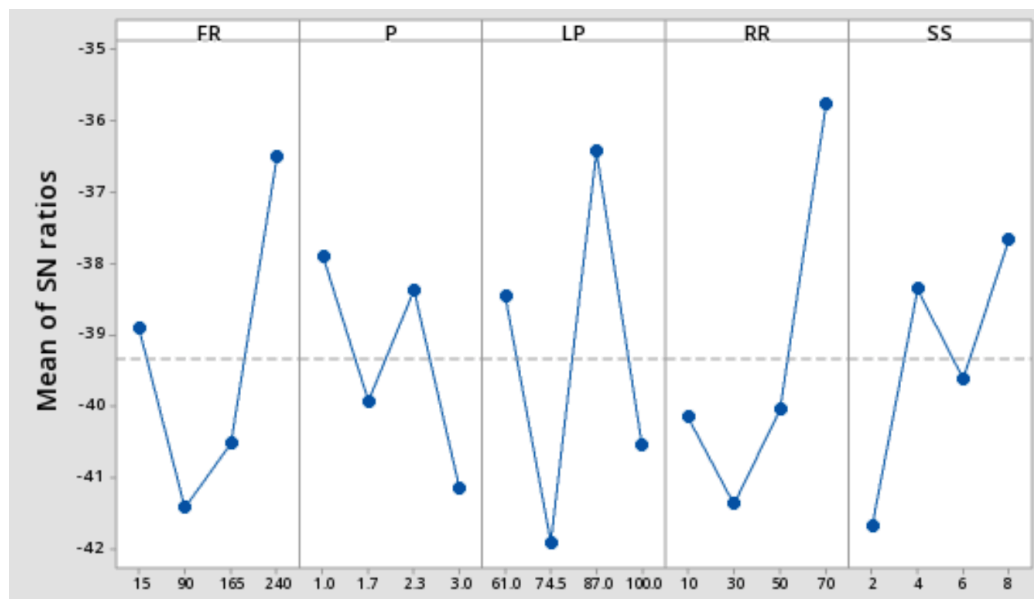*Figure 7.5: Main effects plots for S/N ratios of data means for colloid absorbance.*

Figure 7.6: Main effects plots for S/N ratios of data means for Nps size.

221

7.3.3 Definition of ANOVA terms

A series of terms used in the ANOVA analysis performed is described in table 7.6 below.

Table 7.6: Glossary of ANOVA terms from DesignExpert 7.0 software.

Parameter	Definition
2FI	Two factor interaction.
Adequate precision	Compares the range of predicted values to the average prediction error. Ratios greater than 4 indicate adequate model discrimination.
Adjusted R^2	R-squared adjusted for the number of terms in the model, relative to the number of points in the design, estimates the overall variation in the model.
Degrees of Freedom (DoF)	The number of levels in the term minus 1.
Corrected Total (Cor Total)	The total of the Sum of Squares for the model corrected for the mean.
F-value	Test for comparing model variance with residual (error) variance. The larger the F-value signifies that the variance contributed by the model is larger than the random error.
P-value	Probability value, usually relating the risk of falsely rejecting a given hypothesis.
P-value (Prob > F)	The probability of getting an F Value of this size if the term did not have an effect on a response.
Predicted R^2	Measures the variation from the predicted data.
Residual error	The difference between the response and the model prediction for a data point.
Sum of Squares	The sum of the squared deviations from the mean.
Mean Square	The Sum of Squares divided by the Degrees of Freedom.
R^2	Correlation coefficient - indicates the degree of relationship (as a fraction) between the data and the linear model.

7.3.4 Taguchi model ANOVA analysis

Table 7.7 indicates the primary Analysis of Variance (ANOVA) parameters sourced from the absorbance and Nps size models developed. The absorbance model had an adjusted R^2

of 0.92 which was close to the predicted R^2 of 0.83. However, the difference between the adjusted R^2 and the predicted R^2 for nanoparticle size was greater than 0.2, indicating that the model required more training data to describe the process correctly.

Table 7.7: Primary ANOVA parameters for the Taguchi models

Response	DoF	Adjusted R^2	Predicted R^2	Adequate precision	F value
Absorbance (A.U)	7	0.92	0.83	16.20	31.25
Nps size (nm)	8	0.75	0.49	10.75	7.71
Filtered Nps size (nm)	3	0.31	0.17	5.77	1.07

The Adequate Precision of the Absorbance model was 16.20, i.e. the signal-to-noise ratio was large (>4) indicating that noise is not a significant factor in the model. The F-value, which compares the model variance to the residual variance was 31.25 which indicates that the model is significant. The equation derived to predict absorbance is as follows:

$$Abs.(A.U.) = \big(0.594 - (5.577^{-3} \times FR) + (0.130 \times P) - (2.71^{-3} \times LP)$$
$$- (0.011 \times RR) - (0.045 \times SS) + (8.04^{-5} \times FR \times LP)$$
$$+ (1.09^{-3} \times RR \times SS)\big)^2$$

(Eq 7.3)

where Abs is the colloid Uv-Vis spectra absorbance in (A.U.), FR is the liquid flowrate, P is the liquid pressure (bar), LP is the command laser power (%), RR is the laser repetition rate (kHz) and SS the scan speed (mm/s). The model derived was complex, containing 12 factors and 12 degrees of freedom. This complex behaviour is expected as many interactions between the variables contribute to colloid production. It was seen that increasing RR had a negative effect on concentration; this result was expected as the pulse energy drops with RR for the experimental laser system. Scan speed also had a negative effect on concentration, with a slight reduction in concentration observed with increasing scan speeds. The linear behaviour colloid absorbance as a function of increased laser power seen in Figure 7.9 is in agreement with fluence tests performed in chapter 5. This observed linearity indicates that saturation response of the variables due to process conditions such as photo fragmentation and particle occlusion of target was not reached, also thermal effects was not observed. The

data set normality was determined using a residuals plot as illustrated in Figure 7.7, showing random variation in absorbance over the tests performed. This indicated that replacing the target had no significant effect on the process. A linear correlation of model prediction vs experimental data was also observed (Figure 7.8) for colloid absorbance, indicating the model is capable within the design space.
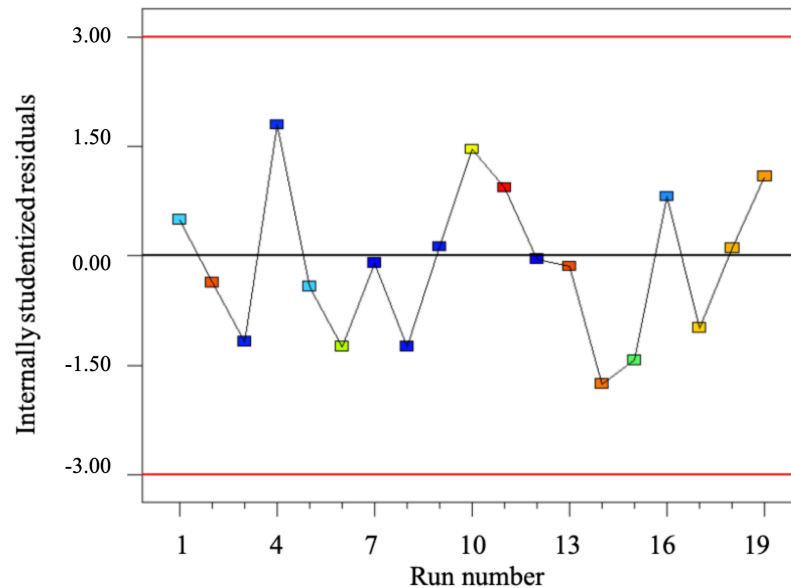
Figure 7.7: Plot of residuals vs run number for the Taguchi absorbance model.
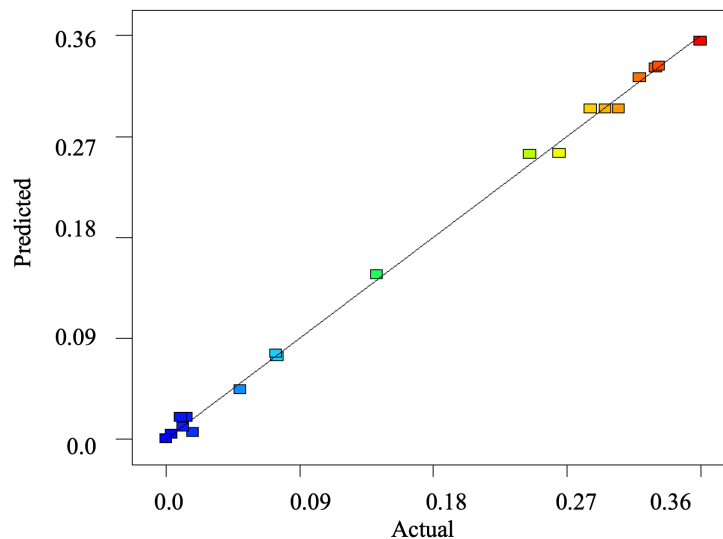
Figure 7.8: Plot of Taguchi model prediction vs experimental absorbance values (A.U.).

The surface plots illustrated in Figure 7.9 show the linear relationship between the input parameters and absorption, this would indicate that the Taguchi model does not offer high

enough resolution to model the interaction effects, or that no process local maxima were reached within the design space chosen.

(a)

(b)
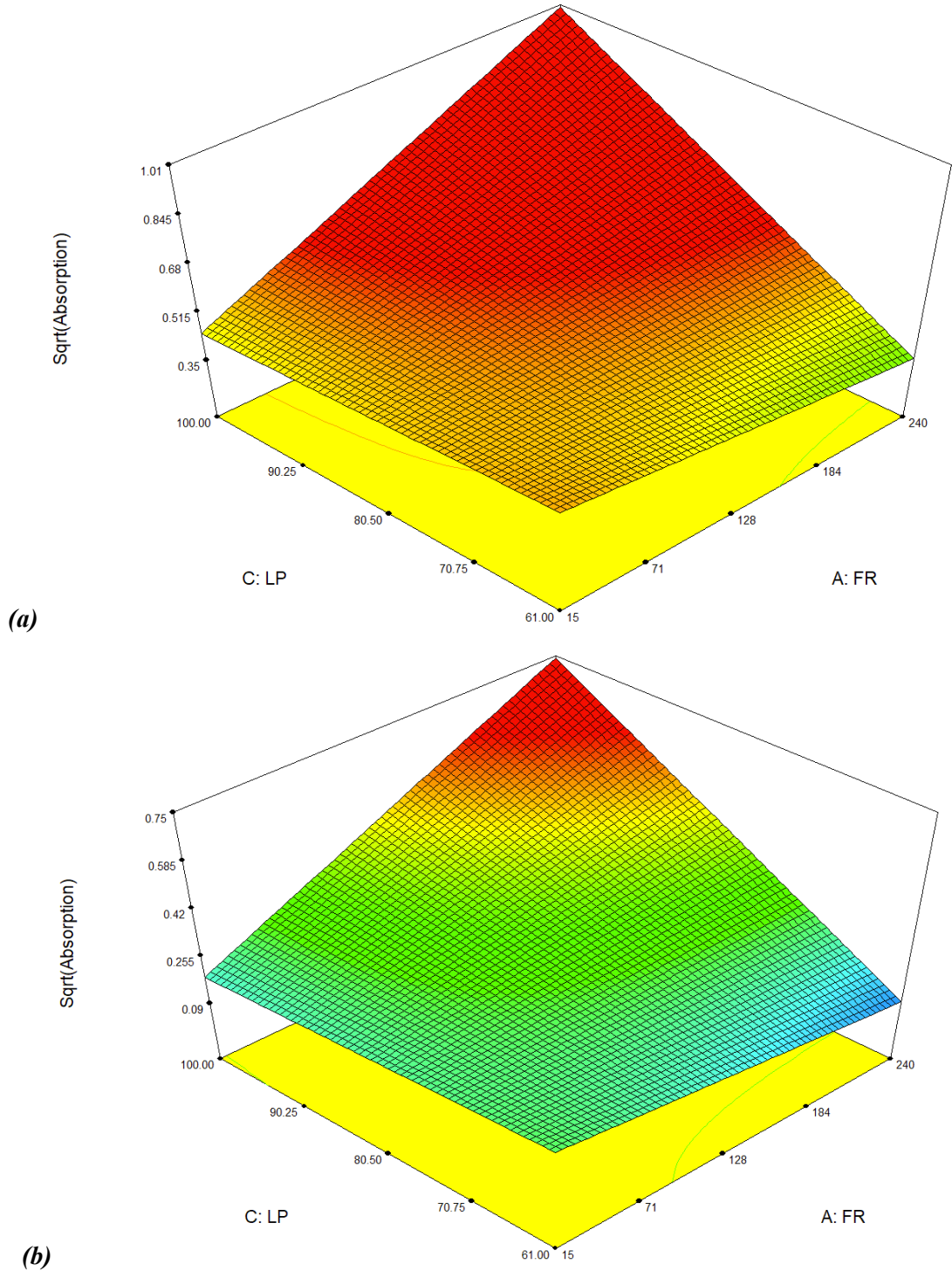
Figure 7.9: Surface plots of the effect of Laser command power (%) and liquid flowrate on colloid absorption for repetition rates at (a) 10 kHz and (b)30 kHz. The colour coding transitions from blue-green-yellow-red as colloid absorbance increases.

225

7.3.4.1 Nanoparticle size modelling

The Np size model developed was statistically significant, with an F-value of 7.71. The predicted R^2 of 0.49, is not as close to the adjusted R^2 value of 0.75 to traditionally describe the model as being precise. The adequate precision value of 10.75 is greater than 4, indicating that noise is not a significant factor. The residuals chart (Figure *7.10*) shows that the process was under control and contained no systematic errors. The model predicted vs actual plot (Figure 7.11) determines that there is a linear correlation with experimental data. The model developed containing 8 degrees of freedom is described below:

$$Np\ size\ (nm) = 718.85 - (4.131 \times FR) + (165.901 \times P) - (6.795 \times LP) -$$
$$(4.34 \times RR) - (63.467 \times SS) + (0.055 \times FR \times LP) - (2.240 \times P \times RR) +$$
$$(1.717 \times RR \times SS)$$

$$(Eq.7.4)$$

The model developed using the filtered colloid Np size data was not statistically significant, possessing an F-value <4, and adequate precision of 1.07. The model prediction performance was low, with an R^2 of 0.31, the adequate precisions proved that noise was not a determining factor in the model. This result shows that with a limited number of data points, the Taguchi models could not model the relationship between process variables and Nps size. The Np size response only varied by 25% from the mean value for the runs tested, indicating that perhaps a higher resolution Design of Experiment model would prove more successful.
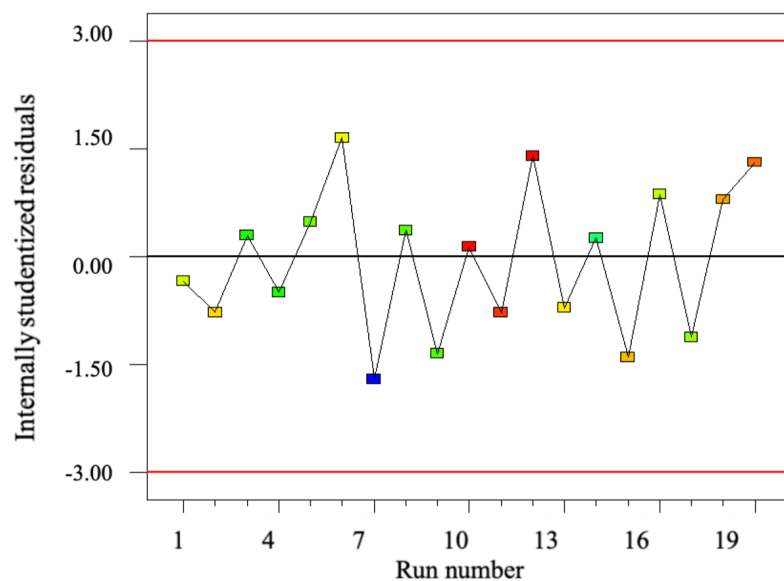
Figure 7.10: *Chart of residuals vs run number for Taguchi colloid size modelling.*
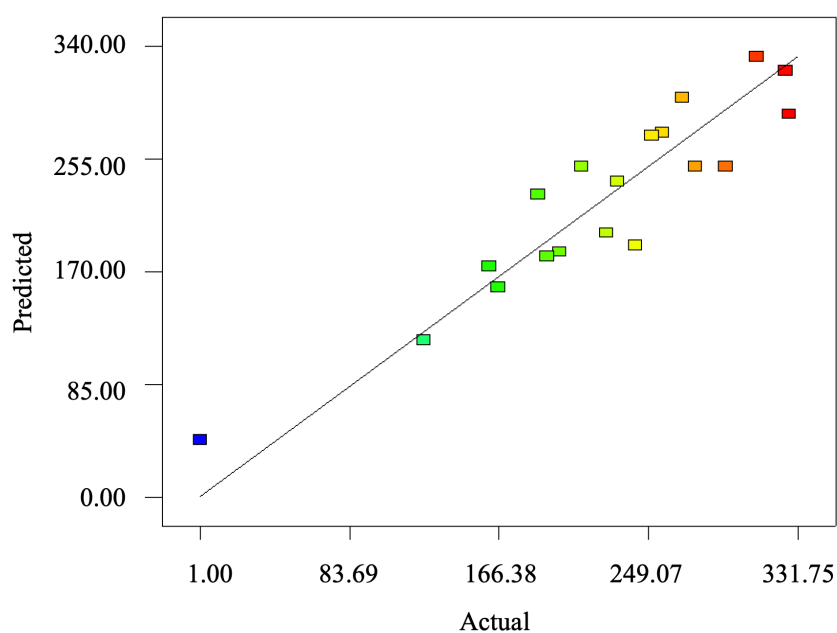
Figure 7.11: Plot of Taguchi model predicted size vs experimental size measurement (nm).

7.3.5 *Full Factorial model ANOVA analysis*

The colloid absorbance model developed via Full Factorial Design (FFD) is described in Table 7.8. It was seen to be significant, with an F-Value of 122.34, significantly greater than 4. The predicted R^2 term was within 0.02 of the Adjusted R^2 (0.926) indicating that the prediction model represents the process well.

Table 7.8: Primary ANOVA parameters for the FFD models

Response	DoF	Adjusted R^2	Predicted R^2	Adequate precision	F value
Absorbance (A.U)	3	0.926	0.910	31.48	122.34

Adequate precision indicates that noise is not a significant factor in the model. The quadratic model was developed via backward elimination; Scan speed was removed as a significant term. The final model equation possessed 3 degrees of freedom and is described below:

$$Abs\,(A.U.) = -0.095 + (4.22^{-3} \times LP) + (4.258^{-3} \times RR) - (1.246^{-4} \times RR^2)$$

(Eq.7.5)

The model is also in agreement with the general process models [6], for laser ablation and LASiS, which states that increasing total laser power, i.e. laser fluence and repetition rate will increase ablation rate. The quadratic relationship of colloid concentration with repetition rate as illustrated in the response charts (Figure 7.12) is a function of the laser system used. The response agrees with repetition rate tests performed in Chapter 5, where it was observed that above 30 kHz RR Nps production rate decreased. This decrease was determined to be a function of reducing pulse energy and increasing pulse duration for the laser system used. The residuals chart (Figure 7.13) for the tests conducted indicated that the process was within control at all times. Modelling of Nps size data was unsuccessful for the FFD, where the process mean was recommended as the most reliable description of the process.

Figure 7.12: Response surface for colloid absorbance (A.U.) vs laser repetition rate and laser command power with beam scan speed at 1.8 mm/s.

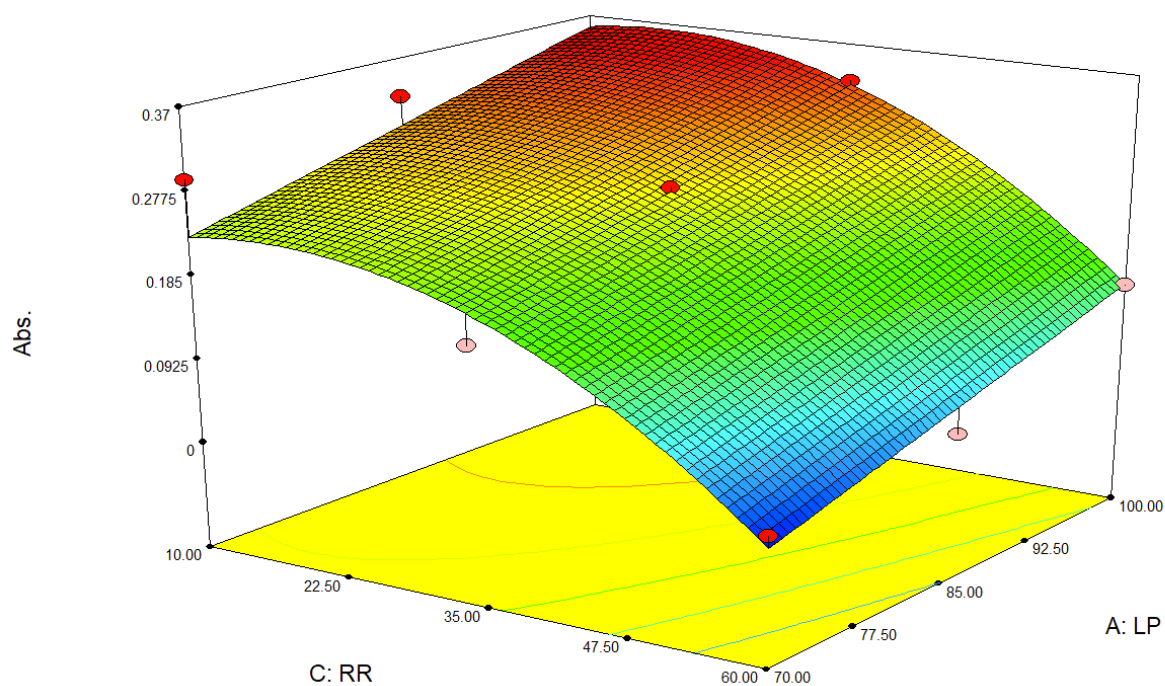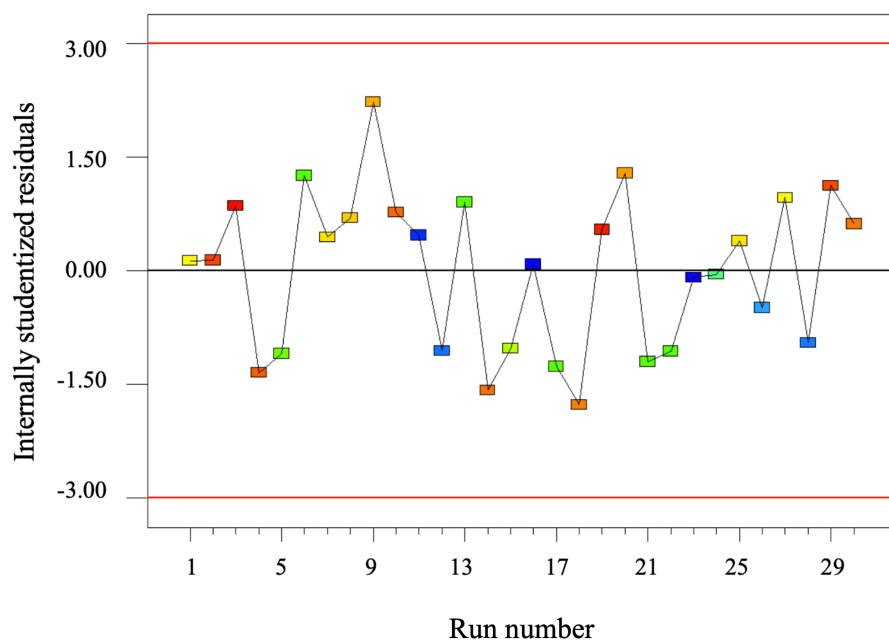*Figure 7.13: Chart of residuals vs run number for FFD colloid absorption modelling.*

229

7.3.6 *Taguchi model verification and optimisation*

In order to validate the absorbance Taguchi model-independent verification tests were performed, and the model prediction was compared against experimental data as described in Table 7.9. The model prediction performance was seen to be good with parameters on the edge of its design space (V1-V3) with a mean relative error (MRE) of 6.5%. However, the model's interpolation accuracy was reduced with an MRE of 30.9% when tested against experimental data using parameters towards the centre of its design space (V4 – V6). This alludes to a lack of resolution of the Taguchi DOE, where only linear variable interactions were found, along with no parameter process maxima.

Now optimal process conditions were investigated by maximising equation 7.3 to maximise the possible colloid concentration produced. The process parameters were maximised within the bounds of the operating range. Afterwards, the model was solved to maximise the response, as described in Table 7.9. The absorbance target was set at 0.4 A.U., the resulting experiment produced a colloid with an absorbance of 0.372 A.U., offering an MRE of 7 % from experimental data. The prediction indicated higher colloid concentration produced than observed in the training dataset. Therefore using the techniques, a higher colloid concentration was reached than previously determined for the process variables. The model optimised parameters correspond well with the parameters found in Chapter 5 when performing single factor optimisation. The non-linear relationship of Nps productivity with RR determined from experimental data in Chapter 5 indicates that the optimum RR would be found in the range of 20 - 30 kHz for similar process conditions suggested in this work. The model optimised ambient pressure value of 2.5 bar would provide higher efficiency compared with the pump-limited single-factor optimisation testing of 2 bars in chapter 5. A scan speed of 2 mm/s was seen in Chapter 5 to provide the highest production efficiency, and maximising laser power has been proven to maximise Np production. The model performed well when predicting absorbance close to the edge of the trained design space. It also offered a rapid method to reach process variables for optimised production, very close to those found in chapter 5.

Table 7.9: Taguchi model testing & productivity maximum (n=3)

Label [-]	FR [ml/min]	P [bar]	LP [%]	RR [kHz]	SS [mm/s]	Abs. Pred. [A.U.]	Abs. Exp [A.U.]	MRE [%]	Ablation rate [mg/h]
Ver 1 (V1-V3)	199	1	92	25	6	0.25	0.327 ± 0.01	30.98	24.3 ± 3.9
Ver 2 (V4-V6)	101	2.4	100	10	4	0.36	0.337 ± 0.01	6.5	21.0 ± 0.2
Test$_{max}$ (T1-3)	188	2.5	100	24	2	0.44	0.372 ± 0.01	38.2	25.2 ± 2.5

Maximised production

The UV-vis absorbance spectra of the colloid produced under optimum process conditions is illustrated in Figure 7.14. The spectra found are typical of silicon Nps described previously in Chapters 3 – 5. TEM analysis showed that the Nps are spherical and DLS determined the colloid to have a peak diameter of 106 ± 65 nm. The SEM images (Figure 7.15) illustrate the point discussed in Chapter 5 that heating of the target must contribute to increasing Nps production efficiency. Significant melt can be seen on the process optimum target (T3) compared with a target ablated with conditions towards the centre of the design space.
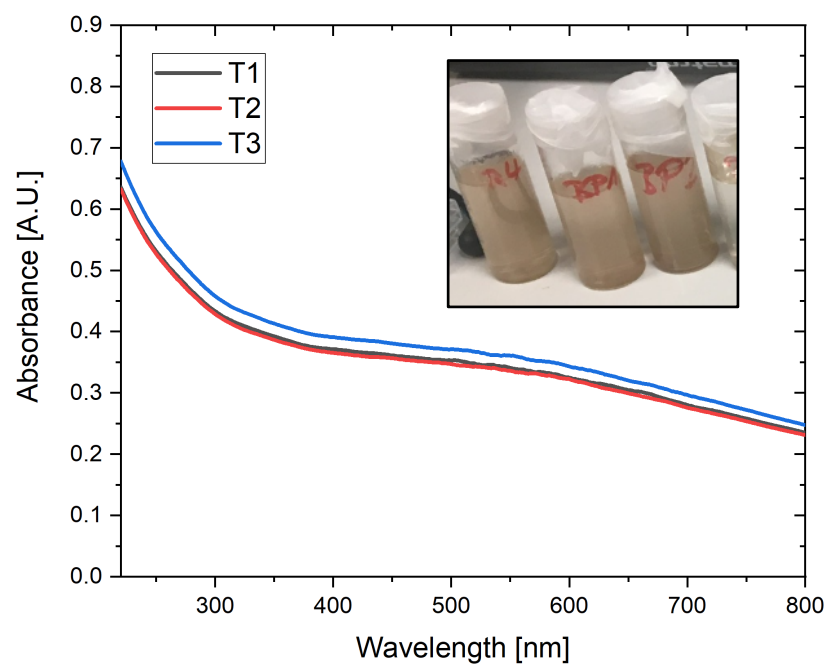
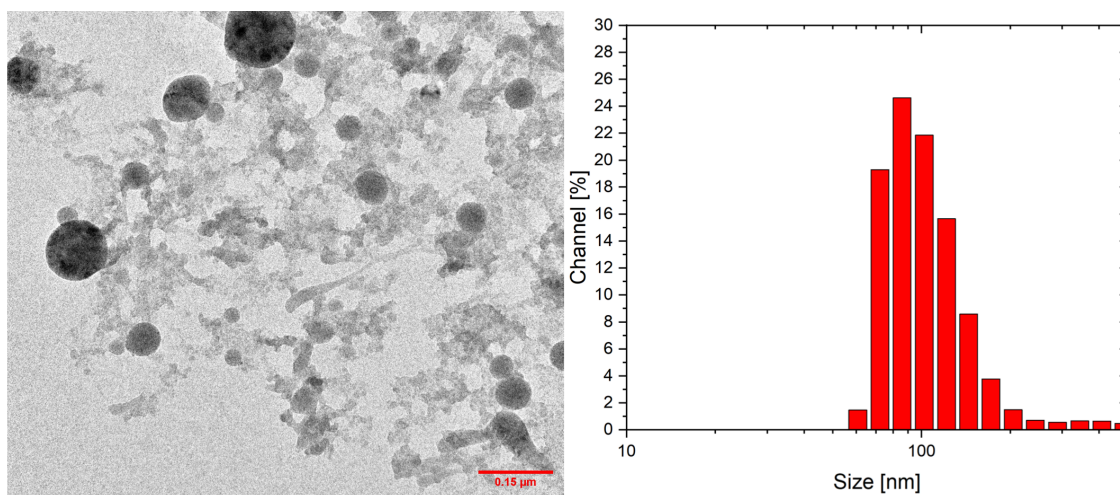*Figure 7.14: UV-vis absorption of triplicate process optimisation tests.*

Figure 7.15: TEM image of the colloid produced under optimised conditions and (b) DLS measurement showing a peak at 106 ± 65 nm.
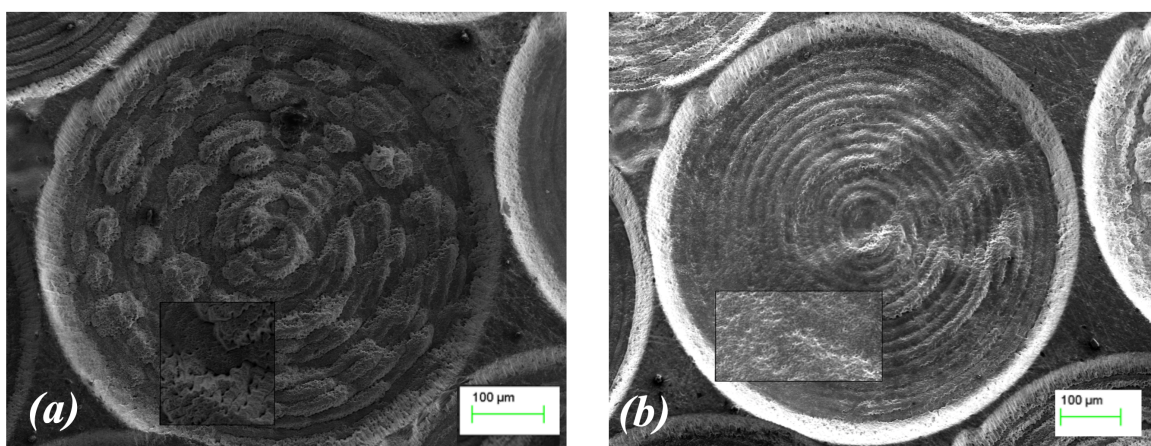
232

Figure 7.16: (a) Sample T3 ablation spiral utilising optimised parameters as described in Table 7.9, SEM operating at 12.05 kV, WD = 8 mm and (b) spiral 13, produced via FR = 90 ml/min, P=1.7 bar, F = 1.83 J/cm^2,RR = 10 kHz, SS = 4 mm/s, SEM operating at 13.53 kV, WD=8.5.

7.4 Conclusions

The Taguchi DOE employed in this test offered a rapid technique to examine the effects of process parameters on ablation efficiency. A wide range of colloid concentrations were produced, indicating a range of ablation rates, which suggests the possibility of promising results with future development. Results achieved from the Taguchi model were broadly in agreement with Full Factorial Testing performed and with the extensive single-factor testing conducted in Chapter 5. This confirms that the Taguchi model, coupled with the developed system automated process parameter trialling, offers a rapid method to optimise the production process with a limited number of experiments required, correlating well with high-resolution experimentation. The Taguchi model lacks resolution in order to describe the non-linear interactions of the process; however, it was successful to optimise colloid concentration. Both models struggled to model Nps size. The Taguchi model offered a prediction model for Nps size with Prediction R^2 of 0.49, whereas the FFD was unable to yield a description of Nps size based on the input parameters. It is concluded that for the FFD tested, the SiNps could be produced with size dispersions from 63.4 nm to 267 nm but the Nps resultant size and relationship to the process variables could not be well mapped within the narrow range investigated. This highlights the importance of performing comprehensive single-factor experimentation compared with relying on a low-resolution DOE to explain a Nps fabrication process. The single-factor tests performed in chapter 5

233

could identify specific process variable values required to fabricate Nps at defined size distribuations, however this was not possible with DOE. In order to produce more defined size response to aid modelling capabilities in future a series of steps can be taken: Firstly, low repetition rate laser systems (<1kHz) could be used (as discussed in chapter 5). Secondly, as employed in chapter 6 salt addition in the solvent can have a "size quenching effect" on Np nucleation and aggregation, promoting the production of smaller particles [11]. Thirdly solvent selection is a major determining factor in Nps size, solvent selection is well documented for chemical synthesis of nanoparticles such as AuNps [12] and SiNps [13]. The choice of solvent can impact the surface oxidation [14] of the Nps and the physical differences in the solvent (viscosity, density, oxygen concentration) [15] can impact on the size and lifecycle of the cavitation bubble which would have an impact of size [16],[15].

The automatic experimental rig worked satisfactorily. It performed the 16 DOE experiments in 5 hours, requiring manual input only to change targets and automatically performed response monitoring, data logging and analysis. The combination of a Taguchi model with the automatic rig allowed for the prediction of a comparable process optima for Nps productivity, compared with the result achieved from several months experimental time for the single-factor tests conducted in chapter 5. The combination of the autonomous rig and DOE paves the way for future rapid experiments to characterise the Np synthesis process for many other materials. However single-factor testing may be still required for accurate Nps size control.

7.5   References

[1]   R. McCann, K. Bagga, G. Duaux, A. Stalcup, M. Vázquez, and D. Brabazon, "Taguchi method modelling of Nd:YAG laser ablation of microchannels on cyclic olefin polymer film," *Opt. Laser Technol.*, vol. 106, pp. 265–271, 2018.

[2]   T. H. Loutas, G. Sotiriadis, E. Tsonos, S. Psarras, and V. Kostopoulos, "Investigation of a pulsed laser ablation process for bonded repair purposes of CFRP composites via peel testing and a design-of-experiments approach," *Int. J. Adhes. Adhes.*, vol. 95, no. July, p. 102407, 2019.

[3]   A. Schatz, D. Pantel, and T. Hanemann, "Application of DoE methods to establish a model for the pulsed laser deposition of PZT thin-films," *2016 Jt. IEEE Int. Symp.*

Appl. Ferroelectr. Eur. Conf. Appl. Polar Dielectr. Piezoelectric Force Microsc. Work. ISAF/ECAPD/PFM 2016, pp. 2–5, 2016.

[4]   D. El-Ghwas, T. Mazeed, A. El-Waseif, H. Al-Zahrani, O. Almaghrabi, and A. Elazzazy, "Factorial Experimental Design for Optimization of Zinc Oxide Nanoparticle Production," *Curr. Nanosci.*, vol. 15, pp. 1–11, 2019.

[5]   A. Santini and E. B. Souto, "Alpha-Pinene-Loaded Solid Lipid Nanoparticles Dispersion Analysis," pp. 1–17, 2019.

[6]   R. Intartaglia, K. Bagga, and F. Brandi, "Study on the productivity of silicon nanoparticles by picosecond laser ablation in water: towards gram per hour yield.," *Opt. Express*, vol. 22, no. 3, p. 3117, 2014.

[7]   S. Barcikowski *et al.*, "Handbook of Laser Synthesis of Colloids," 2016.

[8]   J. Lopez, A. Lidolff, M. Delaigue, C. Hönninger, and E. Mottay, "Comparison of picosecond and femtosecond laser ablation for surface engraving of metals and semiconductor," *12th Int. Symp. Laser Precis. Microfabr.*, vol. 8243, pp. 1–5, 2011.

[9]   R. Intartaglia, K. Bagga, M. Scotto, A. Diaspro, and F. Brandi, "Luminescent silicon nanoparticles prepared by ultra short pulsed laser ablation in liquid for imaging applications," vol. 2, no. 5, pp. 510–518, 2012.

[10]   C. L. Sajti, R. Sattari, B. N. Chichkov, and S. Barcikowski, "Gram scale synthesis of pure ceramic nanoparticles by laser ablation in liquid," *J. Phys. Chem. C*, vol. 114, no. 6, pp. 2421–2427, 2010.

[11]   C. Rehbock, V. Merk, L. Gamrad, R. Streubel, and S. Barcikowski, "Size control of laser-fabricated surfactant-free gold nanoparticles with highly diluted electrolytes and their subsequent bioconjugation," *Phys. Chem. Chem. Phys.*, vol. 15, no. 9, pp. 3057–3067, 2013.

[12]   N. A. Cortez-Lemus, A. Licea-Claverie, F. Paraguay-Delgado, and G. Alonso-Nuñez, "Gold nanoparticles size design and control by poly(N,N ′-diethylaminoethyl methacrylate)," *J. Nanomater.*, vol. 2015, 2015.

[13]   S. Semlali *et al.*, "Effect of solvent on silicon nanoparticle formation and size: A mechanistic study," *Nanoscale*, vol. 11, no. 11, pp. 4696–4700, 2019.

[14]   V. Amendola and M. Meneghetti, "What controls the composition and the structure of nanomaterials generated by laser ablation in liquid solution?," *Phys. Chem. Chem. Phys.*, vol. 15, pp. 3027–3046, 2013.

[15]   S. Yang, W. Cai, H. Zhang, X. Xu, and H. Zeng, "Size and Structure Control of Si Nanoparticles by Laser Ablation in Different Liquid Media and Further

Centrifugation Classification," *J. Phys. Chem. C*, vol. 113, no. 44, pp. 19091–19095, 2009.

[16] G. Bajaj and R. K. Soni, "Effect of liquid medium on size and shape of nanoparticles prepared by pulsed laser ablation of tin," *Appl. Phys. A Mater. Sci. Process.*, vol. 97, no. 2, pp. 481–487, 2009.

Chapter 8:   Conclusions and future work

8.1   Conclusions and outlook

The overall aim of this thesis was to investigate the possibility of providing scale-up of the LASiS process for nanoparticle manufacture and develop a detailed understanding of this production route. This aim was accomplished through a series of iterative designs and experimental improvements detailed within Chapters 3 - 7. The foundation of the development includes the application of a low-cost, low-power laser system combined with the design and construction of a novel Np flow-reactor (flow cell) which ensures uniform solvent flow and enables efficient removal of occluding material from the irradiation site. A number of process engineering principles were applied such as: identifying and controlling critical process parameters (CPPs), implementing process analytical tools (PAT) to monitor the process in real-time and implementing quality by design (QbD) methodology at each stage in development. These ensured that the process developed was in -control, stable and highly repeatable, with production rates varying by 1.1% from the mean. It was proven through this work that the at-line process measurement could be used for final production characterization and was in agreement with standard off-line characterization. From the integration of the PAT tools within the production process, a complete manufacturing platform was developed.

Silicon was chosen as the development material due to a number of factors, namely: material availability, environmental disposal, costs, biocompatibility, applicability to the electronics, biomedical and biopharmaceutical industries. The developed continuous Nps production process, was seen to operate at steady state, within the confines of the laser beam focal length. Under continuous flow SiNps of 78 ± 60 nm were produced, similar to the historical batch technique tested. Initial tests showed that not only did continuous production allow for steady state production but prior to optimization it offered production rates seven times greater than batch mode. Using the automatic test platform, a series of single-factor tests were completed in order to optimize process conditions to maximum Nps productivity. As

237

part of understanding the process; three production-applicable prediction models were developed, concluding that a 37 W laser would be required to produce 1 g of SiNps within an hour. During optimization, productivity was increased by 56%. It was determined that solvent flowrate and solvent pressure played key roles in determining production rates. They contributed to the removal of particles and bubbles from the ablation site and were also seen to reduce cavitation bubble size and lifespan, providing an optimum production rate of 43.5 mg/h. To aid comparison with state-of-the-art, the productivity value was converted into a production efficiency metric. The process achieved 27.7 mg/Wh power-specific productivity, this value was a factor of seven higher than the best efficiency reported [1] to date for SiNps production. For further comparison a series of tests were conducted producing common nanomaterials at the optimum flow conditions determined for silicon. Those experiments produced Silver, Zinc Oxide and Gold nano colloids at significantly higher production efficiencies than reported in literature. Gold colloids were produced at 66.7 mg/h, at a power-specific productivity of 29.9 mg/Wh, 4.6 times greater than a comparable middle-class laser system [2]. The main outcome of the work is that for the first time an LASiS process can produce gold nanoparticles at a lower overall cost ($354.5/g) than wet chemical synthesis ($373/g) [3]. These results offer a solution towards scalable "on-the-bench" Np production in R&D environments and provides a new approach to scale LASiS via middle-power laser systems operating at high efficiencies.

8.2   Future work

The Np production platform developed in this thesis has large scope for further development and testing. In its current form, using Taguchi design of experiments, an optimised production process map can be developed with one day of experimentation. In the short-term it would be worthwhile to the research community to utilise the automatic rig to characteristic the range of nanomaterials that could be fabricated with the production system, along with the resulting colloid concentrations and Nps dimensions. Within this work, the flow cell and automated rig was utilised only on a low power micro-machining laser system. Further investigation would be needed to determine if indeed the production efficiencies would scale using higher power laser systems. It would be expected that the flow cell dimensions would have to increase to accommodate a larger plume depth. Operating at higher powers could also test the accuracy of the scale-up prediction models developed. Due to the multi-variate nature of LASiS and inherent non-linearities in the process, this problem

would be well suited to applying Artificial Neural Networks (ANN) modelling. Such models could be implemented towards model predicative control (MPC) of on-line nano-colloid concentration and size distributions, similar to work reported for laser deposition [4].

In this work, a defined relationship between the process parameters and SiNps size ranges was not defined. Although defined size dispersions between 75 nm – 119 nm were produced repeatedly under experimental conditions. The addition of salts as seen in Chapter 6 (and Appendix F5), or the choice of solvent as documented in Appendix D3 may help produce smaller Nps. The author postulates that perhaps the small inter-pulse distance during the test may have led to reirradiation of molten particles within the cavitation bubble, or directly expelled particles, resulting in possible aggregation and uniform particle sizes irrespective of the repetition rates tested in this study. To this end it would be recommended to perform further repetition rate tests at high scan speeds (1000 - 9000 mm/s), where no pulse overlap would occur to determine if significantly different SiNps sizes could be fabricated. Optical examination of the effects of process variables on plasma generation and bubble dynamics such as tests reported elsewhere [5],[6],[7],[8],[9] would aid greatly in understanding the Np synthesis process developed in this work. It would be recommended to perform high-speed imaging under various process conditions, to understand the effects of flowrate (50 - 240 ml/min) and moderate fluid pressure (1-3 bar) changes has on bubble dynamics and hence Np fabrication efficiency.

Though not discussed in this thesis, Nps thin-film production via commercial ink-jet printing was developed and is described in the Appendix D. This provides a controllable method to deposit Nps on surfaces. Nano colloid thin-films printing utilizing defined colloids could find various applications from conductive surfaces [10]–[12] , anti-microbial surfaces [13]–[16] (as tested in the Appendix E & F) and sensing devices [17]–[20]. Due to the current market for nanoparticles and the production costs and efficiencies of the system developed, commercial development of the system may be investigated. The speed of Np process development possible with the developed rig may offer routes towards commercialization of a bench mounted automatic LASiS device for R&D.

8.3 References

[1] S. I. Kudryashov *et al.*, "High-throughput laser generation of Si-nanoparticle based surface coatings for antibacterial applications," *Appl. Surf. Sci.*, vol. 470, no. November 2018, pp. 825–831, 2019.

[2] S. Dittrich, R. Streubel, C. McDonnell, H. P. Huber, S. Barcikowski, and B. Gökce, "Comparison of the productivity and ablation efficiency of different laser classes for laser ablation of gold in water and air," *Appl. Phys. A Mater. Sci. Process.*, vol. 125, no. 6, pp. 1–10, 2019.

[3] S. Jendrzej, B. Gökce, M. Epple, and S. Barcikowski, "How Size Determines the Value of Gold: Economic Aspects of Wet Chemical and Laser-Based Metal Colloid Synthesis," *ChemPhysChem*, vol. 18, no. 9, pp. 1012–1019, 2017.

[4] X. Cao and B. Ayalew, "Robust multivariable predictive control for laser-aided powder deposition processes," *J. Franklin Inst.*, vol. 356, no. 5, pp. 2505–2529, 2019.

[5] M. Dell'Aglio, A. Santagata, G. Valenza, A. De Stradis, and A. De Giacomo, "Study of the Effect of Water Pressure on Plasma and Cavitation Bubble Induced by Pulsed Laser Ablation in Liquid of Silver and Missed Variations of Observable Nanoparticle Features," *ChemPhysChem*, vol. 18, no. 9, pp. 1165–1174, 2017.

[6] J. Tomko *et al.*, "Cavitation bubble dynamics and nanoparticle size distributions in laser ablation in liquids," *Colloids Surfaces A Physicochem. Eng. Asp.*, vol. 522, pp. 368–372, 2017.

[7] M. Dell'Aglio, R. Gaudiuso, O. De Pascale, and A. De Giacomo, "Mechanisms and processes of pulsed laser ablation in liquids during nanoparticle production," *Appl. Surf. Sci.*, vol. 348, pp. 4–9, 2015.

[8] N. Walsh, J. T. Costello, and T. J. Kelly, "Optical diagnostics of laser-produced aluminium plasmas under water," *Appl. Phys. B Lasers Opt.*, vol. 123, no. 6, pp. 1–13, 2017.

[9] W. Nicola, "Laser Produced Plasmas in Liquid Environments." p. 277, 2016.

[10] L. Cao *et al.*, "The preparation of Ag nanoparticle and ink used for inkjet printing of paper based conductive patterns," *Materials (Basel).*, vol. 10, no. 9, 2017.

[11] Y.-H. Yu *et al.*, "Electrical, morphological, and electromagnetic interference

shielding properties of silver nanowires and nanoparticles conductive composites," *Mater. Chem. Phys.*, vol. 136, no. 2, pp. 334–340, 2012.

[12] M. Chien Dang, T. M. Dung Dang, and E. Fribourg-Blanc, "Silver nanoparticles ink synthesis for conductive patterns fabrication using inkjet printing technology," *Adv. Nat. Sci. Nanosci. Nanotechnol.*, vol. 6, no. 1, 2015.

[13] C. Rode *et al.*, "Antibacterial Zinc Oxide Nanoparticle Coating of Polyester Fabrics," *J. Text. Sci. Technol.*, vol. 1, no. August, pp. 65–74, 2015.

[14] F. Elmi *et al.*, "The use of antibacterial activity of ZnO nanoparticles in the treatment of municipal wastewater," *Water Sci. Technol.*, vol. 70, no. 5, pp. 763–770, 2014.

[15] M. Gao, L. Sun, Z. Wang, and Y. Zhao, "Controlled synthesis of Ag nanoparticles with different morphologies and their antibacterial properties," *Mater. Sci. Eng. C*, vol. 33, no. 1, pp. 397–404, Jan. 2013.

[16] B. Yu, K. M. Leung, Q. Guo, W. M. Lau, and J. Yang, "Synthesis of Ag-TiO2 composite nano thin film for antimicrobial application," *Nanotechnology*, vol. 22, no. 11, 2011.

[17] H. Gan, L. Chen, X. Sui, B. Wu, S. Zou, and A. Li, "Materials Science & Engineering C Enhanced delivery of sorafenib with anti-GPC3 antibody-conjugated TPGS- b - PCL / Pluronic P123 polymeric nanoparticles for targeted therapy of hepatocellular carcinoma," *Mater. Sci. Eng. C*, vol. 91, no. April, pp. 395–403, 2018.

[18] M. Arruebo, "Antibody-Conjugated Nanoparticles for Biomedical Applications," vol. 2009, 2009.

[19] P. Chandra, J. Singh, A. Singh, A. Srivastava, R. N. Goyal, and Y. B. Shim, "Gold Nanoparticles and Nanocomposites in Clinical Diagnostics Using Electrochemical Methods," *J. Nanoparticles*, vol. 2013, pp. 1–12, 2013.

[20] J. Golab, M. Korbelik, D. Russell, D. Preise, A. Scherz, and Y. Salomon, "Photochemical & Photobiological Sciences Targeted photodynamic therapy of breast cancer cells using," 2011.

Appendix A

Wavelength production efficiency comparison

A.1. Overview

Initial continuous production tests were performed to compare the ablation efficiency of Nps produced at 1064 nm and 532 nm using ps laser systems. The initial results are illustrated below using a Brightsolutions Wedge HF 1064 nm (6W, 500 ps) and a Brightsolutions Wedge 532 nm (4W, 700 ps) laser system. Tests showed that at the same operating fluence of 0.8 J/cm^2, 532 nm irradiation attained a higher production rate compared with 1064 nm, as seen in the diagram below.
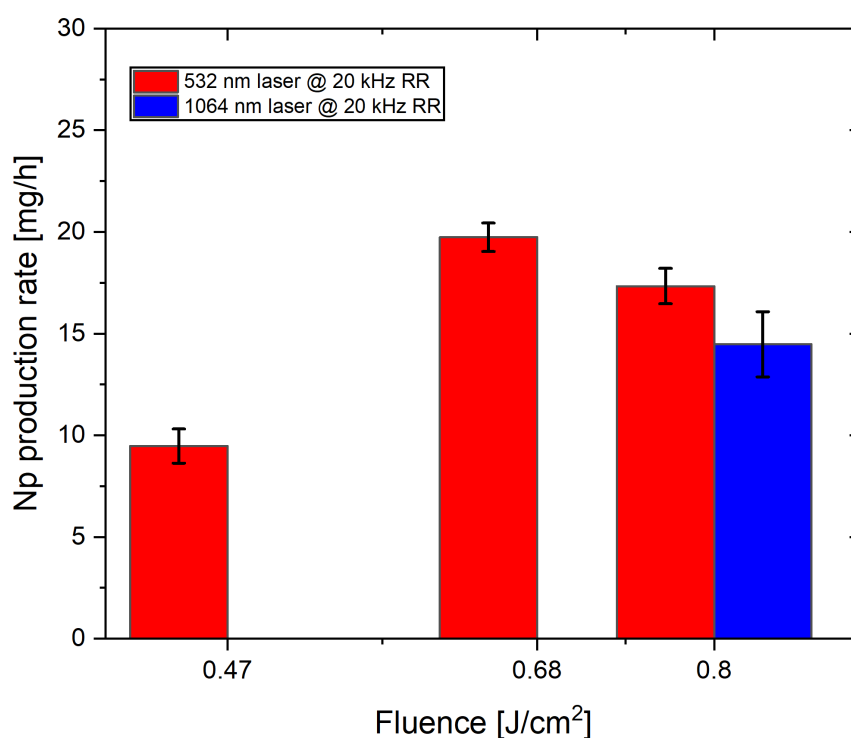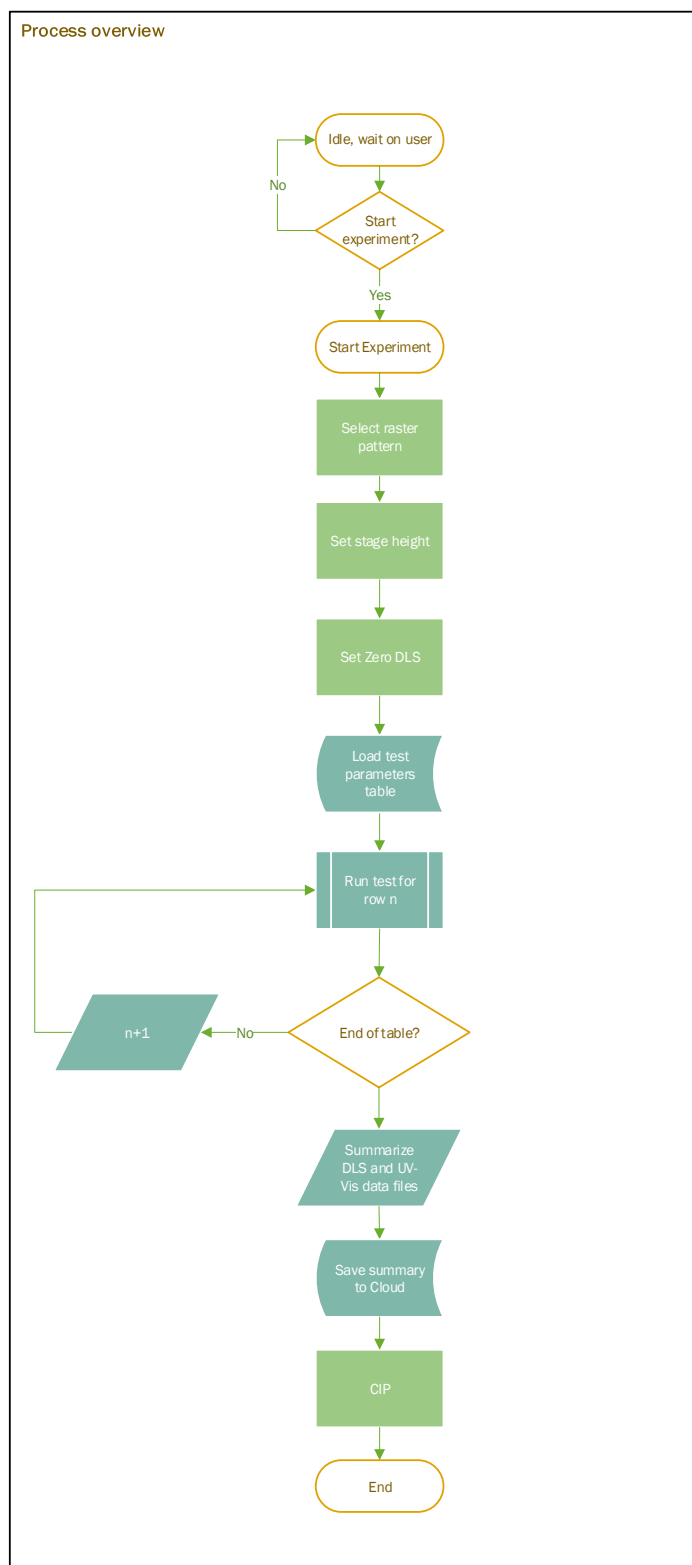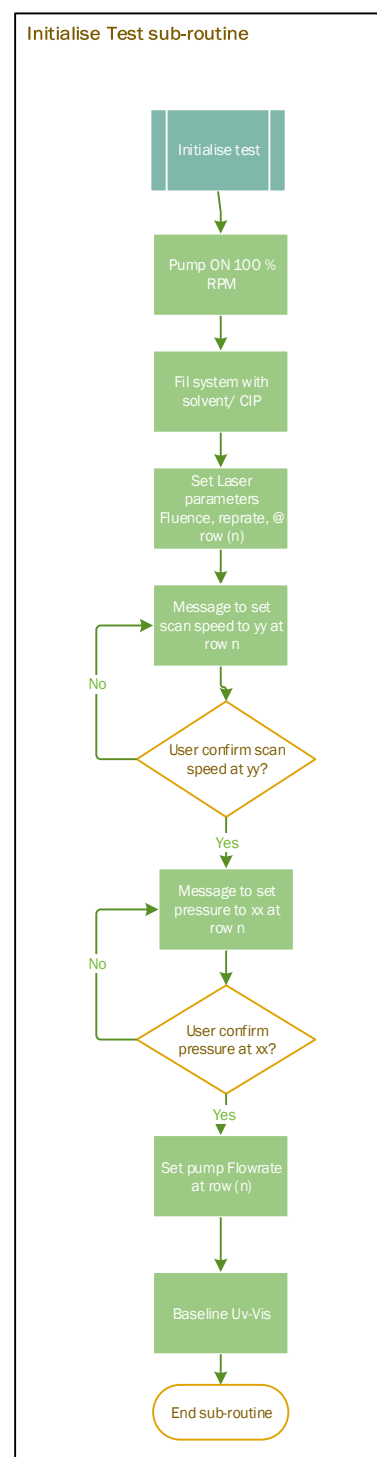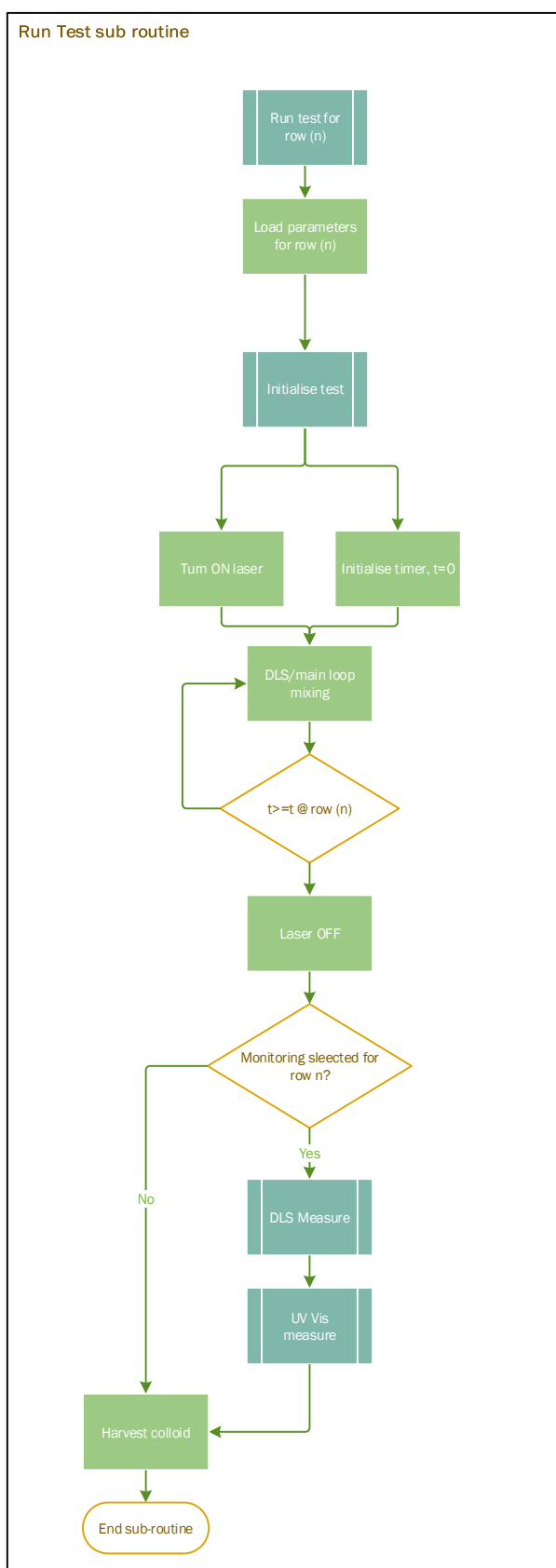

Figure A1: Laser wavelength productivity comparison: continuous ablation tests (Flowrate = 140 ml/min, RR = 20 kHz, pressure unregulated) 532 nm (τp = 700 ps) and 1064 nm (τp = 500 ps) laser systems at varying fluences. 532nm laser system provides higher production rate compared with 1064 nm at 0.8 J/cm2. Production decrease from 0.68 – 0.8 J/cm2 may indicate particle occluding laser irradiation and photo-fragmentation occurring.

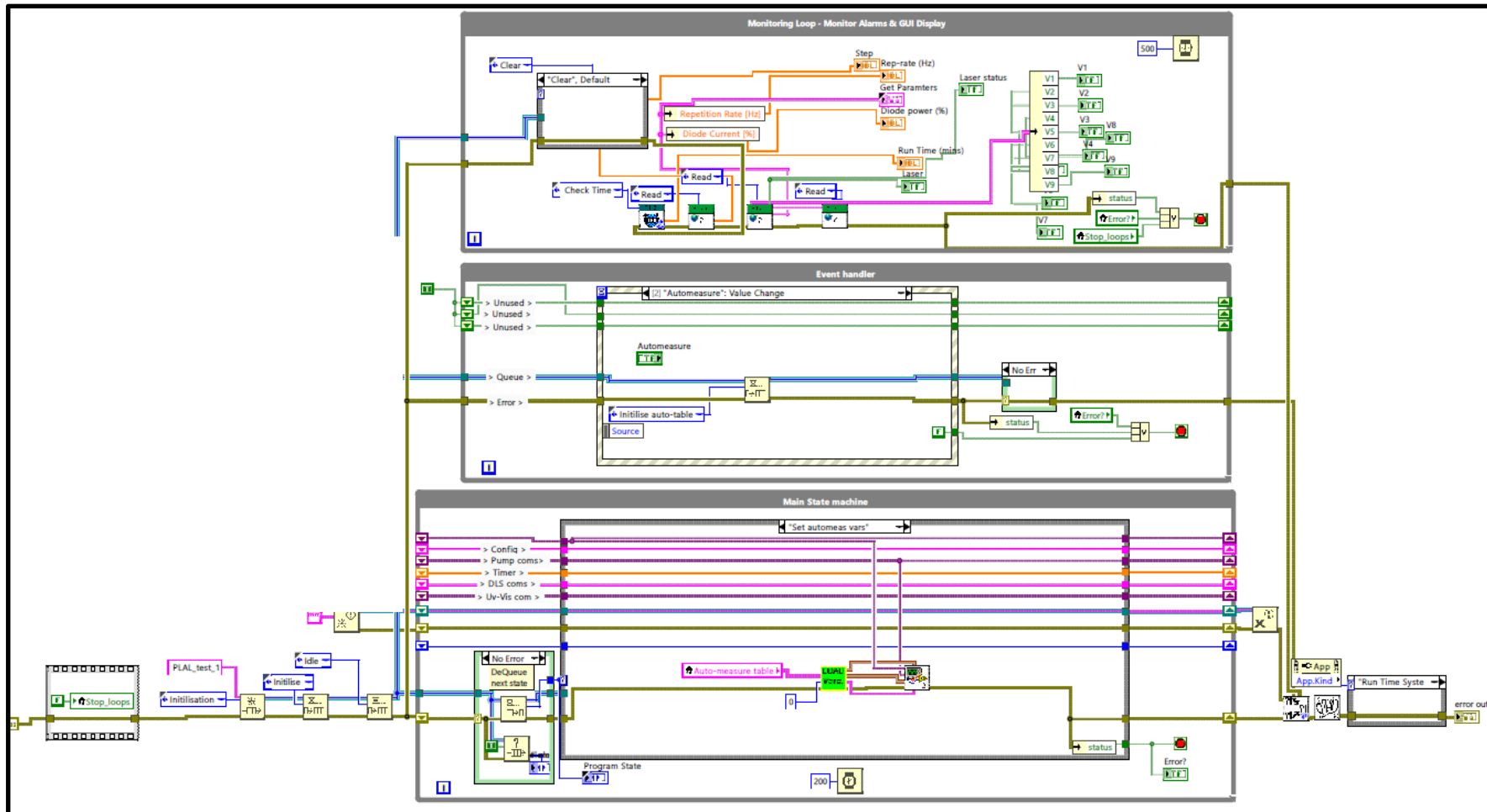# Appendix B

B.1. LabVIEW experimental test routine

Process overview

- Idle, wait on user
- Start experiment? — No (loop back to Idle)
- Yes
- Start Experiment
- Select raster pattern
- Set stage height
- Set Zero DLS
- Load test parameters table
- Run test for row n
- End of table? — No → n+1 (loop back to Run test for row n)
- Summarize DLS and UV-Vis data files
- Save summary to Cloud
- CIP
- End

B.2. LabVIEW experiment test sub-routines

B.3. LabVIEW program architecture

Queued message handler with observer loop software platform architecture.

Appendix C

C.1. LASiS production costs per year [65]

Description	Details (Jendrzej et. al., (2017))	Cost ($)*	Details DCU	DCU cost (€)
Raw material costs	Gold foil, Sigma-Aldrich, Germany.	159/g	Gold bulk target, https://www.bullionbypost.ie/gold-bars/1-gram-gold-bar/ (accessed 16th December 2019).	52/g
Investment costs	(Rofin Powerline 20 E, Rofin-Sinar, Germany, operated at 8.9 W output power, 10 ns)	54,646.0	Bright solutions Edge HF 1064 laser system	12,000.0
	Supplies (scanner, computer, power supply, lenses)	5,487.0		5,000.0
10% depreciation per year		6,013.0		1,700.0
3% maintenance per year		1,804.0		510.0
Diode (exchange every 10 years)		1,316.8	NA	0.0
Energy costs	Laser (supply and cooling)	1,067.1	Calculated at Irish electricity rates* assuming 130 W power consumption, as 24 V, 10A PSU spec to power laser.	35.9
Labour costs	Chemical laboratory assistant (1664 working hours/a)	44,317.0	DCU laboratory assistant (Grade 1)	29,459.0
	Total laser costs per year	**$10,200.9**		**€2,245.9**

C.2. Costs to produce 1 g of Gold Nps [65].

Description	Details (*Jendrzej et. al., (2017))	Cost ($)*	Details DCU	DCU cost (€)
	Personal cost per hour	26.6		17.7
	Laser cost per hour	6.1		1.3
	Total cost per hour	32.8		19.1
Synthesis time for 1 g of gold	at projected 85 mg/h	11.8	at experimental 80 mg/h	12.5
	Cost of laser production time	72.1	Converted to $ on 16th December 2019, €1 = $1.12	18.8
	Cost of personal & laser time ($)	385.4		265.4
Total production cost including bulk material for 1 g of AuNps	**$544.4**		Converted to $ on 16th December 2019, €1 = $1.12	**$323.3**

Appendix D

Controlled synthesis of Zinc Oxide Nanoparticles towards production of thin films via inkjet printing

D.1. Overview

Zinc oxide Nps were manufactured in recirculation mode using the 532 nm Bright Solutions laser system, F = 0.8 J/cm^2, RR = 20 kHz, flowrate = 100 ml/min are shown in Figure D1. At-line DLS measurements were taken at 30 minute intervals showing a reduction in ZnO Nps peak diameter and width over time. It is thought that this reduction in peak diameter and size dispersion size is due to photofragmentation of the Nps as they recirculates in the flow cell for 120 minutes.

Time (min)	Peak dia. (nm)	Width (nm)
30	87	74
60	65	100
90	56	67
120	42	38
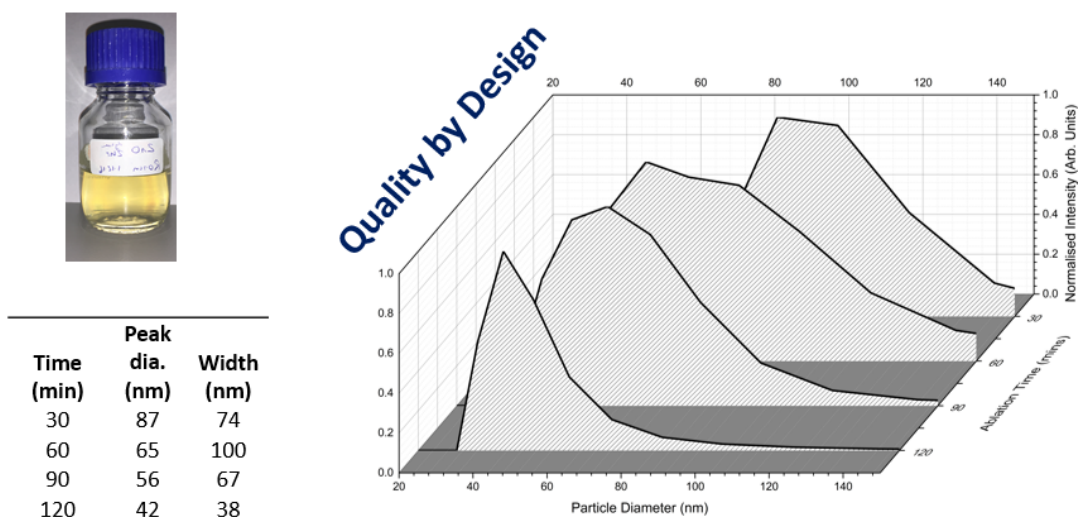
Figure D1: Real-time monitoring of ZnO production in IPA using 532 nm ND: YAG laser system.
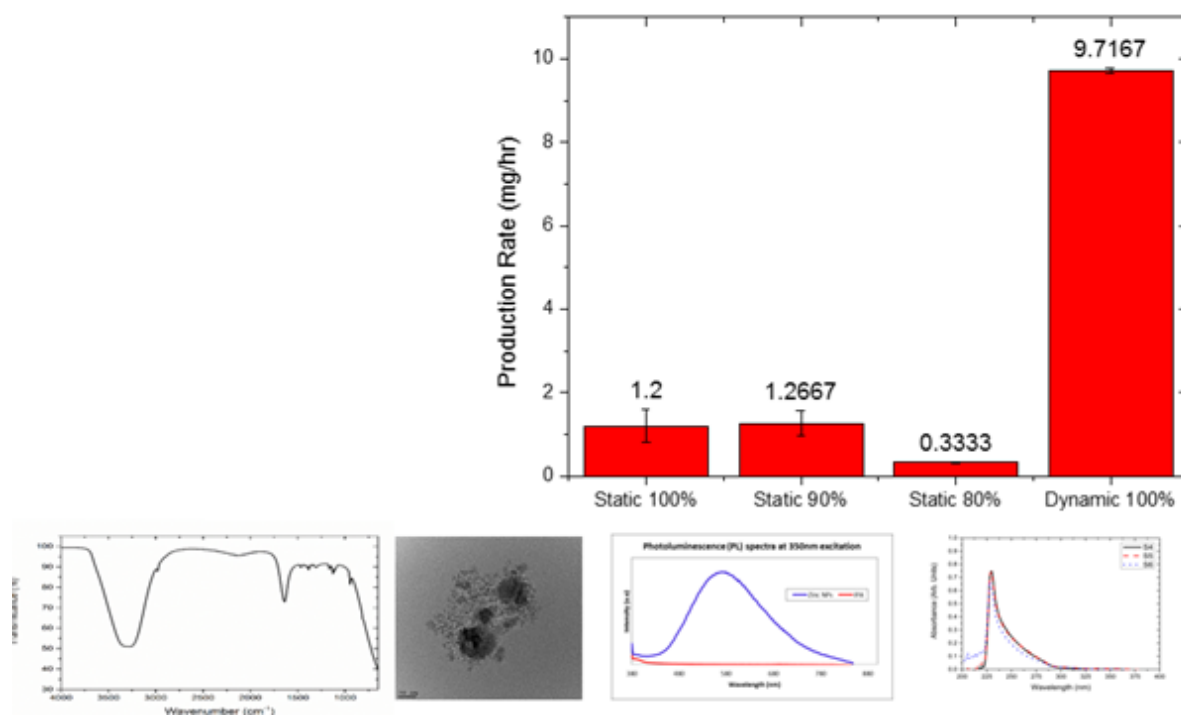
Figure D2: Production rate, Nps size, morphology, optical and chemical properties of ZnO Nps produced via 532 nm laser system.

D.2. Real-time monitoring of ZnO Nps produced via 1064nm laser system

Real-time DLS monitoring was implemented in order to determine the best solvent choice to fabricate ZnO Nps. A snapshot of DLS analysis taken after 10 minutes ablation is seen in Figure D3, where it can be seen thatsolvent choice can have an effect on Nps size produced.
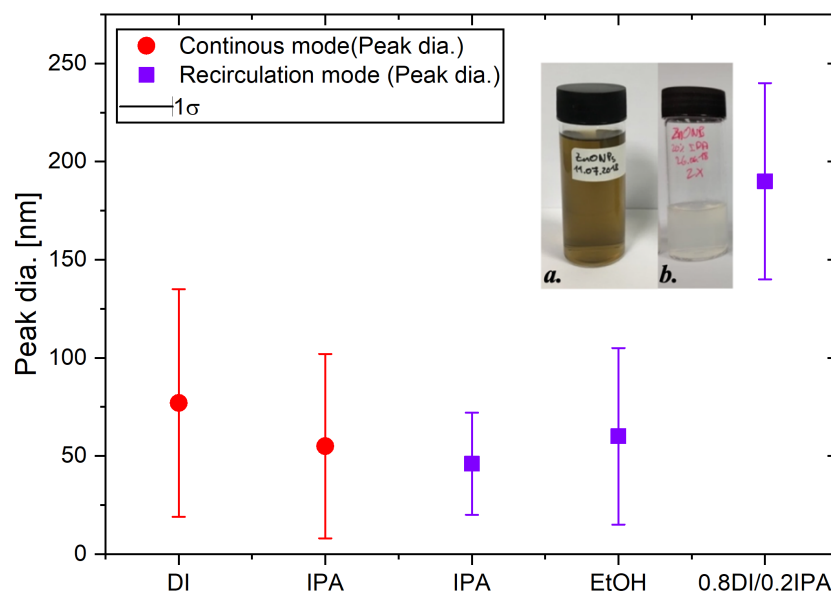

Figure D3: Effect of solvent selection on ZnONps size, colloids produced in (a) EtOH and (b) DI/IPA mix.

At-line DLS monitoring was continued on the ZnO colloids being fabricated for over 2 hours as illustrated in Figure D4. It can be seen that IPA and EtOH produced smaller size dispersions and more stable nanocolloids.
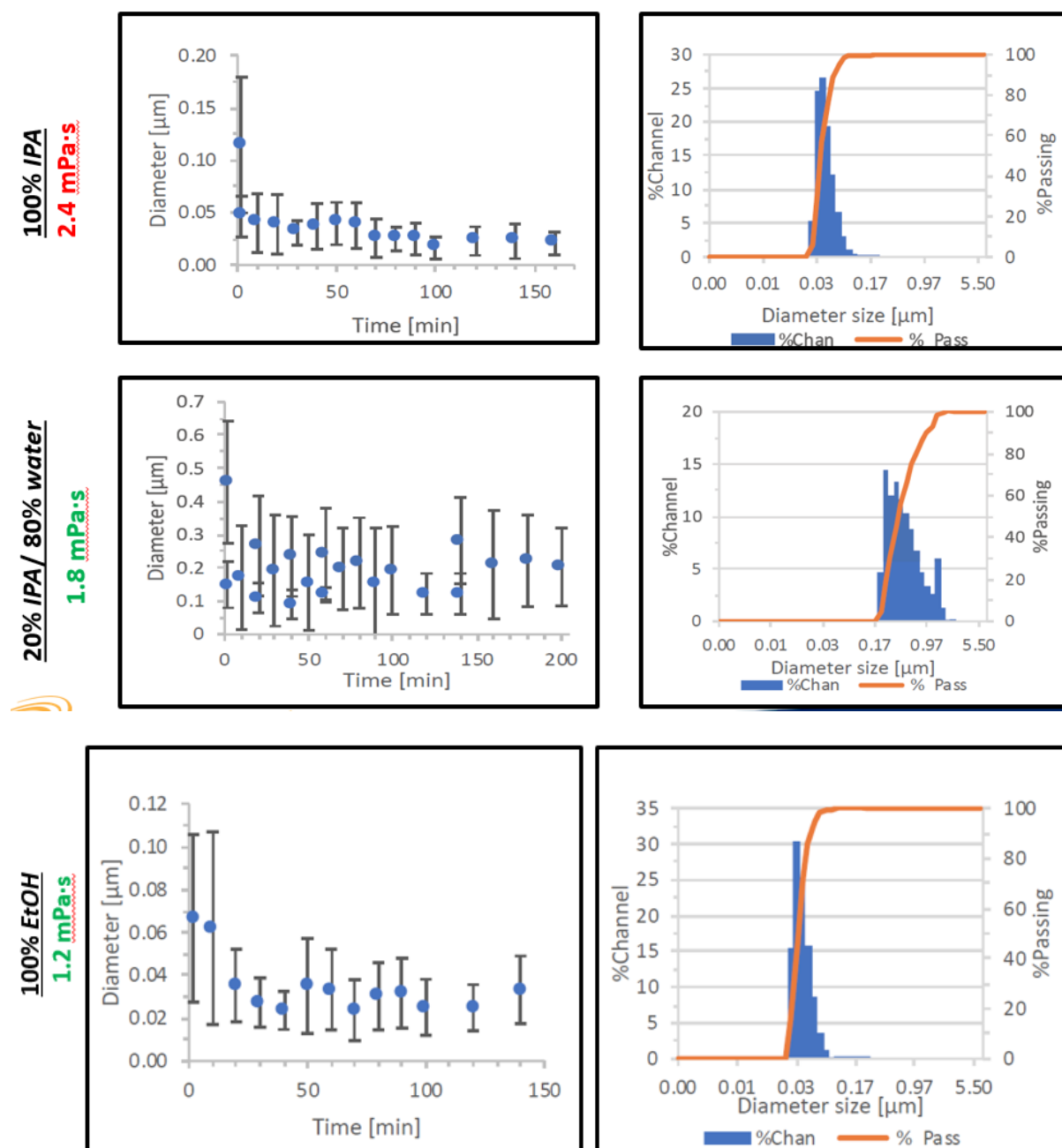

Figure D4: Real-time monitoring of fabrication of ZnO colloids produced with various solvents.

Appendix E

Nano-ink development

E.1. Overview

In order to print nanocolloid thin films development work was performed to characterise the viscosity of commercial inks, in order to produce a nanocolloid at a similar dynamic viscosity ranage. Initial test results are displayed below.
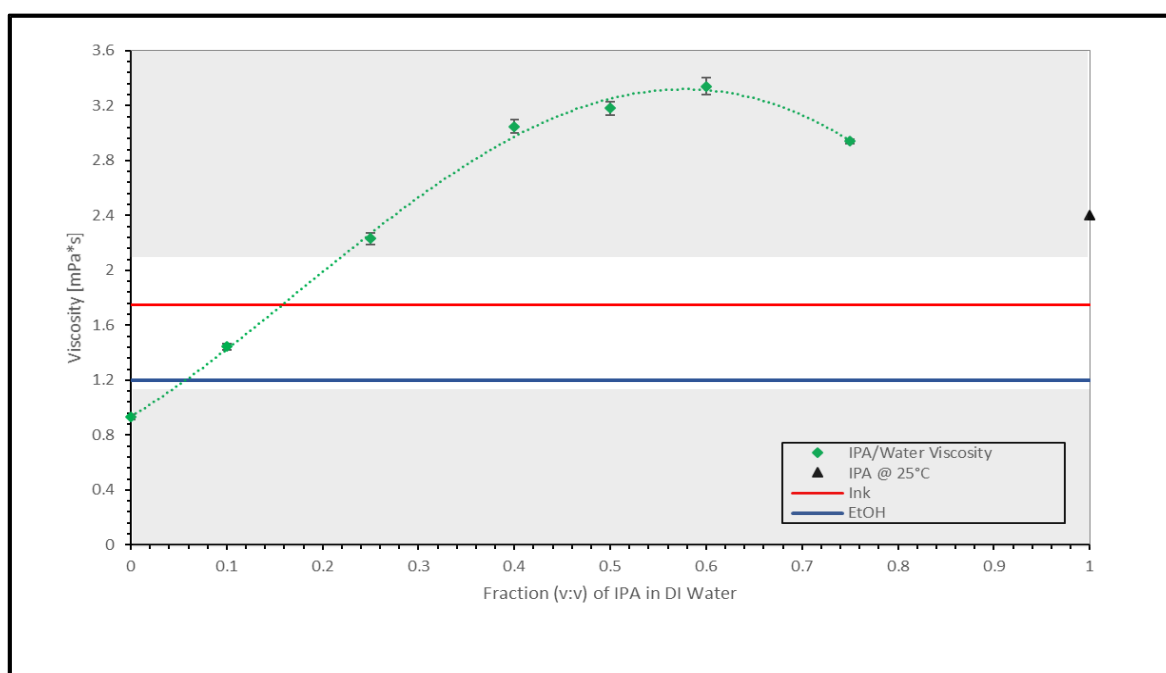
Figure E1: Viscosity tests of IPA/DI water fractions, commercial ink and EtoH. The white band on the graph indicates the dynamic viscosity limit for successful printing.

Viscosity (mPaS)	0.9	1.2	1.8	1.91	2.3
Ink Fractions	0.99 Water/ 0.1 food colouring	0.99 EtOH/ 0.1 Food colouring	0.2 IPA/0.7 Water/ 0.1 food colouring	0.2 IPA/0.8 Water + Au NPs	0.99 IPA/0.1 food colouring
Printing performance	Misfiring, unstable jet.	Jetting (stable) - controlled, even coverage.			Non-jetting (clogging)
Printed Image on cellulose	No image				No image

Figure E2: Custom ink produced and printing performance.

E.2. Production of ZnO thin-films

After the correct viscosity for printing was identified, ZnO colloids were printed onto COP as seen below. The SEM image shows homogenious coverage over the polymer.
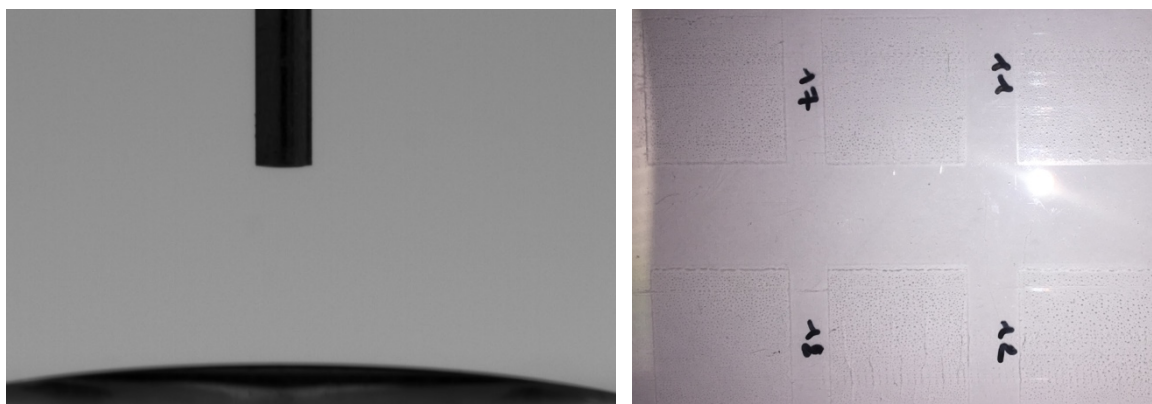

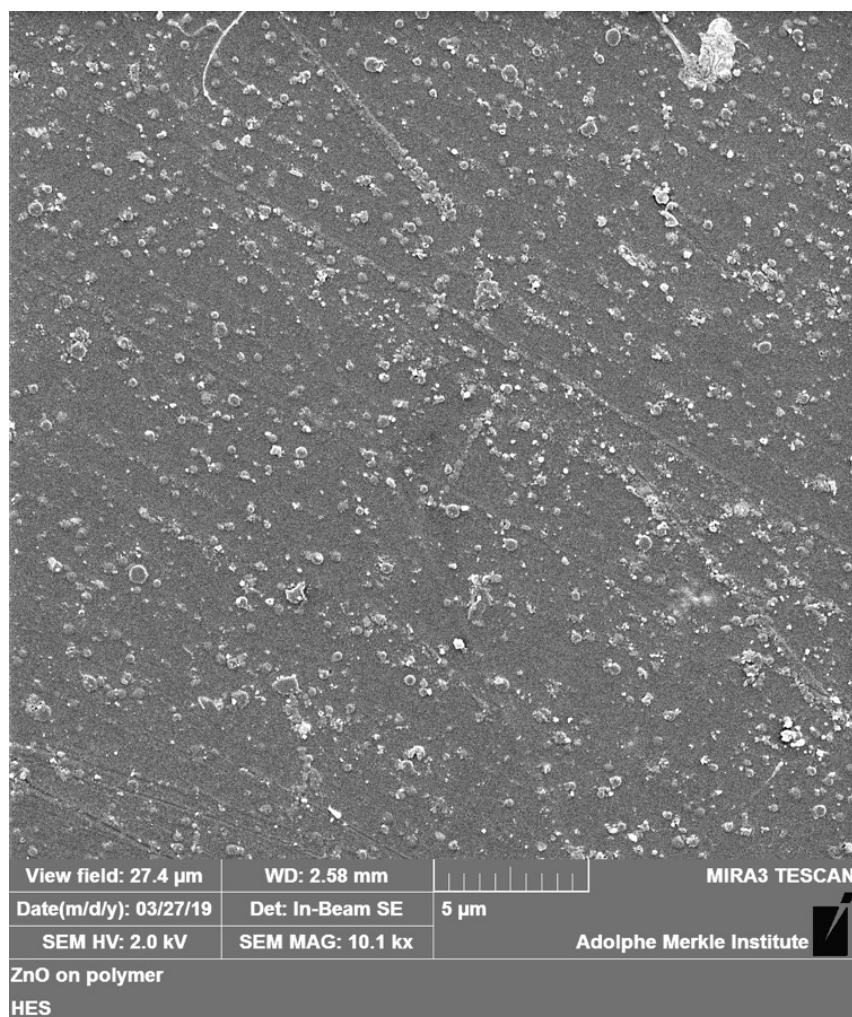*Figure E3: Contact angle test on ZnO printed thin-films.*

Figure E4: SEM image of ZnONps inkjet printed onto COP.

Appendix F

Production of AgNPs via LAsiS and USP: a comparison.

In collaboration with Gozde Alkan and Prof. Bernd Friedrich, Institute of Process Metallurgy and Metal Recycling (IME), RWTH Aachen University, Intzestraße 3, Aachen 52056, Germany.

F.1. Introduction

A further development of work conducted in chapter 6 was determining the anti-bacterial properties of AgNps produced by LASiS. Firstly AgNps were produced via LASiS in DCU, along with AgNps produced via USP in RWTH Aachen University. This Appendix briefly examines the Nps produced and their antibacterial properties.

F.2. Results and Discussion

F.2.1. Nanoparticle Morphology and Size

The morphology of the AgNPs produced via the two techniques were examined using Transmission Electron Microscopy (TEM) analysis, shown below. AgNps using both production techniques exhibited a spherical morphology, however the AgNps produced via USP were seen to have less ellipticity than those produced via LASiS.
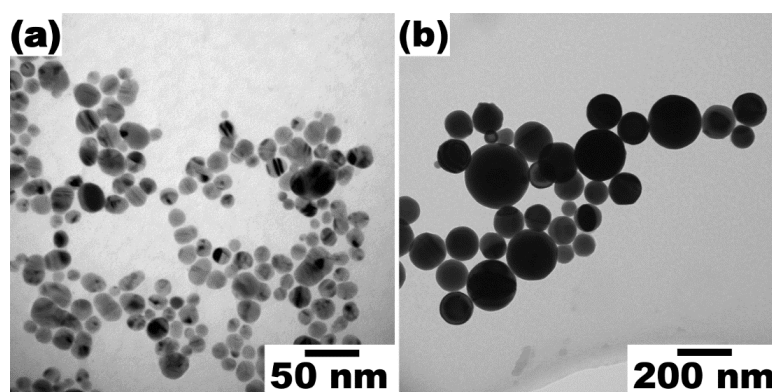

Figure F1: TEM Images of AgNPs fabricated via LASiS (a) and USP (b) with scale bars of 100 nm and 200 nm respectively.

DLS analysis shows the size distributions for the AgNPs produced via batch and recirculation LASiS and USP. AgNps produced via LASiS had the smallest peak diameter

and distribution width. AgNps produced via batch LASiS had a peak diameter of 30 nm ± 25 nm while those produced via continuous LASiS had a smaller size and size distribution of 10 nm ± 8 nm. The smaller NP size seen for dynamic ablation when compared to static, was attributed to the nanoparticles undergoing zero-dimensional ablation as the colloid is recirculated over the ablation size. This process reduces the size of the nanoparticles as a function of ablation time. Particles produced via USP had a size of 89 nm ± 115 nm. These values are larger than those Nps produced via wet-chemical (9nm ± 8nm) techniques.
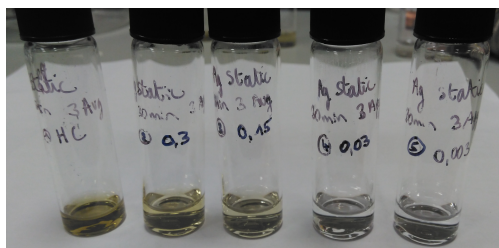

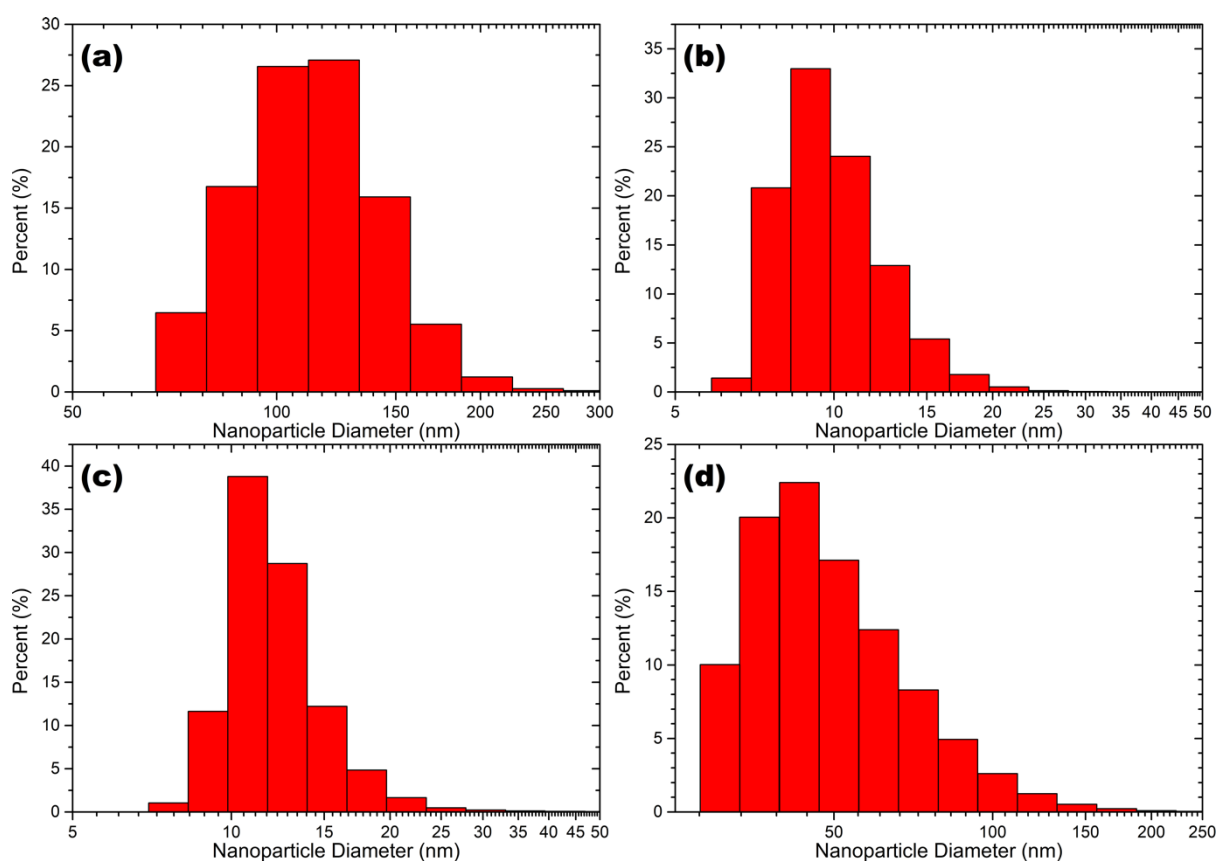
Figure F3: Dilution of LASiS AgNps colloid produced.

Figure F2:Nanoparticle size distributions for AgNps produced via (a) USP, (b) Commerical AgNps (Sigma Aldrich) (c) continuous LASiS and (d) batch LASiS.

F.2.2. Nanoparticle Morphology and Size

Table F2: Materials used to plate cells and for the addition of nanoparticles to 6 mm cellulose filter discs.

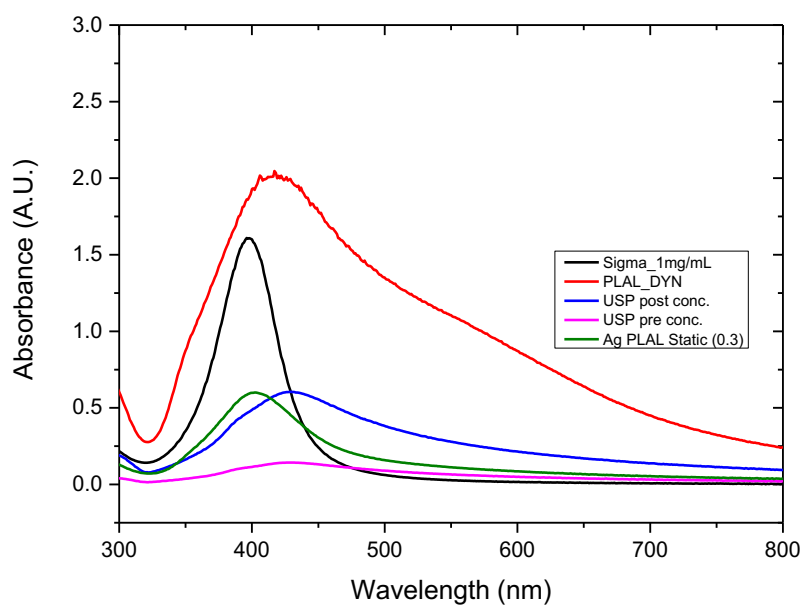| Material	Volume (µl)	Concentration (g/ml)	Concentration (mg/ml)
Silver (Sigma Aldrich)	20	1-0.005	5 – 1000
Batch LASiS	20	0.004-0.0004	0.4 – 4
Continuous LASiS	20	0.012-0.004	4 – 12
USP (Tube 1)	20	0.000367-0.0000367	0.037 - 0.367
USP (Tube 3)	20	0.000271-0.0000271	0.027 – 0.271

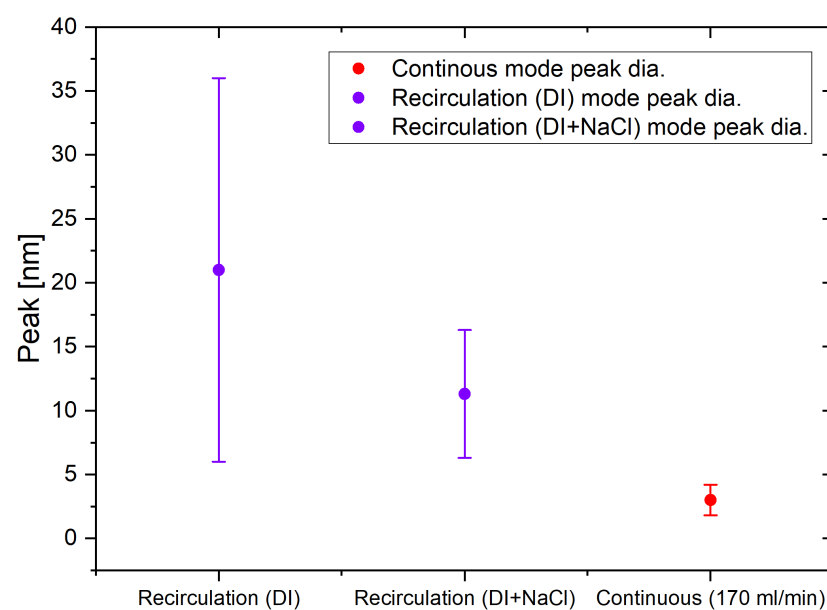*Figure F4: UV-vis of LASiS, USP samples produced.*

Figure F5: AgNps size produced via recirculation and continuous production with DI water and DI and salt addition.

Appendix G

G.1. Anti-bacterial tests of a polymer sheet coated with AgNps thin-film via inkjet printing

In collaboration with Allan Robert McGivern, Dimitrios Kakavas & Konstantinos Grintzalis, School of Biotechnology, DCU.

G.2. Materials and Methods

G.2.1. Antibacterial effects of nanomaterials

Bacteria (*E. coli*) were cultured in LB media at 30°C under agitation (200 rpm). Bacteria were pelleted (3000 *g*, 4°C, 5 minutes) and washed in sterile phosphate buffer saline (PBS) and pelleted twice. A dilution of bacteria in PBS was prepared at a concentration of 2300 cells/ml and 100 μl was exposed to AgNPs coated on a biopolymer film (approximate dimension of 0.25 cm^2) and incubated for 2 hours at 30°C under agitation (200 rpm). After exposure in PBS, 900 μl LB media were added and surviving bacteria were allowed to grow for 20 hours under agitation (200 rpm). Growth was measured by absorbance at 600 nm and converted to cell concentration. For comparisons of growth inhibition, penicillin G (50 μM) was incubated in the presence of the uncoated biopolymer.

G.2.2. Ecotoxicological effects of nanomaterials

Daphnids were cultured in conformity with OECD guidelines in 4 liters beakers in OECD media (final concentrations 0.29 g $CaCl_2.2H_2O$ /l, 0.123 g $MgSO_4.7H_2O$/l, 0.065 g $NaHCO_3$/l, 0.0058 g KCl/l, 2 μg Na_2SeO_3/l, pH 7.7) using 16h:8h of light:dark photoperiod at 20 °C and a density of 100 adults per 4 liters of media (Grintzalis et al., 2017). Neonates (<24 hours) were collected and exposed at 50 ml OECD media against unexposed controls and mortality was measured after 24 and 48 hours of exposure.

G.2.3. Statistical analysis

Data were analysed and plotted using Excel software and Student's *t*-test analysis was performed using the GraphPad Prism software. Results were expressed as average ± SD and considered statistically significant for P <0.05.

G.3. Results

AgNPs coated on biopolymer showed a 22% decrease in bacteria growth compared to 33% from penicillin G incubation (Figure 1).
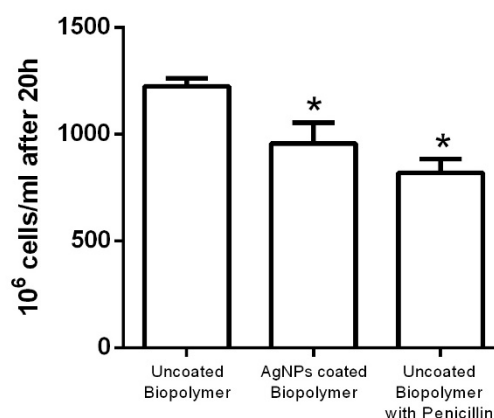

Figure G1: Impact of coated silver nanoparticles on bacterial growth. Data represent average ± SD (N=4) and considered statistically significant (*) compared with uncoated biopolymer by Student's t-test (p<0.05).
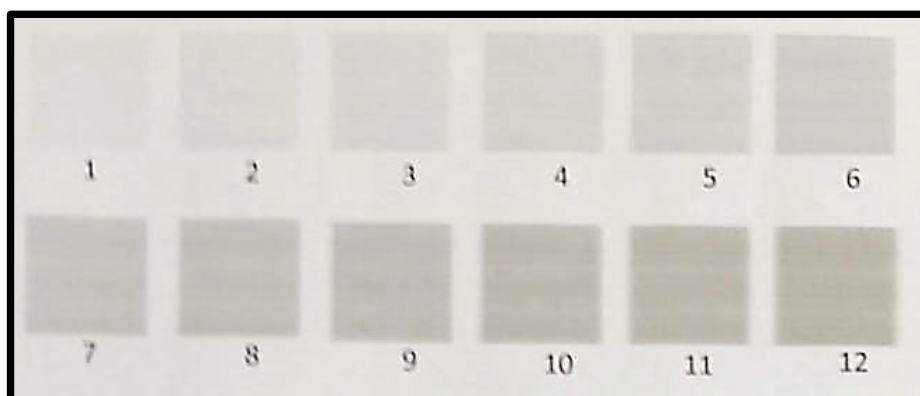

Figure G2: AgNPs printed onto COP.

Among the aquatic organisms studied in freshwater ecology and ecotoxicology, the water flea; *Daphnia magna*, has gained significant interest mainly because of their geographical distribution, central role in freshwater food webs, adaptation to a range of habitats and sensitivity to anthropogenic chemicals (Shaw et al., 2008). With nanomaterials being present in the environment and nanosilver being by far the greatest number of consumer product applications of nanomaterials the dose dependent mortality upon exposure to AgNPs was measured exposing daphniids. Toxicity curves at 24 and 48 hours of exposure (Figure 2A) of AgNPs in suspension showed a value of EC50 for 24 and 48 hours of 100 μl AgNPs/l. AgNPs coated on biopolymer showed a time dependent mortality of 0% at 24 hours, 21% after 48 hours and 49% after 72 hours of exposure (Figure 2B) in comparison with the control where all animals survived.
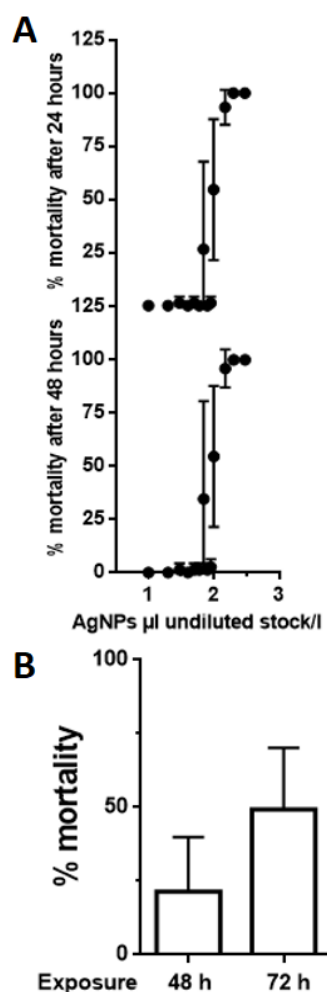
Figure G3: Mortality of daphniids upon exposure to silver nanoparticles in (A) suspension and (B) on coated biopolymer. Data represent average±SD (N=5).

F.G. References

1. Grintzalis, K., Dai, W., Panagiotidis, K., Belavgeni, A., Viant, M.R., 2017. Miniaturising acute toxicity and feeding rate measurements in *Daphnia magna*. Ecotoxicol Environ Saf. 139, 352-357. https://doi.org/10.1016/j.ecoenv.2017.02.002.

2. Shaw, J.R., Pfrender, M.E., Eads, B.D., Klaper, R., Callaghan, A., Colson, I., Jansen, B., Gilbert, D., Colbourne, J.K., 2008. *Daphnia* as an emerging model for toxicological genomics, In: Comparative Toxicogenomics, C Hogstrand, P Kille, Eds. Elsevier Science, 2, 165-219. https://doi.org/10.1016/S1872-2423(08)00005-7.

Appendix H

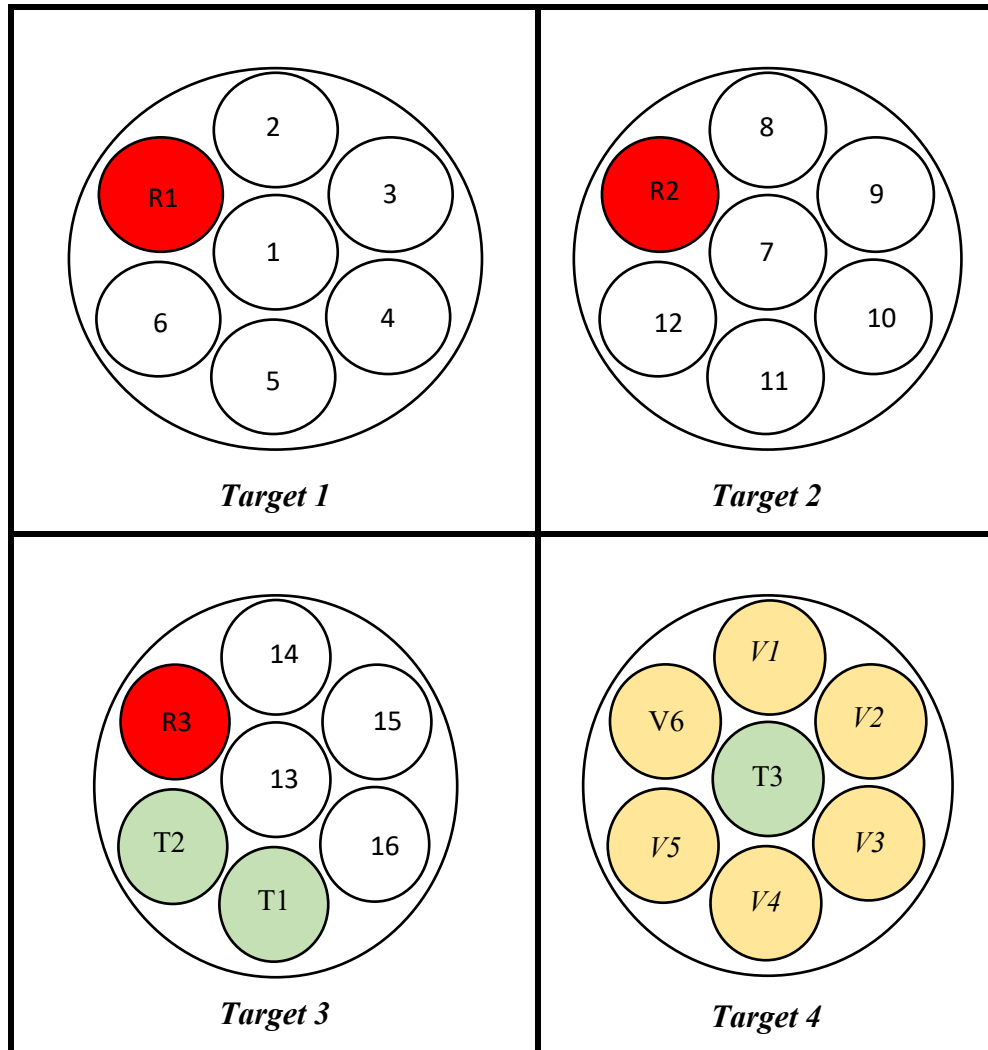*H.1. Rapid LASiS process characterization via automated design of experiments (DOE)*

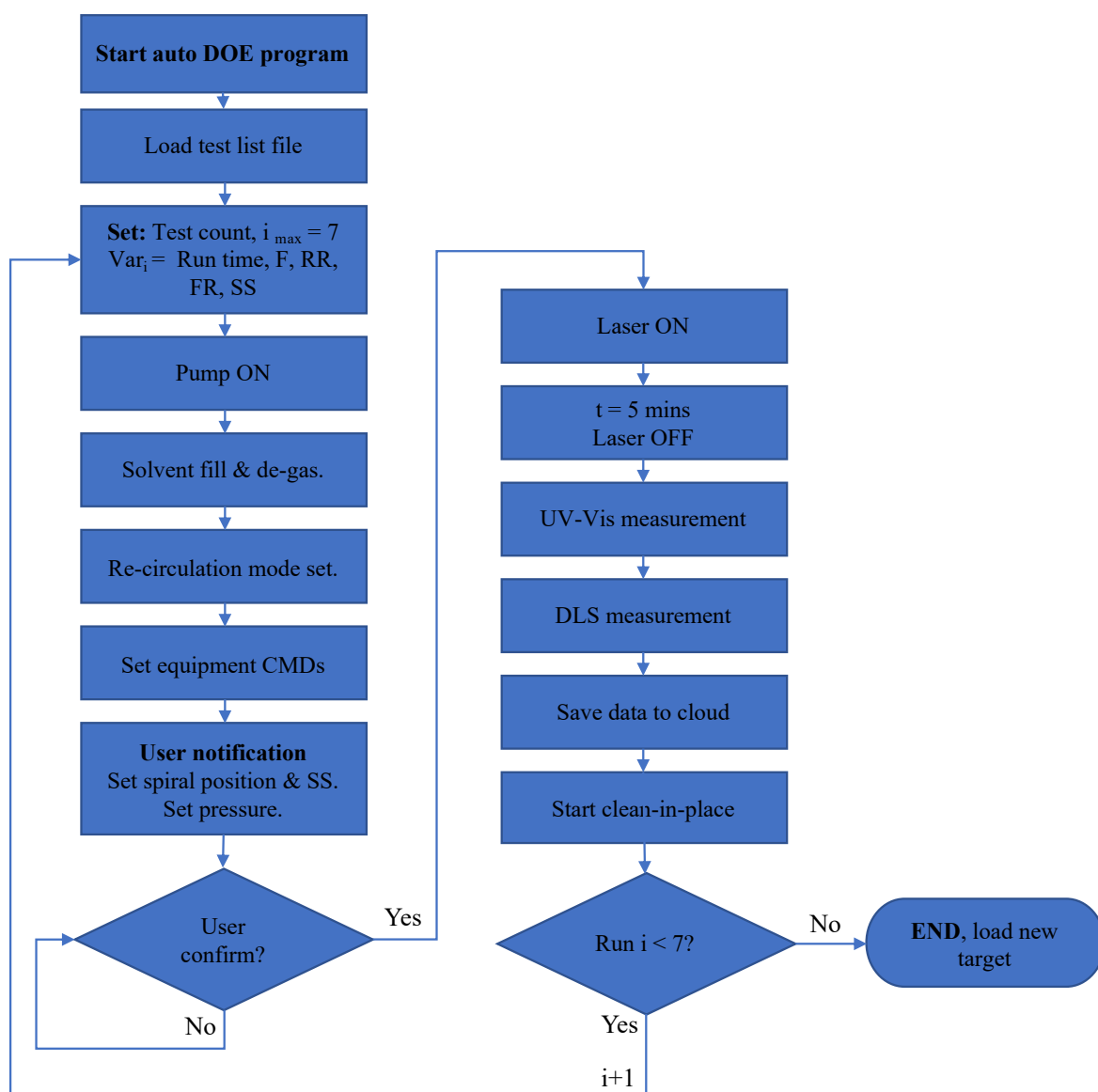*Figure H1: Spiral placement on targets 1 - 4, for Taguchi DOE.*

Figure H2: Flow chart of semi-automatic DOE program

Step	Run time (min)	Laser Power (%)	Rep rate (Hz)	Period (microS)	Pump Flowrate (rpm)	DLS meas (Y/N)	Uv meas (Y/N)	Ablation state	SetZero dls	Baseline uv
1	5	50	10000	3.5	20	y	y	Recycle	y	y
2	5	70	20000	3.5	45	y	y	Flow-through	y	y
3	5	66	30000	3.5	50	y	y	Recycle	y	y
4	5	82	40000	3.5	77	y	y	Recycle	y	y
5	5	46	50000	3.5	15	y	y	Recycle	y	y
6	5	100	11000	3.5	23	y	y	Recycle	y	y
7	5	94	10000	3.5	82	y	y	Recycle	y	y

Figure H3: Example of automatic experiment table loaded into the automatic LASiS test software.

H.2. Full-factorial experiments target layout